Colliding and Moving Bose-Einstein Condensates: Studies of superfluidity and optical tweezers for condensate transport

by

Ananth P. Chikkatur

Submitted to the Department of Physics
in partial fulfillment of the requirements for the degree of

Doctor of Philosophy

at the

MASSACHUSETTS INSTITUTE OF TECHNOLOGY

October 2002

Author .....
Department of Physics
October 18, 2002

Certified by .....
Wolfgang Ketterle
John D. MacArthur Professor of Physics
Thesis Supervisor

Accepted by .....
Thomas J. Greytak
Professor of Physics, Associate Department Head for Education

Colliding and Moving Bose-Einstein Condensates: Studies of superfluidity and optical tweezers for condensate transport

by

Ananth P. Chikkatur

Submitted to the Department of Physics
on October 18, 2002, in partial fulfillment of the
requirements for the degree of
Doctor of Philosophy

Abstract

In this thesis, two different sets of experiments are described. The first is an exploration of the microscopic superfluidity of dilute gaseous Bose-Einstein condensates. The second set of experiments were performed using transported condensates in a new BEC apparatus.

Superfluidity was probed by moving impurities through a trapped condensate. The impurities were created using an optical Raman transition, which transferred a small fraction of the atoms into an untrapped hyperfine state. A dramatic reduction in the collisions between the moving impurities and the condensate was observed when the velocity of the impurities was close to the speed of sound of the condensate. This reduction was attributed to the superfluid properties of a BEC.

In addition, we observed an increase in the collisional density as the number of impurity atoms increased. This enhancement is an indication of bosonic stimulation by the occupied final states. This stimulation was observed both at small and large velocities relative to the speed of sound. A theoretical calculation of the effect of finite temperature indicated that collision rate should be enhanced at small velocities due to thermal excitations. However, in the current experiments we were insensitive to this effect. Finally, the factor of two between the collisional rate between indistinguishable and distinguishable atoms was confirmed.

A new BEC apparatus that can transport condensates using optical tweezers was constructed. Condensates containing 10-15 million sodium atoms were produced in 20 s using conventional BEC production techniques. These condensates were then transferred into an optical trap that was translated from the 'production chamber' into a separate vacuum chamber: the 'science chamber'. Typically, we transferred 2-3 million condensed atoms in less than 2 s. This transport technique avoids optical and mechanical constrainsts of conventional condensate experiments and allows for the possibility of novel experiments.

In the first experiments using transported BEC, we loaded condensed atoms from the optical tweezers into both macroscopic and miniaturized magnetic traps. Using microfabricated wires on a silicon chip, we observed excitation-less propagation of a BEC in a magnetic waveguide. The condensates fragmented when brought very close to the wire surface indicating that imperfections in the fabrication process might limit future experiments.

Finally, we generated a continuous BEC source by periodically replenishing a condensate held in an optical reservoir trap using fresh condensates delivered using optical tweezers. More than a million condensed atoms were always present in the continuous source, raising the possibility of realizing a truly continuous atom laser.

Thesis Supervisor: Wolfgang Ketterle
Title: John D. MacArthur Professor of Physics

To my parents
Purushotham and Indira

for making all of this possible...

Acknowledgments

There are many people who have made my life most productive and satisfying during the last five years on the 2nd floor hallway of building 26 at MIT. I am grateful to Wolfgang Ketterle for giving me the opportunity to become a part of the AMO community here. Wolfgang has been an inspiration for me throughout my graduate school career. I am most impressed by him as a scientist. He has that eternal curiosity, the joy of working in the lab and being able to communicate his excitement to rest of us. His ability to focus on what really matters is impressive. This characteristic of Wolfgang has only grown over the years, despite winning various accolades and prizes, including the Nobel. Wolfgang has also been a wonderful physics teacher and a mentor to me. I owe him many thanks for teaching me to be a better scientist.

I also thank Dave Pritchard for his insightful discussions. Dave has been collaborating with us since 1999, and it is truly a privilege to have worked closely with scientists such as Wolfgang and Dave. I have also had the pleasure of interacting with Dan Kleppner, who was my academic advisor.

When I joined the group in the summer of 1997, it was the twilight of Wolfgang's time in the lab. I was one of his first students who did not work with him directly in the lab due to his expanding work load. Therefore, it has been the cadre of graduate students and post-docs to whom I owe a great deal for teaching me to be an AMO experimentalist. Specifically, I thank Dan Stamper-Kurn, Axel Görlitz and Todd Gustavson. At different stages of my graduate career, each of them have been invaluable to me as colleagues and as teachers.

In the summer of 1997, when I first joined the group, I worked with Dan Kurn (later Dan Stamper-Kurn) on setting up the optics for the optical dipole trap. This was my first taste of the teamwork and camraderie that has always been a hallmark of the Ketterle labs. I spent many weeks working with Dan, Hans Miesner and Mike Andrews trying confine a BEC optically. I thank Mike Andrews for patiently answering all of my initial questions about how the apparatus worked. I was impressed by his ability to rapidly change things and knowing exactly how to fix something in the lab. During 1998-1999, there were two teams working on the 'old lab' apparatus, one lead by Dan Stamper-Kurn and Hans Miesner, and the other by Jörn Stenger and Shin Inouye. I participated with both teams and benefitted from learning various techniques and sharing the excitement of discovering new BEC effects with them.

Dan was not only my colleague and office-mate at MIT, but most importantly, he is my friend and teacher. His views on physics and scientific community at large inspired me and I learned a lot of the BEC physics from him. We also had long discussions on various other topics ranging from Jewish traditions to politics in science. He was the person that I most looked up to in the lab. I benefitted both scientifically and personally by working closely with Dan. The two post-docs, Hans and Jörn, taught me to balance life in the lab

with the world outside. The lab-life was always entertaining with Jörn's lively description of power supplies and magnetic coils. 'Shunty' Shin was the quietest and the most modest member of the group, yet at the same time his insights and experimental skills were amazing. Although I did not get to spend much time with him during his last year, he has always been a good friend and trusted colleague. Tilman Pfau, in a very short period of time, became an important member of group because of his deep understanding of physics and general helpful nature.

In spring of 1999, we were joined by Axel Görlitz. Axel and I worked as a team on the collisions project. We spent a lot of time together in the lab sorting out various technical issues, and with his experience we made fast progress on understanding the collision physics and implementing it in the lab. This period of time, working with Axel, was my most productive time in the lab in terms of the AMO physics I learned. The team work and spirit remained at high levels when we were joined by Todd Gustavson and Aaron Leanhardt in late 1999. I had then decided to work on building a new BEC machine to transport condensates. Todd and I took charge of building this new apparatus: the 'science chamber'. We worked as a true team and spent a lot of time getting ultra-high vacuum, and then BEC in the new chamber. Todd's high spirit and ever optimistic approach was inspiring. Despite the fact that Axel, Todd and I also had lots of heated discussions on physics and design of the chamber, we always compromised and worked together such that the personal chemistry in the lab was never better. It was truly my good fortune to learn from Todd's large technical capabilities and ability to design things. Aaron joined our group as a new graduate student in fall of 1999. He quickly got engaged in the lab by designing the new magnetic trap and by helping Deep with the Zeeman slower. I have always been impressed by his stamina, work ethic and attention to details. He is an excellent leader and scientist, and will be a wonderful professor one day. Last year, Yong-Il Shin and David Kielpinski joined Aaron and I to work exclusively on the science chamber. I am grateful to Yong for all his efforts in ensuring the success of the continuous BEC. Yong and Aaron embody the kind of self-motivated students that I have had the privilege of working with at MIT.

Last, but not least, I express my thanks to Deep Gupta for being not only my colleague, but also my good friend and house-mate. Deep joined Dave Pritchard's interferometry group at the same time I joined the Ketterle group in 1997. He and Dave Pritchard later joined forces with us. Although we worked most closely during the construction of new apparatus, my best memories of him will always be of us drumming together at various occasions. I am also very grateful to him for a careful reading of my thesis.

While I have worked intimately with the people described above, the larger Ketterle group has also been important for making my MIT life memorable. I thank Chandra Raman and Roberto Onofrio for their kindness and humor, Jamil Abo-Shaeer for breaking the stress-filled tension in the lab with his quirky humor and antics, Zoran Hadzibabic for his ever-present calmness, Chris Kuklewicz and Johnny Vogels for helping me build

and improve the word generator, Johnny for his amazing patience with me and for his entertaining wildness in the lab, James Anglin for explaining the nuances underlying BEC theory, and finally Dominik Schneble and Deep for reading through large parts of this thesis. I would also like to acknowledge the contributions of Till Rosenband, Robert Löw and Edem Tsikata for building parts for the science chamber, Claudio Stan for technical help, Kaiwen Xu, Kai Dieckmann, Micah Boyd and Gretchen Campbell for helping me with my computer troubles, and finally Gretchen and Jit Kee Chin for being my coffee partners. The interactions with the larger MIT physics community has also been wonderful, in particular with the hydrogen, ICR and interferometer groups. It has been my pleasure to have known James Thompson, Simon Rainville, Mike Bradley, Julia Steinberger, Kendra Vant, Lia Matos, David Kokorowski, Alex Cronin, Joel DeVries, Pradeep Sarin and Augustine Urbas. We have had the best of times both at MIT and on the softball field as 'Balldrivers'. Especially after the birth of the Center for Ultra-cold Atoms (CUA), I have had increased contact with members of Harvard AMO groups, in particular with the Doyle and Prentiss groups. I especially thank Mukund Vengalatorre and Mara Prentiss for their assistance with our first atom chip.

Carol Costa, our secretary, was the first person that I met at MIT when I joined the group in 1997. Throughout the last five years, she has been a great help for simplifying and solving the complex bureaucracy of MIT, and generally making life in building 26 better. I also would like to thank the support staff at RLE, in particular Al McGurl, Gerry Power, Bill Gibbs and Maxine Samuels, for their understanding and patience. During the construction of the science chamber, Fred Cote of the Edgerton Center Student Shop was extremely helpful and generous to us.

I have also benefited personally interacting with the larger MIT community, especially volunteering with the student group, Asha-MIT. This group provided me with an opportunity to explore issues outside of physics. I am grateful to all of the Asha volunteers at MIT for sharing many of their Sunday afternoons with me. I am deeply thankful to my friends, Kerry and Rajesh, who have always supported me through thick and thin. Their friendship is very dear to me, in ways I cannot even express. Our discussions have led me to see the world in a new light and made me a better person. I am also grateful for the larger friendships that I have developed with the Indian community here in the Boston area. I also thank all of my friends from Rochester and in Boston for their support and encouragement throughout the last five years.

Finally, I would like to thank Anita, my sister, who has always supported me with my 'crazy' decisions, and my parents, Indira and Purushotham. I am forever grateful for the sacrifices that they have made in their lives to give me the opportunity to study at a place like MIT. They have always been, and continue to be, my first and foremost teachers. With love...

This work was supported by the National Science Foundation (NSF), the Office of Naval Research (ONR), the Army Research Office and the Joint Services Electronics Program (JSEP) of the Army Research Office (ARO), the National Aeronautics and Space Administration (NASA), and the Packard Foudation. I also appreciate the support of a NSF Graduate Fellowship and a JSEP Graduate Fellowship.

Contents

List of Figures

List of Tables

Chapter 1

Introduction

1.1 What is Bose-Einstein Condensation

Bose-Einstein Condensation (BEC) is so well known now that it has almost become a household name, at least in the houses of most physicists. Awarding of the 2001 Nobel Prize for Physics to Wolfgang Ketterle (my adviser and mentor), Eric Cornell and Carl Wieman "for the achievement of Bose-Einstein condensation in dilute gases of alkali atoms, and for early fundamental studies of the properties of the condensates," [20–22] has increased the public awareness and curiosity about BEC. Most lay people tend to understand BEC as atom lasers. Analogous to photons in an optical laser, the Bose condensed atoms are in a coherent state that forms the key ingredient for an atom-laser [23, 24]. The output of the laser is coherent, diffraction-limited, and very bright, which is in stark contrast to the properties of the more familiar particle sources, such as the photons emanating from light bulbs and the atoms in the air that we breathe.

To lay people, I usually answer the question, "What is a BEC?", by the statement, "BEC is the giant matter-wave that is formed when atomic matter waves begin to overlap". Technically, this 'giant matter wave' is the macroscopic occupation of a single-particle wave-function of a many-body system. And, the atomic waves 'begin to overlap' when the spacing between atoms, $d = n^{-1/3}$, becomes equal to their de-Broglie wavelength, $\lambda_{dB} = \sqrt{\frac{h}{2\pi M k_B T}}$, or in other words, when the phase space density $\rho = n\lambda_{dB}^3$ is of order unity. The mass of the atom is denoted by M, T is the temperature of the system, n is the gas density, and h and k_B are Planck and Boltzmann constants, respectively. Entering the regime where $\rho \sim 1$ requires high density or low temperatures. At high densities, such as the density of water ($\sim 10^{23}$ cm^{-3}), the strong interactions between atoms preclude Bose condensation as gases transition into liquids and solids. Therefore, in order to minimize interactions between atoms in a gas, one uses dilute gases ($n = 10^{13} - 10^{15}$ cm^{-3}), implying that dilute gas BEC occurs only at low temperatures (μK to nK range). At low temperatures, the quantum effects become more apparent and a deeper understanding the phase transition from a 'normal' gas to a Bose condensed gas requires the synthesis of classical statistical

mechanics with quantum mechanics.

1.1.1 History of BEC

Given the maturity of the field, it almost meaningless to write yet another summary of the historical roots of BEC. I will, however, give a very brief summary of the important theoretical concepts for understanding BEC and then describe its manifestation in the laboratory. The first chapter of the Varenna lecture notes [25], the doctoral theses of Dan Stamper-Kurn [26] and Shin Inouye [27], and the Physics 2001 Nobel Lectures [21, 22] provide an excellent overview of the history of BEC. These references and the references therein discuss both the theoretical and the experimental efforts leading to the first observation of BEC in dilute gases[28–31].

1.2 The BEC theory: understanding a quantum gas using statistics

Theoretical understanding of Bose-Einstein condensation requires knowledge of the basic assumptions underlying of quantum statistical mechanics, the consequence of indistinguishability of atoms, and of atom number conservation.

1.2.1 Basics of Quantum Statistical Mechanics

Statistical mechanics explains the phenomena of the macroscopic physical world based on the statistics of the microscopic world. The claim is that regardless of how a system reaches equilibrium, the equilibrium state can be derived using only statistics. Since the microscopic world is governed by the laws of quantum mechanics, especially at low temperatures, it is quantum statistical mechanics that is of interest. The fundamental assumption of statistical mechanics is that for a system in interacting with an external world such that its total energy is approximately constant, all micro-states of that system satisfying the conservation laws (such as energy, momentum, and number) *are equally likely* to be occupied. This is the principle of *equal a priori probability*. Quantum mechanically, the wavefunction of the system $|\Psi\rangle$ at equilibrium is given by

$$\Psi = \sum_i b_i \Phi_i, \tag{1.1}$$

where $\{\Phi_i\}$ is complete orthonormal basis set of wavefunctions of the system, and

$$|b_i|^2 = \begin{cases} 1 & : \text{ if } \Phi_i \text{ satisfies the conservation laws,} \\ 0 & : \text{ otherwise.} \end{cases} . \tag{1.2}$$

The coefficients $\{b_i\}$ depend only the system coordinates and its phases are random numbers, therefore averaging over the Hilbert space of $|\Phi_i\rangle$ implies averaging over the external world in an average manner[1]. The value of any observable of the system $\mathcal{O}$ can be calculated by averaging over the eigenfunctions of the system:

$$\langle \mathcal{O} \rangle = \frac{\sum_i |b_i|^2 \langle \Phi_i | \mathcal{O} | \Phi_i \rangle}{\sum_i |b_i|^2}. \tag{1.3}$$

Thus, we can imagine averaging over an ensemble of systems each representing an eigenfunction Φ_i of the system. This ensemble is the micro-canonical ensemble. In the density matrix formulation, the elements of the density matrix of the system can written as

$$\rho_{ij} = \delta_{ij} |b_i|^2, \text{ with} \tag{1.4}$$

$$|b_i|^2 = \begin{cases} \Gamma(E)^{-1} & : \text{ if } \langle \Phi_i | \mathcal{H} | \Phi_i \rangle = E, \\ 0 & : \text{ otherwise.} \end{cases}, \tag{1.5}$$

where $\mathcal{H}$ is the system Hamiltonian and $\Gamma(E)$ is the volume of phase space that has energy E. All thermodynamic functions can be derived using the density matrix above [32].

The classic pedagogical problem in statistical mechanics is to derive the equilibrium properties of a N-particle ideal gas in a volume V by enumerating the microscopic states that the N-atoms in the gas occupy and the probability of their occupation. The dynamics of the N-particle microstates can be very complicated and hence studying the evolution of a gas to its equilibrium is very difficult. However, using the ergodic hypothesis, one can perform an ensemble average over these states to determine the most probable distribution of states, which is the equilibrium distribution. In fact, one need not even study the N-body distribution function, but only a single-particle function. This is valid assuming that the gas is very dilute and that the correlations between particles are lost immediately after any collisions, i.e., the gas is under *molecular chaos* [32]. Interatomic interactions, or collisions, is the responsible for molecular chaos. Some aspects of these collisions in BEC are studied in Chapter 2.

1.2.2 Quantum gas of indistinguishable atoms

The statistics of identical atoms dramatically depends on the atoms' spin. By the spin-statistics theorem [33], the occupation probability of identical atoms is different for bosons (integer-spin atoms) and fermions (half-integer spin atoms). This arises from a fundamental symmetry (parity) consideration that requires the total wavefunction be either symmetric (bosons) or anti-symmetric (fermions) under exchange of any two particles:

$$\Psi(1, 2, 3, ...k..l...N) = \pm \Psi(1, 2, 3, ...l..k...N) \tag{1.6}$$

[1]Note that the external coordinates are time averaged with the assumption of *random phases* [32].

with + sign corresponding to bosons and − for fermions. The Hilbert space of wavefunctions with energy E is then divided into fermionic and bosonic wavefunctions, where these wavefunctions satisfy the symmetry conditions. The occupation number of these new energy eigenstates is then

$$n_i = \begin{cases} 0, 1, 2...N & : \text{ for bosons,} \\ 0, 1 & : \text{ for fermions.} \end{cases}, \tag{1.7}$$

with $\sum_i n_i = N$ and $\sum_i n_i E_i = E$.

Using the Grand Canonical formulation where the number of particles in the system is also allowed to vary, with the average number of particles being N, the average occupation number is

$$\langle n_i \rangle = \begin{matrix} \left[\exp\left(\frac{E_i-\mu}{k_B T}\right) - 1\right]^{-1} & : & \text{for bosons,} \\ \left[\exp\left(\frac{E_i-\mu}{k_B T}\right) + 1\right]^{-1} & : & \text{for fermions.} \end{matrix}, \tag{1.8}$$

where μ is the chemical potential.

In the high temperature limit, the equations for fermions and bosons both reduce to the classical Maxwell-Boltzmann distribution:

$$n_i^{MB} = \exp\left(\frac{\mu - E_i}{k_{\mathrm{B}} T}\right), \tag{1.9}$$

As discussed earlier, this equilibrium distribution can be derived without any consideration for how the system evolves into that equilibrium state.

1.2.3 Number Conservation

Studying eq. 1.8, it becomes obvious that the fraction of bosons occupying the lowest single particle energy state ($E_i = 0$ for an ideal gas) is

$$\frac{N_0}{N} = \frac{z}{1-z}, \tag{1.10}$$

where $z = \exp\left(\frac{\mu}{k_B T}\right)$ is the fugacity. As the temperature of the gas gets close to zero, a large fraction of atoms occupy the single particle ground state. This macroscopic occupation of the ground state is the result of the *conservation of atom number*: the atoms cannot be destroyed! This situation is very much different from photons and phonons in a solid, where lowering temperature only leads to a reduction in the number of photons/phonons as they disappear into the blackbody cavity or the crystal.

In the thermodynamic limit, BEC transition is a first order phase transition with the total density of the system being

$$n = \frac{g_{3/2}(z)}{\lambda_{dB}^3} + \frac{N_0}{V}, \tag{1.11}$$

where Bose function $g_n(z) = \sum_{k=0}^{\infty} \frac{z^k}{k^n}$. In finite systems, the transition is smooth. First term in eq. 1.11 is the number of atoms in the excited states and the second term is the density of condensed atoms. As noted in section 1, the number of condensed atoms becomes macroscopic only when $n\lambda_{dB}^3 > g_{3/2}(1)$, where $g_{3/2}(1) = \zeta(3/2) = 2.612...$[2]. The transition temperature T_c is

$$k_B T_c = 2\pi\hbar^2/m \left(\frac{n}{\zeta(3/2)}\right)^{2/3}, \tag{1.12}$$

and the fraction of condensed atoms is

$$\frac{N_0}{N} = \begin{cases} 0 & : \quad n\lambda_{dB}^3 \leq \zeta(3/2), \\ 1 - \left(\frac{T}{T_c}\right)^{3/2} & : \quad n\lambda_{dB}^3 \geq \zeta(3/2). \end{cases} . \tag{1.13}$$

Typically, for our sodium Bose-Einstein condensates, the number density is 10^{14} cm^{-3} and the transition temperature is around a μK. For trapped gases, the physics is essentially the same except that the critical temperature and condensate fraction depend on the number N and the average trap frequency $\overline{\omega}$. See [34] for details.

1.3 Superfluid helium: the road to dilute quantum gases

While the theoretical framework for quantum gases and BEC presented above was understood as early as 1925 by Einstein, its experimental manifestation had occurred earlier with the liquefaction of ^{4}He in 1911 by K. Onnes. Although preliminary evidence indicated a new phenomenon below 2.2K [35], it was only in 1938 the 'superfluid' aspects of helium-II became apparent when the viscosity of the liquid was shown to drop dramatically near the 'lambda' transition at 2.19K. London [36, 37] first posited a BEC of ^{4}He to explain the low viscosity of helium II as measured by Allen and Miesner [38] and Kapitza [39], and the fountain effect [40]. London's daring idea was further improved by Lazlo Tisza by his two-fluid model [41], a normal fluid and a superfluid, which explained all the observed phenomena and also predicted the mechano-caloric effect and a temperature wave, i.e., second sound, which is the out of phase oscillation of the normal fluid and the superfluid. This second sound was observed in helium II in 1960 [42] and related phenomenon was observed in gaseous BECs in 1998 [43]. Around the same time, Landau derived another two fluid model using a phenomenological approach to quantum liquids, in which the normal fluid was replaced by a weakly interacting gas of elementary excitations: phonons and rotons. Landau's superfluid did not mention Bose-Einstein statistics at all; nevertheless, his superfluid contained atoms in the ground state. It was intuitive and phenomenological, unlike London and Tisza's microscopic approach. One big difference between the two appears at low temperature: Landau's theory predicts phonon like excitations whereas the London

[2] $\zeta(x)$ is the Riemann zeta function and $\zeta(3/2) \sim 2.612$

and Tisza theory predicts free particle excitations. The dispersion relation of superfluid ^{4}He confirmed Landau's predictions of phonons at low momenta.

Bogoliubov's microscopic theory of weakly interacting Bose gases in 1947 was the first attempt to understand the underlying physics behind superfluid ^{4}He [44]. He modified the ideal Bose gas by including a weak two-body interaction, and used a field theoretical approach to diagonalize the many-body density matrix. The essentials of this theory will be discussed more in detail in chapter 2.2. Bogoliubov's theory, like Landau's, predicted a phonon spectrum at low temperatures, but unlike Landau, it does not have any roton excitations. Despite the fact that this theory does not explain superfluid ^{4}He too well, it forms the basis of the theory of dilute-gas Bose-Einstein condensation [45].

1.3.1 Helium to dilute gases

Initial experiments to achieve Bose condensation in dilute gases were pioneered by groups studying spin-polarized hydrogen (for review, see [46]). It was known that hydrogen would remain a gas even at $T = 0$ [47, 48], and efforts to reach BEC in spin-polarized hydrogen were underway since the late 70's. However, it was only in 1998 that BEC in hydrogen was first realized at MIT [49].

Another avenue towards gaseous BEC opened up with the advent of laser cooling and trapping of alkali atoms in the 100 μK range. Further cooling in a magnetic trap using forced RF evaporation [50] led to the first achievement of a dilute rubidium gas Bose condensate in 1995 by Eric Cornell and Carl Wieman [51]. Four months later, the MIT group led by Wolfgang Ketterle also produced a BEC in sodium atoms [52].

As mentioned earlier, for a summarized history on BEC theory and experiments prior to 1995, see [25, 46].

1.4 My life on the second floor of MIT Building 26

My life as a Bose condenser at MIT began two years after the first discovery of BEC. I arrived in the summer of 1997 to the second floor of MIT's building 26 and have ever since been engaged in exploring the physics at the edge of quantum mechanics and condensed matter. In my first project I helped to confine condensates in optical traps [6]. The summer months were spent trying to align and transfer the condensate from a magnetic trap to the optical trap. It was during this time that I was exposed not only to the physics of BECs but also the ways in which the Ketterle group functions. The entire group worked as a team, which I quickly became part of as I learned about the experimental apparatus.

The apparatus that I worked on was then termed as the 'old lab', where the first BEC experiments were performed. The 'new lab' was the second glass cell based BEC apparatus that was just getting started. This project was led by Chandra Raman, Roberto Onofrio and Dallin Durfee. The 'new lab' apparatus came online in early 1999.

I was involved in various projects from summer of 1997 to early 2000 in the 'old lab'. The optical confining of atoms immediately led to studies of Feshbach resonances [53, 54][3]. The old lab group consisted of Dan Stamper-Kurn, Hans Miesner, Jörn Stenger and Shin Inouye and myself. We explored the physics of reversible formation of a BEC in a combined magnetic and optical trap [7], spinor physics [8, 9, 11], and Bragg scattering [10]. We also discovered superradiance [12] and used it for amplifying matter waves [14]. The physics explored during this time has been summarized in the theses of Dan Stamper-Kurn [26] and Shin Inouye [27]. In addition, a brief history of our Bragg scattering and related experiments is described in sec. 2.6.

While doing Bragg spectroscopy in BECs, we discovered that Bragg outcoupled atoms can collide (see fig. 2-4). Exploration of these collisions is a significant part of my thesis (chapter 2). Along with Axel Görlitz and Dan-Stamper-Kurn, I led the exploration of superfluid collisions. During this time, various parallel projects were being taken up led by Shin Inouye, Deep Gupta and Tilman Pfau [17, 55]. Although we were working on two sets of projects at any given time, the entire old lab team was actively involved in performing the experimental analysis and maintaining the apparatus[4].

During the summer of 1999, the experiments were halted as the laboratory infrastructure was to be renovated. The old lab apparatus could not be moved, and so the experiment on the optics table was boxed up and rest of infrastructure such as the electronics, powersupplies, etc. was removed and then put back together. The renovations significantly improved the lab life. The dark and dull second floor hallway of building 26 became bright and oddly colorful. The first experiments, after the apparatus was put back together, explored superfluidity using BEC collisions [1] and matter-wave amplification [14]. With the arrival of Todd Gustavson in Fall of 1999, we were also geared up to build a third BEC machine.

At this time, I decided to stop working fulltime on current projects and apply myself to building a new BEC machine, which is described in chapter 3. While I was still involved in some experiments in the old lab, I was more engaged with the construction of new BEC apparatus. The building effort was a singular example of team work and spirit.

With an additional BEC apparatus, the lab terminology had to be changed. In keeping with MIT tradition[5], the original apparatus was now called 'BEC-I', the glass cell apparatus being 'BEC-II' and the new 'science chamber apparatus' was 'BEC-III'. All of these three experiments made BEC using sodium atoms, whereas the latest 'BEC-IV' experiment, which essentially followed the design of BEC-III, used rubidium atoms to make condensates. In addition, the BEC-I apparatus was given a new life by mixing fermionic lithium atoms with a sodium BEC, by adding a two-species oven [56]. This is the current nomenclature of the experiments at the MIT BEC factory.

[3] I was not involved in this work since I was busy taking MIT physics classes.
[4] Hence, the reason for all of team members being co-authors on all of the papers.
[5] At MIT, the buildings are named by numbers rather than names.

Having worked on functioning BEC experiment (BEC-I) for $2\frac{1}{2}$ years, I end my graduate career by building a BEC apparatus [2]. The apparatus has a moving optical tweezers, with which we have transported condensates more than 40 cm (limited only by the vacuum chamber). Interestingly, the beginning and the end of my career as a graduate student has involved optical trapping of BEC. The optical trap, which was the cause of many sleepless nights during the summer of 1997, is now used routinely to move condensates around. Even now, it is simply amazing to imagine the invisible infrared light clutching the cold condensate from the security of its magnetic blanket and gently gliding it into a new chamber.

1.5 Outline of this thesis

This thesis is essentially a summary of experiments on which I was the lead graduate student. Chapter 2 describes the experiments on collisions with BEC, where we first demonstrated microscopic superfluidity in gaseous BEC [1]. This work was on done using the BEC-I apparatus. Chapter 3 describes the construction of BEC-III apparatus [2]. The chapter is written not only as a guide for future Bose condensers who will experiment with it, but also for people in the field who might want to build a similar apparatus. Although rarely done, the technical design of the apparatus is included in appendices A and B. I believe that at this point of time future researchers should be not be too burdened by building BEC machines, but should rather focus on the physics that can be explored with them. Making a BEC should not be much harder than making a magneto-optical trap (MOT).

The first experiments in BEC-III studying Bose condensed atoms in macroscopic and miniaturized magnetic wiretraps [2, 3] is described in chap. 4. Finally, the demonstration of a continuous source of Bose condensed atoms [4] is discussed in chap. 5. Such a continuous source is the key element in a continuous wave atom laser.

Chapter 2

Suppression and enhancement of collisions: BEC Superfluidity

In this chapter I will discuss the effects of atomic collisions in Bose-Einstein condensates that was presented in the following publication:

- *A. P. Chikkatur, A. Görlitz, D. M. Stamper-Kurn, S. Inouye, S. Gupta, and W. Ketterle, "Suppression and enhancement of impurity scattering in a Bose-Einstein condensate," Phys. Rev. Lett.* **85***, 483-486 (2000). Included in Appendix D.*

Many phenomena in physics involve enhancement or suppression of scattering processes. A classic example of enhancement is in the optical laser, where photons are amplified due to bosonic stimulation. For suppression, we need to look no further than superfluidity of liquid helium and superconductivity of metals at low temperature. Both the suppression and enhancement are collective effects. In the laser, the macroscopic occupation of a single laser mode enhances the probability to scatter into that mode, and in superfluid liquid helium and superconductors, the dissipative effects are suppressed due to collective interactions. Similarly, even in Bose condensates we have already seen such enhancement and suppression. For example, in BEC-light interactions where we have observed enhancement of Rayleigh scattering in superradiance [12], and suppression of light scattering due to quantum depletion [13]. For material particles colliding with BECs, we have observed both a suppression due to superfluidity and an enhancement due to bosonic stimulation [1]. In this chapter, I describe these experiments on particle scattering from a BEC. First, I will present a general theory of scattering in BECs, describe aspects of superfluidity relevant for this work, and compare it to analogous work in liquid ^{4}He. Then I will discuss the history of BEC collision studies in our laboratory, and then finally present details of the experiment concerning the superfluid properties of a BEC that was published in ref. [1]. This early work has led to more recent BEC collision studies by my colleagues in BEC-II, where pair correlated beams were generated [57], using the enhanced scattering we had first

observed [1].

2.1 Collisions in general

Before describing the basic theory underlying scattering of atoms in a BEC, I would like to emphasize some aspects of atomic collisions that are relevant for both theory and experiments. Collisions underpin the theoretical foundations of statistical mechanics in kinetic theory. Equilibrium statistical mechanics tells us that Bose-Einstein condensation occurs when the phase-space density $\rho \sim 1$. However, it does not tell us *how* a gas of atoms initially at room temperature reaches that equilibrium state to BEC. The kinetic theory of gases provides that missing link. A fundamental assumption of kinetic theory is that atoms collide: it is through collisions/interactions between atoms that the equilibrium state of a system is reached. Using Boltzmann transport equations [32] one can explain the manner in which equilibrium is reached from a non-equilibrium state. This is true not just for making BECs but for all equilibrium phenomenon in general.

While the role of atomic collisions in statistical mechanics is now well accepted, as an experimentalist working on making BECs, collisions are far more important because of their critical role in evaporative cooling. Laser cooled gases at temperatures of a few hundred microkelvins enter into the degenerate regime via atomic collisions by evaporative cooling. In evaporative cooling, the high energy tail of the equilibrium Maxwell-Boltzmann distribution for atoms is eliminated. This tail is then 'regenerated' by collisions between the atoms within a few collision times [58], and the temperature of the system is lowered[1]. In fact, for evaporative cooling to work, the ratio of "good" to "bad" collisions needs to be large. The "good" collisions are elastic collisions, which conserve and redistribute energy, such as the s-wave collisions discussed in this chapter. The "bad" collisions are inelastic collisions arising from dipolar relaxation and three-body recombination, where atoms gains kinetic energy while changing their internal states. Three-body recombination is an important mechanism that limit the lifetime of condensates at high densities. However, it is elastic two-body collisions that matter the most for understanding the physics of weakly interacting gaseous BEC.

2.1.1 2-body collisions and the scattering length

During elastic collisions the kinetic energy is conserved, which implies that in the center-of-mass frame, the initial relative momentum merely rotates into a final relative momentum with the same magnitude. And for most low-energy collisions of interest, and certainly for the collisions between atoms in a BEC, the rotation of the initial relative momentum is also independent of the scattering angles, i.e., the collisions scatter atoms into all angles

[1] For atoms in a magnetic trap, an rf of frequency ν expels atoms with velocities larger than $\sqrt{2h(\nu-\nu_0)/m}$, where $h\nu_0 = \mu_B B_0$ and B_0 is the magnetic field at the bottom of the magnetic trap.

with equal probability. Since only the $l = 0$ partial wave contributes to the collision, the collision process is commonly referred to as "s-wave collisions." For all BECs produced thus far, this is the relevant collision process. For atoms with a large magnetic dipole, such as chromium with $6\mu_B$, magnetic dipolar interactions may also become important and the spatial isotropy of the collisions no longer holds [59, 60]. For sodium atoms, the s-wave regime is below a temperature of $T \sim \frac{1}{k_B}\frac{\hbar^2}{Ma^2} \simeq 2.8$ mK, where a is the two-body scattering length for sodium. The scattering length, a, is the effective "hard-sphere range" of cold atoms. While the scattering process only depends on a, and not on the details of the inter-atomic potential, the value of the scattering length is very sensitive to this potential. The scattering length is determined by the energy of the last bound state of the inter-atomic potential, where $E_{bound} \simeq -\frac{\hbar^2}{2Ma^2}$. It is the most important parameter for the mean-field theory of Bose-Einstein condensed atoms. Basics of this theory are presented in the next section 2.2.

The scattering length for sodium atoms has been measured most accurately by photoassociating two sodium atoms. Initial measurements by the NIST group measured a s-wave scattering length of 2.75 ± 0.26 nm [61], which has been later narrowed down to $a = 2.80 \pm 0.02$ nm [62][2]. Besides these molecular spectroscopy measurements, the scattering length was also determined from the mean-field energy of a BEC [63]. This measurement was consistent with the photoassociation results, but with a large error bar. The BEC collision experiments that will be described here (sec. 2.8) offer another distinct technique for measuring the scattering length independent of the mean-field theory. The term containing the scattering length in the mean-field approximation is due to the coherent 'forward scattering' ($\propto a$) that results from a first order perturbative calculation for the energy of the system, whereas the scattering length in BEC collisional cross-section described in this chapter arises from the 'incoherent' elastic scattering ($\propto a^2$). This is due to calculating the change in the initial wavefunction using second order perturbative theory. Forward scattering and incoherent scattering can be related by the optical theorem for scattering [64].

2.2 Understanding BEC - mean field theory

In this section, I will briefly describe the Bogoliubov theory [44] for dilute weakly interacting Bose gases. This linearized many-body field theory that can be applied directly to most of the experiments that have been done in dilute gases so far. This theory has been explained in various review papers [26, 34]. The theory includes only the two-body interaction between atoms, which is treated as a pseudo-potential,

$$\mathcal{V}(\mathbf{r_1} - \mathbf{r_2}) = \frac{4\pi\hbar^2 a}{M}\delta(\mathbf{r_1} - \mathbf{r_2}), \tag{2.1}$$

[2]In this thesis, value of a is assumed to be 2.75 nm based on [61], since the more recent photoassociation measurement occurred after the experimental analysis on BEC collisions was done in early 2000.

where a is the two-body scattering length between the atoms. The interaction strength is usually denoted by $g = \frac{4\pi\hbar^2 a}{M}$. The Hamiltonian in the second quantized notation for a homogeneous gas of atoms in a volume V is

$$\begin{aligned}\mathcal{H} &= \mathcal{H}_0 + \mathcal{H}_{int} \\ &= \sum_k \frac{\hbar^2 k^2}{2M}\hat{a}_k^\dagger \hat{a}_k + \frac{g}{2V}\sum_{k,l,m,n} \hat{a}_l^\dagger \hat{a}_n^\dagger \hat{a}_k \hat{a}_m \delta_{l+n-k-m}. \end{aligned} \tag{2.2}$$

The operators $\hat{a}_k^\dagger(\hat{a}_k)$ are creation(destruction) operators for particles with wavevector $\mathbf{k}$. Since the atoms are all indistinguishable, there is a factor $1/2$ in $\mathcal{H}_{int}$ to prevent overcounting.

When a Bose condensate is present, a large number of particles, N_0, is in the ground state. In the Bogoliubov prescription the operators $\hat{a}_0^\dagger, \hat{a}_0$ are replaced by the c-number $\sqrt{N_0}$. After making this substitution, the Hamiltonian can be diagonalized as

$$\mathcal{H} = \sum_k \hbar\omega_k^B \hat{b}_k^\dagger \hat{b}_k, \tag{2.3}$$

where the Bogoliubov operator $\hat{b}_k^\dagger = u_k \hat{a}_k^\dagger + v_k \hat{a}_{-k}$. The coefficients $u_k = \cosh\phi_k$ and $v_k = \sinh\phi_k$, with $\tanh 2\phi_k = \mu/(\hbar\omega_k^0 + \mu)$, $\hbar\omega_k^0 = \hbar^2 k^2/2M$ is the free-particle kinetic energy and $\mu = gN_0/V$ is the chemical potential of the BEC. The quasi-particle excitations are created and destroyed by the Bogoliubov operators, $\hat{b}_k^\dagger$,$\hat{b}_k$, with energy

$$\hbar\omega_k^B = \sqrt{\hbar\omega_k^0(\hbar\omega_k^0 + 2\mu)}. \tag{2.4}$$

Figure 2-1 illustrates the behavior of the dispersion relation of the condensate and a free particle. At low momenta, the energy of quasi-particle excitation is phonon-like with $E = \hbar kc = pc$, thus the excitations have a constant speed, c. At momenta larger than Mc, the excitations are free-particle-like ($E \sim \frac{(\hbar k)^2}{2M}$) with an energy shift of μ. It is this dispersion relation which gives rise to the Landau critical velocity, which is discussed in sec. 2.4.

2.2.1 Static structure factor

An important property of the condensate relevant for understanding collisions is the static structure factor, $S(q)$. The structure factor is the density-density correlation of the condensate wavefunction,

$$S(q) = \langle\psi_c|\hat{\rho}(\mathbf{q})\hat{\rho}^\dagger(\mathbf{q})|\psi_c\rangle/N, \tag{2.5}$$

where $|\psi_c\rangle$ is defined by $\hat{b}_k|\psi_c\rangle = 0$, and $\hat{\rho}(\mathbf{q}) = \sum_m \hat{a}_{m+q}^\dagger \hat{a}_m$ is the Fourier transform of the atomic density operator at wavevector $\mathbf{q}$. Evaluating eq. 2.5 gives $S(q) = (u_q - v_q)^2 = \omega_q^0/\omega_q^B$ (see fig. 2-2). For large q, $S(q) \to 1$. This is the value for thermal clouds, indicating

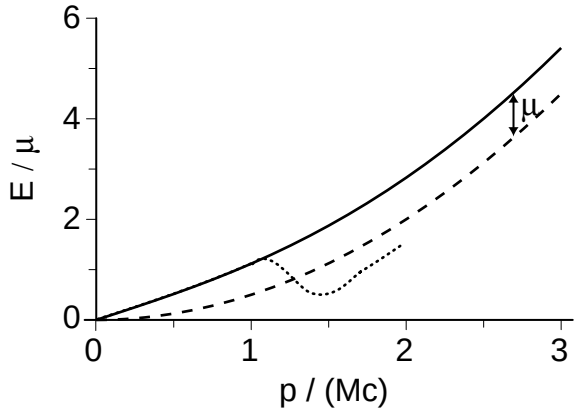

Figure 2-1: The energy-momentum dispersion relation for free particles (dashed line) and a condensate (solid line). The energy is in units of the chemical potential μ and the momentum p is in units of Mc, where $c = \sqrt{\mu/M}$ is the speed of sound of the condensate. For comparison, the dotted line shows the dispersion line for superfluid ^{4}He, indicating the roton branch. The energy scale and momentum are arbitrary for this curve.

that large momentum density fluctuations do not involve the whole condensate. At low q, the fluctuations involve the whole condensate through phonon excitations, which are more difficult to excite; this is indicated by $S(q) \rightarrow \frac{\hbar q}{2Mc}$. This suppression was first measured by our group when we excited phonons using Bragg beams [13], see sec. 2.6.5. The structure factor can also be derived using a mean-field Gross-Pitaevskii approach. Details can be found in sec. 8.5 of Dan Stamper-Kurn's thesis.

2.3 Scattering of light and massive particles

In this section, I will describe the theory of scattering in Bose-Einstein condensates and derive the collisional scattering rate starting from the basic four-wave mixing Hamiltonian. Aspects of the collisional rate will be discussed in the following sections. Parts of the theoretical formulations presented here are summarized in section I of ICAP-2000 proceedings [65], and also in the Cargese notes of 2001 [66]. Those parts are slightly edited and expanded here.

The rate equations for scattering (both for light and massive particles) can be derived using Fermi's Golden Rule. This is useful to see the similarities and differences between the different processes. The use of Fermi's Golden rule is valid when the scattering populates many 'incoherent' collisional modes. This is a perturbative approach which excludes any coherent oscillations and only includes the production of elementary excitations in the condensate.

When a condensate scatters a photon or material particle, the scattering is described

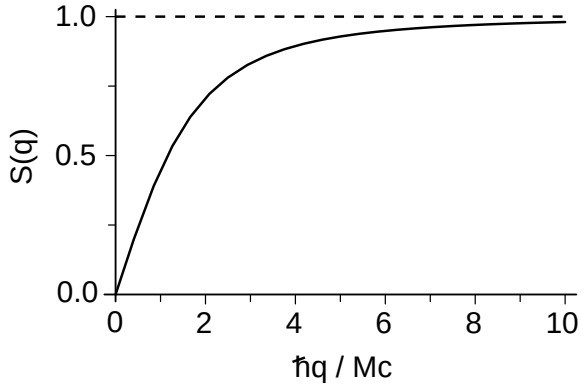

Figure 2-2: The static structure factor of a condensate. The dashed line is the value for a thermal cloud, and the solid is for a condensate.

by the 4-wave mixing Hamiltonian

$$\mathcal{H}' = C \sum_{k,l,m,n} \hat{c}_l^\dagger \hat{a}_n^\dagger \hat{c}_k \hat{a}_m \delta_{l+n-k-m} \tag{2.6}$$

Here $\hat{c}_k$ ($\hat{c}_k^\dagger$) is the destruction (creation) operator for the scattered particles, and $\hat{a}_k$ ($\hat{a}_k^\dagger$) is the destruction (creation) operator for atomic plane waves of wavevector $\mathbf{k}$. The strength of the coupling is parametrized by the coefficient C, and the δ function ensures momentum conservation (with an uncertainty of $\hbar/D$, where D is the dimension of the condensate).

When the scattered particles are indistinguishable from the condensate atoms, the Hamiltonian, eqn. 2.6, describes the mean-field energy of a single condensate:

$$C\hat{a}_0^\dagger \hat{a}_0^\dagger \hat{a}_0 \hat{a}_0. \tag{2.7}$$

Comparing eqns. 2.2 and 2.7, we can identify the coefficient for indistinguishable particles as

$$C = \frac{g}{2V} = \frac{2\pi\hbar^2 a}{MV}. \tag{2.8}$$

The Hamiltonian $\mathcal{H}'$ also describes pair correlations and quantum depletion ($C\sum_q \hat{a}_q^\dagger \hat{a}_{-q}^\dagger \hat{a}_0 \hat{a}_0$) and the damping of collective excitations where a quasi-particle in mode k decays into two other excitations (Beliaev damping, $2C\sum_{l,n} \hat{a}_n^\dagger \hat{a}_l^\dagger \hat{a}_k \hat{a}_0 \delta_{l+n-k-0}$) or promotes an existing quasi-particle in mode l to higher energy (Landau damping, $4C\sum_{k,n} \hat{a}_0^\dagger \hat{a}_n^\dagger \hat{a}_l \hat{a}_k \delta_{0+n-l-k}$).

Consider now the scattering process where a system with N_0 atoms in the condensate ground state and N_q quasi-particles with wavevector $\mathbf{q}$ scatters particles with incident momentum $\mathbf{k}$ into a state with momentum $\mathbf{k}-\mathbf{q}$. The initial and final states are

$$|i\rangle \quad = \quad |n_k, n_{k-q}; N_0, N_q\rangle$$

$$|f\rangle \quad = \quad |n_k - 1, n_{k-q} + 1; N_0 - 1, N_q + 1\rangle, \tag{2.9}$$

respectively, where n_k denotes the population of scattering particles with wavevector $\mathbf{k}$. This choice of final states implies that we neglect scattering between quasi-particles and consider only processes involving the macroscopically occupied zero-momentum state of the condensate. Formally, we replace the Hamiltonian (Eq. 2.6) by $C\sum_{k,q}(\hat{c}^\dagger_{k-q}\hat{a}^\dagger_q\hat{c}_k\hat{a}_0 + \hat{c}^\dagger_{k-q}\hat{a}^\dagger_0\hat{c}_k\hat{a}_{-q})$.

It should be emphasized that, due to the interatomic interactions, the quasi-particles with occupation N_q are *not* the plane waves created by the operator $\hat{a}^\dagger_q$, but the quanta of collective excitations with wavevector $\mathbf{q}$. The quasi-particle states are eigenfunctions of the Bogoliubov operator $\hat{b}^\dagger_q\hat{b}_q$. Therefore, the square of the matrix element M_1 between the initial and final state is

$$\begin{aligned} |M_1|^2 &= |\langle f|\mathcal{H}'|i\rangle|^2 \\ &= |C|^2|\langle N_0 = N-1, N_q = 1|\hat{\rho}^\dagger(\vec{q})|N_0 = N, N_q = 0\rangle|^2(N_q+1)(n_{k-q}+1)n_k \end{aligned} \tag{2.10}$$

where $\hat{\rho}(\mathbf{q}) = \sum_m \hat{a}^\dagger_{m+q}\hat{a}_m$ is the Fourier transform of the atomic density operator at wavevector $\mathbf{q}$. Including the static structure factor of the condensate, we obtain for the scattering matrix element M_1

$$|M_1|^2 = |C|^2 S(q)(N_q+1)(n_{k-q}+1)N_0 n_k. \tag{2.11}$$

The scattering rate W_1 for the process $|n_k, n_{k-q}; N_0, N_q\rangle \to |n_k - 1, n_{k-q} + 1; N_0 - 1, N_q + 1\rangle$ follows from Fermi's golden rule as

$$W_1 = \frac{2\pi}{\hbar}|M_1|^2\delta(E_k - E_{k-q} - \hbar\omega^B_q), \tag{2.12}$$

where E_k is the energy of the incident particle with momentum $\hbar\mathbf{k}$, and $\hbar\omega^B_q$ is the energy of quasi-particles with momentum $\hbar\mathbf{q}$. To obtain the net scattering rate, one has to include the reverse process $|n_k, n_{k-q}; N_0, N_q\rangle \to |n_k + 1, n_{k-q} - 1; N_0 + 1, N_q - 1\rangle$ by which atoms scatter *back* into the condensate. The square of the matrix element M_2 for this process is

$$|M_2|^2 = |C|^2 S(q) N_q n_{k-q}(N_0+1)(n_k+1). \tag{2.13}$$

The *net* rate W_+ of scattering atoms from the condensate into the quasi-particle mode $\mathbf{q}$ is the difference of the two partial rates $W_+ = W_1 - W_2$. Assuming $N_0 \gg 1$ (i.e. $N_0 + 1 \approx N_0$), we obtain for the net rate

$$W_+ = \frac{2\pi}{\hbar}|C|^2 S(q) N_0[n_k(N_q + n_{k-q} + 1) - N_q n_{k-q}]\delta(E_k - E_{k-q} - \hbar\omega^B_q) \tag{2.14}$$

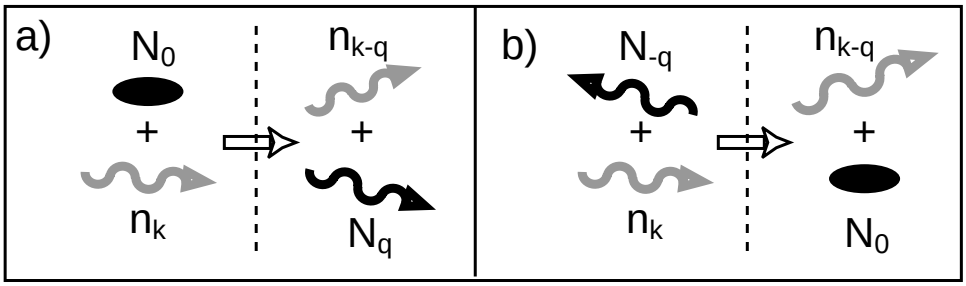

Figure 2-3: A schematic of Stokes and anti-Stokes process where the condensate gains momentum $\hbar\mathbf{q}$. a) Stokes process where the scattering particle (gray) with momentum $\hbar\mathbf{k}$ collides with the condensate, loses energy while being transferred to momentum $\hbar(\mathbf{k}-\mathbf{q})$. A quasiparticle (black) with momentum $\hbar\mathbf{q}$ is created such that a net momentum $\hbar\mathbf{q}$ is transferred to the condensate. b) Anti-Stokes process where the scattering particle annihilates a quasiparticle with momentum $-\hbar\mathbf{q}$, transferring it into the condensate, while *gaining* energy. The scattering particle, however, loses momentum $\mathbf{q}$ to the condensate. The left side of the dashed line is the initial state and right side is the final state.

With the dynamic structure factor $S(\mathbf{q},\omega) = S(q)\delta(\omega - \omega_q^B)$ eq. 2.14 simplifies to

$$W_+/N_0 = \frac{2\pi}{\hbar^2}|C|^2 n_k\, S(\mathbf{q},\omega)(N_q + n_{k-q} + 1) \tag{2.15}$$

The rate W_+ in eq. 2.14 is the rate for the Stokes process where $E_k > E_{k-q}$. Momentum transfer $\hbar\mathbf{q}$ to the condensate is also possible as an anti-Stokes process where a quasi-particle with momentum $-\hbar\mathbf{q}$ is scattered into the condensate, and the scattered particle *gains* energy (see fig. 2-3). The net rate W_- for this process is obtained in an analogous way as

$$W_- = \frac{2\pi}{\hbar}|C|^2 S(q) N_0[n_k(N_{-q} - n_{k-q}) - (N_{-q}+1)n_{k-q}]\delta(E_k - E_{k-q} + \hbar\omega_q^B). \tag{2.16}$$

The net scattering rates in eqs. 2.14 and 2.16 are the product of three terms.

- The static structure factor $S(q)$ represents the squared matrix element for the condensate to absorb momentum $\hbar\mathbf{q}$.
- The delta function denotes the density of final states.
- The bosonic stimulation term represents stimulation by the occupation in the final state either of the scattering particles or the condensate.

The interplay of these three terms is responsible for the suppression and enhancement of physical processes in a condensate. The properties of the condensate as an intriguing many-body system are reflected in the structure factor, which was defined earlier in sec. 2.2.1. The density of states is responsible for superfluidity because it vanishes for incident particle velocities that are smaller than the Landau critical velocity, which is discussed in sec. 2.4.

Finally, bosonic stimulation by the occupancy N_q of final states was responsible for the observed enhanced collisions that will be discussed in sec. 2.9.1. This bosonic stimulation is also responsible for interesting light-condensate interactions, such as superradiance, matter wave amplification and optical amplification in a condensate [12, 14, 55]. The concept of bosonic stimulation is itself quite interesting and I would like to describe some of the subtlety surrounding this concept in the next section.

2.3.1 Bosonic stimulation or matter wave interference?

Traditionally, bosonic stimulation is thought to arise from proper normalization of a symmetric wavefunction. The stimulation is presumed to occur only for a system of bosons, and hence the name. However, in this section, I would like to emphasize that bosonic stimulation in eqs. 2.14 and 2.16 can also be considered as arising from density fluctuations from the macroscopically occupied states, i.e, enhanced diffraction off matter-wave gratings are responsible for the enhanced rate. This is the classical understanding of Bragg diffraction. This alternative view, which I personally like, was first put forth by Wolfgang Ketterle during the discussions in our lab on whether fermionic atoms can show superradiance-type effects and 4-wave mixing. Ref. [67], section 10 of Cargese notes [66], and Shin Inouye's thesis [27] discuss this issue in detail. I want to present a 'historical' account of this idea as an example of kind of 'wild' theorizing that comes out of second floor of building 26; these ideas have almost always led to new insights in our understanding of atomic physics.

After the matter-wave amplification experiment [14] it became very interesting for us to consider whether fermions could also be amplified in this manner. The group had many discussions, primarily in the hallway where all of us would gather and hash our idea. During these discussions, we intuitively felt that fermions should be able to undergo matter-wave amplification, and the gain would be limited only by its very short coherence time. This view was buttressed by the fact that thermal clouds could undergo superradiance. As we noted in our paper [12], the coherence time for thermal atoms is very short and hence the threshold for superradiance is higher than for BECs[3]. Many hallway discussions on the second floor of Building 26, primarily involving Wolfgang, Shin, Axel and myself, led to fine-tuning of the arguments that are presented in ref. [67]. When Wolfgang presented these ideas to the rest of the atomic physics community, they were met with surprise and disagreement despite the fact that nobody could come up with a good counterargument for why fermions could not 4-wave mix or be amplified at temperatures above degeneracy. It seemed that the idea that only bosons could produce bosonic stimulation was well entrenched in the field. This only seemed to imply to us that there was some fundamental misconception of bosonic stimulation.

From what I remember there were two key insights: one evening, Wolfgang, Shin and

[3] In fact, in our experiments, even with high light intensities, we were never able to observe superradiance for thermal clouds close to T_c.

I were discussing the problem in the hallway, when Shin posited that since there is no difference between fermionic or bosonic atoms in Dicke superradiance, it should be possible for fermionic atoms to undergo superradiance and matter wave amplification. Wolfgang then added that this was possible if the fermionic state was prepared in such a way that a part of the wavefunction would be symmetrized, while the total wavefunction was still anti-symmetric. Then bosonic stimulation and matter wave amplification can still occur for the quantum numbers that were symmetrized.

We were all confident at this point that fermions would undergo matter wave amplification and that it could be considered as diffraction of a matter wave grating. It seemed that bosonic stimulation is not required for four-wave mixing. Perhaps, bosonic stimulation can be fully explained using matter-wave interference. However, there was still one place where bosonic stimulation seemed to play a big role, and that was in the formation of a BEC. In other words, bosonic stimulation arising simply from proper symmetrization of the wavefunction, rather than from any physical process, was believed to be responsible for making a BEC. Even now, this idea has simply been accepted as one of the bizarre effects in quantum statistics: a statistical 'attraction' to the ground state [21, 68]. During a group picnic of sorts at Dave Pritchard's summer house in Rhode Island, Wolfgang pointed out that BEC formation can also be considered as enhanced scattering into the macroscopic ground state due to an enhanced matter wave grating between a thermal atom and the large number of atoms in the ground state. Another thermal atom diffracting off this grating would then have an enhanced rate to enter the ground state similar to the enhancement in Dicke's superradiance. So, the 'mysterious influence' [21] is demystified as amplification due to the presence of macroscopic occupation of the ground state[4] [67]. This simple picture completed the idea that bosonic stimulation can be considered as nothing but enhanced matter wave diffraction!

I have always been fond of this idea of Wolfgang. As an experimental physicist, I have much better intuition for physical processes that I can imagine in my mind. Atoms diffracting off a matter-wave grating to form a BEC is much easier to understand and imagine than the unphysical picture of normalization of wavefunctions somehow leading to BEC.

The bosonic stimulation (or grating enhancement) played a constant role in the lab, because all experiments involving light and BECs, because any Raman and Bragg interaction with condensates led to superradiance if we were not careful. Secondly, during the data analysis for the collision work, we realized that bosonic stimulation was responsible for the enhanced elastic collisions we observed (see section 2.9.1). Once again it was not something we expected.

Although I have emphasized that similarity between fermions and bosons regarding four-wave mixing and matter wave amplification, there are some key differences. The first obvious

[4]The matter wave amplification has a broad profile.

fact that the occupation number of states for fermions can only be 0 or 1, whereas bosons can have any number of particles occupying a state. This Pauli blocking has important consequences for collisions between fermionic atoms [69]. Therefore, fermions must be non-degenerate ($T > 0$) and *only a part* of their wavefunction can be symmetrized (i. e. bosonic), and the total wavefunction must be anti-symmetric [67]. For fermions, this state must be created somewhat artificially, whereas bosons are always in a symmetrized state. So, two clouds of fermions that overlap will not show matter-wave interference unless they are specially prepared, but two bosonic clouds will always interfere. Finally, the coherence time for fermions is limited by Doppler broadening inherent in the finite temperature cloud. This short coherence time could imply that parasitic incoherent processes can dominate over the stimulated process.

2.3.2 The structure factor, again

As shown in sec. 2.3, the scattering rate is proportional to the static structure factor $S(q)$, which is a measure of the density-density correlations at wavevector $\mathbf{q}$ associated with the momentum transfer. Although it was defined in sec. 2.2.1, I would like to expand on the role of the structure factor in scattering in this section.

The factor consists of two parts, one reflects the average atomic density $\tilde{\rho}(\mathbf{q}) = \langle\psi_c|\hat{\rho}(\mathbf{q})|\psi_c\rangle$ and the other one the fluctuations $\delta\hat{\rho}(\mathbf{q}) = \hat{\rho}(\mathbf{q}) - \tilde{\rho}(\mathbf{q})$,

$$S(\mathbf{q}) = \frac{1}{N}\langle\psi_c|(\tilde{\rho}(\mathbf{q}) + \delta\hat{\rho}(\mathbf{q}))(\tilde{\rho}^*(\mathbf{q}) + \delta\hat{\rho}^\dagger(\mathbf{q}))|\psi_c\rangle \tag{2.17}$$

$$= \frac{1}{N}\left(\tilde{\rho}(\mathbf{q})\tilde{\rho}^*(\mathbf{q}) + \langle\psi_c|\delta\hat{\rho}(\mathbf{q})\delta\hat{\rho}^\dagger(\mathbf{q})|\psi_c\rangle\right) \tag{2.18}$$

In a system without fluctuations ($\delta\hat{\rho}(\mathbf{q}) = 0$), there is only scattering when the stationary density modulation allows for a momentum transfer at wavevector $\mathbf{q}$ ($\tilde{\rho}(\mathbf{q}) \neq 0$) and the incident particles fulfill the Bragg condition. For electromagnetic waves, one well known example is X-ray scattering off a crystal lattice. Electrons in such a lattice form stationary Bloch waves (superpositions of plane waves and Bragg scattered plane waves) and propagate without attenuation. Scattering only occurs at irregularities of the lattice or thermal fluctuations. For atomic waves, such non-zero density modulations are created during four-wave mixing, where the interference between a condensate and moving matter wave forms a density grating from which condensate atoms diffract.

For a system without any density modulations ($\tilde{\rho}(\mathbf{q}) = 0$), scattering occurs randomly due to the density fluctuations. A Bose-Einstein condensate might appear perfectly ordered. However, as we have learned from our Bragg experiments [10, 13], it has density fluctuations similar to a classical ideal gas. The structure factor only differs from an ideal gas when the momentum transfer is comparable or less than the speed of sound (times the mass M). For electromagnetic waves, these density fluctuations cause Rayleigh scattering. In close analogy, if a matter wave propagates through a condensate, there will be elastic

scattering. It is this elastic scattering that is described in this chapter. On length scales larger than the healing length, the condensate has reduced density fluctuations, and we have seen that electromagnetic radiation of sufficiently long wavelength can propagate with little scattering [13], i.e., Rayleigh scattering of long wavelength photons is suppressed. In the next sections, the equivalent result for long wavelength matter waves, and also a new effect, namely the complete suppression of scattering for velocities below the Landau critical velocity, will be discussed.

2.4 Landau's critical velocity

The δ function in the eq. 2.14 ensures energy conservation. The dispersion relations for excitations in a condensate and for the scattering particle determine the density of states available for the scattering.

Energy-momentum conservation for impurity particles, the delta function in eq. 2.14, requires $E_k - E_{k-q} = \hbar\omega_q^B$. Expanding this equation gives

$$(\hbar k/M)q\cos\theta = \omega_q^B + \hbar q^2/2M, \tag{2.19}$$

where θ is the angle between $\mathbf{k}$ and $\mathbf{q}$. Since $\cos\theta \leq 1$, the l. h. s. is always less than vq, where $v = \hbar k/M$ is the initial velocity of the impurities. For simplicity, equal mass M for the impurity and condensate atoms is assumed. Thus, collisions with the condensate are only possible if the maximum energy transfer from the impurity particles is sufficient to excite a quasi-particle, i.e., $v > \omega_q^B/q + \hbar q/2M$. The minimum velocity, in the limit of large impurity mass, is $v_L = \min(\omega_q^B/q)$, where v_L is the Landau critical velocity [70] for superfluidity below which no dissipation occurs because the density of final states vanishes. For finite impurity mass, the second term in the r. h. s. of the eq. 2.19 cannot be ignored, and this term becomes important when calculating the suppression of the scattering rate (see sec. 2.7.1). Thus, the Landau critical velocity is derived from a kinematic condition that determines the density of states available for the scattering process.

For light scattering, the dispersion relation is $E_k = \hbar k c_l$ with c_l denoting the speed of light, whereas for impurities, it is $E_k = (\hbar k)^2/2M$. Since $c_l \gg v_L = c$, the density of states is always non-vanishing for light scattering even at low momenta. Only the matrix element in eq. 2.12 is relevant for the process.

It is important to note that for a true ideal gas BEC, the Landau critical velocity is zero. So, BEC of an ideal gas is not a superfluid. The question of whether one can have a superfluid without a BEC is interesting. The requirements for defining a superfluid and a BEC are different, and these issues are explored in Tony Leggett's review paper on superfluidity [71]. In this thesis, a superfluid system is defined as one that has a non-zero Landau velocity.

2.5 Macroscopic and Microscopic measurements of critical velocity

Usually, critical velocities for excitations are not limited by elementary excitations, but rather by effects related to turbulence. Experiments studying the critical velocities in liquid helium forced the liquid through channels, packed powder, and adsorbed films, and have found a critical velocity much smaller than the Landau velocity [72]. This was due to turbulence related effects such as formation of vortices. Vortex formation has a lower threshold that is determined by channel dimension and surface effects (see ref. [72] for details). Therefore, suppression of vortex formation by using *microscopic* ions was important in observing the Landau velocity in liquid helium. In liquid helium (for low pressures), as discussed in the next section, the drift velocity of ions is limited by the formation of charged vortex rings [72] before the roton excitations. It was only by putting superfluid liquid He under high pressure that the Landau velocity was observed.

Even for similar experiments in BEC, turbulence-related effects such as vortex formation determine the critical velocity when using macroscopic objects inside the superfluid. If the size of an object is larger than the condensate's healing length $\xi = 1/\sqrt{8\pi na}$, then the object can be considered as macroscopic and the probability for vortex generation is increased. The critical velocity for vortex excitations is lower than the Landau velocity. The condensate healing length is the size scale over which the wavefunction of a condensate with a given chemical potential can vary, $\hbar^2/(2M\xi^2) = \mu$. Only a microscopic impurity can probe the Landau velocity because its effective size, which is given by the scattering length between the impurity and the condensate atoms ($\sim$ nm), is usually smaller than the condensate's healing length ($\sim$100 nm).

2.5.1 Liquid Helium

The first direct measurement of the Landau critical velocity in a superfluid was explored in the liquid helium-II system. Landau's dispersion curve for helium, which is shown in fig. 2-1, has a phonon branch at low momenta and a roton branch at intermediate values. This curve predicts a critical velocity that is determined by roton excitation at about 46 m/s [72, 73]. The first experimental measurements of the velocity was done by pushing negative ions through helium II at high pressure and low temperature, and measuring the drag on these ions [73]. Low temperatures of about 0.5 K were required to ensure that scattering from the thermal phonons did not dominate the measured drag. High pressures ($>$ 20 bars) were required to prevent turbulence and charged vortex-rings were not excited as the ion was accelerated through the superfluid by an electric field E. At low pressures, the ions are actually semi-macroscopic as they are surrounded by hundreds of helium atoms (see references cited in [73]). Therefore, these large balls could not be accelerated to velocities larger than 30 m/s because their energy was converted into vortex

rings rather than into their velocity. Meyer and Reif [74] showed that under pressures close to solidification at 25 bars, these vortices were not nucleated and hence negative ions could be accelerated to speeds of 50-60 m/s. More details on the experiments are given in [73]. Allum and collaborators then measured the drag on an ion, which was zero below 46 m/s for 25 atm. and dramatically rose up when accelerated to velocities larger than this value. This was close to the predicted value of the Landau critical velocity at 25 atm. Another important measurement was the determination of excitations for velocities larger than v_L. By measuring the drift velocity as a function of the electric E, they showed that these excitations were due to two-roton emission, rather than single-roton emission [73]. Further experiments measured the critical velocity as a function of pressure in isotopically pure ^{4}He [75].

However, it is interesting that even at high pressures of 25 atm. the ions form a "semi-macroscopic" ball with a mass of about $72m_4$, where m_4 is the mass of ^{4}He [73]. Nonetheless, the ions were able to reach the Landau velocity without exciting vortex rings. Such macroscopic balls of atoms could also be formed in a BEC if the impurities are ions.

2.5.2 Critical velocity for dilute gas BEC

For the excitation spectrum of the condensate (eq. 2.4), the Landau velocity is the Bogoliubov speed of sound $v_L = c = \sqrt{\mu/M}$. There is no roton branch for a BEC. Impurity (distinguishable) particles moving below this speed cannot transfer their energy to the condensate. In contrast, for photons, $\mathrm{d}E_k/\mathrm{d}(\hbar k) = c_l \gg c$, and scattering is always possible.

It is important here to note that one needs distinguishable, impurity particles to observe the superfluid "drag-free" flow for BECs. If instead of using impurity particles, one uses atoms of the same kind as the atoms in the condensate to scatter off the condensate, then the δ function will always be satisfied. The density of states is always available, and it can be regarded as scattering between a quasi-particle and a condensate. Note that although the density of states is non-vanishing it is *not* constant [76]. So, there is no Landau critical velocity for scattering of atoms which are indistinguishable from condensate atoms.

In contrast, microscopic impurity particles traversing through a condensate *collide* only above a critical velocity, and by studying the rate of collisions one can probe superfluidity. One would expect that if the particles are travelling below the Landau velocity (speed of sound) then they simply move through the condensate without colliding: a key signature of superfluidity. This collision-less flow is in fact a limiting process for sympathetic cooling of fermions using condensates [77].

In order to observe any measurable collisions in a finite sized BEC, the collisional density, as defined by $n\sigma l$, must be on the order of one, where n is the condensate density, σ the collisional cross-section and l is the path length of particle through the condensate. Typically, with 20 million atoms in our condensates, the collisional density along the condensate radius of about 10 μm is about one. So, an impurity particle will collide with the

condensate with a large probability. The collisional density for a inhomogeneous condensate will be discussed in more detail in sec. 2.7.6.

2.5.3 Turbulence in BEC

The first signatures of critical velocities in BEC were measured by stirring a condensate using a focused blue-detuned light beam [15, 78]. These experiments measured a critical velocity of about $c/10$, consistent with the theory that the light beam excited vortices in the condensate, which then resulted in heating of the condensate [79–81]. When the light beam was stirred with speeds below $c/10$, practically no heating was observed. At larger velocities, vortex formation due to stirring was actually observed by the observation of a fringe dislocation in a matter wave interference between a stirred condensate and a undisturbed local oscillator [17]. This experiment was also the first experiment where we observed the phase wrap of $\pm 2\pi$ associated with vortices of opposite polarities produced during the stirring process. A similar matter wave interference experiment was also observed in the Paris group [82], where the vortices were produced using rotating laser beams. The vortex formation in a BEC is related to excitations of unstable surface modes [83–85]. In more recent experiments, rotating laser beams can be used to produce large number of vortices, which then form ordered lattices [86, 87]. Both the critical velocity experiments and the experiments exploring vortex lattices will be covered in a future Ph.D. thesis of my colleague Jamil Abo-Shaeer. Studies of vortices in dilute gas BEC have become an exciting field both experimentally and theoretically.

2.6 A brief history of BEC collision studies in our lab

Studying collisions in BEC was serendipitous in that we saw the first evidence of elastic collisions between a BEC and atoms moving with large relative velocity during our initial experimental studies of Bragg spectroscopy [10] in September of 1999. We were not looking for collisions, it just happened.

2.6.1 Bragg spectroscopy

The long summer of 1997 led to a very successful period in the laboratory where we explored BEC physics in optical dipole traps (ODTs) [6] (see sec. 1.4). After this exploration, we decided to explore the physics of condensates in optical lattices, i.e., BECs in 1D standing and "walking" light waves. We spent a couple of months trying to setup the lattices using the infrared laser that was used for ODT, a 980 nm MOPA. Unfortunately (or fortunately) we never succeeded due to technical limitations of the MOPA laser[5]. We finally decided to

[5]The output of the MOPA laser was externally controlled by the current for the MOPA diodes. The diode temperature was not stablized and hence the frequency of the laser was randomly changing along with mode-hops. This random frequency noise was irrelevant for the ODT, but destroyed lattices due to phase

just use the laser light that was used for making the MOT. This light was detuned from the condensate resonance by about 1.8 GHz. We immediately obtained our first evidence for BECs in optical lattices when we saw a condensate being split into many orders of Kapitza-Dirac diffraction [27]. The Kaptiza-Dirac diffraction occurs for short pulses of counter-propagating laser beams [88]. We also observed Bragg diffraction for longer pulses when the relative detuning between the laser beams was equal to 100 kHz= $(2\hbar k)^2/(2M)$, where the wavevector $k = 2\pi/\lambda$ with $\lambda = 589$ nm. We then decided to probe the linewidth of the condensate using Bragg spectroscopy [10].

2.6.2 First evidence of collisions

We obtained the first evidence of elastic collisions in our lab while studying Bragg scattering in Bose condensates. Initially, we explored the outcoupling of atoms using counter-propagating Bragg beams along the radial and axial directions of the condensate. Bragg spectroscopy worked well along the radial direction, and in fact, all of the data for the paper on Bragg spectroscopy [10] were taken with the counter-propagating beams oriented perpendicular to the condensate axis (see [26, 27] for details). When we outcoupled atoms along the axial direction, we discovered to our surprise that the outcoupled atoms collided with the condensate! These collisions resulted in the time-of-flight image shown in figure 2-4. It was immediately obvious to us that this was a result of s-wave elastic scattering. The collided atoms fall uniformly on a sphere with radius $Mv/2$, where v is the relative velocity between the condensate and outcoupled atoms. In the time-of-flight images, we observed the integrated collisional sphere: the collisional halo. Compared to the radial direction, the collisional density along the condensate axis was 10 times larger, and therefore the collisions became more noticeable and obvious. I was quite moved by the beautiful symmetry of the process. We were *seeing* elastic scattering! The scattering that is responsible for making the BEC itself.

2.6.3 An aside: Superradiance

We decided to explore these elastic collisions in a BEC after we wrapped up the experiments on Bragg spectroscopy. However, before we ever got to studying the collisions, we discovered another effect again due to serendipity or just dumb luck! This was the phenomenon of superradiance.

During a routine Bragg spectrocopy run, we accidently turned up the power of the Bragg beams, and to our amazement, we discovered condensate-like atom clouds shooting out with momentum *perpendicular* to the Bragg beams. This was impossible to explain using the optical lattice physics we were exploring. Even more surprisingly, the effect happened even with a single beam! That very night, we understood this phenomenon as collective Rayleigh

noise.

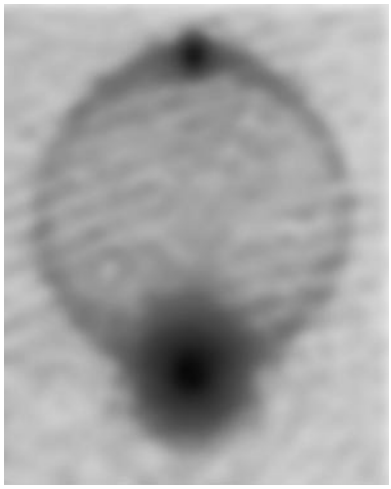

Figure 2-4: Observation of elastic collisions between the condensate (lower black dot) and Bragg diffracted atoms (upper spot). The image is taken after a time-of-flight of 30 ms, and shows the velocity distribution after the collision. The products of the collision are distributed over a sphere in momentum space leading to the observed s-wave halo. The height of the image is 3.2 mm.

scattering or Briоulloin scattering. Wolfgang has given a good description of the events of that night in his Nobel lecture [22].

We spent a couple of months exploring the physics of superradiance in a BEC before getting back to studying collisions. This physics is very much related to the scattering theory described in sec. 2.3, where photons from the single laser beam, n_k, Rayleigh scatter from the condensate, and resulting quasi-particles N_q bosonically enhances further stimulation. In other words, the matter wave grating between the condensate, N_0, and the quasi-particles, N_q, stimulate further scattering in the mode with the highest gain [12].

2.6.4 A 'condensate collider'

Initially, we decided to study collisions between two condensates, since we were interested in studies of interaction between atom lasers and condensate-condensate collisions in general. So, we studied collisions using magnetically accelerated condensates. Two condensates were created in a magnetic trap, one sitting at the bottom, the other one held up in the trapping potential by a blue-detuned light sheet that forms a repulsive potential for atoms. This initial situation was created by splitting a condensate into two roughly equal halves using a light sheet [89] and then shifting the center of the magnetic trap by applying a magnetic field gradient. By varying the strength of the gradient, we could control the separation distance and hence the relative potential energy of the two condensates. When the light sheet was switched off, one condensate accelerated and slammed into the other. The violent collision was observed *in situ* by phase contrast imaging and was also analyzed by absorption

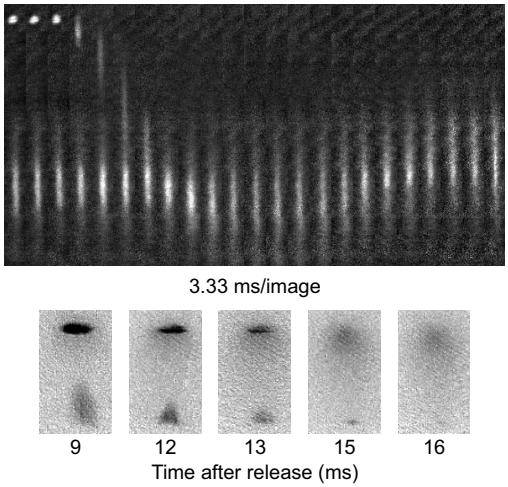

Figure 2-5: Collisions between two condensates. One condensate was held up in the magnetic trapping potential by a blue-detuned light sheet and suddenly released. A series of phase-contrast images (upper part) and time-of-flight absorption images display the collision. The phase contrast pictures show the spreading of the upper condensate during acceleration, its collision, and merging with the stationary cloud. The time-of-flight pictures represent the velocity distribution. Before the scattering event, there were two distinct peaks representing the accelerated and the stationary condensate. After the collision, only one cloud was left which was heated up by the collision.

imaging after ballistic expansion (fig. 2-5).

This 'condensate collider' method shown in fig. 2-5 suffered from large initial velocities and a large velocity spread of the incident condensate. By using the green light sheet, we would never be able to make the relative velocities smaller than the speed of sound of the condensate. Separating the two clouds necessarily meant that the second condensate had to be at least a Thomas-Fermi radius away from the condensate at the bottom of the trap, which implied that the energy per atom of the separated condensate had to be larger than the chemical potential of the condensate at rest. Hence, the relative velocity of the collisional pairs would always be larger than the speed of sound of the bottom condensate. The large velocity spread of the top condensate resulted from the spatial compression in the small trap formed by the magnetic gradient and the light sheet.

2.6.5 Small-angle Bragg scattering

Both a narrower velocity distribution and small velocities could be achieved using light scattering rather the condensate collider. Also, at this time, we became interested in probing the superfluid aspects of collisions. For this we needed distinguishable atoms, or impurity atoms, and the relative velocities had to be less than the speed of sound. Impurity atoms could be created using a Raman transition, where the outcoupled atoms could be in the $m_F = 0$ hyperfine state and could act as impurity atoms (see section 2.8.1). It was for these

reasons that we set up the laser beams for small-angle Bragg/Raman scattering. 'Bragg' scattering is defined as scattering where the internal hyperfine state of the atoms do not change, as opposed to 'Raman' scattering where the diffracted atoms are in a different hyperfine state (see section 2.8.1).

We had used counter-propagating beams for all our work on Bragg spectroscopy. This created outcoupled atoms moving at a relative velocity of $2\hbar k = 6$ cm/s, far larger than the usual speed of sound of our condensates, which is typically about 1 cm/s. Therefore to probe aspects of superfluidity, we needed to reduce the angle between our Bragg beams. The momentum transferred to the condensate is $2\hbar k \sin(\theta/2)$, where θ is the angle between the beams. We set up optics such that the laser beams propagated with an angle of 14° between them, through the top window of the vacuum chamber (see pg. 149 of Dan Stamper-Kurn's thesis for a schematic of the experimental setup). We expected the out-coupled atoms to be moving with a velocity less than 1 cm/s through the condensate, in the phonon regime rather than in the free-particle regime. Before setting up beams to produce $m_F = 0$ atoms, we decided to reproduce Bragg scattering at the small angle. To our great surprise, we simply could not outcouple any atoms! Strangely, we were able to do so after a short amount of ballistic expansion when the condensate density was reduced, but not in the trap. We soon realized that this suppression of long-wavelength excitations was not due to any technical problems but due to the ordered nature of the BEC with interacting atoms. As was noted in eq. 2.14, the rate of excitation is proportional to the static structure factor $S(q)$, which approaches zero as $\frac{\hbar q}{2Mc}$, where c is the condensate speed of sound. We then explored the physics of the static structure factor [13] before finally returning to studying collisions.

2.7 Theory of collisions in a BEC

When we finally got around to studying collisions, the first experiments explored the difference in cross-section between distinguishable and indistinguishable atoms. These experiments were performed by producing atoms using counter-propagating light beams which produced atoms moving at 6 cm/s. The collisional density of the condensate was probed, and the collisional density for indistinguishable atoms was found to be twice that for the distinguishable atoms. These large angle collisions are discussed in sec. 2.8.

The second set of experiments used distinguishable impurity atoms at small velocities that were produced using small-angle Raman scattering. By varying the condensate density, and hence the speed of sound, we were able to study the condensate collisional density as function of v/c. We observed a dramatic reduction in the collisions as the speed of the impurities, v, was reduced to a value close to the speed of sound c. This suppression is due to the superfluid nature of condensates. These experiments are described in detail in sec. 2.9.

In both these experiments, we observed bosonic stimulation of the collisional products which increased the rate of collisions. This stimulation exploited in experiments concerning 4-wave mixing [90] and entangled squeezed beams [57]. A theoretical formulation of the stimulated collisions is presented in sec. 2.7.7. However, before describing the experimental realization, I will first describe the perturbative theory for collisions in the next sections.

In this section, I will derive some basic expressions relevant for condensate collisions. Some of these expressions have been derived earlier [77, 91]. In sec. 2.7.1, I will describe how one obtains the collisional cross section at large impurity velocities for both distinguishable and indistinguishable atoms from the Hamiltonian (eq. 2.6). Then impurity scattering at velocities close to the speed of sound is discussed(sec. 2.7.5), and an expression for the collisional density of an inhomogeneous condensate is presented in sec. 2.7.6. Finally, a basic theory of collisional superradiance is presented in sec. 2.7.7.

2.7.1 Collisional cross section

Before the experiments described in this thesis, most theory papers on condensates only considered mean-field repulsion between outcoupled atoms in mode **k** and the condensate at rest (mode **0**); see for example, [92, 93]. Thus, they only considered the term $2C\hat{a}_k^\dagger\hat{a}_0^\dagger\hat{a}_0\hat{a}_k$ in the Hamiltonian, eq. 2.6. This term leads to a distortion of the outcoupled beam. However, this two-mode approximation neglects the scattering into the empty modes, described by

$$\mathcal{H}' = 2C\sum_{l,n}\hat{a}_l^\dagger\hat{a}_n^\dagger\hat{a}_k\hat{a}_0\delta_{l+n-k-0} \tag{2.20}$$

that results in a scattering rate for particles in mode k

$$W_{\text{swave}} = n_0\sigma v \tag{2.21}$$

with the condensate density $n_0 = N_0/V$, the cross-section σ and the relative velocity $v = \hbar k/M$. Eq. 2.21 describes the cross-section for the quantum mechanical interaction between two matter waves.

2.7.2 Lab frame

Let us assume that the incident velocity is much larger than the speed of sound $v \gg c_s$. Therefore, there is no distinction between free particles and quasi-particles. For indistinguishable atoms in a homogeneous system, I will derive the expression 2.21 both in the lab frame and in the center of mass frame for pedagogical reasons. In the lab frame, the Hamiltonian (2.20) can be written as

$$\mathcal{H} = 4C\sum_{q}{}' \hat{a}_{k-q}^\dagger\hat{a}_q^\dagger\hat{a}_k\hat{a}_0, \tag{2.22}$$

where the prime indicates that we are integrating over only one hemisphere in $\mathbf{q}$-space since we have indistinguishable atoms. The additional factor of 2 (compared to eq. 2.20) accounts for the fact that for indistinguishable atoms, the final state $(\mathbf{k}-\mathbf{q},\mathbf{q})$ appears twice in the summation (as $\mathbf{k}-\mathbf{q},\mathbf{q}$ and $\mathbf{q},\mathbf{k}-\mathbf{q}$). In the perturbative limit, consider the collision between one particle with momentum $\hbar\mathbf{k}$ with a pure condensate with N_0 atoms. The initial and final states $|n_k, n_{k-q}; N_0, N_q\rangle$[6] (see eq. 2.9) are

$$\begin{aligned} |i\rangle &= |1,0;N_0,0\rangle \\ |f\rangle &= |0,1;N_0-1,1\rangle. \end{aligned} \tag{2.23}$$

The square of the matrix element for the Hamiltonian (eq.2.22) between these two states is $|M|^2 = 16|C|^2 N_0$. Using Fermi's golden rule (eq. 2.12), the scattering rate is given as

$$\begin{aligned} W_{\text{swave}} &= \frac{2\pi}{\hbar}\sum_{E_f}|M|^2\delta(E_f-E_i) \\ &= \frac{2\pi}{\hbar^2}|M|^2{\sum_q}'\delta(\omega^0_{k-q}+\omega^0_q-\omega^0_k) \\ &= \frac{2\pi}{\hbar^2}|M|^2\frac{V}{(2\pi)^3}\int \mathrm{d}\Omega'\,\mathrm{d}q\; q^2\delta(f^0_q(\cos\theta)), \end{aligned} \tag{2.24}$$

where $f^0_q(\cos\theta) = \hbar/M(q^2 - kq\cos\theta)$. The δ-function above implies that the transferred momentum, $q = k\cos\theta$, can only vary between $[0,k]$, with $\theta\in[0,\pi]$. Thus, the collisional products fall on a sphere with radius $k/2$ that is centered on $\mathbf{k}/2$, which is exactly what we see in time-of-flight images (fig. 2-4). Evaluating the δ-function and substituting $C = 2\pi\hbar^2 a/MV$ (see sec. 2.3) gives $W_{\text{swave}} = (N_0/V)(8\pi a^2)(\hbar k/M)$, where the cross-section $\sigma_{indist} = 8\pi a^2$.

Note that in order to derive the simple result for the cross-section $(8\pi a^2)$, I have assumed a free-particle dispersion relationship in eq. 2.24. While this is valid at very high particle velocities, a more accurate result valid at all velocities would need to explicitly consider the indistinguishable particles as Bogoliubov excitations such that the δ-function becomes $\delta(\omega^B_{k-q}+\omega^B_q-\omega^B_k)$. The s-wave cross-section of $8\pi a^2$ is then valid only in the large velocity limit of the colliding particle. See ref. [76] for the full description for the collisions between indistinguishable atoms and the condensate.

2.7.3 Center-of-mass frame

It is also instructive to perform the same calculation as above in the center-of-mass (c-o-m) frame. In this description that it becomes obvious that the speed v in eq. 2.21 is due to the

[6]The distinction between n_l and N_l becomes irrelevant for distinguishable atoms

density of final states. The Hamiltonian in the c-o-m frame becomes

$$\mathcal{H}' = 4C \sum_q{}' \, \hat{a}_q^\dagger \hat{a}_{-q}^\dagger \hat{a}_{k/2} \hat{a}_{-k/2}. \tag{2.25}$$

Using equivalent initial and final states in the perturbative limit (eq. 2.23), the square of the matrix element is again $|M|^2 = 16|C|^2 N_0$, and Fermi's Golden rule gives

$$\begin{aligned} W_{\rm tot} &= \frac{2\pi}{\hbar} \sum_f |M|^2 \delta(E_f - E_i) \\ &= \frac{2\pi}{\hbar} |M|^2 \int \left(\frac{{\rm d}\rho}{{\rm d}E_f} \right) \delta(E_f - E_i) \, {\rm d}E_f \end{aligned} \tag{2.26}$$

with the final and initial energies $E_f = 2 \times \hbar^2 q^2 / 2M$, $E_i = 2 \times \hbar^2 (k/2)^2 / 2M$. The density of final states ${\rm d}\rho/{\rm d}E_f$ is equal to half the density of single particle states evaluated at $E_{\rm single} = E_f/2$. The density of single particle states at energy E is

$$\left. \frac{{\rm d}\rho}{{\rm d}E} \right|_{single} = \frac{1}{2} \times \frac{V}{(2\pi)^3} 2\pi \left(\frac{2M}{\hbar^2} \right)^{3/2} \sqrt{E} \tag{2.27}$$

The additional factor of (1/2) comes from the fact that for pairs of indistinguishable particles, we only count the number of states in one hemisphere for indistinguishable particles.

Thus, the density of final states is

$$\frac{{\rm d}\rho}{{\rm d}E_f} = \frac{1}{2} \left. \frac{{\rm d}\rho}{{\rm d}E} \right|_{E=E_f/2} = \frac{V}{(2\pi)^3} \frac{\pi}{2} \left(\frac{2M}{\hbar^2} \right)^{3/2} \sqrt{E_f/2} \tag{2.28}$$

Substituting eq. 2.28 into eq. 2.26 with $q = k/2$ finally gives eq. 2.21 with $\sigma_{indist} = 8\pi a^2$, as expected.

In the c-o-m frame, it is obvious that the scattered particles occupy a shell in momentum space at $q = k/2$ (see fig. 2-4). The quantum-mechanical origin of the relative velocity v in eq. 2.21 is now seen to lie in the density of final states which is proportional to $\sqrt{E} \propto v$.

The scattering of atoms into empty modes as laid out here is not described by the Gross-Pitaevskii equation (which only describes macroscopically occupied modes), but can be accounted for by introducing a complex scattering length into the Gross-Pitaevskii equation [94].

2.7.4 Impurity scattering: large momentum

For the scattering of impurity atoms with the same mass as the condensate atoms the constant C in eq. 2.6 is

$$C = \frac{4\pi\hbar^2 a'}{MV}, \tag{2.29}$$

	Indistinguishable	Distinguishable
C in Hamiltonian	$\frac{2\pi\hbar^2 a}{MV}$	$\frac{4\pi\hbar^2 a'}{MV}$
The number of relevant terms in the Hamiltonian	4	1
Square of the matrix element	$\sim 64a^2$	$\sim 16a'^2$
Density of states	$\frac{1}{2} \times \frac{V}{(2\pi)^3}$	$\frac{V}{(2\pi)^3}$
Cross-section	$8\pi a^2$	$4\pi a'^2$

Table 2.1: The various numerical factors relevant for getting the correct value of the cross-section of indistinguishable and distinguishable collisions.

or more generally $C = 2\pi\hbar^2 a'/\mu V$, where μ is the reduced mass and a' is now the scattering length for collisions between condensate and impurity atoms. For the experimental situation described here, a' is the scattering length between condensate atoms in the $|F = 1, m_F = -1\rangle$ hyperfine state and atoms in the $|F = 1, m_F = 0\rangle$ state. For sodium, $a' \approx a$ [26]. The factor of two between eqs. 2.29 and 2.8 is necessary to avoid double counting of identical atom pairs. If we repeat the above derivations for impurity atoms, we obtain a cross-section of $\sigma_0 = 4\pi a^2$, whereas the cross-section for indistinguishable particles is twice as large. This reflects several factors of 2 and 4, as shown in table 2.1.

For distinguishable atoms, the constant C is 2 times larger, but the factor of 4 in eq. 2.22 is 1 for impurity atoms, which expresses that each initial and final state appears only once in eq. 2.6; finally, the momentum integral for distinguishable particles extends over the whole hemisphere whereas indistinguishable particles have half the number of possible final states. With these changes, one can easily obtain the fact that the cross-section is $4\pi a^2$ when $v \gg c$. Typically, however, the $8\pi a^2$ cross-section for indistinguishable atoms is explained as due to the 'exchange term'.

2.7.5 Impurity scattering: small momentum

When the speed of the impurities is close to the speed of sound of the condensate, then the impurities can excite only phonons rather than free particles, and as noted earlier, there can be no excitations when the impurity velocity is below the Landau critical velocity, which for particle scattering is the condensate's speed of sound.

The matrix element in the perturbative limit (no stimulation by the final states) becomes $|M|^2 = |C|^2 S(q) N_0$, where C is defined as in eq. 2.29. Using Fermi's golden rule in the lab frame, the rate of excitations is

$$W_{\text{swave}} = \frac{2\pi}{\hbar} \sum_{E_f} |M|^2 \delta(E_f - E_i)$$

$$= \frac{2\pi}{\hbar^2} N_0 |C|^2 \sum_q S(q)\delta(\omega^0_{k-q} + \omega^B_q - \omega^0_k) \tag{2.30}$$

$$= \frac{2\pi}{\hbar^2} N_0 |C|^2 \frac{V}{(2\pi)^3} \int \mathrm{d}\Omega \, \mathrm{d}q \; q^2 S(q)\delta(f^B_q(\cos\theta)), \tag{2.31}$$

where $f^B_q(\cos\theta) = \hbar q^2/2M + \omega^B_q - vq\cos\theta$, and we have assumed that the impurity atoms have the same mass as the condensate atoms. The δ-function restricts the q-space to values between 0 and Q, where $\hbar Q = Mv(1 - 1/\eta^2)$ with $\eta = v/c$ being larger than 1. For large η, the maximum momentum transfer is $\hbar k = Mv$. If $\eta < 1$, then the δ-function cannot be satisfied and the integral vanishes. This explicitly shows that the Landau criterion is intimately connected to the accessible density of states. The integral above then simplifies to

$$\begin{aligned} W_{\text{swave}} &= (N_0/V)(4\pi a^2)\left(\frac{2\hbar^2}{M^2}\right)\frac{1}{v}\int_0^Q \mathrm{d}q \; q \, S(q) \\ &= (N_0/V)\,\sigma(\eta)\,v. \end{aligned} \tag{2.32}$$

The collisional cross-section is now $\sigma(\eta) = \sigma_0 F(\eta)$ where $\sigma_0 = 4\pi a^2$ and

$$F(\eta) = \begin{cases} 1 - 1/\eta^4 - \ln(\eta^4)/\eta^2 & : \text{ if } \eta > 1, \\ 0 & : \text{ otherwise.} \end{cases} \tag{2.33}$$

The suppression factor $F(\eta)$ is determined by two factors: the phase space restriction due to the δ function in eq. 2.31, and an additional suppression at low momentum transfers by the structure factor of the condensate. For decreasing velocity, the possible scattering angles θ become restricted to a forward scattering cone ($\theta < \arccos(1/\eta)$), which shrinks to zero solid angle at the Landau critical velocity (fig. 2-6). This reflects that near the Landau velocity, the scattered particle has "difficulties" to provide enough energy per momentum to create phonons. The maximum energy transfer occurs when the momentum transfer is collinear with the incident velocity, i.e., for small scattering angles. In contrast, for large impurity velocities, the scattering is isotropic in the center-of-mass frame and the density of states is uniform. A graph of the suppression factor as function of impurity velocity is shown in fig. 2-7. In the figure, the dotted line is the suppression where only the phase-space restriction (Landau criterion) is included. However, the dotted line does not have a real physicl meaning since the same interactions, which are responsible for the Landau criterion, are also responsible for $S(q) < 1$ at low q.

2.7.6 Collisional density for a trapped BEC

The collisional density is defined as the particle density that an impurity particle experiences as it travels through the condensate. For a homogeneous condensate, the relevant quantity is actually the collision rate ($= n\sigma v$), however, for an inhomogeneous condensate, the

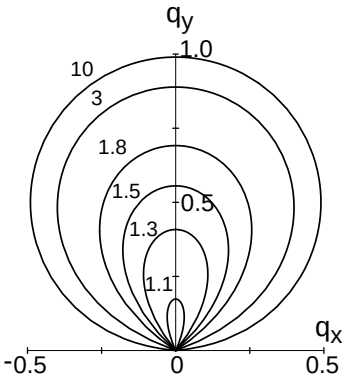

Figure 2-6: Momentum transfer in collisions. The polar diagram shows the momentum transfer (in units of the initial momentum) vs. scattering angle θ for different values of $\eta = v/c_s$ (10, 3, 1.8, 1.5, 1.3, 1.1). As the impurity velocity approaches the speed of sound ($\eta \to 1$), the scattering cone shrinks to zero solid angle.

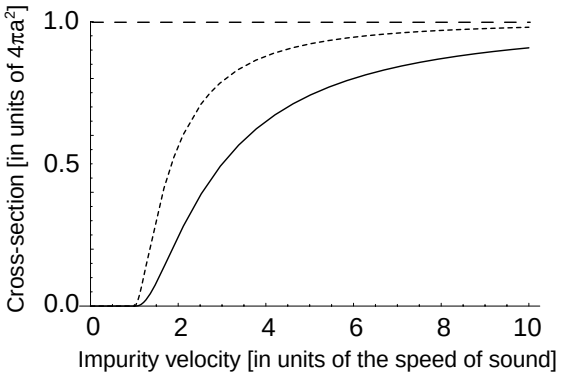

Figure 2-7: Suppression of collisions. Shown is the suppression factor as a function of the impurity velocity (normalized by the speed of sound c_s, solid line). The dotted line represents the suppression due to phase-space restriction alone (i.e., setting the structure factor $S(q) = 1$).

collisional density is more relevant and is defined as $\int n(\mathbf{r})\sigma \mathrm{d}l$, where $\int \mathrm{d}l$ is the impurity path length. The collisional density is proportional to the rate of collisions for impurities as they transverses through the condensate, since the $\mathcal{C} = \frac{n_{k-q}}{n_k} = \frac{1}{n_k}\frac{dn_{k-q}}{dt} \times t$, where $t = l/v$ is the time for completely traversing the condensate.

Generally, when N particles impinge upon a scattering media, the number of particles that are scattered $dN = -rN\ dt$, where $r = n\sigma v$ is the scattering rate. Thus, after traversing a distance l in time t, the particle number is reduced by $e^{-n\sigma l}$, and the number of collided particles is given by $1 - e^{-n\sigma l}$.

In our experiments, the situation is similar to the "half-collision" process that is described in ref. [95], where the impurity atoms are created from the "parent" BEC. When impurity atoms travel radially (in the $\hat{x}$-direction) out of the condensate, they experience a collisional density of $\int dx n(x, y, z)\sigma$, where $n(x, y, z) = n_0\left[1 - (x/x_{TF})^2 - (y/y_{TF})^2 - (z/z_{TF})^2\right]$ is the condensate density with $x_{TF} = \sqrt{\frac{2\mu}{M\omega_x^2}}$ (similarly for y_{TF} and z_{TF}) being the Thomas-Fermi radius. n_0 is the peak condensate density, ω_x is the trapping frequency in the x direction, and μ is the chemical potential.

The fraction of atoms that collide is then given by

$$1 - \frac{\int d\mathbf{r}\, n_I(\mathbf{r}) \times \exp\left[\int dx'\, n(x', y, z)\sigma\right]}{\int d\mathbf{r}\, n_I(\mathbf{r})} \tag{2.34}$$

where the impurity density $n_I(\mathbf{r}) = \alpha\ n(\mathbf{r})$ is a small fraction α of the condensate density $n(\mathbf{r})$. This impurity density profile is created using light scattering where the pulse duration is shorter than the mean field broadening for the condensate. See section 2.8.1 for more details. Here, I have assumed that the cross-section is constant, i.e., the impurity velocity is large compared to the condensate speed of sound, and in addition, the atoms all exit the condensate in the radial direction ($\hat{x}$) only. Therefore the influence of the mean-field repulsion and gravity (in the $\hat{z}$-direction) is ignored.

For the large velocity scattering, the out-coupled atoms travel in the radial direction (x), and the peak collisional density experienced by an atom at the edge of the condensate as it traverses through the entire condensate in the Thomas-Fermi approximation is given by $\beta = 4/3 \times n_0\sigma x_{TF}$. Performing the integration in eq. 2.34 gives the fraction of collided atoms as[7]

$$1 - \frac{5}{2\beta}[1 - \mathrm{HyperGeometric1F1}(2/3, 5/3, -\beta)]. \tag{2.35}$$

where the HyperGeometric1F1 is the Kummer confluent hypergeometric function. Experimentally, β is solely determined by the chemical potential of the condensate and the collisional cross-section $\beta = 4/3 \times (\frac{\mu M}{4\pi\hbar^2 a}) \times \sigma \times \sqrt{2\mu/(M\omega_x^2)}$. The chemical potential μ is determined by a fit to the ballistic expansion of the condensate [96]. The collisional density

[7] The integration is easy to do in Mathematica.

experienced by an atom scattering off the condensate is given by

$$-\ln\left(\frac{5}{2\beta}[1-\text{HyperGeometric1F1}(2/3,5/3,-\beta)]\right). \tag{2.36}$$

Inclusion of the suppression of the collision cross-section (eq. 2.33), mean-field repulsion and gravity requires a numerical integration of eq. 2.34 assuming a local density approximation [34, 97]. However, eq. 2.36 is valid in the limit of high impurity velocities.

2.7.7 Collisional superradiance: theory

In the above sections, I have assumed a perturbative approach, where the population of the final states is ignored, to the calculation of the collisional cross-section and hence the collisional density. However, bosonic stimulation (i.e. stimulation by the occupation of the final states) can lead to an enhancement in the observed collisional density. This enhancement can occur both due to occupation of the condensate quasi-particle modes at finite temperature $N_q(T)$, and due to the occupation of impurity particle modes ($n_q > 1$). In all of the experiments studying the condensate collisional density, the temperature T was close to the chemical potential μ. Thus, only the phonon quasi-particle modes were occupied at these temperatures and for the large-angle collisions the final states were quasi-free-particle states. Therefore, finite temperature effects did not play a role for $2\hbar k$ collisions. The only possible stimulation is from large occupation of the impurity modes. However, at small impurity momentum, stimulation due to finite temperature effects may become important and is discussed in sec. 2.10.

The number of possible modes for impurity scattering is calculated by the number of allowed states within an energy interval $\Delta E \approx h \times v/r_{TF}$ using a modified eq. 2.28 as

$$\begin{aligned} N_{mode} &= \frac{V_k}{(2\pi)^3}\pi\left(\frac{2M}{\hbar^2}\right)^{3/2}\sqrt{E_f/2}\,\Delta E \\ &\approx \frac{V_k}{4\pi}\frac{k^2}{r_{TF}}, \end{aligned} \tag{2.37}$$

where $V_k = N_k/n_k$ is the volume in which impurity atoms are coupled out, $E_f = 2 \times (\hbar k/2)^2/2M$, and r_{TF} is the Thomas-Fermi radius along the condensate's radial direction. Let $\mathcal{C}_r = n_0\sigma r_{TF}$ be defined as the collisional density experienced by an impurity atom as it traverses along the radial direction of a condensate. This is also the probability for an atom to be scattered into a collisional mode. Thus, when the number of collided atoms $N_k \times \mathcal{C}_r$ is larger than the number of modes, bosonic stimulation can begin to enhance the scattering. This condition can be expressed in terms of the outcoupled fraction $\alpha = N_k/N_0$ as

$$\alpha > \left(\frac{ka}{\mathcal{C}_r}\right)^2. \tag{2.38}$$

For sodium atoms with v= 6 cm/s, ka=0.06; thus, a unity collisional density for impurities results in all of the modes being occupied for only 0.4% of atoms outcoupled! For scattering of indistinguishable atoms, the condition is the same, but the cross-section in the collisional density is twice as large as that for impurity scattering. The condition shown above can also be derived using a more involved theory that explicitly includes bosonic stimulation [57, 98].

Experimentally, we measured the time-integrated collisions after all of the outcoupled atoms had fully traversed the condensate. The collisional density is obtained from counting the number of atoms that collide and the number passes through without colliding (see sec. 2.8.2). The bosonic enhancement becomes obvious when the measured collisional density increases with number of outcoupled atoms. In the perturbative limit, this collisional rate is independent of the number of outcoupled atoms, and hence, the number of collisions is proportional to N_k. With bosonic stimulation the number of collisions is proportional to $(N_{k-q}+1)N_k \sim N_k^2$. Thus, the measured collisional density per particle increases with N_k. The enhancement increases as the number of outcoupled atoms scattered into the finite modes is larger than the number of modes, similar to superradiance of light in a condensate [12].

2.8 S-wave scattering at large momentum

Experimentally, we used light scattering to outcouple a small fraction of atoms from the condensate. These atoms were produced using counter-propagating light beams and hence collided with the condensate with a relative velocity of 6 cm/s. This was large compared to the speed of sound in the condensate. In time-of-flight imaging, the collisions resulted in s-wave halos as shown in fig. 2-4. By counting the number of the atoms that had collided and the number outcoupled from the condensate, we could measure the fraction of collided atoms, and thus determine the collisional density of condensate. The collisional density gives a measure of the cross-section for collisions.

2.8.1 Raman and Bragg light scattering

Light scattering was used to produce both distinguishable and indistinguishable atoms. To create indistinguishable atoms, i.e., atoms in the same hyperfine state as the condensate ($|F=1, m_F=-1\rangle$), an moving optical intensity grating is imprinted on the condensate using two counter-propagating light beams that are detuned 1.6 GHz below the $|F=1\rangle \rightarrow |F'=0,1,2\rangle$ optical transitions. A small number of atoms is then diffracted with a velocity of 6 cm/s. This is referred to as *Bragg* scattering. The diffracted atoms are still in the same magnetic hyperfine state as the condensate, since the optical intensity grating alone does not couple to the atomic spins. Whereas, for *Raman* scattering, a polarization grating is imprinted on the condensate, which couples to the electron's spin. This transfers the diffracted atoms with velocity 6 cm/s to the $m_F = 0$ hyperfine state. Details on the

Bragg/Raman scattering can be found in refs. [26, 99]. In most of the literature, both of these scattering mechanisms are considered as "Raman" scattering. We use "*Bragg*" scattering to refer to processes which do not change the hyperfine state, and "Raman" for those that do.

In the particle picture, light scattering can be viewed as a process where an atom absorbs a photon from one beam and is then stimulated to scatter it into the other beam. In this picture, Bragg scattering requires the same transition for both atom-light interactions, i.e., a $\sigma^{+(-)}$ transition for absorption and $\sigma^{+(-)}$ transition for the stimulated emission or π^0 transitions for both absorption and emission. Therefore, the hyperfine state of the scattered atoms remain the same. For Raman scattering, $|m_F = -1\rangle \rightarrow |m_F = 0\rangle$, the required transitions are σ^+ followed by π^0 or vice-versa, with the diffracted atoms changing their magnetic quantum number.

Most of the experimental details for the collision work can be found in ref. [1], which is reproduced in appendix D. Few more details regarding the production of the scattered atoms are given below.

For producing indistinguishable atoms at 6 cm/s, the counter-propagating Bragg light beams had the same polarizations, typically linearly polarized in the plane defined by the magnetic field (also the condensate axis) and the wavevector of the light beam. This polarization suppressed superradiance [12]. The beams were passed through two acousto-optic modulators operating with a frequency difference $\omega = \hbar q^2/2M = 100$ kHz for $\hbar q/M = 6$ cm/s. For the Raman transitions, one of the Raman beams was linearly polarized along the direction of the magnetic field (inducing π^0 transitions), similar to the Bragg beams, and the other beam was polarized perpendicular to the magnetic field (which drove σ^+ and σ^-) transitions). The frequency difference between the two beams was $\omega = \hbar q^2/2M + \omega_{Zm}$, where ω_{Zm} was the Zeeman splitting between the $|m_F = -1\rangle$ and $|m_F = 0\rangle$ states in the offset field of the magnetic trap. The number of outcoupled Raman atoms was proportional to the product of intensities of the two beams, $N_{imp} \propto I_{\parallel} I_{\perp}$. In order to suppress superradiance [12], the intensity of laser beam whose polarization was perpendicular to the condensate axis, $I_{\perp}$, was lower than $I_{\parallel}$. The beam $I_{\parallel}$ had the lower frequency compared to $I_{\perp}$ in order to ensure that the Rayleigh scattered atoms (from the higher intensity $I_{\parallel}$ beam) did not overlap with the collisions resulting from the outcoupled atoms during the ballistic expansion. See figure 2-8.

2.8.2 Comparing distinguishable and indistinguishable collisions

For both Bragg and Raman scattering, the light pulses were on for only 10 μs. Thus, the pulse-width broadening ($\sim$ 16 kHz) was larger than the mean-field broadening($\sim$ 2 kHz). This resulted in the density distribution of outcoupled atoms being a copy of the original condensate, satisfying the condition $n_I(\mathbf{r}) = \alpha\ n(\mathbf{r})$ (see sec. 2.7.6). After the production of the scattering atoms, we held the condensate in the magnetic trap for 4-5 ms in order to

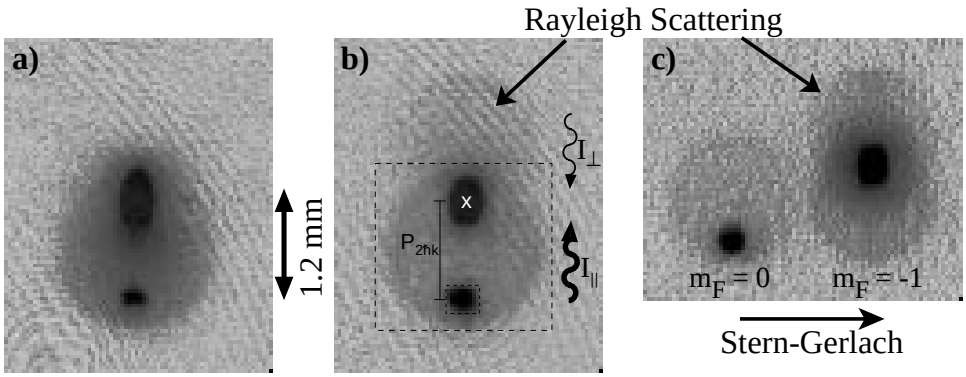

Figure 2-8: Indistinguishable and distinguishable atom scattering. Shown are absorption images resonantly imaged on the cycling transition after ballistic expansion. **a)** Scattering of indistinguishable (Bragg) atoms results in the typical s-wave halo. The outcoupling fraction is about 30%. **b)** A similar image with distinguishable (Raman), $m_F = 0$, atoms results in a lower number of collisions although the outcoupling fraction is slightly larger (37%). The time of flight for both images is 30 ms. The total number number of atoms, N^{tot}, is calculated by counting the atoms in the large dashed box and the number of unscattered atoms, $N^{unscatt}$, is counted in the small box. The momentum transferred, $P_{2\hbar k}$, is given by M/t_{tof} multiplied by the distance between the condensate and unscattered atoms. **c)** An absorption image after 25 ms of ballistic expansion along with an applied magnetic field gradient which separates the $m_F = 0$ atoms from the $m_F = -1$ atoms. The strong beam $I_\parallel$ induced Rayleigh scattering mainly in the $m_F = -1$ condensate atoms. The beam $I_\perp$ has a larger frequency compared to $I_\parallel$, which results in outcoupling of atoms away from the Rayleigh scattering.

ensure that all of the atoms had exited the condensate, before suddenly switching off the trap and imaging the atoms on the cycling transition [100].

To determine the collisional density that the distinguishable and indistinguishable atoms experienced as they traversed through the condensate, we took data with variable outcoupling fractions using both Raman and Bragg beams. Typical images comparing the two are shown in figure 2-8. The images are of comparable outcoupled fractions. It is immediately clear that the indistinguishable, $m_F = -1$, atoms collide more than the distinguishable, $m_F = 0$, atoms. In the images (fig. 2-8), the object plane of the imaging axis was not perpendicular to the momentum transfer $\hbar\mathbf{q}$, but at an angle of about 45°, which resulted in the unscattered outcoupled atoms and the condensate appearing *inside* the observed integrated collisional halo[8].

The fraction of collided atoms was measured using a momentum analysis of time-of-flight absorption images similar to fig. a,b. These images provide the momentum distribution of the atoms, and the total transferred momentum is obtained from the time-of-flight images

[8]For example, if the imaging axis was *along* $\hbar\mathbf{q}$, then we would not have observed the unscattered atoms at all, but only would have seen the condensate at the center of a collisional halo.

by multiplying the number of collided atoms by the distance from the condensate.

$$P^{tot} = \frac{M}{t_{tof}} \sum_i N_i x_i \tag{2.39}$$

$$= \left(N^{outcop} f_{unscatt} + \frac{N^{outcop}}{2} f_{halo} \right) \times P_{2\hbar k}, \tag{2.40}$$

where the first equality (eq. 2.39) is calculated from the images, N_i is number of atoms at position x_i (which is along the momentum transferred $\hbar\mathbf{q}$) integrated along the y-direction, and the sum is over the total number of pixels in the x-direction in a large box enclosing the collisional halo (see fig. 2-8b). $P_{2\hbar k}$ is the momentum of the outcoupled atoms. The momentum $P = 0$ is defined to be at the center of the condensate (marked by $\times$ in fig. 2-8b). $f_{unscatt}$ is defined as fraction of unscattered (non-collided) outcoupled atoms and f_{halo} is the fraction of atoms in the collisional halo. The factor of 2 in eq. 2.40 is because the collision between an outcoupled atom and a condensate results in two atoms with momenta lower than $2\hbar k$, both of which are in the halo[9]. The momentum of unscattered atoms measured as $P^{unscatt} = \sum_i N_i^{unscatt} x_i^{unscatt}$, where $N_i^{unscatt}$ and $x_i^{unscatt}$ are defined similarly to N_i and x_i, but only in a small box surrounding the unscattered atoms (see fig. 2-8b). The fraction of outcoupled atoms is given by $f^{outcoup} = P^{tot}/P_{2\hbar k}$ and the measured collisional density is then given by

$$< \mathcal{C} > = -\ln \left(\frac{P^{unscatt}}{P^{tot}} \right). \tag{2.41}$$

A key advantage of using this technique is that secondary collisions do not affect measurement since all collisional products are present in the time-of-flight image. In addition, since it is the ratio of two momenta that is related to the collisional density, a lot of systematics in absorption imaging is eliminated, including the actual value of $P_{2\hbar k}$. In addition, since the condensate is at $P = 0$, the effect of the "blacking out" of the condensate due to high optical density is lowered when measuring P^{tot}. The imaging axis being at 45° to $\hbar\mathbf{q}$ is not relevant for measuring $< \mathcal{C} >$.

The collided fraction can also be determined by counting the number of collided atoms and the un-collided atoms. The number counting technique is only better than the momentum analysis when counting atoms that are separated using Stern-Gerlach magnetic field, because number counting then has no counting errors resulting from Rayleigh scattering and the presence of a thermal cloud surrounding the condensate. However, in order to minimize systematic errors for comparing collisions between distinguishable and indistinguishable atoms and the condensate, a Stern-Gerlach separation for Raman scattered atoms was not used. The number counting technique was used for calculating collisional density for impurity atoms at low velocities (see sec. 2.9).

The measured collisional density using the momentum analysis is shown in figure 2-9 as

[9]This is only true when Stern-Gerlach separation is *not* used, because then both collided atoms are in the halo.

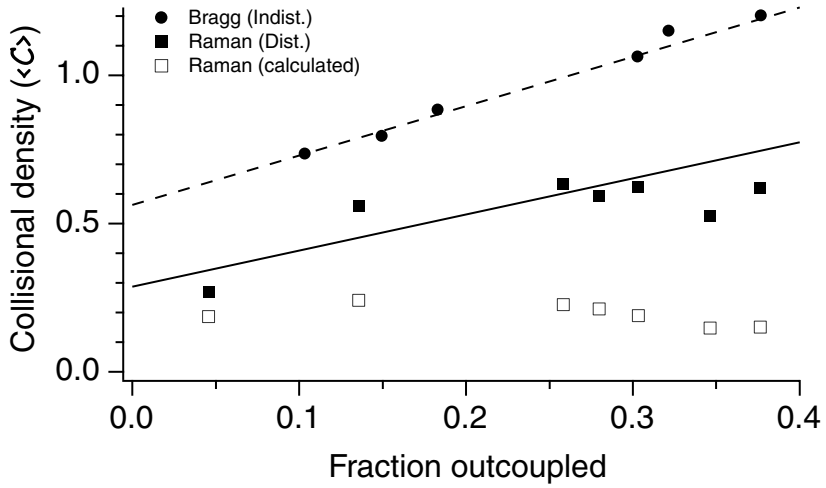

Figure 2-9: The measured collisional density vs. fraction of outcoupled atoms for large velocities ($2\hbar k$). The circles represent the collisional density of the condensate for indistinguishable (Bragg) atoms, calculated using eq. 2.41 and solid squares are for distinguishable (Raman) atoms. The open squares is the theoretical collisional density calculated using the measured chemical potential of the condensate and eq. 2.36 with $\sigma = 4\pi a^2$. The dashed line is a straight-line fit to the circles and solid line for the solid squares for values with less than 30% outcoupled fraction. See text for more information.

a function of the outcoupled fraction. The solid circles and squares are the measured collisional density of the condensate using eq. 2.41 for scattering from the with indistinguishable and distinguishable atoms, respectively. The dashed and solid lines are straight-line fits to the circles and squares, respectively. Only values with less than 30% outcoupling are included in the fits. The non-zero slopes imply that bosonic stimulation is responsible for the increase in the measured collisional density. The collisional density in the perturbative limit, i.e., at zero outcoupled fraction, can be estimated by the intercepts of the fitted lines. For Bragg scattering, the value was 0.56 ± 0.02 and for Raman scattering, 0.29 ± 0.08. For these measured collisional densities, the expected fractions above which bosonic stimulation is important is 1% and 4% for Bragg and Raman scattering, respectively. The ratio of collisional densities for Bragg and Raman scattering was 1.93 ± 0.54, which is consistent with the expected value of 2. However, the large error bar is indicative of the fact that in the perturbative regime where the factor of 2 is expected, precise measurements where hindered by the difficulty of counting very small numbers of atoms.

In the initial stages of the experiments, we were unaware of the fact that we were sensitive to collisional superradiance. In fact, all of the data for scattering at both large momentum and small momentum was taken assuming that we were in the perturbative limit. However, we were not! It was only during Dan Stamper-Kurn's visit back to MIT, in early January 2000, that we realized that the collision rate was increasing with increased outcoupling. We then retook the data for low velocites at small outcoupling (discussed in

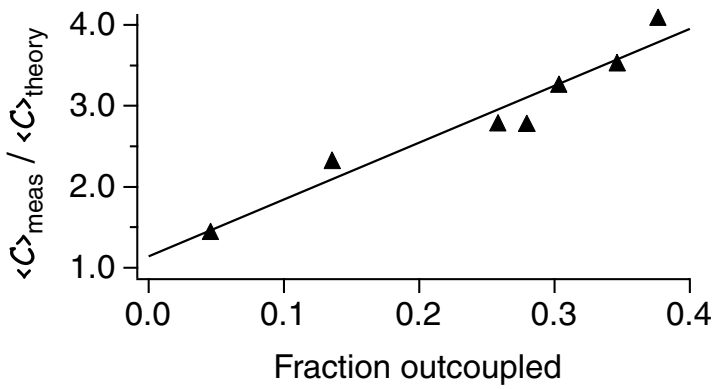

Figure 2-10: Ratio of measured collisional density to the expected perturbative collisional density as a function of outcoupled fraction. In the perturbative limit (small outcoupling fraction), the measured values correspond to the expected theoretical values.

sec. 2.9) such that we were less sensitive to bosonic stimulation. However, we did not retake the data for comparing the collisional densities for Bragg and Raman scattering. Hence, the dearth of data at low output coupling.

The value of the ratio stated here (1.93 ± 0.54) is different from the value quoted in the published work, 2.1 ± 0.3 [1]. In the published work, we had ignored the systematic error resulting from bosonic stimulation. But, both values agree within error bars.

The open squares in fig. 2-9 represent the theoretical collisional densities calculated using eq. 2.36 and the chemical potential of the condensate in images similar to fig. 2-8b. The chemical potential was calculated using its relation to the radial width of the condensate in time-of-flight absorption images [96] as

$$\mu = \frac{1}{2} M \frac{\omega_r^2}{1 + \omega_r^2 t^2} r_{tof}^2, \tag{2.42}$$

where t is the time-of-flight, ω_r is the radial trapping frequency, r_{tof} is the radial half-width of the condensate in the absorption image obtained using a one-dimensional fit to the central region of the condensate in the radial direction. Regions of the condensate profile that were 'blacked out' due to high optical density and near the collisional halo and Rayleigh scattering were ignored in the fit.

The ratio of the measured collisional density using the momentum analysis and the theoretical collisional density in the perturbative limit is shown in fig. 2-10 using the same data as those of fig. 2-9. As expected, the ratio approached 1 at low outcoupling. The straight-line fit extrapolated to zero outcoupling gives a ratio of 1.1 ± 0.2, once again indicating the presence of bosonic stimulation at large outcoupling values. This can be considered as another measurement of the scattering length, where $\frac{a^{meas}}{a^{theory}} = 1.05 \pm 0.10$. As mentioned earlier, a more accurate measurement can be obtained by taking more data at low coupling,

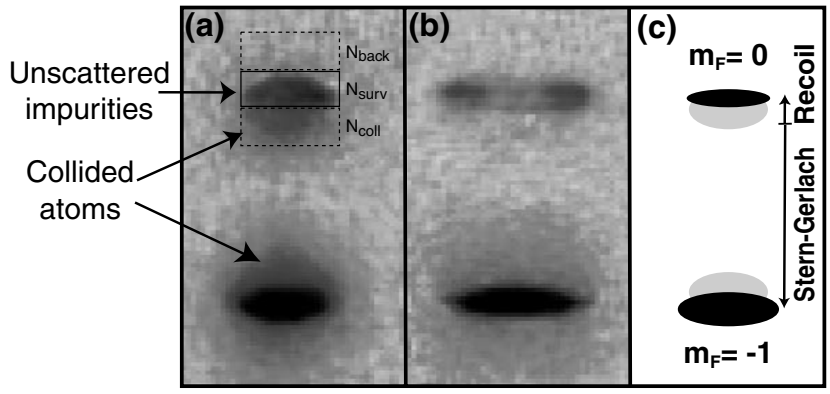

Figure 2-11: Superfluid suppression of collisions. The impurity $m_F = 0$ atoms (top) traveled at 7 mm/s along the condensate axis (upward in image) and were separated from the condensate (bottom) by a magnetic field gradient applied during ballistic expansion (see (c)). (a) Absorption image after 50 ms of time of flight shows the collisional products as indicated by the arrow. For this image, $v_g/c = 2.7$, and the collided fraction is about 20% is determined by counting atoms in the boxes shown in the figure (see text). (b) Similar image as (a) with $v_g/c = 1.6$, where the collisions are suppressed. The outcoupled atoms (impurities) were distorted by mean-field repulsion. The images are 2.0×4.0 mm.

thereby reducing the effect of bosonic stimulation.

2.9 Impurity collisions at small velocities

The superfluid aspects of a condensate can only be explored when the impurity velocity is close to the speed of sound. For that, impurities were produced with an initial velocity of 7 mm/s along the condensate axis using Raman light scattering at small angle (see sec. 2.6.5 and 2.8.1). The peak speed of sound of the condensate was varied between 1.1 and 0.55 cm/s by adiabatically decompressing the gradient field of the clover-leaf magnetic trap [100], and thus η was varied over a range from 1 to 5. The initial impurity velocity (along the condensate axis) quickly gets modified by two main effects: gravity (in the downward direction) and mean-field repulsion (in the radial direction of the condensate). In the experimental condition, the predominant velocity was actually the mean velocity due to gravitational acceleration when the impurity atoms left the condensate, $v_g = \sqrt{2gz_{TF}}$, and it ranged between 17 mm/s for the tightly confined condensates (large c) and 26 mm/s for the loosely confined condensates (small c).

Unlike collisions observed in the large velocity limit, the collisions at low velocities simply appear below the outcoupled Raman atoms in ballistic images, since the collided atoms have lower axial velocities, fig. 2-11a. The superfluid suppression of impurity collisions is evident in fig. 2-11b, where the collisions have dramatically decreased when the velocity is closer to the speed of sound.

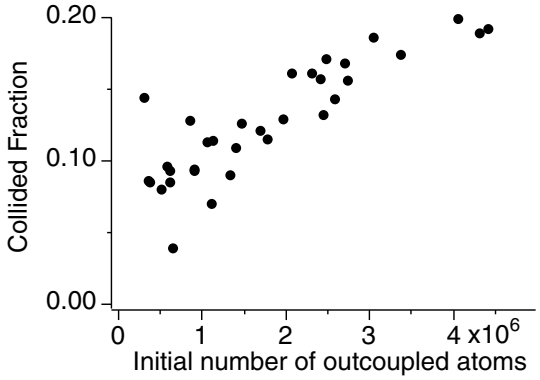

Figure 2-12: Collective amplified elastic scattering in a Bose-Einstein condensate. Shown is the fraction of collided atoms vs. the number of initially outcoupled atoms. For this data, v_g/c=4.9 and the chemical potential was 1.8 kHz.

The number of collided atoms is determined by counting the number of collided atoms in a surrounding box in time-of-flight absorption images (N_{coll} in fig. 2-11a). The collided atoms in the box N_{coll} also overlapped with the small Raman outcoupled $m_F = 0$ thermal cloud. This thermal background was subtracted by counting the number of atoms in a box N_{back} that is above the unscattered Raman atoms. The collisions are expected only to be below the unscattered (survived) Raman atoms (measured in the box N_{surv}), whereas the thermal cloud should be distributed equally above and below the surviving atoms. Thus, the measured number of collided atoms was given by $N_{coll} - N_{back}$. However, the total number of collided atoms was about twice the measured number, since we expect only half of the collisional products to be in the box N_{coll}: the rest was overlapped with the unscattered atoms in the box N_{surv} because the distribution of the unscattered atoms has an axial width roughly equal to the axial displacement of the Raman scattered atoms in the time-of-flight images. The collided fraction f_{coll} is given by

$$f_{coll} = \frac{2 \times (N_{coll} - N_{back})}{(N_{coll} - N_{back}) + N_{surv}} \tag{2.43}$$

The initial number of outcoupled atoms is $(N_{coll} - N_{back}) + N_{surv}$.

2.9.1 Collective Amplified Elastic Scattering

A plot of the collided fraction as a function of number of outcoupled atoms is shown in figure 2-12. Similar to the large velocity collisions (fig. 2-9), the increase in the collided fraction is due to bosonic stimulation or collectively amplified elastic scattering. One might speculate that instead of bosonic stimulation, outcoupling Raman atoms from the condensate itself might result in an observed increase in collided fraction. As the number of outcoupled atoms increased, the collisional density of the condensate might *decrease* slightly due to the

reduction in the condensate density, or *increase* slightly due to a smaller critical velocity for dissipation. However, these effects are small (10-20%) compared to observed two-fold increase in collided fraction.

A calculation of the threshold for the stimulation is complicated by the fact that the number of available collisional modes is hard to estimate. It is complicated by two main factors: an increasing velocity, hence increasing k in eq. 2.37, as the impurities traverse the condensate, and the additional complication of the phase-space restriction in the angular distribution. Also, the threshold for bosonic stimulation is even harder to estimate since the collisional density ($\mathcal{C}$) is changing as the impurities traverse through the condensate, due to the varying $F(\eta)$.

It is important to note here that at very low outcoupling fractions, the measured collisional densities become sensitive to signal-to-noise in the absorption images. Both the number of collided atoms and the unscattered atoms are small, and hence dividing two small numbers can give rise to increased fluctuations in the measured collisional densities. This is the main reason for the observed increase of fluctuations for small outcoupling fractions in fig. 2-12. Also, the collisional enhancement is not directional such as in superradiance [12], but similar to omni-directional superfluoresence [101].

2.9.2 Observation of Superfluidity

The probability of collisions is measured by the collided fraction in the limit of low bosonic enhancement. The collided fraction (at low values) at various values of η is a measure of the collisional density: $f_{coll}(\eta) = 1 - \exp(-\mathcal{C}(\eta)) \approx \mathcal{C}_{meas}(\eta)$. In the experiment, η changes as the impurity particle traverses through the condensate due to the gravitational acceleration and due to the inhomogeneous density distribution. So, the data is compared to $\overline{\eta} \equiv v_g/c$, where $v_g = \sqrt{2gz_{TF}}$ and c is the peak speed of sound. To compare with theory, $\mathcal{C}_{meas}(\overline{\eta})$ is divided by collisional density at large velocities, $\mathcal{C}_\infty \approx (5/12)n\sigma_0 z_{TF}$; the exact value of $\mathcal{C}_\infty$ is given by eq. 2.36. The measured relative collisional density as a function of $\overline{\eta}$ is shown in figure 2-13. The theoretical expected relative collisional density is given by

$$\frac{\mathcal{C}(\overline{\eta})}{\mathcal{C}_\infty} \approx \frac{\int d\mathbf{r}\; n_I(\mathbf{r}) \times \int dz'\; n(\mathbf{r}')\; \sigma_0\; F(\eta)}{\int d\mathbf{r}\; n_I(\mathbf{r}) \times \int dz'\; n(\mathbf{r}')\; \sigma_0}, \tag{2.44}$$

where $F(\eta)$ is given by eq. 2.33. The solid circles in fig. 2-13 are determined by averaging the collided fractions obtained by many iterations of the experiment where the outcoupled number of atoms was less than 10^6. The error bars are a measure of the statistical uncertainty[10]. The number of outcoupled atoms was kept below 10^6 to minimize the effects of bosonic stimulation. However, the measured collisional density is clearly higher than the expected value. This could be due to the fact that bosonic enhancement is affecting the

[10]The error bar is the standard deviation divided by $\sqrt{N}$, where N is number of iterations where the condensate number was below 10^6.

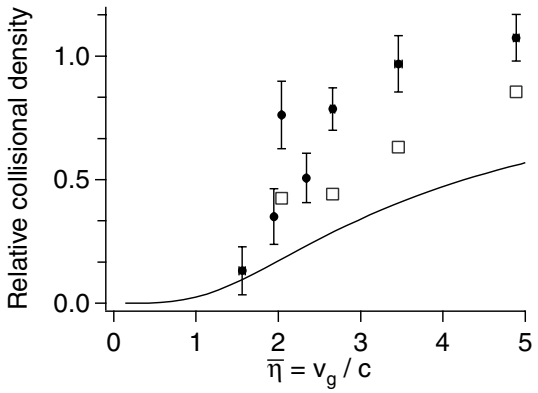

Figure 2-13: Onset of superfluid suppression of collisions. The solid circle and open squares are two measures of the observed collisional density normalized to the predicted collisional density in the limit of high velocities $\mathcal{C}_\infty$ as the density of the condensate was increased (plotted from right to left). The solid circles were obtained by averaging the measured collisional density where the outcoupled fraction was less than 5% ($< 10^6$ impurity atoms), and the squares were obtained by extrapolating to zero outcoupling fraction (see text). The x-axis is $\overline{\eta} = v_g/c$ which is a measure of the impurity velocity over the speed of sound. The solid line is the theoretically expected collisional density calculated by a numerical integration of Eq. 2.44.

measured collisional density even at outcoupling fractions of less than 5-10%. This is not unreasonable since at high velocities (6 cm/s) with $\eta \sim 10$, bosonic stimulation already starts at 4% outcoupling.

Another method of extracting the perturbative collisional density is to extrapolate to the zero outcoupling fraction by fitting the collided fraction (such as in fig. 2-12) to a straight line; these extrapolated values are shown as squares in fig. 2-13. Since the data was taken at low outcoupling fractions only, the extrapolation is not always accurate, especially at low η. Such unreliable data is excluded in fig. 2-13. Nevertheless, the extrapolated values are closer to the theoretically expected perturbative values. Thus, it is clear that bosonic stimulation might be present even at reasonably low outcoupling fractions and hence it is difficult to get an accurate measurement of the perturbative collisional density. In addition, it is possible that there is some other systematic error in the measurement of the absolute density, which can result in higher measured values of the collisional density [1].

Another systematic that one might consider is the effect of the mean-field and the initial axial velocity of the atoms on the collisional density. All of the analysis above was done assuming that gravity is key force that accelerates the atoms out of the condensate. However, mean-field repulsion expels the atoms out radially, which might reduce or increase the path length of the outcoupled atom, and the initial axial velocity might increase the collisional density by having the atom travel longer through the condensate. A numerical simulation of the collisional density experienced by atoms under these different forces indicated that

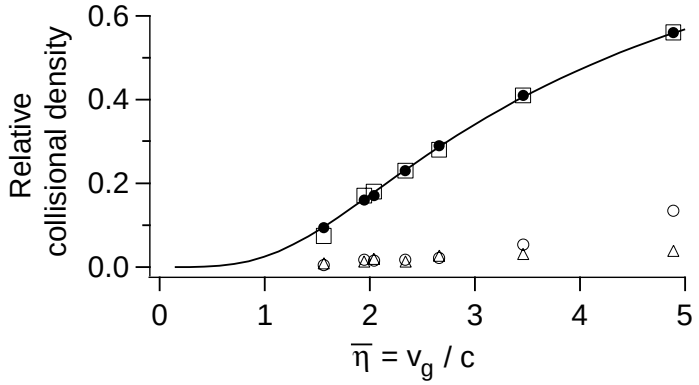

Figure 2-14: A numerical simulation testing the effect of various factors on the collisional density. The solid line is the relative collisional density as a function of $\overline{\eta} = v_g/c$ similar to fig. 2-13. The solid circle is the relative collisional density including only the gravitational force. As expected these circles fall on the solid curve. The open square is the calculated collisional density where the atoms experience all three effects: gravity, mean-field repulsion and the initial axial velocity. The open circle includes only the initial axial velocity and the open triangles only the mean-field repulsion.

gravity is indeed a major effect and inclusion of the mean-field repulsion and the initial axial velocity only changed the results due to gravity alone at most by 10% (see fig. 2-14).

However, the dramatic decrease in collisional density near $\eta \sim 1$ is *the* signature for microscopic superfluidity, and that result is valid regardless of the systematic effects of bosonic stimulation and absolute density measurements. Note that with bosonic stimulation, the dramatic decrease in the collisional cross-section is actually enhanced. One might hope that by fitting these data points to a theoretical curve, we can extract a measurement of the Landau critical velocity and therefore a measurement of the scattering length. However, the systematic effects mentioned above and the finite temperature effects that is discussed in the next section preclude such a possibility.

2.10 Finite temperature effects

As mentioned earlier in sec. 2.7.7, in addition to bosonic stimulation by occupation of the final states, the thermal occupation of phonons can also stimulate scattering. In this section, I will discuss the perturbative effects of these thermal phonons on the collisional density.

At finite temperatures ($kT \sim \mu$), the condensate is in thermal contact with phonon-like quasiparticles with energy $\hbar\omega_q^B$ and momentum $\hbar\mathbf{q}$ that have an occupation probability of

$$\langle N_q \rangle = \frac{1}{\exp(\frac{\hbar\omega_q^B}{k_B T}) - 1}. \tag{2.45}$$

These thermally excited quasi-particles can induce both the Stokes and the anti-Stokes

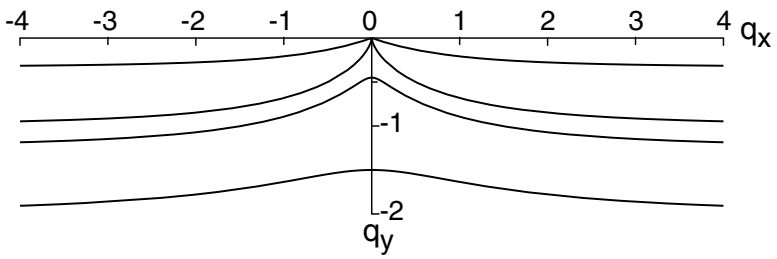

Figure 2-15: Momentum transfer for the cooling anti-Stokes process. The polar diagram shows the momentum transfer (in units of Mc) vs. scattering angle θ for different values of $\eta = v/c$=(0.5, 0.8, 1.0, 3.0), from bottom to top. As the impurity velocity decreases below the speed of sound, the scattering occurs with a minimum q, and extends to infinity, whereas for above the speed of sound, all values of q are allowed.

processes (eqs. 2.14, 2.16 with $n_k, n_{k-q} \ll N_{\pm q}$). The Stokes process adds energy to the condensate, whereas the anti-Stokes process cools the condensate by removing a quasiparticle and transferring the quasiparticle energy to the impurity. The total rate per particle including the thermal excitations is

$$\begin{aligned}
\langle W^T_{\rm swave}\rangle &= \langle W_+\rangle + \langle W_-\rangle \\
&= \frac{2\pi}{\hbar^2} N_0 |C|^2 \sum_q \big\{ S(q)[1+\langle N_q\rangle]\delta(\omega^0_{k-q} - \omega^0_k + \omega^B_q) \\
&\qquad\qquad + S(q)\langle N_{-q}\rangle \delta(\omega^0_{k-q} - \omega^0_k - \omega^B_q)\big\} \qquad (2.46) \\
&= \frac{2\pi}{\hbar^2} N_0 |C|^2 \frac{V}{(2\pi)^3} \int \mathrm{d}\Omega\, \mathrm{d}q\; q^2 S(q) \\
&\qquad \big\{ (1+\langle N_q\rangle)\delta(f^{B+}_q(\cos\theta)) + \langle N_{-q}\rangle \delta(f^{B-}_q(\cos\theta))\big\} \qquad (2.47)
\end{aligned}$$

where $f^{B+}_q(\cos\theta) = \hbar q^2/2M - vq\cos\theta + \omega^B_q$ (defined earlier in sec. 2.7.5 as f^B_q) and $f^{B-}_q(\cos\theta) = \hbar q^2/2M - vq\cos\theta - \omega^B_q$. The properties of $f^{B+}_q(\cos\theta)$ are that the momentum transferred $\hbar q$ can range from 0 to $\hbar Q = Mv(1-1/\eta^2)$ where the angle $\theta \in [0, \arccos(1/\eta)]$ with $\eta > 1$. However, the properties of $f^{B-}_q(\cos\theta)$ are that for $\eta > 1$, all values of q are allowed and $\theta \in [\pi/2, -\arccos(1/\eta)]$. For $\eta < 1$, only momentum transfer *above* a minimum value $\hbar Q_{min} = Mv(1/\eta^2 - 1)$ is allowed, implying $\theta \in [\pi/2, \pi]$. Fig. 2-15 shows the phase space allowed for the anti-Stokes process, similar to fig. 2-6. For $\eta < 1$, one can see the minimum q required by the distance that line is shifted from the origin. Unlike fig. 2-6, this figure shows a negative q, indicating that the momentum is transferred *to* the impurity.

So, if the velocity of the impurity is small or if η is close to 1, the anti-Stokes process dominates and all momentum transfers are essentially allowed. This can effectively cool the condensate by transferring the quasiparticles with low values of momentum $-|\mathbf{q}| \sim 0$ into the condensate. These low momentum quasi-particles have the largest population (see eq. 2.45). In addition, as the temperature increases, quasi-particle populations with higher

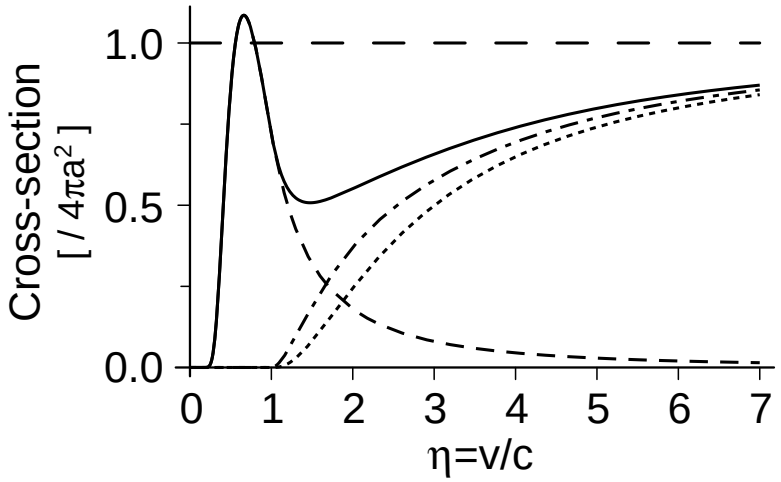

Figure 2-16: Stokes and anti-Stokes contribution to the total cross-section at finite temperature. Shown is the total cross-section as a function of η for $k_BT = \mu$ (solid line). The dashed line and dashed-dot line are the anti-Stokes and Stokes contributions, respectively. These plots of compared with the zero temperature result (dotted line).

q increases, and this population gets transferred into the condensate at low values of η. Interestingly, unlike the Stokes process, where the maximum q was equal to the impurity momentum, the anti-Stokes can transfer limitless energy into the impurity from the thermal quasi-particles, although the probability of finding such a large energy thermal quasi-particle is very small. Note that after the cooling collision, a non-equilibrium distribution is created, which must then be equilibrated to a lower temperature. This requires further collisions between the condensate and the thermal cloud.

Simplifying the Stokes rate in eqn. 2.47 gives

$$W_+(\eta > 1, \overline{\beta}) = (n\sigma_0 v)\frac{8}{\eta^2}\int_0^{\frac{1}{2}(\eta-1/\eta)} \mathrm{d}y\, \frac{y^2}{\sqrt{1+y^2}}\ \frac{\exp(\overline{\beta}y\sqrt{1+y^2})}{\exp(\overline{\beta}y\sqrt{1+y^2})-1}, \tag{2.48}$$

where $y = \frac{\hbar q}{2Mc}$ and $\overline{\beta} = \frac{2\mu}{k_BT}$. The anti-Stokes rate for $\eta > 1$ is

$$W_-(\eta, \overline{\beta}) = (n\sigma_0 v)\frac{8}{\eta^2}\int_\gamma^\infty \mathrm{d}y\, \frac{y^2}{\sqrt{1+y^2}}\ \frac{1}{\exp(\overline{\beta}y\sqrt{1+y^2})-1}, \tag{2.49}$$

where $\gamma = 0$ for $\eta > 1$, and $\gamma = \frac{1}{2}(1/\eta - \eta)$ for $\eta < 1$. Similar results have been derived later in ref. [102]. As expected, for $T = 0$ ($\overline{\beta} \to \infty$), $W_+ \to W_{\mathrm{swave}}$ given by eqns. 2.32 and 2.33, and $W_- \to 0$. A plot of W_+, W_- and the total rate at $k_BT = \mu$ is given in fig. 2-16. The plot shows the enhanced probability for cooling collisions for $\eta < 1$. In addition, the total rate for various temperatures are plotted in fig. 2-17. As noted earlier, at higher temperatures, the cooling collisions dominate and impurities are transferred to higher momentum with greater probability at low η than at higher values of η. However, these collisions would

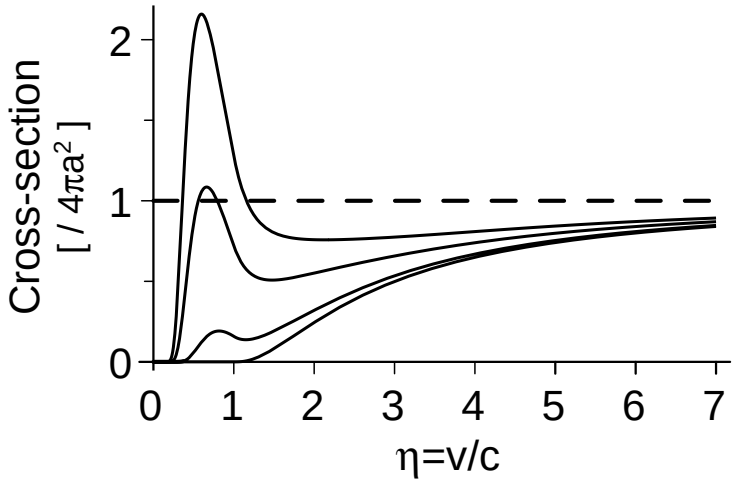

Figure 2-17: Effect of finite temperature on the cross-section. Shown is the total cross-section as a function of η for various temperatures $k_BT = \{0, \mu/2, \mu, 2\mu\}$, from the bottom to the top in the graph.

transfer momentum *perpendicular* to the initial impurity momemtum (see fig. 2-15).

Given the apparent large scattering that seems to be present at even $\eta < 1$, one might ask how close to $T = 0$ do we need to be, in order to observe the superfluid like behavior. In our experiments, by fitting the condensate profile one can extract the temperature of the condensate. Since the various values of η were attained by decompressing the magnetic trap, the temperature of the cloud was not constant as η was varied, but it decreased as the trap was decompressed. So, for $\eta = v_g/c \sim 1$, the temperature is around 350 nK and dropped to around 100 nK for the largest measured $\eta \sim 5$. Therefore, the more relevant quantity is the ratio of the temperature to the chemical potential, which is shown in fig. 2-18; on average $k_BT \sim \mu$ to within 40%. Therefore, one might naively expect that thermally populated quasi-particles might enhance both the Stokes and anti-Stokes scattering[11]. However, due to the gravitational acceleration, we were not able to probe well below the Landau critical velocity where only the thermally assisted collisions are possible. Most importantly, using the number counting technique that was used to determine the collided fraction (sec. 2.9), we explictly subtracted the small signal of the energy gain collisions from the energy loss collisions, thus cancelling most of the finite-temperature effects[12]. Thus, our measured collision rate is actually measuring $W_+ - W_-$, which is close to the zero temperature result, as shown in fig. 2-19. The triangles in the figure are numerically calculated net cross-section $(\sigma_+ - \sigma_-)$ based on the measured temperatures shown in fig. 2-18.

[11] This possible effect was pointed out to us by Sandro Stringari in late 2000. His inquiries inspired me to calculate the effect of finite temperature on the collision rate that has been described in this section, and I re-analyzed the data to extract the temperatures shown in fig. 2-18.

[12] Also, we would not have counted the anti-Stokes collisions with large q since they would be present outside the number counting boxes (see fig. 2-11).

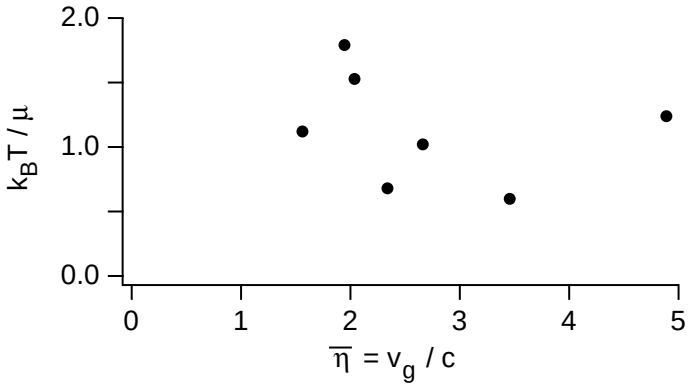

Figure 2-18: The condensate temperature. Shown are the ratio of measured temperatures extracted from a bimodal fit to the condensate to the chemical potential of the condensate as a function of $\eta = v_g/c$.

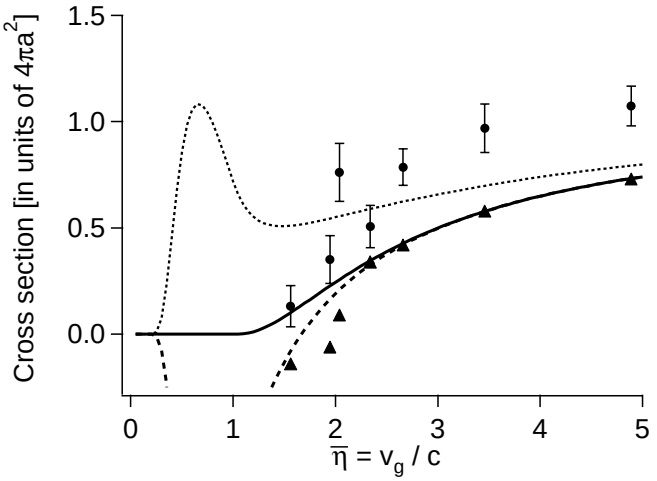

Figure 2-19: Temperature dependent cross-section vs. η. Shown is the cross-section at zero temperature (solid line) and at a finite temperature $kT = \mu$, which is typical for our experimental conditions (dotted line). The finite temperature cross-section includes collisions involving thermally occupied quasi-particles where the impurities lose or gain energy. In the experiment, we measured the number of impurities which lost its energy minus the number which gained energy. Thus, the relevant theory is the net cross-section defined as $\sigma_{\rm loss} - \sigma_{\rm gain}$ (dashed line). The experimental measured cross-sections (solid circles) should be compared to this dashed curve. The triangles are numerically calculated net cross-section ($\sigma_{\rm loss} - \sigma_{\rm gain}$)using measured temperatures shown in fig. 2-18. Note that when the gain process is dominant over the loss process (near $\eta \sim 1$), the net cross-section can be negative.

It is important to note again that I have only calculated and described the finite temperature effects at a perturbative level. The thermally occupied modes not only enhance the scattering as described here, but also lead to bosonic stimulation which further scatters atoms into these modes.

2.11 Discussion: 4 wave mixing/pair correlations/superfluidity

The discussion, thus far, has been on scattering of atoms off a condensate. We have seen that this scattering can be enhanced by bosonic stimulation and suppressed by the collective nature of the Bose condensate: $S(q)$ and superfluidity (for distinguishable atoms). It is important to note that the s-wave scattering process that we have studied is *spontaneous* 4-wave mixing[13], in analogy with the stimulated 4-wave mixing first demonstrated by the NIST group [90]. The Hamiltonian eq. 2.20 is the same for both cases. The NIST group showed that 3 macroscopically occupied states will stimulate the formation of a fourth wave due to bosonically stimulated collisions. The initial theory for the NIST experiments did not take the spontaneous scattering into account [103]. However, spontaneous scattering was an important process in the NIST experiment as shown by the theoretical treatments including the elastic scattering [94, 95], which are in better agreement with the experiments. Nevertheless, even these theories do not include the possibility of Bose-enhanced spontaneous scattering.

The NIST experiment exemplifies the omniprescence of collisions in most BEC experiments. Similar to the parasitic effect of superradiance in BEC experiments involving strong laser light, any experiment that involves large number of atoms in different momentum states will result in s-wave collisions, especially for condensates with high densities. For these experiments, the collisions are more parasitic rather than being interesting [104]. One such example is shown in figs. 2-20.

The observation of enhanced scattering (fig. 2-12) was the first observation of collisional gain which can be used to generate macroscopic pair-correlated beams of atoms that are number squeezed [105, 106]. Of course, in our case, we did not observe "beams" but the entire halo was enhanced. While I was engaged with the building of the science chamber apparatus, my colleague Johnny Vogels pushed this idea further and generated pair correlated beams using a very small number of seed atoms. Although this experiment is similar to the NIST experiment, it used a smaller seed and observed a gain of 20! [57]. The NIST group observed a gain of 1.5 [90], and our collision experiment at small angle observed a gain of 2 (fig. 2-12) and a gain of about 4 for $2\hbar k$ collisions (fig. 2-10).

In addition, the collisions will also play a role in the output coupling of atoms lasers [107–110] from large BEC reservoirs [4]. Collisions between the outcoupled atoms and the reservoir condensate can limit the coherence of atom laser output. Hence, condensate reservoirs

[13]The spontaneously generated collisions were then stimulated.

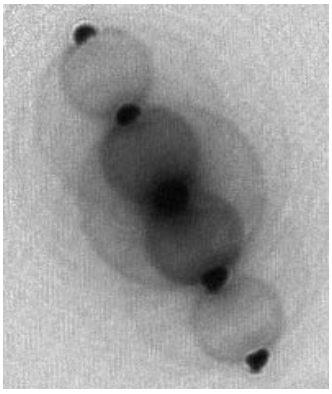

Figure 2-20: Condensates undergoing collisions after Kapitza-Dirac diffraction in a 1D optical lattice.

will need to be of low density to minimize such collisional losses.

The superfluid properties of BEC continue to hold great interest for researchers all over the world. Many techniques for producing vortices have been implemented [3, 78, 111]. Studies of vortex lattices have yielded rich results (e.g. [87, 112]). The critical velocity for breakdown of superfluidity has been studied in optical lattices [113]. Our experiment has been been the only microscopic test of superfluidity in a BEC thus far, and theoretical studies of impurities in a BEC continue to hold great interest [114–116]. Further experiments involving collisions of the kind studied here could in principle measure the scattering length and thus provide another measurement of this important parameter.

Finally, all of these experiments were mainly in the microscopic regime. However, using an optical trap [6], one can study collisions from the microscopic to the mesoscopic regime. In an optical trap, both the $m_F = 0$ and the $m_F = -1$ atoms can be trapped. In fact, the two components are immiscible and therefore form 'bubbles' [9, 11]. Using RF techniques, we can vary the amount of $m_F = 0$ atoms, and hence, we can control the size of these bubbles. By applying magnetic field gradients, one can induce motion of the $m_F = 0$ bubble relative to the condensate, which then collide. Collisions between the $m_F = 0$ bubble and the condensate could reveal the transition of excitations from phonon regime to vortex generation. Another advantage of optical traps is that it can trap all spin states which implies that there is no acceleration due to mean-field repulsion between the $m_F = 0$ and $m_F = -1$ states, but only a weak spin-dependent repulsion that makes them immiscible.

Chapter 3

Construction of the Science Chamber apparatus

In this chapter I will describe the key features of the new apparatus (BEC-III) for transporting condensates using optical tweezers. The transport technique and the new chamber was presented in the following publication:

- *T. L. Gustavson, A. P. Chikkatur, A. E. Leanhardt, A. Görlitz, S. Gupta, D. E. Pritchard and W. Ketterle, "Transport of Bose-Einstein Condensates with Optical Tweezers" , Phys. Rev. Lett.* **88***, 020401 (2002). Included in Appendix E.*

The first experimenters who produced BEC in 1995 [28, 30, 52] did not specifically design their apparatuses for studying BEC physics because the experimental realization of BEC was still speculative then, and it was considered a risky endeavour [22]. They were more focused on realizing BEC rather than experimenting with it. Of course, after the spectacular demonstration of BEC in 1995 and the exploration of BEC physics in the following years, many groups started to build experimental apparatuses that were specifically geared to produce a BEC and study its properties. A common feature amongst these new systems was that, similar to the initial experiments, they experimented with condensates in the same physical location as where they produced the condensates. In other words, the production and the "science" was done in the same location. By 2001, a few groups had magnetically transported 'hot' MOT-cooled atomic clouds into a separate region where they were then evaporated to BEC [117–119]. The main impetus for this was to eliminate the double MOT configuration. While these groups had moved hot atoms, we had a more daring goal: we wanted to move *condensates* over distances of up to half a meter using optical techniques. We hoped to combine the well-oiled condensate making machinery we had developed with a moving optical tweezers that could transport condensates to separate vacuum chamber. We hoped to then perform novel BEC experiments in this separate, 'science', chamber such as loading BECs in miniaturized atom traps and waveguides, continuous atom lasers, BECs

in optical and microwave cavities, low-magnetic field spinor physics, and precision atom interferometry.

In this and the next chapters I will discuss the construction of the new apparatus (BEC III) [2] and describe some of the first experiments. I am writing this chapter as a guide of sorts to BEC-III for future graduate students in the Ketterle group, and for people in the field who might want to construct a similar apparatus in their own laboratories. While some of the technical details are specific, a lot of it might be useful for other experimentalists. Appendix C provides information about the products and companies from which we bought some of the major equipment. Appendices A and B give technical drawings for the main vacuum chamber and some of the oven parts. The early successes are discussed in the next chapters. In chapter 4, I will discuss some aspects of the macroscopic and microscopic wiretraps into which we loaded condensates that were transported using optical tweezers. The production of the continuous source of BEC is discussed in chapter 5.

3.1 Overview and goals of BEC-III

As noted in the introduction, the 'old-lab' group that was working with the BEC-I apparatus decided in the Fall of 1999 to focus its efforts on the construction of a new BEC-III apparatus. The decision to build the chamber was a long time in the making. For a year prior to 1999, there was a general consensus in the group to build a new chamber in which we could transport condensates from one chamber to another, however, it was only after Todd Gustavson joined our group as a post-doc in October 1999 that the project really began to take shape. The main reason for the delay was that our group was really productive in 98/99 and we were discovering and studying various aspects of BEC using the BEC-I apparatus; some of this work is described in sec. 2.6. We simply did not have the manpower to start a new building project. So, Todd's arrival finally gave us the impetus to fully focus on the project. As mentioned in the introduction (sec. 1.4), I decided to be the lead graduate student in this endeavour, so it was Todd and I who led the overall effort for the project.

The construction of BEC-III was deemed as a team effort right from the start. All of us were to be involved in experimental efforts in BEC-I while developing equipment for BEC-III. After completing the experimental work on BEC collisions and some initial work on developing the pancake shaped optical dipole trap [18, 19], I thoroughly focused my efforts on the new apparatus. The essential breakdown of tasks was as follows: Todd developed the design for the new vacuum chamber incorporating input from the group. Deep Gupta took charge of building an oven and a Zeeman slower: he provided the chamber with a large flux of cold sodium atoms. Deep and Aaron Leanhardt wound the slower solenoid and tested the slower. Aaron also designed the clover-leaf magnetic coils and provided it with cooling water and power supplies. All of the cooling and probing laser light was to

be transported to the apparatus using optical fibers. So, Axel Görlitz fiberized all of the cooling and probing light and delivered light to the chamber. Initial tests of transporting condensates in BEC-I using optical tweezers was led by Axel, Todd and Robert Löw. Shin Inouye, Aaron and I built some electronics for the apparatus. I was in charge of putting the chamber together, getting ultra-high vacuum (UHV) with Todd, building the computer control ('the word generator'), and finally, along with Todd, managing the entire project so that our dream of moving condensates came to fruition during late summer of 2001.

During the initial discussions on how to move condensates, we considered moving atoms magnetically, similar to the Hänsch group [117], or by using 1D optical lattices, similar to work done in the Raizen and Salomon group [120, 121]. Given our key goal of transporting the condensates into a separate vacuum-isolated science chamber, magnetic transport implied that we had to devise methods by which we could maintain the magnetic trap through the vacuum gate valve[1]. Although technically possible, it was a much more complicated task than moving condensates optically. However, using lithographic wires, the Hänsch group has succeeded in moving BECs about a cm [122]. The Bragg accelerator technique requires a tight 1D lattice. Although the confinement along the lattice direction is high, transverse confinement is weak unless the beams are focused. Thus, transporting atoms in the horizontal plane would limit the travel distance to the Rayleigh range of the laser beam and a large trap depth would require lots of laser power, which might heat up the cloud. We could attempt to transport the atoms in the vertical direction such that the tight direction is in the direction of gravity. Even here, the condensate might spread out in the transverse direction due to the weak confinement. Of course, transverse confinement can be provided using an another focused beam or magnetic coils, which would only lead to additional complexity.

Thus, we converged on the optical tweezers as a method to transfer condensates. We had developed the first techniques for confining BECs in a singly focused optical trap [6] using far off-resonant infrared laser light. We felt that the step of moving the condensate by moving the focus of this trap was simpler than other possibilities. In essence, our static optical trap of 1998 would be used as a moving optical tweezers for condensates. Moving optical tweezers can also provide the same confinement for the condensate during its travel. Steve Chu had pioneered the field of using optical tweezers [123] for moving, holding, pushing and manipulating bacteria, dna, polymers, etc. Now, we wanted to use it to transport BECs.

The apparatus would then be similar to a beamline, viz. accelerator particle physics. Our accelerator would be an optical tweezers and our particles were condensed macroscopic quantum objects. We would be able to deliver condensates on demand for various applications. It would almost be a users facility, where many experimental setups could be appended onto the main chamber. Perhaps, in the future, our group could collaborate with

[1]For example, by winding external coils around the valve or by putting coils inside vacuum, which could then be translated into the open valve during the transport.

groups who would want a BEC for their experiments, but not necessarily want to build a whole apparatus required for making it[2].

A remark on units in this chapter: most of units are mixed, i.e., SI along with English units. While I could have used a consistent system of units, I felt that it would be artificial. For example, describing vacuum flanges and fitting would be confusing in SI, since inches are the standard units in the U.S. On the other hand, magnetic field gradients are typically measured in G/cm, not G/inch. So, I hope that these mixed units only convey the confusion and clarity that exists while building a new machine.

3.2 Design and structure of the apparatus

By 1999, our lab had produced BECs in both a steel vacuum chamber [52](BEC-I) and a glass cell chamber [78, 124] (BEC-II). However, right from the start it was obvious to us that we wanted to build BEC-III using a steel chamber. Common arguments in favor of using glass cells are the increased optical access, the possibility of putting coils for the magnetic trap close to the atoms, and the lack of eddy currents when the magnetic trap is turned off. However, putting magnetic traps close to the cell will inevitably decrease the available optical access. Also, we did not observe any serious problems with eddy currents in BEC-I. The glass cell in BEC-II was simply much more fragile than the steel chamber of BEC-I. The addition of the pumps near the glass cell requires glass to metal seals which are susceptible to vacuum leaks and breaking of the cell itself[3]. A long glass cell also limits the conductance to the vacuum pumps, thereby making it difficult to reach UHV. Therefore, we decided to build our apparatus around a steel vacuum chamber that was specifically designed for making BEC. Besides, while our main chamber was to be made of steel, we could always use a glass-cell as our science chamber.

A steel chamber design almost automatically limits the type of magnetic coil configuration to be of the cloverleaf type [26, 100], especially if the coils are to be outside the chamber. Compared to the standard Ioffe-bar and pinch coil configuation, the cloverleaf configuration maximizes the optical access, since all 360° between the coils is available for use[4]. We decided against placing our magnetic coils inside the chamber based on our previous vacuum problems with coils inside the chamber [22]. So, we decided to use similar re-entrant 'bucket' ports as in BEC-I, but one that was more shallow and larger. The inner diameter and the depth of the buckets were 14.6 and 10 cm, respectively (see appendix A for the exact specifications). This allowed us to build slightly bigger cloverleaf coil sets (sec. 3.6), that were then placed inside the buckets.

[2]Realistically, such a user facility might be unfeasible currently since constructing BEC machines is not as expensive as building a particle accelerator.

[3]In fact, during the construction of BEC-II, we broke two glass cells before finally aligning the current glass cell.

[4]Dan Stamper-Kurn's new BEC apparatus in U.C. Berkeley uses a steel chamber with Ioffe bars and pinch coils that are placed *inside* the chamber [125].

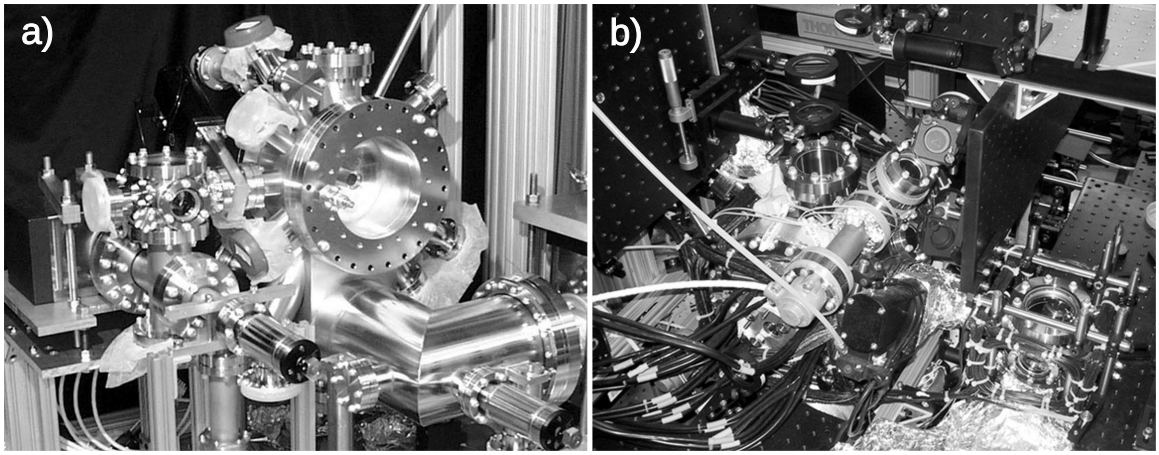

Figure 3-1: BEC-III apparatus. a) The vacuum chamber in August 2000 with all of the windows and the re-entrant bucket ports mounted on it. The Kimball physics science chamber (left of the main chamber) is attached. b) The same chamber in summer 2001, with all of the infrastructure for making a BEC attached on the main chamber (left). The science chamber with the external compensation coils is on the right. Note the relatively free access to the science chamber when compared with the main chamber.

The vacuum chamber, which was built by Sharon Vacuum Inc. was based around the re-entrant bucket ports and was shaped like a wheel with ports surrounding the inner space between the buckets (see fig. 3-1). A schematic of the chamber is shown in figure 3-2. Details of the chamber design are given in appendix A. The chamber was made out of 304 stainless steel that was initially mechanically polished on the inside and then electropolished. The electropolishing minimizes the inner surface area, which helps reduce the 'dirt' inside the chamber and also decreases the surface area of chamber walls onto which gases can adsorb.

The bucket ports (Fig. MIT/L2a,b in appendix A) were built by Sharon vacuum and the small $1.25''$ outer diameter (OD) bucket windows were built by UKAEA, who welded these windows onto the buckets supplied to them by Sharon Vacuum. UKAEA windows have good flatness over a large clear aperture for given port size. We had $0.75''$ OD windows. In addition to these bucket windows, we also got UKAEA to build two other windows for the chamber where we needed large clear aperture: the imaging window (port #6) and the tweezers window (port #3). Similar to the bucket ports, these windows were offset into the chamber. This could allow for a lens to be moved closer to the atoms inside the chamber and thereby maximize the solid angle for imaging. Designs for these windows are also in appendix A. None of these windows, including the bucket windows, had anti-reflection coatings. Only the MOT windows (on ports # 4, 7, 10, 12, 18), the slower window (# 13) and bottom probe window (# 16) had anti-reflection coatings centered at both 589 and 1064 nm.

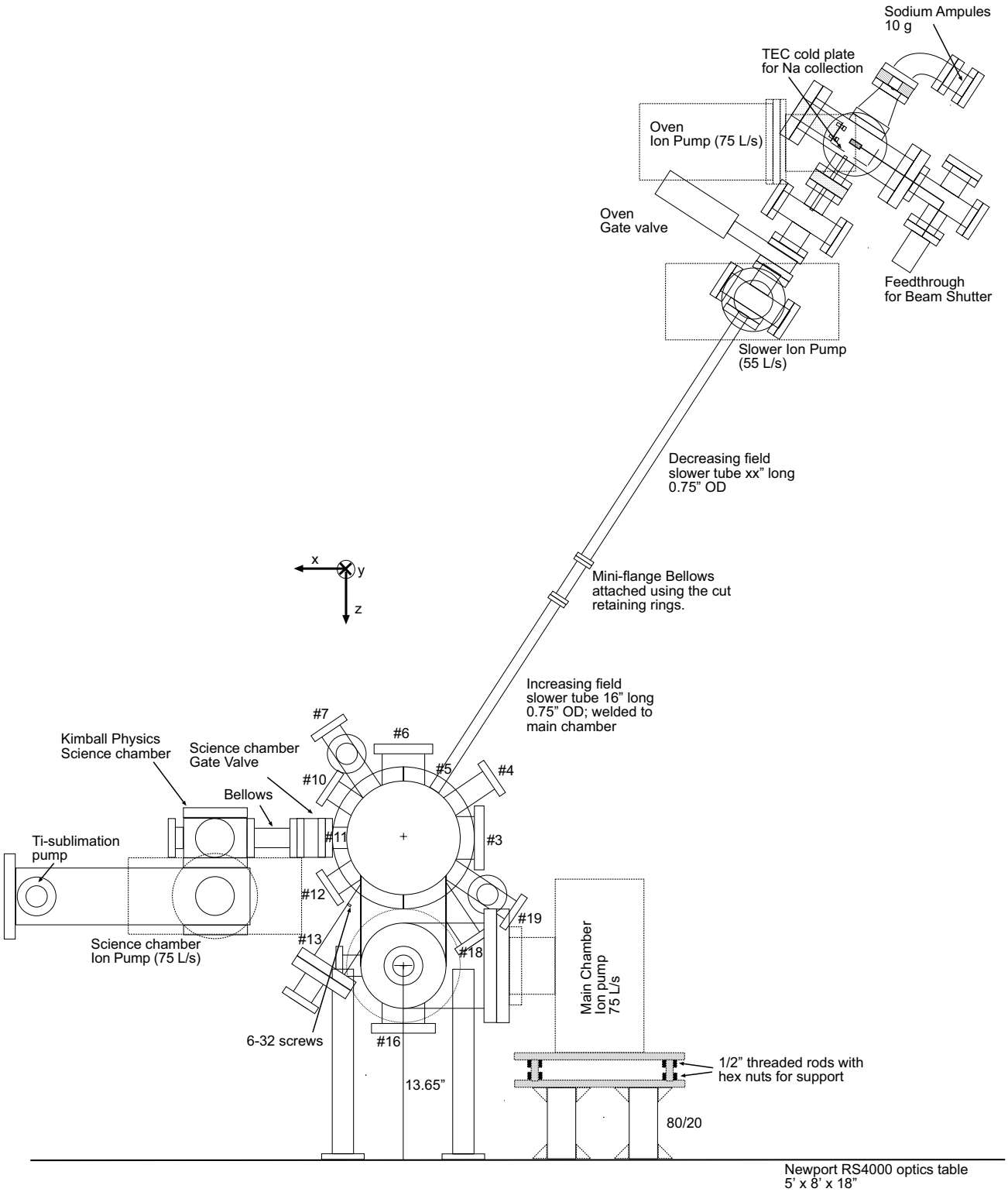

Figure 3-2: The essential features of the BEC-III apparatus, including the science chamber. Details about the design are presented in appendix A. The schematic is drawn to scale. The main ports are labelled. See text for more information. The definition of the 'lab directions' is also shown, x is along the direction of the tweezers beam, y is into the page and z is in the direction of gravity. The distance from the optics table to the false ceiling is 92″.

3.2.1 Vacuum pumps

The main chamber port is connected to a large L-shaped tube (6″ OD) that acted as the pumping region via a 4″ × 6″ rectangular port that was 4″ high; see appendix A. Compared to a circular port, the rectangular port increased the conductance of the main chamber to the pumping region [126]. The pumps for the main chamber consisted of a Varian Starcell ion-pump (75 L/s) attached on the short end of the 'L' (shown in fig. 3-2) and two titanium sublimation getter pumps (TSPs). One TSP was attached with a cryoshield on the long side of the 'L' (into the page in fig. 3-2)[5], and the second TSP was directly in front of the ion pump. The two ion pumps coated all of the inner walls of the 'L'-shaped tube with titanium. The length of the long leg of the 'L' was determined by ensuring that TSP did not have direct line of sight into the chamber[6].

The oven region had a 75 L/s Noble diode pump which allowed us to reach pressures of mid-10^{-8} Torr during operating conditions. A narrow 'differential pumping tube' between the oven region and the beginning of the slower region allowed for a factor of 500 pressure differential between the regions (see sec. 3.3.1). At the beginning of the slower, where the pressure was typically high 10^{-10} Torr, we had another ion pump (55 L/s), which when combined with the 1 m long slower tube gave us an additional pressure differential of more than a factor of 1000 between the slower and main chamber. These two pressure differential factors were multiplicative, giving a total differential factor of about 5×10^5 from the oven region to region where the condensate atoms were produced. Thus, we can run the oven with pressures at about 10^{-7} Torr without affecting the lifetime of the condensate in the main chamber. BEC-I and II also had a similar differential pumping tube between oven and the slower. However, neither of them had a pumping region between the beginning of the slower and the main chamber. Hence, the pressure differential factors from the small tube and slower tube were additive rather than multiplicative. BEC-I only had a 1/2 meter slower tube with a large (2″ OD) diameter slower tube. This implied that we had to run the experiment using a liquid nitrogen cooled titanium pumping in the main chamber and a nitrogen cooled oven cold plate [127]. Although we had no problems running the BEC-I apparatus under these conditions for more than 6 years, we decided to provide the new chamber with a large margin of safety.

We measured the pressure inside our vacuum chamber using ion gauges. It was important to place the gauges carefully such that we were able to accurately estimate the pressure near the condensate atoms. In the main chamber, we had two UHV-24p gauges which were placed off ports #7 and #19. We felt that the pressure reading in the gauge

[5] The cryoshield was added safety in case we needed additional pumping at liquid nitrogen temperatures. We have never had to use it since the pumping from the TSP at room temperature and ion pumps were enough to reach below 10^{-10} Torr.

[6] To prevent coating of the probe window (port #16) with titanium, we bent a thin piece of stainless steel sheet metal in a circular shape and wedged it inside port #16, such that the probe window was protected. The spring action held the piece against the port walls.

in port #7 would be worst background pressure limiting the lifetime of atoms, since it was furthest from the pumping region[7]. After baking out the chamber , we reached pressures below $2 - 3 \times 10^{-11}$ Torr[8]. At these UHV pressures, the lifetime of magnetically trapped atoms was longer than a minute.

3.2.2 The slower port

An important design constraint was that the Zeeman slower and the oven had to be at an angle relative to the plane perpendicular to gravity. One axis of the horizontal plane was occupied by the cloverleaf magnetic trap to ensure that the tight radial direction of the magnetic trap was along the direction of gravity. The other axis had to be free for the optical tweezers such that one of the tight directions of the tweezers trap was along gravity. Thus, the Zeeman slower and oven, which were along the horizontal axis in both BEC-I and BEC-II, was at an angle of 57° with respect to the horizontal (see schematic). A 16″ long steel tube with 0.75″ OD (0.68″ ID) was welded onto the main chamber as shown in fig. 3-2; port #5. The increasing field slower solenoid was mounted on this tube (see sec. 3.3.2).

The on-axis magnetic field of the slower solenoid scales as d^2/z^3 (eq. 3.5), where d is the diameter of the solenoid and z is the distance from the coil along the axis. Hence, by decreasing the coil diameter, we can dramatically decrease the drop-off distance of the magnetic field. This is important especially at the end of the slower, where the MOT should be as close as possible to the end of the slower to increase the flux of cold atom. With a standard 0.75″ OD tube with miniflanges (port #5), the inner diameter of the solenoid must be atleast as large as 1.33″. However, a tube without the flanges, but with only the insert[9] is 0.84″. Thus, the solenoid ID could be as small as that if we had only the rotatable miniflange insert rather than the retaining ring on port #5. The inner coil of the slower solenoids was then wound on a 1″ OD brass tube with 0.87″ ID (see sec. 3.3.3). The solenoid was slid onto the tube and later attached to miniflange bellows that connected the vacuum chamber to the decreasing field slower solenoid and the oven (see fig. 3-3). This decreasing field slower tube also did not have its retaining rings on the flange. After the slower solenoids was mounted on the tube, we attached the slower tube to the miniflange bellows using miniflange rings that were split into two semi-circles between the screw holes. This technique allowed us to have a smaller slower solenoid inner diameter.

The bellows allowed for mechanical isolation between the oven and the main chamber. It also could be used for slight tweaks to the oven and decreasing field slower in case of

[7]Unfortunately, the thermal light emitted from the ion gauge in port #7 during its operation affected our imaging since added background light onto the camera. Hence, this gauge is usually off and we only use the bottom gauge at port#19 for checking the pressure.

[8]At these low pressures, the current in the ion gauge filaments were very low. Usually it was out of range, giving rise to an error in the Varian gauges, E03.

[9]The insert is the part with the knife edges on it.

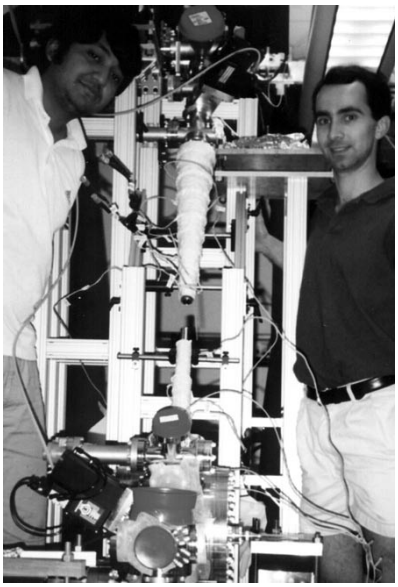

Figure 3-3: Mounting the Zeeman slower. The Zeeman slower is mounted onto the chamber. The center of photo shows the decreasing field slower. The increasing field slower is on the tube attached onto the chamber below it. The gap between the two tubes was bridged using standard mini-flange bellows and the special cutaway mini-flange retaining rings. To the left is my colleague Deep Gupta and right, Todd Gustavson.

misalignments. In addition, the space between the two slower solenoids is important to allow for optical pumping of the atomic beam such that the atoms remain in the cycling transition in the increasing field slower section as well. See sec. 3.3.3. The 3.5″ long bellows provided this space. It was important not to stress the mini-flange bellows too much, since they are prone to leaks.

At the other end of the slower (port #13), it was important to ensure that the hot sodium atoms that were not captured by the MOT do not affect the lifetime of the MOT and the condensate. The hot atoms hit the slower window on port #13 and diffusively reflect from this window. The window was maintained at a temperature around 90°C to ensure that the sodium atoms do not stick to the window. These reflected atoms must be directed quickly into the pumping region so that they will not return to the center of the chamber. In order to do so, we had a large tube (2.5″ OD) that was offset from the slower tube, such that the atomic beam travelled along the top edge of the port (see fig. 3-2). The slowing light beam had to counter-propagate along the atomic beam, hence, an adapter piece was fashioned with a $2\frac{3}{4}''$ flange that was offset from a 4.5″ flange. The large diameter tube (2.5″ OD) provided a region with large conductance to the pumping region, such that the hot sodium atoms could be pumped away. In order to minimize the directly reflected atoms from coming back to the chamber center, we mounted a 2.4″ OD circular aluminum piece along the atomic beam path with a 1″ circular hole whose center was offset such that

slowing beam was not blocked. The piece was mounted to the chamber using two 6-32 hex nuts that were welded near the rectangular flange (see fig. 1c in appendix A). Thus, the large diameter tube combined with the aluminum piece ensured that the reflected hot sodium atoms did not unduly reduce the lifetime of the MOT and the magnetically trapped atoms.

3.2.3 The Science Chamber

One of the key features of the science chamber is that it can be as simple or as complicated as needed. For the first experiments, we decided to use a simple 'spherical square' steel chamber from Kimball physics (MCF450-SS204R04-A). The chamber had two 4.5″ tapped ports, three $2\frac{3}{4}''$ tapped ports, one $2\frac{3}{4}''$ rotatable flange and four miniflange tapped ports. See fig. 3-1b.

The science chamber was isolated from the main chamber by a MDC pneumatically operated gate valve to which a $2\frac{3}{4}''$ bellows is attached. The bellows 'mechanically isolated' the main chamber from the science chamber, such that any science chamber modifications (or attaching a new science chamber) would not stress the gate valve, causing a vacuum leak in the main chamber[10]. The mechanical actuator side (with visible springs) of the gate valve faced the science chamber and the steel plate side faced the main chamber. A $2\frac{3}{4}''$ bellows connected the gate valve to a tapped port of the science chamber.

The pumping region for the science chamber was a long 4″ OD tube to which a 75 L/s ion pump and a titanium sublimation pump were attached. The long tube was attached to the bottom flange of the science chamber (see fig. 3-2). While the chamber was small enough that the ion pump would be sufficient to reach pressures below 10^{-11} Torr, the titanium sublimation provided the extra pumping speed to minimize the pumping and bakeout time for the science chamber. The chamber also had a UHV-24p ion gauge and a Dycor residual gas analyzer (RGA) that was used for analyzing the partial pressure of gases during the bakeout (see sec. 3.4).

Although the chamber described above was designed to as simple as possible, it can easily be replaced by a larger, more complicated chamber. The pumping region (with the long tube) is flexible enough to be used with any other replacement chamber.

3.2.4 Mounting the chamber

The description of the chamber mounting in this section is specific for this apparatus, and is intended mainly as a guide for the future students working on this experiment. However, some of the design principles discussed below might be helpful for other researchers as well.

[10]Initially, instead of the bellows (3.5″ long), we used a short (0.68″ long) adapter from Kimball physics to connect the science chamber to the gate valve. This was to reduce the distance that the optical tweezers had to travel before entering the science chamber. However, we decided that mechanical isolation with the bellows was more important to the future experiments in the science chamber than reducing the travel distance of the tweezers.

The entire apparatus was mounted onto a $8' \times 5' \times 18''$ Newport RS4000 optical table. Given the high center of gravity due to the 1 m height of the slower and the oven, we decided to increase the weight of the table by using an $18''$ thick optical table. The honeycomb core is made of ferromagnetic steel whereas the topskin is a $\frac{1}{4}''$ thick non-magnetic 304-stainless steel plate with $\frac{1}{4} - 20$ tapped holes. The table height had to be as low as possible to ensure that the oven did not hit the ceiling, therefore, four $10''$ high non-isolating legs were tied together with tie-bar flanges that had re-tractable casters[11] Thus, ground vibrations in the Hz to kHz regime can affect the apparatus. Although these vibrations could impact precision measurements, we decided to use the simpler non-floating setup.

The chamber was mounted about a foot off the table using five $1.5''$ Newport posts attached to Thorlabs BA2 bases. The posts were mounted onto $1.75''$ square steel plates that were welded on the centerline of the L-shaped $6''$ bottom steel tube. See appendix A, fig. 1d for details. It was important to place the support structure (the square plates) away from the flanges since the weight of the structure could lead to vacuum leaks as a result of stresses near the flanges[12]. The distance from the table to the center of the bottom tube is $13.65''$.

In addition to these supports, the ion pumps were supported separately in order to minimize the stress on the flanges. The support structure also allowed for easy alignment of the ion pumps. The basic scheme is shown in fig. 3-2 for the main chamber ion pump. The pump was placed on an aluminum plate that was attached to a second plate, separated by about $2''$ using $1/2''$ threaded rods and hex nuts. The bottom plate was mounted to the optics table using $2''$-square T-slotted aluminum posts made by 80/20. By cranking on the hex nuts below the top plate, the height of the top plate was adjusted so that the ion pump flange just 'kissed' the flange on the chamber, whereupon the flanges were tightened together[13]. All of the ion pumps on the apparatus were supported in a similar fashion (see fig. 3-4).

The entire Zeeman slower and oven assembly was supported by 80/20 T-slotted $2''$-square aluminum posts. This aluminum erector set was more flexible than the steel unistrut and dexion system used for BEC-I. The oven assembly had to be about one meter above the main chamber at an angle of $57°$. The arrangement of the supporting posts is shown in fig. 3-4. All of the posts were rigidly connected to each other using 'anchor fastners' that required short posts perpendicular to the ones shown in fig. 3-4. The structure was strong and rigid enough to support the heavy weight of all the vacuum structure and ion pumps. The slower tube and the oven had to be aligned such that it was $57°$ with respect to the horizontal. For this, we fashioned two V-shaped $1/2''$ thick aluminum pieces that were mounted on the 80/20 posts; see fig. 3-4. Two of the ports of the oven $4.5''$ six-way cross

[11] The $10''$ legs could be replaced by pneumatically isolating ones.

[12] During 94-95, BEC-I experienced many vacuum leaks when it was supported near the flanges. See [22].

[13] It was important to use winged copper gaskets so that the gasket did not fall off while adjusting the height of the pump.

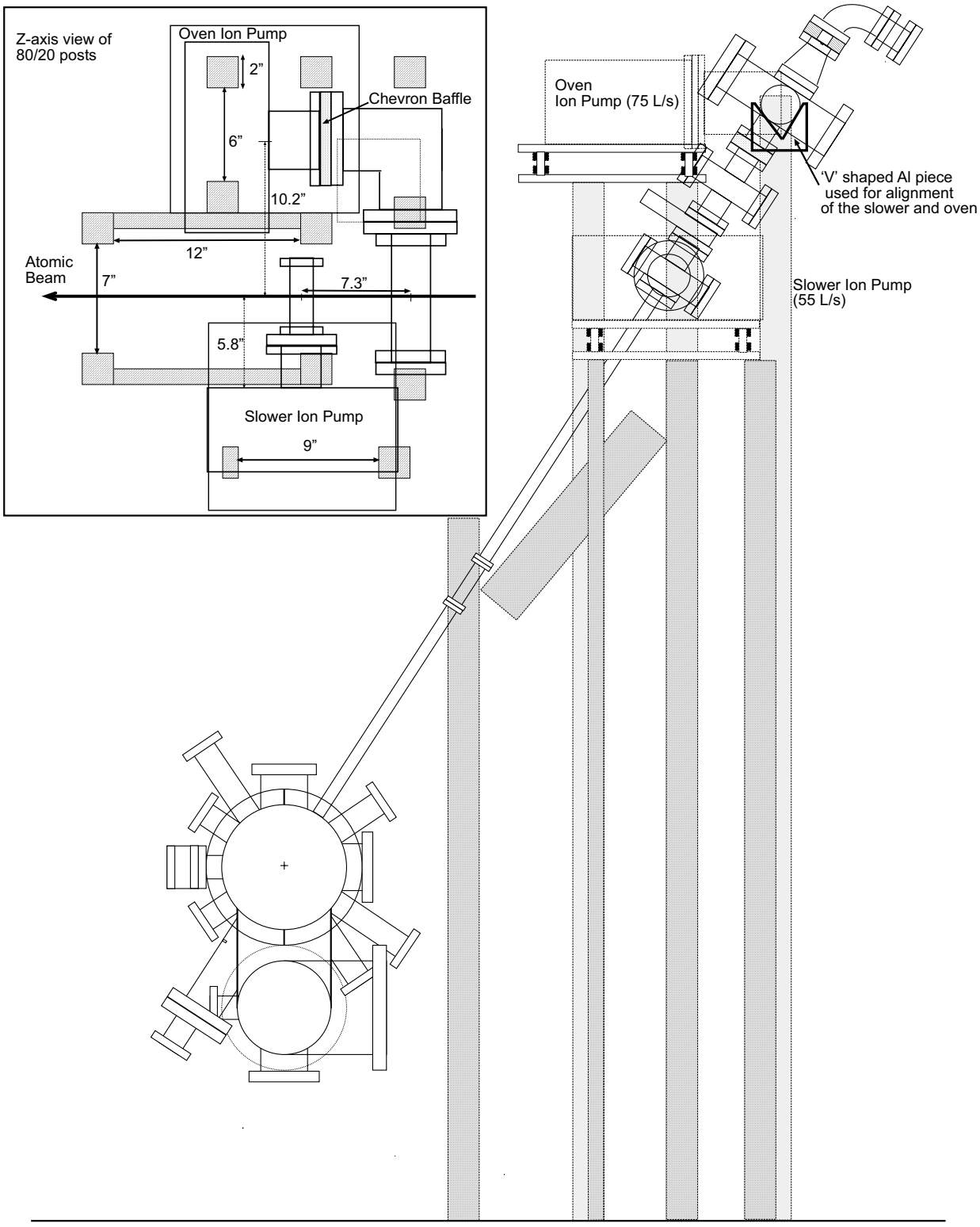

Figure 3-4: Arrangement of 80/20 posts. The view of the posts from the side view. The inset has the view of the posts from above. The entire 80/20 posts are rigidly connected to each other using ‘anchor fasteners’. The ‘V’ shaped aluminum piece used for aligning the slower and oven is also shown. The figure is drawn to scale.

rested inside the V. This allowed us to rotate the entire slower and oven vacuum parts such that they were aligned with the angled main chamber port #5. The fine-tuning of the alignment was done using a He-Ne laser beam as a guide. The laser beam was sent through the center of the slower window (port #13) and centered through port #5. The oven and slower parts were then aligned such that the He-Ne beam passed through the differential pumping tube and the nozzle.

Two angled 80/20 pieces were mounted along the slower tube (as shown in fig. 3-4). By mounting posts attached to these angled pieces, the weight of the slower solenoids were supported. This was to ensure that the solenoid's weight did not stress the long thin slower tubes. The science chamber was held by supporting the $4''$ tube and the ion pump using 80/20 posts similar to the rest of the chamber.

3.3 Sodium atomic beam and Zeeman slower characterization

In this section, I describe the characteristics of the slower and the sodium oven. As mentioned earlier, the oven and the slower were designed, built and tested by my colleagues Deep Gupta and Aaron Leanhardt. I will first describe the essentials of the oven design and the generation of an atomic beam. Some of the designs of the oven parts are in appendix B. The design constraints and characteristics of the slower will be described later.

3.3.1 Sodium oven

In this section, I describe the production of the sodium atomic beam. The beam starts from the oven, where the sodium atoms are first vaporized. The oven is a simple $2\frac{3}{4}''$ steel nipple. Usually, we place two ampules, each containing 5 grams of sodium, in this nipple and heat it to about 260°C when operating the machine (see fig. 3-5). In BEC-I and II, the oven was just a $2\frac{3}{4}''$ elbow into which the sodium ampules were placed and then blanked off. However, since our oven was tilted by 57°, we added a short nipple such that liquid sodium would not just flow into the nozzle when tilted. The melting point of sodium is about 98°C, and the vapor pressure of sodium at 260°C (533 K) is 2.9×10^{-3} Torr. This vapor escaped through a small copper nozzle of 4 mm diameter (see fig. 3-5). The nozzle was maintained at a temperature of 350°C. The sodium vapor, which was at thermal equilibrium at 350°C ($\sim$620 K), sprayed out from the nozzle in $\sim 2\pi$ solid angle into a $4.5''$ six way cross where we had a cold plate. The cold plate served to collect most of the sodium that sprayed out of the nozzle. It was a simple L-shaped copper plate that was attached to a copper slug that could be externally cooled using either liquid N_2 or thermo-electric coolers (TECs)[14]. The design of the cold plate and the slug are given in appendix B. The key element of the design

[14]Since the pressure in the oven was good enough, the cold plate was maintained at room temperature.

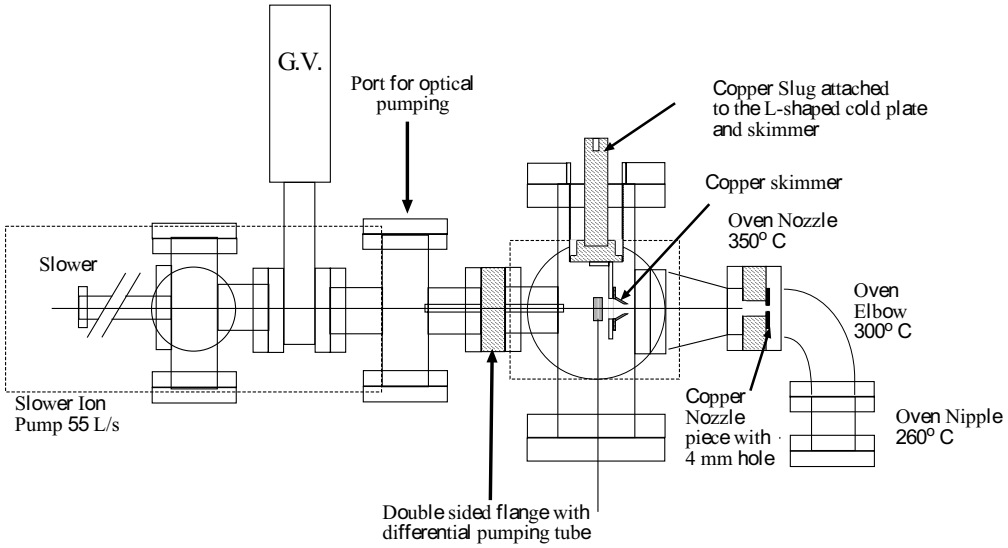

Figure 3-5: The essential features of the oven. More detailed designs of some of the special parts are given in appendix B. The schematic is drawn to scale. The dashed rectangle near the slower indicates the slower ion pump, which is oriented out of the page. The beam shutter rotated in a plane perpendicular to the page, and was controlled by a rotating actuator (not shown). The oven temperatures given correspond to operating conditions. The entire oven is rotated by 57° as shown in figure 3-2

.

was to weld the copper slug onto a very thin steel wall in order to minimize the thermal contact of the cold copper slug to the rest of the steel chamber. The L-shaped copper plate had 0.6″ OD hole with a skimmer attached to it (as shown in fig. 3-5). The skimmer helped to minimize the clogging of the hole in the cold plate by the collected sodium. The entire cold plate assembly can be removed by taking out only one flange and thus, it can be easily cleaned. The beam shutter was located immediately after the cold plate. It was a simple 'flag' made out of 1″ wide copper sheet attached to a copper post that was connected to a rotating actuator. The actuator rotated the flag such that it let the atomic beam pass through (during MOT) or blocked it (all other times).

One of the 4.5″ flanges is connected to a 75 L/s noble diode ion pump, which is the only pump in the oven region (see the inset of fig. 3-4). In order to prevent 'alkali pump poisoning', the pump was connected through an elbow and a Chevron baffle. The baffle and elbow ensured that the sodium atoms do not enter the pump and collect on the pump anodes, thereby shorting them out[15]. The baffle reduced the pumping rate of the ion pump by about a factor of 2. Nevertheless, the ion pump helped maintain a typical pressure of about 5×10^{-8} Torr during running conditions.

The sodium beam after the beam shutter still has a large transverse velocity spread.

[15]Mark Kasevich told us about ion pumps being 'poisoned' by alkalis when pumping cesium atoms with standard ion pumps without any baffles.

However, after the beam passes through the long narrow 'differential pumping tube', the spread is narrowed and an atomic beam is created. The long tube also provided the pressure difference between the oven and slower region. It was 4.75″ long with 0.25″ OD (0.18″ ID). The tube was centered on and welded onto a double-sided $2\frac{3}{4}''$ flange[16]. This tube reduced the conductance between the oven and the slower region. The conductance of a long round tube for air at 22°C is given by[17]:

$$C_{tube} = 12.1\frac{d^3}{l}, \tag{3.1}$$

where the conductance C_{tube} is in L/s, d and l are the diameter and length of the tube, respectively, in cm [126]. Thus the conductance of the differential tube is 0.1 L/s. The differential pumping factor is usually noted by the ratio of the pressures between two chambers P_1/P_2 separated by a region of low conductance, and is given by

$$\begin{aligned} C(P_1 - P_2) &= SP_2 \\ \rightarrow P_1/P_2 &\approx S/C, \end{aligned} \tag{3.2}$$

where P_2 and P_1 are the pressures in the low and high pressure regions, respectively, C is the conductance of the tube connecting the two regions and S is the pumping speed in the low pressure region. In eq. 3.2, $P_1 - P_2 \approx P_1$ since P_2 is usually very small compared to P_1. Assuming pumping speed in the slower region is 55 L/s (from the slower ion pump), the differential pumping factor is about 575 using eq. 3.2.

The flange containing the differential pump tube was connected to a $2\frac{3}{4}''$ 4-way cross that was used to implement optical pumping to increase the flux of the sodium atoms as explained in sec. 3.3.4. The atomic beam then passes through the oven gate valve and into another 4-way cross which then leads to the decreasing field section of the slower.

3.3.2 Spin-flip Zeeman slower: design parameters

As the atomic beam passes through the Zeeman slower, a major portion was slowed from a temperature of 620K to an energy of about 1.2K ($\sim$ 30 m/s). These cold atoms were then captured by the magneto-optical trap, which was 4″ away from the end of the slower. The essential feature of the Zeeman slower is that the slower magnetic fields maintain the resonance between the atoms in the beam and the slowing light by compensating for the Doppler shifts using the Zeeman effect [128].

In contrast to BEC-I, but similar to BEC-II, we decided to use a spin-flip Zeeman slower to increase the capture velocity of the slower. The spin-flip slower has two parts: 1) where the magnetic field is positive and its magnitude is decreasing along the beam path,

[16] It was important to weld the tube on both sides of the flange to minimize virtual leaks.

[17] The main gas load is from hydrogen, not air. However, the conductance for air is a good approximation.

the 'decreasing field' section, and 2) a section where the magnetic field is negative and its magnitude increases along the beam path, the 'increasing field' section. See fig. 3-8.

The slowing light beam counter-propagated relative to the atomic beam and slowed atoms using the $F = 2 \rightarrow F' = 3$ cycling transition. The key constraint for our slower was that we decided to use the same slowing light that was used in BEC-I, which is 1 GHz red-detuned from the $F = 2 \rightarrow F' = 3$ transition (see fig. 3-23 and Dan Stamper-Kurn's thesis [26]). The 1 GHz detuning in the slowing beam implied a maximum magnetic field of about 710 Gauss at the end of the increasing field section of the slower, and thus a maximum capture velocity of 589 m/s, assuming a final slowed velocity of about 30 m/s $[k(v_c - v_f) = \mu_B B$, where $k = 2\pi/\lambda]$. At 620K, the most probably velocity of the beam is about 820 m/s [18]. The average velocity in the beam is 890 m/s [19]. Clearly, this indicated that by increasing the capture velocity in the slower, we could increase the flux of slow atoms at the MOT. The flux of the atoms also decreases as $(L + L_{oven})^{-2}$, where L is the length of the slower and L_{oven} is the length between the oven nozzle and the beginning of the slower. Increasing the capture velocity increases the total length of the slower (see fig. 3-6). Thus, there is an optimum capture velocity where the flux at the slower is maximized. This optimum capture velocity is around 900 m/s.

In general, the capture velocity of a slower can be increased by either increasing the magnitude of magnetic field at the end of increasing field section of the slower or by adding an additional decreasing field section to the slower. Since we wanted to maintain the 1 GHz detuning for slowing light, we had to use a decreasing field slower. We chose an initial field of 440 G with a capture velocity of 950 m/s $[kv = \mu_B B_i - \delta$, where $\delta = -2\pi \times 1\text{GHz}]$.

The next important criterion of the slower is its length. The total length of a slower as a function of the capture velocity v_c is given by (for $v_f = 0$)

$$L = \frac{v_c^2}{2 f a_{max}}, \tag{3.3}$$

where the $a_{max} = \frac{\hbar k \Gamma}{2M}$ is the maximum acceleration (requiring infinite laser power), and f is the fraction of the maximum acceleration that can be achieved given the finite intensity of slowing laser beam. The slower was designed assuming $f = 0.6$, which implied that slowing intensity on resonance had to be at least $1.5 I_0$, where $I_0 = 6$ mW/cm^2 is the saturation intensity for sodium[20]. A plot of the total slower length for various values of f is shown in fig. 3-6. In our case, we also had the constraint of the slowing laser detuning being 1 GHz from the resonance. This implied that the increasing field slower had to be ~ 32 cm long for $f = 0.6$. With this condition, the lengths of the decreasing field for various f are shown in fig. 3-7. The profile of the magnetic field as a function of distance is given by

[18] The most probable velocity is 1.22α, where $\alpha = \sqrt{\frac{2k_B T}{M}}$ [129].

[19] The average velocity is $3/4\sqrt{\pi}\alpha$.

[20] Note that with more slowing laser power, the slowing is more forgiving with respect to magnetic field imperfections.

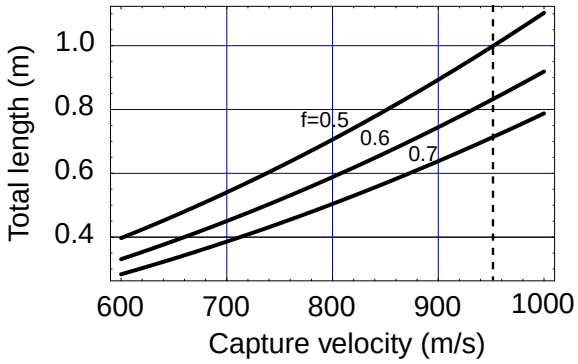

Figure 3-6: The total length of the slower as a function of the capture velocity for $f = 0.5, 0.6, 0.7$. f is the fraction of the maximum acceleration, determined by the available laser power. The dashed line is at 950 m/s where the total length is 83 cm for $f = 0.6$.

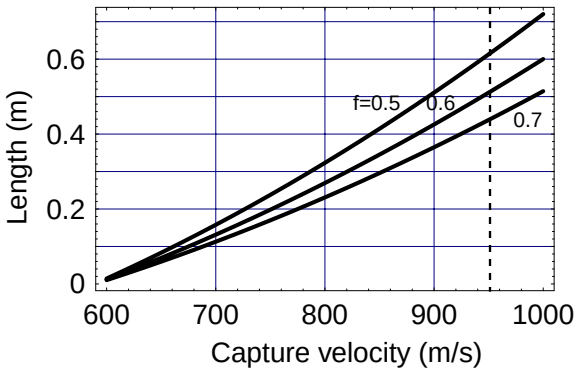

Figure 3-7: The length of the decreasing field slower as a function of the capture velocity for $f = 0.5, 0.6, 0.7$. The dashed line is at 950 m/s where the length is 52 cm for $f = 0.6$.

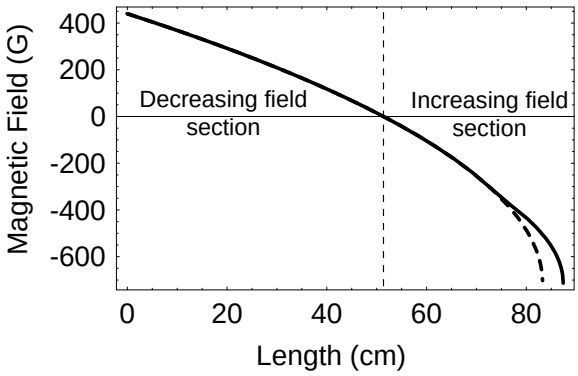

Figure 3-8: The shape of the magnetic field as a function of distance. The plotted field is for B_i=440 G, v_c = 950 m/s. The negative fields indicates the increasing field portion of the slower. The dashed line indicates the magnetic field if the slower is operated at $f = 0.6$, the solid line is the field where $f = 0.4$ after 75 cm. The solid line is the field profile that we used.

$$B(z) = B_i + \frac{kv_c}{\mu_B}\left(1 - \sqrt{1 + \frac{2fa_{max}z}{v_c^2}}\right), \tag{3.4}$$

where B_i is the initial magnetic field of the decreasing field slower and the capture velocity $kv_c = 2\pi \times 1\text{GHz} - \mu B_i$. The theoretical magnetic field is plotted in fig. 3-8. The magnetic fields from the decreasing and the increasing field are oriented in opposite directions, which is indicated by negative fields for the increasing field slower. However, to be safer (assuming lower slowing laser power), the length of the increasing field slower was increased near the end of the slower such that the slowing would occur at $f = 0.4$. So, the slower was designed to operate at $f = 0.6$ until 75 cm, after which it is at $f = 0.4$. The two profiles are shown in fig. 3-8. The length of the increasing field slower increased to ~ 36.4 cm with this modification.

The theoretical analysis of the slower is now complete. The challenge of constructing a successful slower lies in matching the magnetic field produced by real solenoids to the theoretically calculated field. The closer the real field is to the calculated field, the closer it performs to the theoretical expectations.

3.3.3 Building the slower

In BEC-I, the slower solenoid was constructed out of insulated round hollow copper wires[21]. In BEC-II, square hollow copper tubing was used to construct the slower. The advantage of square tubing is that it maximizes electrical conductivity per unit volume since it is easier to wind one loop next to and on top of each other using square wires as opposed to circular wires. The hollow wires allow for water cooling, wherein pressurized water flow through

[21] Incidentally, refrigerator tubing was used for winding the slower.

the hollow core cools the current carrying wires[22]. We used a square copper wire made of copper alloy 101 [23] with $1/8''$ square and $0.0625''$ square hole. The wire was bought from Small Tube Products, and was insulated using Double Dacron Glass Fuse (DDG; see app. C). The turns of the solenoid were then hand-wound around a brass tube of $1''$ OD ($0.87''$ ID) that was mounted on a lathe. With the insulated wire, a solenoid with ten turns was 3.5 cm long (0.35 cm/turn). The magnetic field profile along the symmetry axis of a single current carrying loop is

$$B(z) = \frac{\mu_0 I/d}{\left[1 + (\frac{2z}{d})^2\right]^{3/2}}, \tag{3.5}$$

where I is the current, d is the diameter of the coil and μ_0 is the magnetic permittivity. These loops were combined to make solenoids of varying turns and diameters to match the theoretical profile (fig. 3-8).

One half of the cross-section of the slower solenoids is shown in fig. 3-9. The entire solenoid was broken into sections as labelled in fig. 3-9. The decreasing field solenoid was broken into 3 sections (D1, D2, D3) which were wound on top of each other. Section D1 consisted of 2 layers of 135 and 121 turns, section D2 was made of 2 layers of 107 and 93 turns, and section D3 had 6 layers of 77, 61, 43, 25, 15 and 6 turns, respectively. The spacing between the turns was all uniform. These sections allowed for parallel water flow through them, thereby cooling the coils more efficiently, while being electrically connected in series such that one current flowed through the entire decreasing field solenoid.

In order to prevent the coils and layers from 'springing out', we used an epoxy to the hold the layers of coils in place during the winding. We used a high temperature epoxy from Dexter Hysol (Epoxi-Patch Kit 1C White), which was rated up to 150°C. Although higher temperature epoxies were available, the insulation for the wires were rated only for 150°C. The epoxy gave the solenoids their characteristic white color, as seen in fig. 3-3[24].

The increasing field slower was broken up into two separate current carrying sections, labelled as the 'low-current' and 'high-current' sections (see fig. 3-9). The low-current section was made of 2 sections: IL1 made of 2 layers of 84 and 58 turns, and IL2 made of 3 layers of 37, 17, and 7 turns, respectively. Note the spacing between the turns in IL1 was not uniform throughout, but is double-spaced near the beginning. The high-current section was made of 2 layers of 10 and 9 turns each. The water connections were once again in parallel for maximum cooling, and whereas the current for low-current sections were in series. The key reason for the high current section near the end of the increasing field slower was to reduce the coil diameter at the end of the slower, thereby lowering the stray magnetic field from the slower solenoid in the MOT region, which was $4''$ away from the end of the slower; also see sec. 3.2.2. With 100 A on the high-current section, a stray field of about 4 G was compensated by running current in an extra coil (18 turns) that was

[22] This tubing was first suggested to us by Mark Kasevich.
[23] This alloy had the right tempering for winding.
[24] After heating the slower to about 100°C during the bakeout, the epoxy turned yellow.

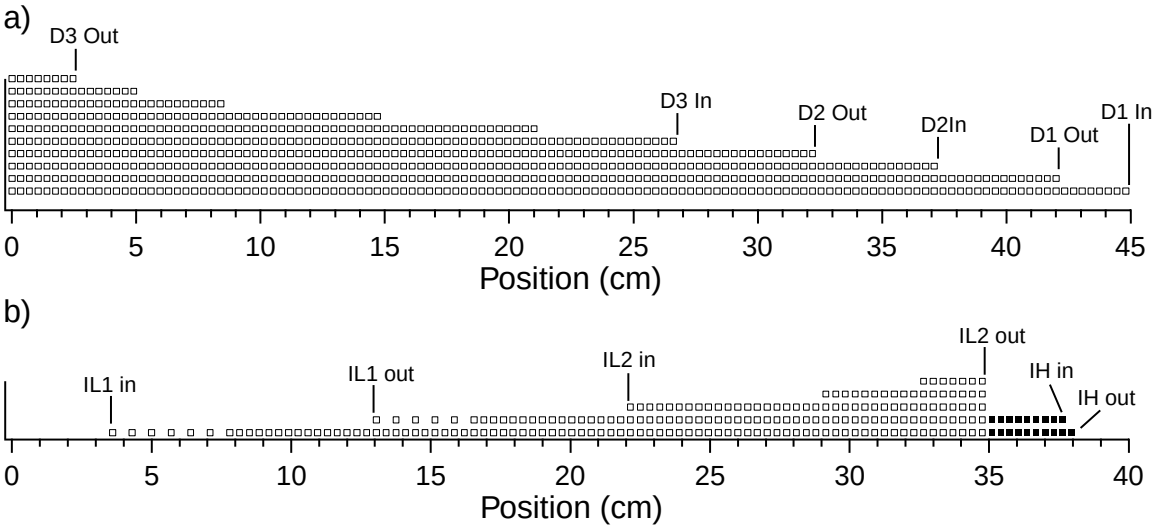

Figure 3-9: Half cross-sections of the slower solenoids. a) decreasing field solenoid, b) increasing field solenoid. For the increasing field, the low current section is indicated by open squares and the high current by the solid squares. The numbers near the end of the coils indicate the solenoid sections. The measured flow rates for the decreasing field slower sections are 100, 90, 60 ml/min for D1, D2 and D3, respectively. For the increasing field, the flow rates are 140, 200 and 400 ml/min for IL1, IL2 and IH, respectively.

wound around the chamber[25]. There was also an additional 0.8 G/cm gradient along the slower axis, which was not compensated.

Typically, the slower solenoids are operated with 15 A in the decreasing field solenoid, and 38 and 105 A in the increasing field low-current and high-current sections, respectively. As mentioned earlier, it was essential to cool the solenoids using pressurized water. The total length of wire for the decreasing field solenoid was about 109 m, excluding about 3 m of additional length for connecting the solenoid to power supplies and water connections. The wire length for the increasing field solenoid was 37 m, with extra 2 m of connecting wires.

The power dissipated in the solenoids can result in large temperature increase in the absence of cooling. For the $1/8''$ square hollow tubing, the dissipated power (in watts) is given by

$$P = 2.65 \times 10^{-3} \times I^2 \times l, \tag{3.6}$$

where I is the current in amperes and l is the length of the wire in meters. About 65 W is expected to be dissipated in the decreasing field solenoid for 15 A of current flowing through the 109 m of $1/8''$ square tubing. Without water cooling, the copper would begin heat up rather rapidly especially since conduction or convection is small. The required flow rate for

[25]The plane of this slower-compensation coil was approximately perpendicular to the slower axis.

cooling the square tubing is

$$F = 14.3 \times P/\Delta T_{H_2O}, \tag{3.7}$$

where F is the flow rate in ml/min, P is the dissipated power in watts and ΔT_{H_2O} is the estimated change in the water temperature in Celsius. For cooling of all high current solenoids, we set the maximum temperature change in the flowing water to be 25°C. The chosen flow rate was at least higher by about a factor of 2 from this maximum value. Thus, for a typical flow rate of 80 ml/min through the decreasing field slower solenoid, 65 W would result in a temperature increase of the water by about 12°C. Typical flow rates for each section of the slower solenoid are listed in the caption of fig. 3-9.

The calculated field of the slower (using eq. 3.5) is plotted in fig. 3-10. Using a gaussmeter, the magnetic field produced by the solenoids was measured and compared with the calculated fields (fig. 3-11). The gap between the two slower solenoids was bridged by the miniflange bellows (see sec. 3.2.2). This gap was also used for optical pumping the atoms back into the cycling transition when the magnetic field changes direction. Since the Larmor precession is very fast, the atoms follow the local magnetic field and is always in the $|F = 2, m_F = -2\rangle$ state. However, the polarization of the light changes its polarity as the magnetic field changes direction. Thus, in order to be on the cycling transition, the atoms must be pumped from the $m_F = -2$ to the $m_F = +2$ state before they enter the increasing field solenoid.

3.3.4 Testing the slower

Once the slower solenoid was constructed, its performance was measured using a test sodium atomic beam apparatus. The atomic beam profile in the test apparatus was similar to the one described above in sec. 3.3.1. The test chamber had a pressure of between 10^{-7} – 10^{-8} Torr and was pumped using a turbo pump. The flux of cold atoms was measured using both fluorescence and differential absorption techniques, where a probe laser frequency was scanned over a range of 10 GHz, which was much larger than the Doppler broadening. The scanning probe laser beam was generated by operating a separate Coherent 699 dye laser and slowing beam was obtained using the 899 dye laser (see sec. 3.7). While the probe light was transported to the test beam apparatus using an optical fiber, the slowing light simply travelled through air about 20 m to the test setup. Although it is to measure the slow atom flux using differential absorption technique, the initial tests of the slower were done using fluorescence of the atomic beam since it was easier to implement. Both Doppler-free and Doppler-sensitive fluorescence were measured, where the probe beam was at an angle 90° and 45° relative to the atomic beam, respectively. Scans of the hot thermal 'raw' beam are shown in fig. 3-12. The fluorescence signal was collected by a photo-diode and amplified. Although the velocity scale was not calibrated to the probe laser frequency, the width of the Doppler sensitive scan was consistent with the expected thermal velocity of the atoms

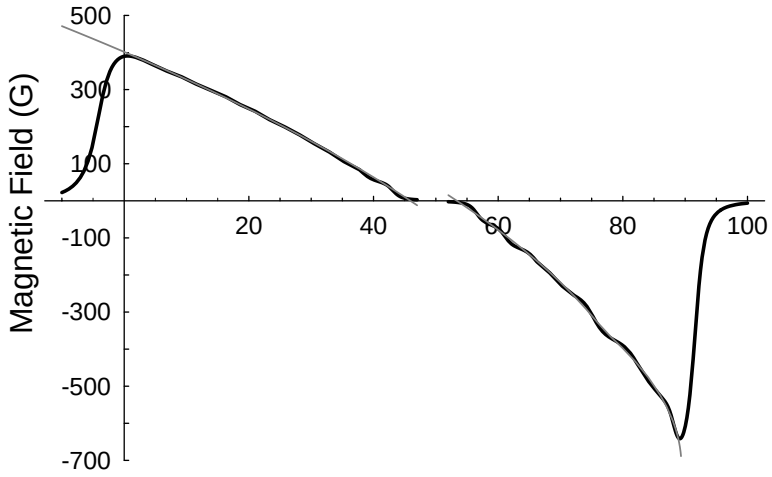

Figure 3-10: The calculated shape of the magnetic field produced by idealized slower solenoids as a function of distance (cm). Both the increasing and decreasing magnetic field are shown. The profiles shown are for 13.8 A in the decreasing field, -15 A and -100 A in the increasing field slower. The gray line is the theoretical curve based on eq. 3.4. Note that due to the small diameter of the coils near the end of the increasing field slower, the magnitude of magnetic field outside the slower rapidly decreases, especially when compared to the beginning part of the decreasing field slower, which has coils with a larger diameter. The gap of about 7 cm between the two solenoids is also indicated. This gap was bridged by the miniflange bellows (see sec. 3.2.2) and is used for optical pumping. See text.

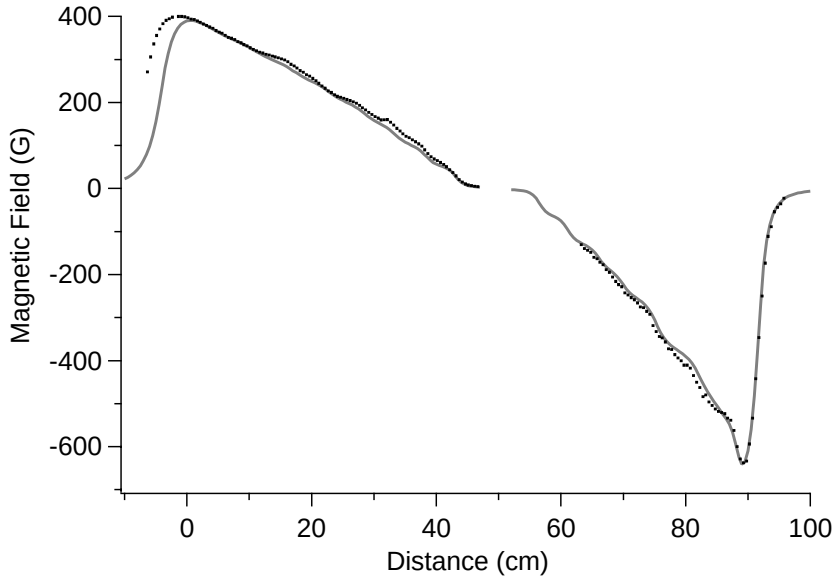

Figure 3-11: Bench measurements of the magnetic field produced by the slower solenoid as a function of distance (cm). The gray lines are the calculated curves shown as black lines in fig. 3-10. The black dots are the magnetic fields measured using a Gauss-meter.

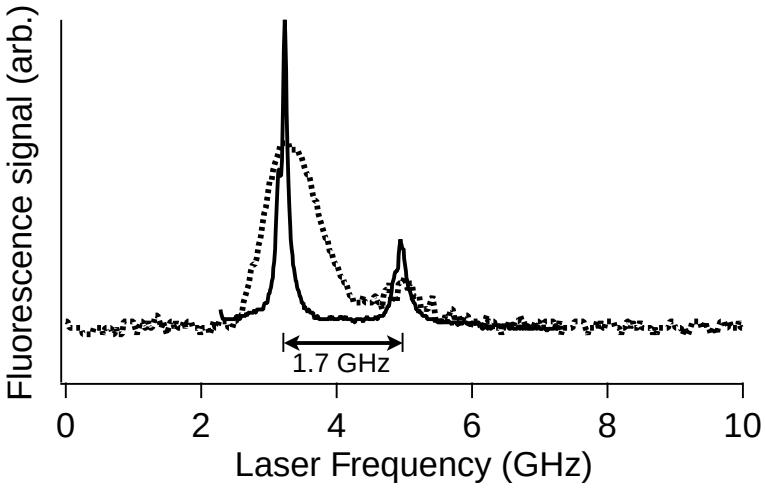

Figure 3-12: Fluorescence from the raw atomic sodium beam. The solid line is a Doppler-free scan and the dotted line is a Doppler-sensitive scan (45°). The probe laser beam is scanned over a range of 10 GHz for the Doppler sensitive scan and only 5 GHz for the Doppler-free scan. The larger peaks are the fluorescence from the $F = 2$ atoms and smaller ones, separated by 1.7 GHz, are the $F = 1$ atoms. The hyperfine splitting (60 MHz) is also visible in both peaks of the Doppler insensitive scan. The y-axis for both scans are arbitrary and different.

in the beam.

A typical Doppler sensitive (45°) scan of slowed atomic beam is shown in fig. 3-13. The slowing light counter-propagated relative to the atomic beam and the probe beam was 45° relative to the atomic beam. The fluorescence signal was collected at a window that was perpendicular to the sodium beam. The black solid line in fig. 3-13 is the slowed atomic beam with about 40 mW in the slowing beam and the slower solenoids fully energized. The slowing beam had sidebands at 1.75 GHz that were created using an electro-optic modulator. Before the atoms enter the slower solenoid region, the blue sideband optically pumps the atoms from the $F = 1$ manifold into $F = 2$ cycling transition. The dashed line is similar except without the slowing sidebands. The gray line is the unslowed, 'raw' atomic beam. As the dashed line indicates, without the blue sideband the flux of the slowed atoms is small due to lack of optical pumping. Secondly, due to off-resonant scattering, the cooling is inefficient as indicated by larger width of the dashed-line peak. Nonetheless, there is slowing and some cooling as indicated by comparable area, since atoms in the cycling transition remain in this closed cycle as they are slowed. Finally, without the blue sideband, the atoms leaving the slowing solenoid region are scattered into the $F = 1$ manifold, presumably due to off-resonant scattering. With the sideband, the efficiency of slowing is high and the atoms are maintained in the $F = 2$ manifold. The 'L' in the figure denotes the location of the slowing laser detuning from the $F = 2 \rightarrow F' = 3$ transition. As noted earlier, this detuning is $2\pi\times$ 1 GHz. This location also indicates the velocity of atoms which are resonant with the

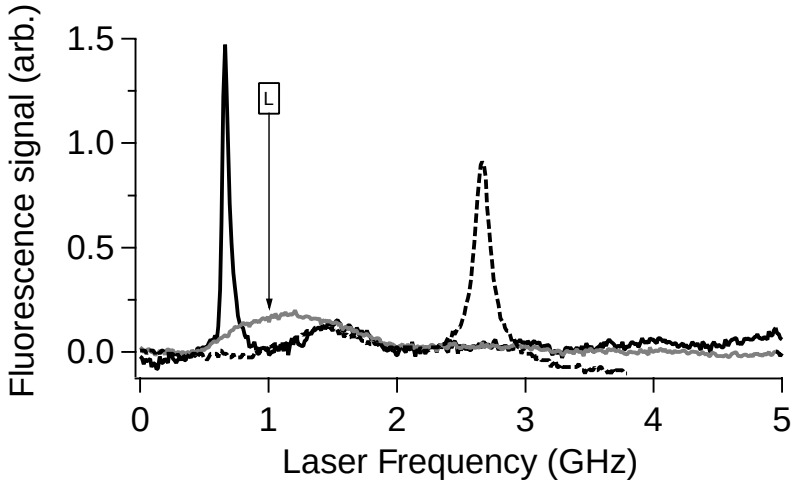

Figure 3-13: Doppler sensitive fluorescence from the slowed sodium beam. The black solid line is the fluorescence of the slowed atomic beam with about 40 mW of slowing power with sidebands at 1.75 GHz. The dashed line is fluorescence without the slowing beam sidebands. The gray solid line is the 'raw' atomic beam without any slowing light. The decreasing field solenoid was energized with 12 A and the increasing field solenoid with 16 and 100 A for low current and high current sections, respectively. 'L' marks the detuning of the slowing laser beam from resonance (1 GHz) at zero magnetic field.

laser light at zero magnetic field ($kv = \delta = 2\pi\times$ 1 GHz). This graph clearly indicates the efficient transfer of the hot atoms into the cold atom peak.

Using a differential absorption technique, we obtained a more quantitative measure of the slow atom flux, since the minimization of background light and the calculation of the solid angle for the fluorescence light collection were harder to do. For absorption, the key technical issue is that the sensitivity had to be less than 0.1%. The schematic of the setup is shown in fig. 3-14. The probe light, which was scanned over a range of 5 GHz, was split using a beam splitter. One of the beams passed through the atomic beam into photodiode A, and the other simply entered into photodiode B without passing through the atomic beam. The path lengths of the two beams were roughly equal to ensure that the beam pointing fluctuations due to various optical elements were comparable. In order to minimize polarization fluctuations, the beam A was sent through windows that were at Brewster's angle before and after the atomic beam. The differential signal $(A - B)$ was obtained using a SRS differential amplifier. The sensitivity of the absorption signal is given by $\frac{A}{A-B}$ and was typically of the order 5×10^3. In order to attain such high sensitivity, we had to minimize the r.m.s. value of $A - B$. This required us to tilt the probe beam optics at large angles relative to the laser beam to minimize etaloning effects.

A typical signal is shown in fig. 3-15. The signal from the 'raw' thermal atomic beam (solid gray line) shows both the $F = 2$ and the $F = 1$ manifold, which were not clearly visible in the fluorescence scans (compare fig. 3-12). The sensitivity of the differential absorption

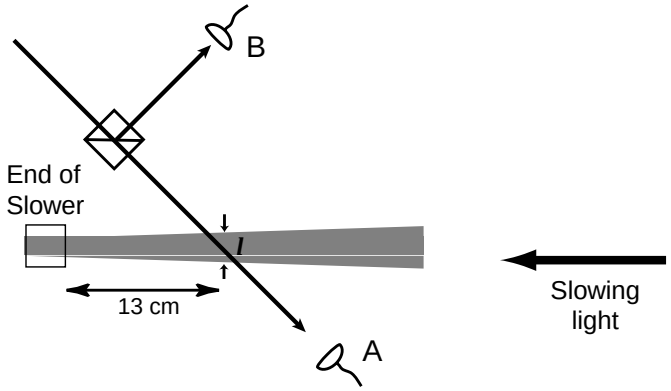

Figure 3-14: A schematic of the differential absorption measurement of the slowed atomic beam. The slowed atomic beam is shown in gray. The photodiode signals, A & B, are subtracted and amplified using a Stanford Research Systems (SRS) differential amplifier. The transverse spread of the atomic beam due to scattered photons is indicated by l.

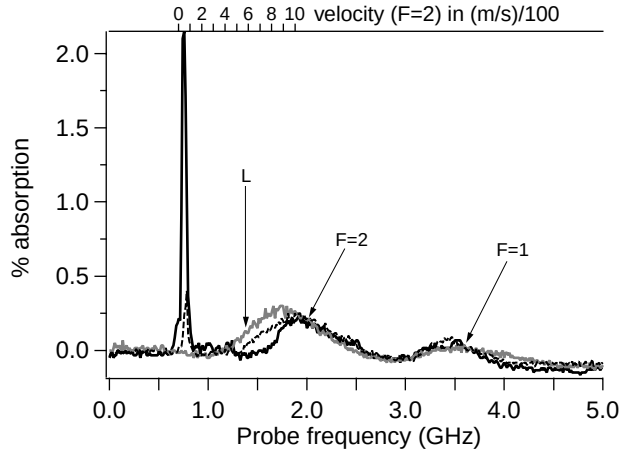

Figure 3-15: A typical differential absorption signal. The black solid line is the slowed beam with both slower solenoids fully energized. The dashed line is with only the increasing slower solenoid on, and the gray line is the 'raw' atomic beam without any slowing. Note that both $F = 2$ and $F = 1$ manifold are visible in all three scans. The top scale converts the probe frequency into a velocity scale, where the peak of the slowed atom flux was at ∼100 m/s and peak of the raw thermal beam was at 900 m/s. 'L' again depicts the laser detuning from resonance. The currents for the slowing solenoid were 15, 31 and 80 Amps for the decreasing, increasing low current and high current sections, respectively. The total slowing laser power was about 70 mW with the sidebands.

was $> 2 \times 10^3$ and the maximum 'raw' beam absorption was 0.3%. The dashed line in the figure is the absorption when only the increasing field solenoid is on, and the solid line is the result with the full slower solenoids. With the decreasing field slower, the flux of slow atoms is five times larger than without! The transfer of the hot atoms to the cold atom peak is clearly visible here as well.

The flux of hot atoms at location of the MOT is about 2×10^{12} cm^{-2}s^{-1}, where the mean velocity of atoms at the nozzle (620 K) is 770 m/s for a sodium partial pressure of 3.14×10^{-3} Torr (determined by the oven temperature of 530 K). Using the absorption signal, the cold atom flux can be determined. The absorption signal is equal to $1 - \exp(-\alpha) \approx \alpha = n\sigma l$, where n is the peak density of the cold atom flux, σ is the optical absorption cross-section and l is the length of the atomic beam traversed by the probe beam. From the absorption scans, α is the peak absorption (typically 1-2% for oven temperatures near 270°C), σ is assumed to be the on-resonance absorption cross-section $7/15 \times 6\pi/k^2$, and l was determined by the transverse expansion of the slow atomic beam after its exit from the slower[26]. To slow a sodium atom from about 950 m/s to 30 m/s, requires about 30,000 photons $\left(\frac{900 \text{ m/s}}{3 \text{ cm/s}}\right)$. Hence, each component of the transverse velocity at the slower exit due to spontaneous scattering of these photons is about $\sqrt{30,000}/\sqrt{3} \times 3$ cm/s ≈ 3 m/s [27]. Given that the final longitudinal velocity was $v_F = 30$ m/s, and the distance from the exit of the slower to the probe beam was 13 cm, $l = 4.5$ cm. Note that $l \propto 1/v_F$. Due to various line broadening mechanisms, the width of the absorption peak was not the natural linewidth but larger ($\Delta v \sim 40$ m/s), hence the real peak absorption signal ($\sim 1\%$) must also be larger than the measured value by a factor of about $\frac{k\Delta v}{\Gamma} \approx 6.8$. Thus, the peak density was given by $\frac{\alpha}{\sigma l} \times 6.8 \simeq 1.5 \times 10^7$ cm^{-3}. The flux is then given by $nv_F \simeq 5 \times 10^{10}$ cm^{-2} s^{-1}. The rate of atoms entering the MOT region is given by the flux multiplied by the MOT 'capture area' or by $\pi l^2/4$, whichever is smaller[28]. Assuming that the capture area of the MOT is given by the $1''$ diameter MOT beams, we obtained a rate of about 3×10^{11} slow atoms per second being delivered by the slower into the MOT. This rate matched very well with the expected delivery rate of the slower.

To determine the exact final longitudinal velocity of the atoms, differential absorption measurements were done using a crossed-beam technique, as shown in fig. 3-16a, where the A-B signal resulted in a signal that is shown in fig. 3-16b. The velocity of the atoms can be calculated from the distance between the two peaks, since a zero velocity atoms are precisely in the center of the two peaks. The velocity of the slowed atoms as a function of the current in the high current section of the increasing field slower solenoid is shown in fig. 3-17. Typically, the slower is operated around 100 A, where v_F is close to 30 m/s. As the

[26] The polarization of the atoms at the probing region is unknown and they are assumed to be unpolarized. Hence, the Clebsch-Gordon factor of 7/15.

[27] The scattering is assumed to be isotropic, hence the factor of $\sqrt{3}$.

[28] If the area is determined by $\pi l^2/4$, then the rate of atoms entering the MOT region is independent of the final velocity v_F.

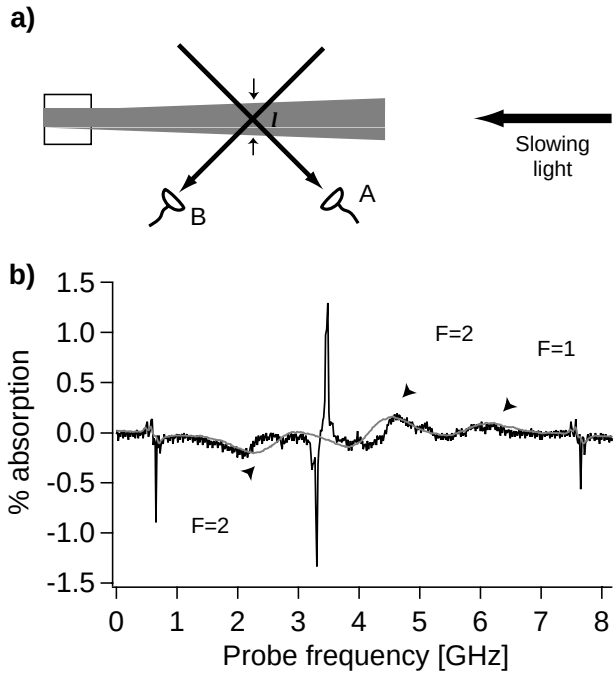

Figure 3-16: Crossed beam differential absorption of the slow atomic beam. a) A schematic of the crossed beam differential absorption measurement of the slowed atomic beam(similar to previous schematic). The photodiode signals, A & B, are subtracted and amplified using an SRS differential amplifier, which results in b). The probe frequency was scanned over a range of 7 GHz (arbitrary offset). The solid black line is the differential absorption of the slow beam, where the center-point between the two peaks gives the zero-velocity marker. The slower currents were 15, 35 and 95 A, and slowing light had sidebands. The solid gray line is the 'raw' beam. Both $F = 2$ and $F = 1$ peaks are visible on the positive absorption scale. The raw beam signal was also filtered, hence the lower noise level.

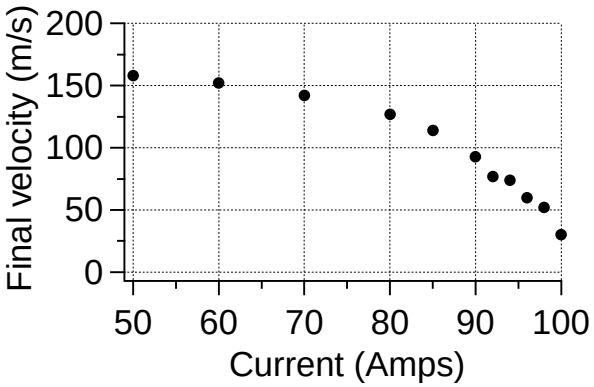

Figure 3-17: Velocity tunability of the slower. The velocity of the slow atoms in the atomic beam as a function of slower current is shown. The velocity is calculated using the crossed-beam absorption technique as a function of the current in the high-current section of increasing field slower solenoid.

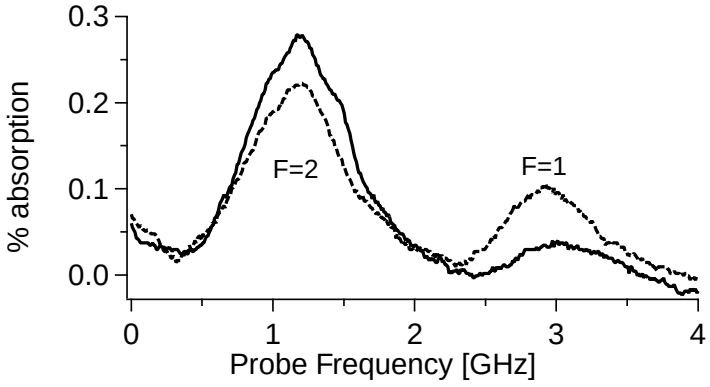

Figure 3-18: Doppler insensitive optical pumping. Shown are the Doppler sensitive differential absorption scans of the hot atomic beam after the slower with (solid) and without (dashed) optical pumping.

velocity is varied from about 100 m/s to about 40 m/s, the flux of atoms (measured by the peak absorption signal) was essentially constant.

As a final test of the slower, we implemented additional Doppler insensitive optically pumping of the atomic beam to test if it would improve the slow atom flux. As noted earlier, the sidebands on the slowing light beam pumped atoms from the $F = 1$ to $F = 2$ manifold, albeit it is Doppler sensitive. Thus, using the extra windows on the 4-way cross immediately after the nozzle (see fig. 3-5), we implemented an optical pumping scheme by illuminating the atomic beam with a 3 mm wide circularly polarized 6 mW laser beam resonant with the $F = 1 \rightarrow F' = 2$ transition. The atoms were polarized by a magnetic field of about 5 G along the pumping beam axis, using coils that were wound on vacuum window ports. The pumping was successful and about 70% of the atoms in the $F = 1$ were transferred into $F = 2$ [29]. See figure 3-18. However, this additional increase did not noticeably improve the slow atom flux as measured using differential absorption. We did not fully explore the optical pump since we had enough slow atom flux to make a dense, dark MOT without it. Thus, in the final setup, side optical pumping was not implemented.

3.4 Bakeout–attaining UHV

During the time the slower was being tested by Deep and Aaron, Todd and I put the vacuum chamber and its associated support structure together (see sec. 3.2.4). This was done using only silver-plated vacuum bolts, rather than using vacuum grease on the threads of standard steel bolts to prevent mechanical seizing of the bolts during the bakeout cycle. In the previous experiments (BEC-I and II), the chambers were baked out to temperatures greater than 300°C. However, we decided that it was unnecessary for us to expose the

[29] In addition, the atoms were also Zeeman pumped into the dark $F = 2, m_F = 2\rangle$ state using the $F = 2 \rightarrow F' = 2$ transition.

chamber to such high temperatures[30], since the vacuum pressure is essentially determined by the 'coldest' part of the vacuum chamber. The most temperature sensitive elements of the chamber were the slower solenoids and the gate valves. The gate valve had a maximum bake temperature of 200°C when the valve was closed (250°C when open)[31]. The epoxy and the wire insulation used for the slower solenoids had a maximum temperature rating of 150°C. Hence, with the slower solenoids mounted, the maximum bake temperature was chosen to be around 120°C to prevent overheating of the solenoids. However, in order to bake the chamber had a hotter temperature, we implemented a two-part bakeout strategy: 1) bake the chamber at a maximum 'high' temperature of 200°C without the slower solenoids to initially rid the chamber of dirt and then 2) bake the chamber with the slower solenoids mounted at a low temperature of 120°C.

Reaching ultra-high vacuum is an art in itself. It is a constant struggle between human creativity and patience versus nature's inherent abhorrence of vacuum. The entire process takes about two weeks, during which any wrong step could lead to poor vacuum in the chamber and a repetition of the whole process from the start. The nominal pressures needed for our experiments is low-10^{-11} Torr, where the lifetime of the magnetically trapped atoms is a few minutes. During the pump-down, the main physical processes limiting the pressure inside the chamber are the desorption of gases from the inner surfaces of the chamber and the diffusion of hydrogen from the steel. Permeation of gases through steel and glass is the ultimate limit for vacuum. The rate of desorption from the surface scales as $1/t$, where t is the pump-down time [126]. The rate constant for desorption is exponentially dependent on the binding energy and the surface temperature. Thus, increasing the temperature to a modest value of even 100°C increases the desorption rate of water from steel dramatically. Diffusion of hydrogen from steel takes a longer time; the rate constant for diffusion decreases as $\sqrt{D/t}$, where D is the diffusion constant [126]. The diffusion constant is also exponentially dependent on the temperature of the steel walls and a modest increase in temperature can lead a large rise in the outgassing rate.

For the pump down, we typically used a Varian turbo-molecular pump (70 L/s) backed by a 'roughing' rotary-vane mechanical pump by CIT-Alcatel. Within 15 minutes of operation, we typically reached a pressure of 10^{-5} Torr (if the chamber was clean). For the bakeout, the band heaters were mounted on chamber ports and the chamber was wrapped with heater tape. The band heaters and heater-tapes were connected to variable AC voltage transformers (variacs); see figure 3-19. The chamber was completely covered with two layers of thin aluminium foil to maintain uniform temperatures across the chamber.

Typically, before heating the chamber, the pressure in the main chamber was around 10^{-7} Torr; see figure 3-20. The chamber temperature was raised by about 50° every two hours. It was very important to monitor the temperatures around each heating element

[30] At around 350°-400°C, the knife edges start to lose their sharpness, so one must be careful when re-using vacuum parts baked out to such high temperatures.

[31] The gate valves had Kalrez seals in order to increase the bake temperature.

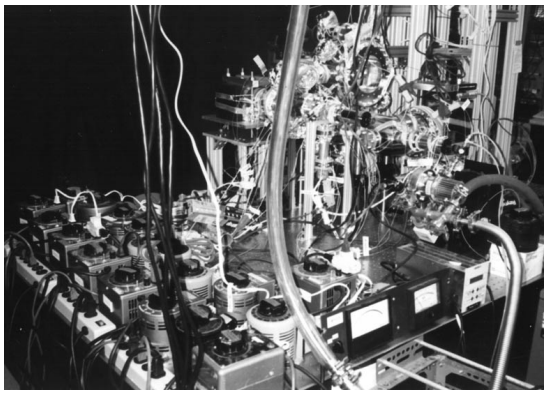

Figure 3-19: A photo of the chamber just prior to the bakeout. The variacs are connected to the band heaters and heater tapes attached to the chamber. The chamber was then covered with aluminium foil and heated up.

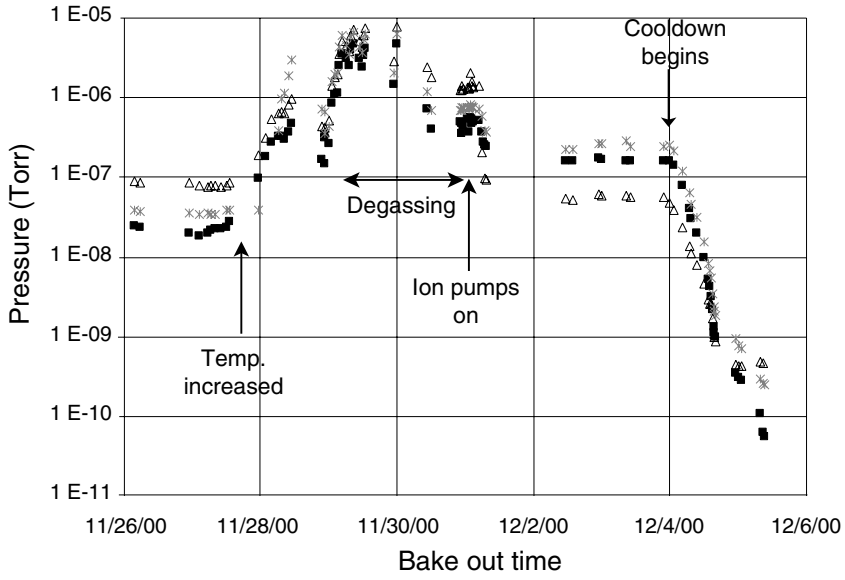

Figure 3-20: Typical variation of the pressure in the vacuum chamber during bakeout. The solid square symbols indicate the pressure measured by the ion gauge at the top of the chamber (port #7), the open triangles the pressure in the science chamber, and the gray crosses the pressure measured by the slower region, right in front of the slower ion pump (see fig. 3-5).

every half hour initially to ensure that we were not raising the temperature too fast or too slow, which could result in cracks in the vacuum windows. The temperatures were measured manually using a hand-held temperature gauge attached to a thermocouple that was placed against the hot chamber walls. During this time, the ion gauges were turned off periodically when the pressure rose about 10^{-5} Torr. Regarding the vacuum windows, it was important to keep in mind that the hot air outside the chamber rises upwards and so maintaining a uniform temperature across the vacuum chamber meant that the heating elements on the windows on the bottom of the chamber (ports # 12, 13, 18, and 19) required more power compared to top ports. The turbo pump was heated to only about 70°C since the turbo pump blades are very sensitive to high temperatures, including thermal radiation. So, we had to even keep the vacuum elbow connecting the turbo pump to the chamber below 70°C [32]. Once the entire chamber was heated to maximum temperature, we degassed the various active elements in the chamber such as the ion pumps (1 hour), TSP (30 A for 2 hours on each filament), ion gauges (1 hour for each filament) and the residual gas analyzer (RGA; 30 minutes). The degassing was performed during both bakeout cycles. During this time, when the chamber was maximally hot, we still had to monitor the chamber temperature at various locations periodically to ensure that no part of the heating elements broke down during the bakeout.

Finally, the ion pumps were turned on and left on for a couple of days before we started to cool down the chamber. During this time, we turned on the RGA and measured the partial pressures of gases present inside the vacuum chamber[33]. The the main gas load in the chamber after heating is from hydrogen (H_2 and H). During its operation, the RGA releases CO, which the same molecular mass as N_2, and hence we see a peak at mass 28. Although similar, this peak does not indicate a leak. A leak in the chamber would be indicated by a 1:4 ratio of the mass peaks at 32 and 28 (O_2 and N_2). In addition, a leak can be detected by measuring the gas load of helium inside the chamber as the gas is sprayed outside the chamber. A strong suppression of all the gases, apart from hydrogen, indicates that the bakeout is nearing its end.

The cool down was a very crucial step where we had to be very careful not to lower the temperature too quickly. Typically, as the temperature is lowered, we observed the pressure drop by about an order magnitude for a temperature drop of about 50°C. When the chamber is cooled to the ambient room temperature, the pressure inside the main chamber was mid-10^{-10} Torr. At this point, we fired our TSP getter pumps (15 min at 47 A), which pushed pressures below mid-10^{-11} Torr, below which our ion gauges become inoperational due to lack of ion current in the filament[34]. Thus, the entire pump-down cycle

[32] In addition, we had a fan cooling the turbo pump such that its air currents only cooled the pump and not the rest of the chamber.

[33] It was important to cool the RGA slightly since the electronics in the attached RGA head cannot handle very high temperatures. We used a fan, similar to the turbo pump, to cool the RGA head during its operation.

[34] As mentioned earlier, this low current error in the Varian ion-gauges is termed 'E03', error #3.

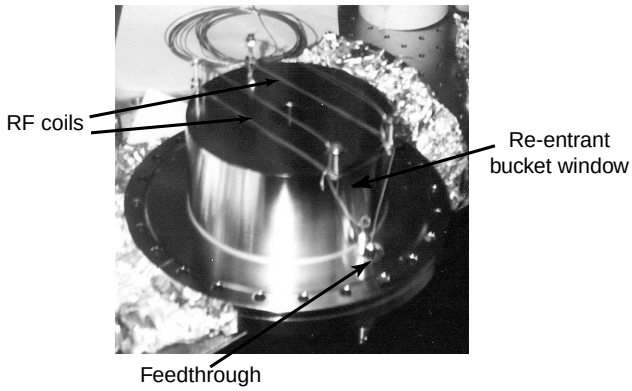

Figure 3-21: A photo of the rf coils mounted on one of the re-entrant bucket windows. Each coil consisted of two turns, and they were attached through a miniflange feedthrough. The ground of the BNC feedthrough unfortunately got shorted to the bucket and hence to the rest of the chamber.

that lasted about two weeks was aimed at eliminating the filament current on the gauges, signalling yet another victory over nature's abhorrence of vacuum.

While the main chamber and oven bakeout cycles were very successful, we had some difficulties with the science chamber. The reason was a mechanical flaw in the Kimball physics steel chamber, where one of the 4.5″ knife-edges was tilted by about 10 mils. This flaw resulted in a leak in the science chamber that was detected by measuring helium pressure using the RGA[35]. This leak limited the pressure to the mid-10^{-10} Torr in the science chamber. Since this was a flaw in the chamber itself, we had to replace the chamber by another similar Kimball Physics chamber. With this replacement, we reached a pressure below 5×10^{-11} Torr in the science chamber after another bakeout.

Attaining UHV in a large vacuum chamber is no easy task. It requires a considerable amount of patience and hard work and the possibility of leaks (virtual and real) only increase with addition of complex elements inside the vacuum chamber. During its operation, the main chamber is surrounded by various infrastructure necessary for making large BECs, such as electronics, magnetic trap coils, optics, etc. Baking out the chamber necessarily requires removing all of the surrounding infrastructure, and therefore, doing the BEC 'science' in a separate vacuum chamber that is easy to remove, install and bakeout is essential for doing more complicated BEC experiments.

3.5 RF coils

As in BEC-I, the RF coils for BEC-III were placed inside the chamber. For details on making of RF coils and RF evaporation, see chap. 3 of Chris Kuklewicz's thesis [130] and

[35]In fact, we accidently vented the main chamber when attempting to check for a leak in the science chamber with the RGA was connected to the oven region.

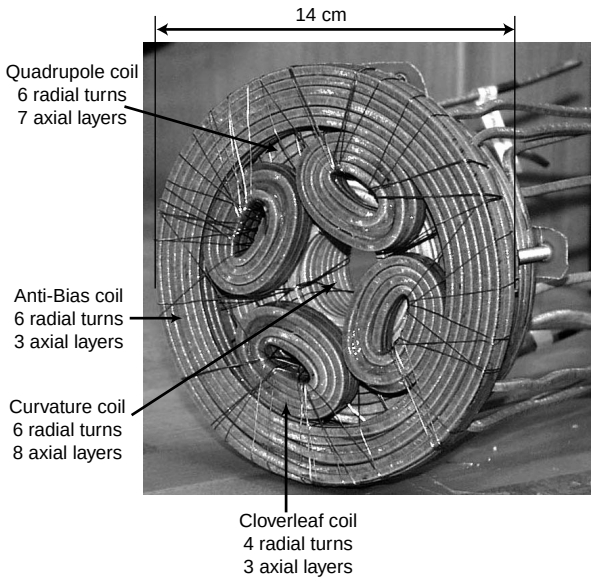

Figure 3-22: A photo of the one of the coil sets for the cloverleaf magnetic trap. The number of turns in each of the coils is shown in the figure. The spacing between the two coil sets was roughly $1.25''$.

the Varenna notes [100]. A review of evaporative cooling is given in ref. [58].

The RF coils consisted of two rectangular coils of two turns each, with dimensions of 14×2.5 cm, as shown in fig. 3-21. The coils were connected in a Helmholtz configuration to produce a bias field at the center of the chamber. The coils were wound using kapton insulated copper wire[36], around four threaded rods that were attached to the chamber using the 6-32 screws welded on the bucket flange (see fig. MIT/L2a,b in appendix A). The coils were connected to a miniflange BNC vacuum feedthrough. This feedthrough was attached to one of the miniflange ports on the re-entrant bucket windows. The output (30 MHz-1 MHz) of a SRS DS345 function generator was amplified by a 1-Watt RF amplifier and sent into the chamber through the BNC feedthrough.

3.6 Cloverleaf trap

As mentioned earlier, we used a Ioffe-Pritchard type magnetic trap in the cloverleaf configuration to make our BEC. The re-entrant bucket ports were designed to hold the cloverleaf trap outside the vacuum chamber, yet close enough to the atoms for providing high magnetic field gradients. The trap was designed, wound, and tested by Aaron Leanhardt. The coils were wound using the insulated $1/8''$ hollow square tubing (3.5 mm OD with insulation) that was used for constructing the slower.

Rather than a schematic, a photo of the actual coils is shown in fig. 3-22. For a wiring

[36] 22 AWG with a maximum current rating of 5.5A.

diagram and a discussion of the magnetic fields produced by the cloverleaf coils, see sec. 3.5 of Dan Stamper-Kurn's thesis [26] and the Varenna notes [100]. Essentially, the cloverleaf coils produce a 2D radial quadrupole field. Each of the eight cloverleaf coils consisted of 4 radial turns and 3 axial layers. The wound coils were held together using DEVCON 5-minute epoxy, whose maximum temperature rating was 93°C [37]. These coils were closest to the chamber, with a separation between two coil sets of about $\sim 1.25''$. By measuring the radial trap frequency of a BEC ($\nu_r \propto B'/\sqrt{B_0}$), we measured the magnetic field gradient produced by the cloverleaf coils to be .617 G/(cm A) [38]. This implied that by running 500 A of current, we could achieve a gradient of about 300 G/cm. Additional bias fields resulting from the cloverleaf coils was partially cancelled by an extra 'trombone' coil mounted behind the entire coil set that could be translated by a few cm, see below.

Directly around the cloverleaves was the anti-bias coil, which was used to cancel the magnetic bias field produced by the curvature coil that was directly behind the cloverleaf coils. The inner diameter of the curvature coil was $1.25''$ such that the coil could just be slid around the 'bucket window'. The curvature coil had 6 radial turns and 8 axial layers, and the anti-bias coil had 6 radial turns and 3 axial layers. The two coils were connected in series, such that the total curvature expected from coils was 0.994 G/(cm^2 A) with a resulting bias field of 0.1 G/A [39]. At 200 A, the net calculated bias field was around 20 G, which was rather large. By measuring the axial trap frequency of a magnetically trapped BEC, we measured the curvature of the final magnetic trap to be 1.062 G/(cm^2 A) and the total bias field measured using a BEC, including the curvature/anti-bias trombone coil (see below) and assuming no contribution from the cloverleaf coils, was 0.087 G/A (8.45 G at 97 A). Since this bias field was rather large, we reduced the final bias field for making a BEC using external y-compensation coils (see secs. 3.6.1 and 3.9) such that the magnetic bias field at the bottom of our trap was typically about 1.5 G.

In BEC-I, one of the curvature coils and an anti-bias coil were run in an anti-Helmholtz configuration to make a 3D quadrupole magnetic field for the MOT (see [26], pg. 59). While it was sufficient, the coils did not make perfect field gradients, since the coils were of different sizes. Instead, we decided to build separate quadrupole coils to make the MOT. This coil was also designed to provide large enough gradients so that we could produce BECs in an optically plugged trap similar to the first experiments at MIT. In this first experiment [52], BEC was made by evaporating atoms in a plugged trap made by combining a spherical quadrupole magnetic trap with a repulsive optical dipole beam focused on the magnetic zero. Evaporation in this quadrupole trap can be very fast ($\sim$ 5-7 s) due to the tight confinement. Thus, with a fast evaporation cycle, we could make a BEC in the plugged quadrupole trap, transfer it into the tweezers trap, and transfer it in the science chamber in less than 10 seconds.

[37] Hence, the coil sets would have to be removed for a bakeout of the main chamber.
[38] A bench test measured the field gradient produced by the coils to be 0.629 G/(cm A).
[39] With the bench test, we measured 0.975 G/(cm^2 A) for the curvature.

The quadrupole coil consisted of two sections wound on top of each other: one with 4 radial and 7 axial layers, and the other with 2 radial and 7 axial layers. The quadrupole coil was placed around the curvature coils. The calculated gradient from these coils was 1.275 G/(cm A) and bench measurements gave a value of 1.288 G/(cm A).

The electrical connections for these coils were all made *outside* the coil structure itself, unlike in the first cloverleaf coils [26]. This allows for a re-arrangement of coil connections in the future. For example for a Feshbach experiment one needs very stable magnetic fields at around a kG [53, 131]. Thus if the curvature and the anti-bias coils were connected in a Helmholtz configuration, we could get upto 3 G/A for each pair such that with 250 A of current, we could get upto 1500 G. In addition, the quadrupole coils can also be configured in a Helmholtz configuration, and they could generate about 980 G for 250 A of current[40].

Apart from these major coils, we also wound additional coils that would produce bias fields in the x and z directions. These coils could be used to control the radial position of the magnetic trap. These coils had 2 axial and 1 radial turns. These coils are expected to produce about 8 mG/A. Finally, we wound two adjustable coils that are called the 'trombone coils' for historical reasons. These coils were supposed to compensate for the bias field produced by the cloverleaf coils and the curvature/anti-bias coils. The coils were run in series with their respective coils, and by adjusting the axial distance from the magnetic trap, we hoped to compensate for the bias fields such that changes in the current would not alter the bias field at the bottom of the trap. The cloverleaf trombone was made of 4 axial layers and 1 radial turn and the curvature/anti-bias trombone coil was made of 5 axial layers and 1 radial turn. The cloverleaf trombone coil effectively cancelled the residual bias field arising from the cloverleaf coils such that the residual field was only 1.6 mG/A in the $+\hat{y}$-direction. However, even with the curvature/anti-bias trombone coil, the net residual bias field from the curvature/anti-bias coils was about 94 mG/A in the $+\hat{y}$-direction. Thus, the trombone coil for the curvature was ineffective, and as mentioned earlier, an additional bias field produced by external y-compensation coils was used to reduce the offset magnetic field of the trap.

The coils (except for the adjustable 'trombone' coils) were all initially held together with a thin kapton insulated wire as shown in fig. 3-22. Finally, the coils were rigidly held by epoxying the entire coil set with Dexter-Hysol epoxi-patch EPK-1C-White (same as the slower epoxy). The coils were attached to $1/2''$-threaded rods that were connected to an aluminum plate. With this aluminum plate, we mounted the coil set onto the bucket flange using the 1/4-20 tapped holes on the flange (see fig. MIT/L2a in app. A). The 'trombone' coils were also connected to these threaded rods, using which the final position of the trombone coils could be adjusted. It was important to be sure that the threaded rods and nuts were non-magnetic. A thin Kapton sheet was glued on the front of the coils

[40]The maximum current in the curvature, anti-bias and the quadrupole coils is limited by present flow rates for water cooling

to insulate the coils from any contact shorts that might result when the coilset was pressed into the bucket port.

Finally, to reduce the resistance of the wires, the 1/8″ hollow square wires were silver-soldered outside the coil set to hollow circular wires of 0.25″ OD and 0.12″ ID. This increased the conductivity of the wires by a factor of 12. Thus, for running 500 A of current through the cloverleafs coils a 30 V power supply was sufficient. In addition, circular wires were easier to connect to water sources using Swagelok connectors.

The high currents in the cloverleaf coils require water cooling. In order to maintain a temperature rise of only 25°C for the flowing water, the flow rate in each cloverleaf coil set (four leaves plus the leads) was about 1.1 L/min and 1.0 L/min in the curvature/anti-bias coils.

3.6.1 Compensation coils

Finally, in order to compensate for stray magnetic bias fields in the main chamber, we wound two external coils in each direction such that in Helmholtz configuration, they produced about 1 G/A at the center of the chamber[41]. They were wound using a 16-gauge stranded wire that was insulated with a high temperature silicone-rubber insulation (200°C). Based on the directions defined in fig. 3-2, the circular y-coils had 15 turns each, and were wound around the 8″ port just behind the bucket flanges. The x and z coils were rectangular with 12 turns each.

For the science chamber, we also wound external coils (two coils in each direction) such that the Helmholtz pair produced about 1 G/A and in the anti-Helmholtz configuration, they produced about 0.2 G/cm/A. See fig. 3-1b.

3.6.2 High current switching

The cloverleaf gradient coils were connected to a 30V-500A Lambda EMI power supply and the curvature/anti-bias and the quadrupole coils were each connected to a 20V-250A power supply. To energize the increasing field section of the slower solenoid and for a mode-matched transfer from the MOT to the Ioffe-Pritchard trap, we used Xantrex power supplies. The 15 A for the decreasing field slower solenoid and 5.6 A for the slower compensation coil were provided by Sorenson power supplies. All power supplies were operated in current-mode. The switching of the high currents was done using high current IGBTs[42] and low currents using 40A-MOSFETs that were all controlled by TTL signals from the 'word generator' (see sec. 3.8). Since IGBTs dropped about 2 V, about a kW had be dissipated in the IGBTs using water cooling.

[41] The y-compensation coils produced 1.4 G/A.

[42] For the cloverleaf coils, we used two IGBTs in parallel and for the curvature/antibias coils we used a single 600 A IGBT.

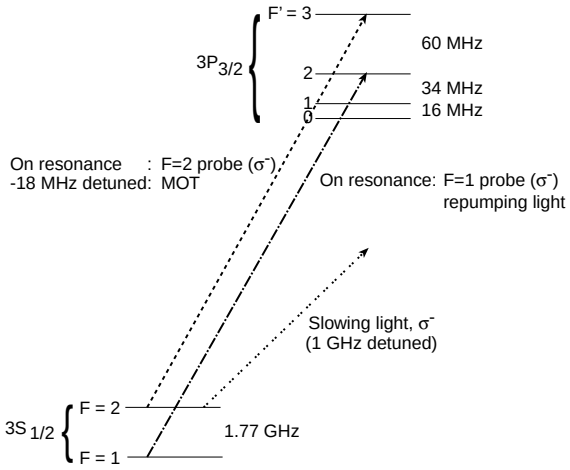

Figure 3-23: A schematic of the relevant atomic transitions in sodium.

3.7 Light for the MOT

The starting point for almost all BEC experiments is the magneto-optical trap[43]. A magneto-optical trap requires nearly-resonant laser light to cool and trap the atoms. This laser light is usually $3\Gamma/2 \sim 15$ MHz detuned from the $F = 2 \rightarrow F' = 3$ cycling transition. A schematic of the atomic levels and the detuning of laser light required for the MOT, slowing and probing beams are shown in fig. 3-23. In all of our experiments, we used a dark-spot MOT [133], which required a separate repumping beam resonant on the $F = 1 \rightarrow F' = 2$ transition. This allowed for a much denser, darker MOT than the standard 'bright' MOT. For a 'bright' MOT, the repumping light was generated by adding 1.71 GHz sidebands on the MOT light. The slowing light, as mentioned earlier, was detuned by 1 GHz from the $F = 2 \rightarrow F' = 3$ transition. For more detailed information on the generation of the laser light, see sec. 3.4 of Dan Stamper-Kurn's thesis [26]. When building the apparatus for BEC-III, we decided to use the existing laser system for BEC-I and split the laser time between BEC-I and BEC-III. This was initially convenient since it was the members of BEC-I who were involved in building BEC-III[44]. The laser system for BEC-I was a Coherent 899 dye laser with a high pressure nozzle[45] that was pumped by Spectra Physics Millenia laser (532 nm, 8.5 W). All of the laser light described above was generated from the output of the dye laser. Typically, about 2 W of the golden-yellow sodium light is generated from the dye laser. The laser frequency was referenced to an external saturation-absorption lock-in scheme and was locked to a Fabry-Perot cavity.

[43] Hydrogen-BEC uses cryogenically cooled atoms instead of a magneto-optical trap for pre-cooling, see [132].

[44] More recently, BEC-III is engaged in building a new laser system for itself to increase efficiency. Details of this new system will be presented in a future thesis.

[45] The dye pressure is typically 12 bars.

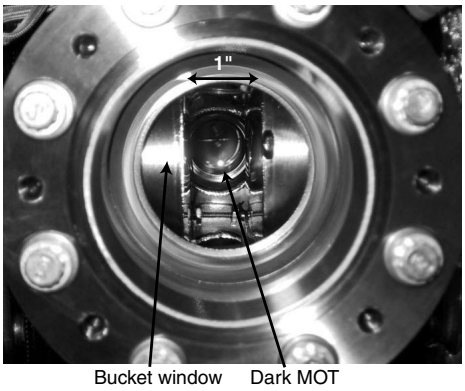

Figure 3-24: A photo of the dark-MOT. The photo is taken through the 'tweezers port' (#3). The bright spot in the middle of the chamber are about 1% of the trapped atoms (the rest are in the dark . The re-entrant bucket windows are also visible. The spacing between the buckets is about $1''$.

Not having to build another laser system enabled us to push ahead with the construction of the new apparatus and focus on transporting atoms. Although we did not have to generate the light, we still had to bring it over onto the optical table. This was accomplished using optical fibers. Optical fibers have now become a standard tool for optics; they are almost as easy to make and use as the BNC-cables for electronics. Axel Görlitz led the effort to fiberize our laser beams and bring them over onto the optics table. Using a standard Thorlabs fiber making kit, we connectorized our optical fibers. All of the fibers were non-polarization maintaining fibers, except the slowing light fiber. This was important to ensure that the slowing light had good polarization to maintain atoms on the cycling transition. Typical laser powers after the fiber are 100 mW for the MOT light, 20 mW for the repumping light, 30 mW for the slowing light and less than a mW for the probing beams.

The MOT light was split into 6 beams, whose relative beam intensities could be independently controlled, and sent into the vacuum chamber through ports #4, 7, 12, 18 and the bucket windows. The repumping beam was sent through an opaque spot[46] of about 4 mm OD, and the shadow from this spot is imaged onto the atoms using port #10. A photo of the dark MOT is shown in fig. 3-24. Typical field gradient for the MOT was 11 G/cm (9 A) along the axial-direction, produced using the quadrupole coils. Despite the fact that we used non-polarization maintaining fibers, the stability of the fibers and optics setup was good enough such that a re-alignment of the MOT beams was not required for more than 3-4 weeks.

[46]The dark spot is just a circular piece of paper glued onto a glass slide.

3.7.1 Looking at the atoms

To observe the atoms in either absorption imaging or in phase-contrast imaging [26, 100], the atoms were imaged onto a Roper Scientific/Princeton Instruments CCD camera using achromatic lenses. Typically, we magnified the atoms by a factor of 2. The CCD camera was back-illuminated[47] and was capable of kinetic mode. The chip size was 6.65×13.3 mm (512×1024, 13 μm long, square pixels). Half of the chip was covered such that the images could be obtained in only 512×512 pixels. The other half was used for frame-transfer. We also used the accompanying Windows based WinView software for transferring the images from the camera.

3.8 The Word Generator – computer control

During its routine operation, a BEC experiment is nothing but precisely timed electronic pulses that add and shift frequency components to our laser light using acousto-optic and electro-optic modulators, open/close optical and mechanical shutters, and turn on/off various MOSFET and IGBT switches for power supplies and function generators. A BEC is created when the sodium atoms dance to this tune of optical and electronic cues. It is amazing that a quantum object (BEC) is created using mainly macroscopic elements. The only microscopic and quantum-mechanical elements are the sodium atoms and the photons from the laser beams.

Controlling the timing of these electronic pulses that make the BEC is extremely important. Fortunately, we could borrow a lot of the infrastructure and expertise from Chris Kuklewicz (from BEC-II), who had written new software using National Instruments LabWindows/CVI software. This new 'Word Generator'[48] (WG) was a significant improvement over the BEC-I computer control equipment using older, now obsolete, Macintosh hardware. We improved upon Chris's WG by increasing the number of digital bits to 64 and the number of analog channels to 16 [49]. Detailed information about the Word Generator and its functioning is given in chap. 4 of Chris's thesis [130]. I will only provide the basic essentials below.

Two National Instruments digital cards (PCI-DIO-32HS) provide the 64 channel digital outputs and two high speed 12-bit 8 channel analog cards (PCI-6713) provide the 16 analog outputs. These four cards, along with a GPIB card (PCI-GPIB), were mounted in a standard PC. The cards were all connected together by a RTSI cable. The timing of all of the cards (except the GPIB card) was controlled by one of the PCI cards[50], with a 2 μs update

[47] The back illumination increases the quantum efficiency at 600 nm from 30% to 85%.

[48] The computer software is called a 'Word Generator' since a single sequence of TTL pulses and analog signals is called a 'word'. One 'word' is made of 64 digital bits and an analog buffer for 16 channels. A combination of these 'words' is then the electronic 'BEC poetry'.

[49] All four BEC experiments at MIT are now using the second generation hardware/software that was developed for BEC-III.

[50] In the current BEC-III WG, an older analog card (C-type) is set as the master timing card, with the

rate for all cards. The GPIB timing was still controlled explicitly by the computer [130]. The GPIB bus directly controlled frequency and amplitude of the rf ouput from a SRS DS345 function generator.

The 12-bit analog channels that provide voltage from -10 to 10 V were fairly noisy and unfortunately had a resolution of only 5 mV (20 V / 4096). Nonetheless, it was used to control the current output of power supplies and the intensity of the infrared laser light for the optical tweezers. This low resolution affected some of the experiments such as moving condensate in miniaturized wiretraps (see chap. 4). The ground of the analog output was typically isolated from the lab using a INA117 differential amplifier which also provided the output with a current output/sink of about 20 mA. The voltage output from each of these channels could be controlled independently and arbitrarily.

Each of the 64 output channels from the digital cards was optically isolated and converted to a standard rail-to-rail TTL (0-5 V) using a 74OL6000 optoisolator. The TTL output was then buffered through an ACTQ-series buffer chip, that provided the channel with a maximum current output/sink of 24 mA. Any spurious switching noise on the TTL output was eliminated by adding a RC element[51] that also increased the $1/e$ rise/fall time for the TTL signals to 400 ns. The TTL outputs controlled various electronics controlling the laser frequency and intensity, and switches for powersupplies during the various stages of making a BEC.

3.9 Making the BEC

Finally, by early 2001, all of the elements for making BECs were added to the BEC-III apparatus. We had the UHV in our chamber, the word generator was online, various switching electronics were being implemented, the cloverleaf coil sets were installed in the buckets, the golden-yellow laser light for the MOT garlanded our optics table, and we were ready to observe some quantum mechanics in action!

A cold dense atomic cloud is an important pre-requisite for making a BEC. Transferring this cold cloud into a magnetic trap and evaporating it to BEC is a relatively simple step. I will not present here the time-sequence for making a BEC, since it will be provided in chapter 5, where the making of the continuous BEC source is described. Rather, a sequence of events in the lab that resulted in a BEC is given in the table 3.1. The final bakeout of the vacuum chamber was finished by Jan 22, 2001, when we had good UHV both in main chamber and the science chamber. About 30 days later, our first BEC was born, shortly after midnight on Feb 24, 2001. See fig. 3-25. It was only due to efficient team-work and experience that we were able to make a BEC in the new apparatus so quickly. A rough estimate indicated that the BEC had about 3 million atoms. And over the next few days,

other cards slaved to it. Usually, a digital card is set as the master.

[51] The output from the buffer is connected in series with a 8.2Ω resistor and a 18 nF capacitor is connected between the BNC output and ground of the TTL breakout panel.

Date	Event
Jan 22, 2001	• The final bakeout of the science chamber is done. • We have good vacuum in both chambers.
Feb 1, 2001	• The optics for the MOT and probing are all aligned. • Various electronics for the power supplies is built. • The computer control 'Word Generator 3' comes online.
Feb 3, 2001	• First atomic beam in the chamber. • A bright MOT is loaded from the hot thermal beam. • No evidence of atomic beam slowing due to lack of laser power in the slowing beam.
Feb 6, 2001	• Beam slowing works. • A good bright MOT and preliminary dark MOT is set up.
Feb 16, 2001	• Most electronics for magnetic trap is setup except for IGBTs. • Good dark MOT with nice polarization-gradient molasses. • Transfer of atoms to the quadrupole magnetic trap. • Long lifetimes (> 60 s) in the magnetic trap is observed.
Feb 20, 2001	• The IGBTs for switching high currents are installed. • Atoms are transferred into the Ioffe-Pritchard-type clover-leaf magnetic trap. • Evaporated atoms, but runaway regime is not reached due to high bias field ($\sim$6 MHz) at the trap bottom.
Feb 23, 2001	• The magnetic bias is reduced using external y-compensation coils to about 1 G ($\sim$ 700 kHz). • The runaway regime of evaporative cooling is reached. • First evidence of BEC just after midnight, Feb 24, 2001.

Table 3.1: The major events in the process of making the first condensates in BEC-III, and their associated dates are listed above.

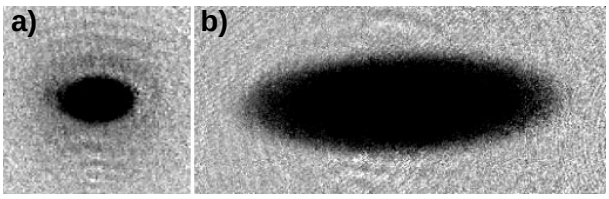

Figure 3-25: The first condensates in BEC-III. a) An absorption image after about 25 ms of ballistic expansion of the condensate on Feb 24, 2001. The condensate number was about 3.2 million. b) An absorption image of a pure condensate after 60 ms of ballistic expansion (Feb 28, 2001). The condensate atom number was about 14 million with a radial and axial trapping frequency of about $2\pi \times 300$ Hz and 17 Hz, respectively. The bias field at the bottom of the trap was about 600 mG. Image size for a) 2×2 mm and b) 1×2 mm. (reCHECK)

after adjusting various parameters, the condensates contained more than 10 million atoms. The lifetime of these large number condensates was about 2 s without an rf-shield [100], > 10 s with an rf-shield. The lifetime increased when we reduced the density by decreasing the radial trap frequency, indicating that we were limited by density-dependent three-body collisions.

To my great amazement, we did not hit any major hurdles in making a BEC. In fact, we even eliminated the polarization-gradient molasses step. The atoms from the MOT appeared to be cold enough that the molasses step was unnecessary. The biggest hurdle was simply the time required to build various electronics. The quick progress is only a testament to the strength and expertise available to us (and me) within the group. As mentioned in the introduction, it is the efficient teamwork that make the Ketterle labs what they are today.

3.10 Moving condensates

Once making a BEC had become routine (which only takes about a week), we focussed our effort on transferring the magnetically confined BEC into the moving optical tweezers trap. The center of the science chamber was about 34 cm from the magnetic trap position in the main chamber. Thus, our goal was to move the condensates 34 cm into the science chamber, where could then load these transported condensates into a wiretrap, see chap. 4. In this section, while I will focus on the final working configuration for the moving tweezers, I want to present some of the failed initial attempts as a guide of what not to do. I hope that some of this information will be useful to future researchers embarking on similar experiments.

3.10.1 The tweezers trap

For the optical tweezers, we used a laser operating at 1064 nm that was generated using a 20 W IPG Photonics fiber laser. The output of this laser was split into two beams. Both beams passed through two separate acousto-optic modulators (AOM) and then coupled into two 5 m long optical fibers. One of the output of the fibers was used for the optical tweezers and the other for making the reservoir trap for the continuous BEC (chap. 5). The AOMs were used to control the intensity of the laser light after the fiber.

Initially, our goal was to transfer the atoms into a pancake shaped optical dipole trap [18, 19], which could be translated. The cylindrical optical dipole trap (ODT) was to be created using cylindrical lenses. A 'standard ODT' uses spherical lenses and the trap is shaped like a highly elongated cigar, almost one-dimensional. The key reason for using the cylindrical ODT was to increase the number of atoms that could be transferred into the science chamber. A cylindrical ODT does not suffer from the enormous three-body losses that result from the high condensate density in the standard ODT [6]. In addition, the larger trap volume implies that we can hold many more condensed atoms ($\sim 10^7$ atoms [19]) than a standard ODT. Initial moving tests in BEC-I, where a cylindrical ODT was implemented, indicated that we could move the trapped condensate by about 2 cm without much loss. In BEC-III, we were unsuccessful in translating the atoms trapped using a cylindrical ODT into the science chamber that was about 30 cm away. We spent many months debugging the system, but eventually we decided to use spherical lenses and move the condensate atoms using the standard pencil-shaped ODT. We believe that the main problem was due to poor beam quality and abberations in the cylindrical ODT that arose while the lens was translated. Although it might be possible to translate a cylindrical ODT created using anamorphic prism pairs, we simply decided to work with a standard ODT. In addition, the use of air-bearing translation stage (discussed in sec. 3.10.5) might also improve the translation of the cylindrical ODT.

For the standard ODT, the beam from the fiber was expanded and then focused into the vacuum chamber. The beam diameter out of the fiber was about 1 mm. We expanded the beam size[52] to about 3 cm using large $f/\#$ telescopes. A parallel beam was then focused by a 500 mm achromatic lens that was on a linear-motion translational stage. The parallel beam had to be aligned to the translational stage's linear motion. The focus of this beam was then imaged onto the atoms using another roughly 1:1 telescope[53]. During the translation, the numerical aperture of the focussed laser beam does not change. At the condensate position, the infrared focus had a $1/e^2$ beam waist radius of $w_0 = 24$ μm.

[52]The beam size was only measured visually on a IR-fluorescence card, which typically over-estimates the beam diameter.

[53]The final imaging telescope was actually about 1:1.3, leading to a 30% magnification of tweezers translation relative to the stage translation.

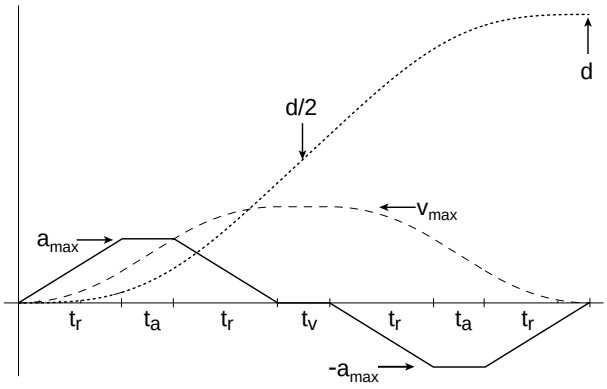

Figure 3-26: The trajectory of the translational stage. a) The motion parameters of the stage. The solid tine is the acceleration, the dashed line is the velocity and the dotted line is the travel distance of the stage. The rate of change of the acceleration is governed by the jerk. For a given distance d and the maximum value of the jerk, acceleration and velocity, the times t_r, t_a and t_v are calculated. See text. b) The power of the infrared laser during the translation.

3.10.2 Motion parameters

Initially, we used a MICOS/Phytron #MT-150-400-DC220 linear translation stage with 400 mm maximum travel and 120 mm/s maximum velocity. The motor was a DC brushless servo type, with 0.5 μm encoder resolution. We observed that the during the motion of the stage, the re-circulating ball bearing system produced a lot of vibration on the stage. Therefore, we had to isolate the lens on the stage. Initially, we just placed pieces of damping rubber, sorbothane, on top of the translation stage and under a breadboard to which the 500 mm lens was mounted. In addition, to decrease the vibration frequency, we added a few kilograms of lead.

The position of the stage was controlled by a Galil motor controller that servoed the stage position to a trajectory specified in terms of jerk (derivative of acceleration) j, acceleration a, velocity v, and distance d. The acceleration profile of the translational stage was trapezoidal (see fig. 3-26), with a rising slope defined by the jerk and a flat top defined maximum acceleration and a decreasing slope defined by the jerk. In addition, if the maximum velocity had been reached, there was a period of zero acceleration. To decelerate, the procedure described above was reversed. The velocity and the distance of the stage at the end of the trapezoidal acceleration was

$$v_{tz} = \begin{cases} jt_r^2 + jt_r t_a & : \text{ if } a = a_{max} \ (t_r = a_{max}/j) \\ jt_r^2 & : \text{ otherwise.} \end{cases}, \tag{3.8}$$

$$d_{tz} = \begin{cases} jt_r^3 + 3/2jt_r^2 t_a + 1/2jt_r t_a^2 & : \text{ if } a = a_{max} \ (t_r = a_{max}/j) \\ jt_r^3 & : \text{ otherwise.} \end{cases}, \tag{3.9}$$

where the rampup time of the acceleration was t_r and t_a is the region of time where the acceleration was flat with $a = a_{max} = jt_r$. The time t_a was calculated by ensuring that either $v_{tz} = v_{max}$ or $d_{tz} = d/2$ at the end of the trapezoid. If $d_{tz} < d/2$, then the velocity was kept constant for a time $t_v = (d - 2d_{tz})/v_{max}$. The total time for the transfer was $t_{tot} = 4t_r + 2t_a + t_v$.

In the initial experiments, apart from the travel distance, we specified the maximum jerk, acceleration or velocity. The transfer time was determined by these parameters as discussed above. However, in the later experiments, based on a given travel time and distance, the maximum jerk, speed and acceleration was determined by assuming a sinusoidal velocity profile. Using the maximum travel parameters (calculated from the sinusoidal curve), the stage was moved using the trapezoidal acceleration profile described above. This ensured that the total travel time was very close to the required travel time.

3.10.3 Vibration isolation

Using this system, we were able to transport the condensate in a cylindrical trap only about 10-15 cm before we lost all of the atoms. Initially, we were concerned about magnetic field gradients that might have reduced the trap depth during the transfer, thereby possibly pulled the atoms out of the trap. However, we lost the atoms even when the atoms were in the $m_F = 0$ state, which is nominally magnetic field insensitive. And in addition, simply increasing the power of the infrared laser to deepen the trap did not help much, since with too much power the lifetime of the atoms was marginal. Therefore, we were then concerned with beam profile changes as the trap was translated and also with vibrations of the t-stage that could parametrically heat the atoms. To test the vibration on the stage, we used an Isotron accelerometer placed on top the stage. We discovered to our amazement that without any vibration isolation, the stage was accelerated to values close to g(!) in the vertical direction near the radial trap frequency when the stage was translated at velocities close to 9 cm/s. Clearly such vibration would expel atoms out of the trap. At slow velocities (5 mm/s), the vibration was close to $0.07g$, which was acceptable but still not very satisfactory. Also, we realized that the damping provided by just the sorbothane was unsatisfactory since it did not reduce these large vibrations by much.

Once we realized this problem, we immediately decided to increase the damping by using four Newport NewDamp elastomeric isolators. This set of four NewDamp isolators were to be used with minimum load of 80 kg, which was provided by a stack of lead bricks. See fig. 3-27. With this lead stack, the amplitude of the vibrations was reduced by more than a factor of 10. The advantage of the NewDamp isolators was that they have a roughly constant resonance frequency over a large range of load weight. However, even with this increased vibration isolation, we were still unable to transport the atoms in a cylindrical ODT for more than 15 cm. Therefore, we might have been plagued by bad beam profile and abberations during the translation. Rather than analyze the beam profile, we decided

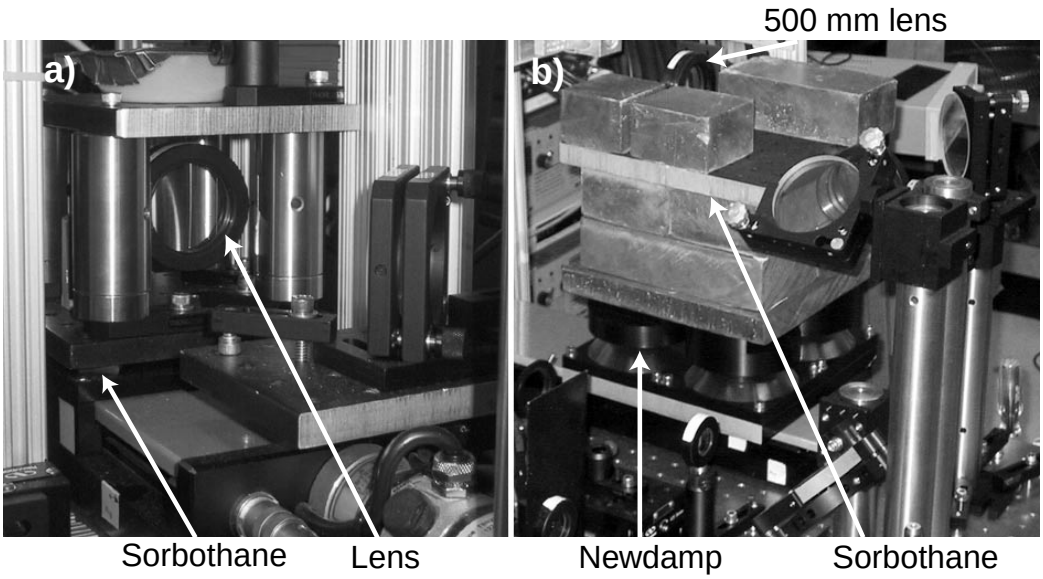

Figure 3-27: Photos of the vibration isolation required for the translation. a) The initial isolation was provided only by sorbothane which was underneath the breadboard. This setup was later modified with additional isolation, as shown in b). The final configuration included 80 kg of lead bricks on top of NewDamp isolation. In addition to the lead stack, we also used sorbothane underneath the breadboard on which the 500 mm lens was mounted. The translation stage moved the lens from right to left in the photo.

to implement the standard ODT using spherical lenses.

3.10.4 Condensates on the move

It is interesting to note that after many months of unsuccessful attempts to transport the BEC in the science chamber using cylindrical ODT, we succeeded on the first try with the standard ODT. All of the transfer was done using the trapezoidal acceleration profile described in sec. 3.10.2. We typically transferred about a million condensed atoms that had a lifetime of 16 s. See fig. 3-28.

The key technical problem to overcome was the transfer of condensates from the magnetic trap into the cigar-shaped standard ODT was not as simple as in our previous experiment [6]. In the earlier experiments, the weak axis of both the magnetic trap and the optical trap were in same direction. However, in our case, the axis of the optical dipole trap was along a radial direction of the magnetic trap. Thus, it was very important to decompress the magnetic trap as much as possible in the radial direction before turning on the optical dipole trap. Else, the condensate was compressed enormously in all three directions and we lost atoms almost immediately due to three-body collisions.

The magnetic trap was first decompressed by increasing the offset magnetic bias field

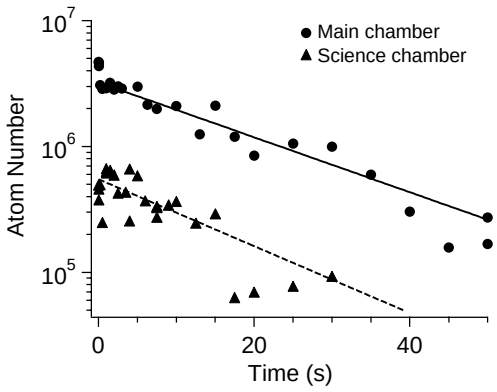

Figure 3-28: Lifetime of optically confined Bose-Einstein condensates in the main and science chambers. The number of condensed atoms is plotted vs. trapping time. Circles and triangles represent data in the main and science chambers, respectively. Both traps had the same characteristics with 90 mW power and trap frequencies of 4 Hz axially and 440 Hz radially. The fluctuations in the science chamber data are mainly due to alignment irreproducibilities in the translation stage (see text). The lines are exponential fits to the data. The lifetimes in the main and the science chambers were 20 ± 2 and 16 ± 4 s, respectively.

from 1.5 G to about 8.5 G [54]. This reduced the radial trap frequency from 200 Hz to about 87 Hz. The trap was further decompressed by lowering the currents in the cloverleaf gradient coils and the curvature coils by a factor of 10 simultaneously. This maintained the position of the trap roughly in the same spot in two dimensions; due to the reduced trap frequency, the condensate dropped down (gravitational sag). The radial trap frequency was reduced to 45 Hz [55]. The condensate was transferred to the optical trap by ramping the infrared laser light linearly up to 180 mW in 600 ms and then suddenly switching off the decompressed magnetic trap. The optical trap depth is proportional to P/w_0^2, where P is the power, and was 11 μK for 180 mW [2]. The transfer efficiency into the optical trap was close to 100%. The laser light was then ramped down to 90 mW during the first second of the transfer into the science chamber, in order to minimize three-body loss. The trap frequencies of the optical trap was 440 Hz (radial) and 4 Hz (axial) with 90 mW of infrared laser power.

After transferring the condensate into the optical trap, we pushed the 500 mm lens on the translation stage and transported atoms into the science chamber. Typical travel parameters were jerk = 20 mm/s^3, acceleration = 37 mm/s^2, and velocity = 70 mm/s, yielding a total transfer time of 7.5 s. Although, the transfer worked for a large range of transfer parameters. However, as the fig. 3-28 indicates, the shot-to-shot number fluctuations was rather high, $\sim$ 20%, because of the alignment uncertainty of the optical tweezers due to variations in

[54] This was done by simply ramping down the current in the y-compensation coils, see sec. 3.6

[55] By lowering the current in the curvature coils, we also reduced the offset field of the magnetic trap, which increased the radial trap frequency

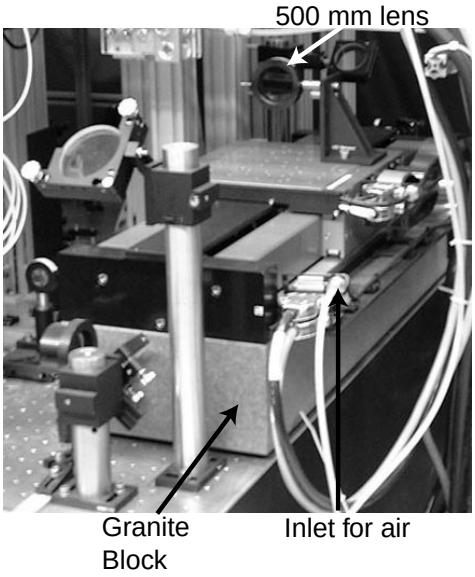

Figure 3-29: Photo of the air-bearing Aerotech translational stage. The 500 mm lens is mounted directly onto the stage. The stage is mounted to a precision polished granite block to maintain the flatness of the stage.

the compression of the rubber vibration dampers as the stage was moved back-and-forth.

The transported atoms were then loaded into a macroscopic Z-shaped wiretrap, which is described in the next chapter.

3.10.5 Air bearing stage

After the first experiments, it became immediately clear to us that we needed to find a translational stage that did not produce vibrations as it translated. On hindsight, the re-circulating ball-bearing system was clearly a bad choice due to the inherent vibrations. Although we were able to circumvent the problem by using vibration isolators and stacks of lead bricks, it is decidedly better not to have the vibrations in the first place.

While the science chamber was being baked out with the new atom chips (see chap. 4), we replaced the MICOS stage with an Aerotech linear air-bearing stage, ABL20040, with 400 mm travel. The stage required 80 psi of clean dry air pressure and is driven by a DC brushless motor. The position of the stage could be read-out using a non-contact linear encoder that is repeatable to 0.3 μm. Using the encoder, we could control the acceleration, velocity and position of the stage by the Galil controller. The maximum load weight is 50 kg. To maintain the flatness of the stage, we had to mount the stage onto an Impala black granite block whose top surface was polished to within 3 μm flatness over 50 cm. The flatness of the optical table was not good enough.

With the air-bearing translation, we now efficiently transfer upto 4 million condensed atoms into the science chamber. Currently, we move the condensates in 2 s, although the

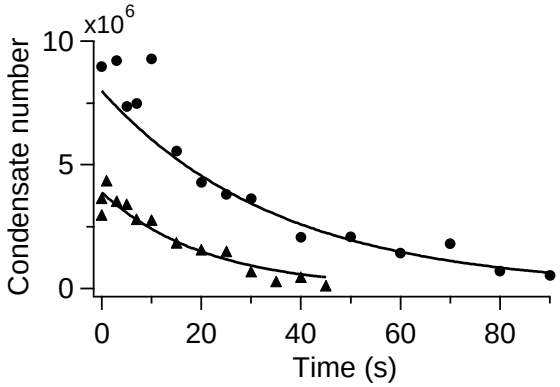

Figure 3-30: Lifetime of the Bose condensed atoms in the main and science chamber. The condensate was transported using the air-bearing stage. Circles and triangles represent data in the main and science chambers, respectively. Both traps were similar but were taken with slightly different infrared power. In the science chamber, the infrared power was (0.3V CONVERT!!) and the radial trap frequency was 425 Hz. In the main chamber, the infrared power was 0.4 V (CONVERT). The lines are exponential fits to the data. The lifetimes in the main and the science chambers were 35 ± 3 and 21 ± 3 s, respectively. The lifetime in the main chamber was obtained by fitting data after 10 s, since during that the number measurement was complicated due to the quadrupole excitations from the magnetic trap switch-off.

transfer has been achieved within 1.25 s. Typical transfer parameters for the 2 s transfer were jerk = 1220 mm/s^3, acceleration = 390 mm/s^2, and velocity = 250 mm/s. Compared to the old stage, we have such reduced vibrations that the 500 mm lens is mounted on the stage without any vibration isolators. See fig. 3-29. We are essentially limited by the loss of atoms due to three-body recombination by the high condensate density. Typical infrared power was around 50 mW, compared to the 90 mW with the older stage. To increase the axial trapping frequency (and the density) during the transfer, we increased the power during the transfer by a factor of six. At the end of the motion, the power was reduced back. Due to this density increase and due to the initial quadrupole sloshing in the optical trap, the condensate is heated up a bit when it arrives in the science chamber. We typically decrease the power slightly and hold the trap at a constant position for about 1 s, to damp out excitations via evaporation. The only remaining excitation is the residual longitudinal sloshing, which is practically impossible to damp out.

The $1/e$ lifetime of the optical dipole trap in the science chamber was about 21 ± 3 s; the lifetime in the main chamber was about 35 ± 3 s (see fig. 3-30), mainly limited by background gas collisions.

3.11 Final thoughts

In this chapter I have described in detail the making and the workings of the new BEC-III apparatus in the Ketterle group. As I had mentioned at the beginning of the chapter, I hope that this chapter will be useful for future experimentalists who may attempt to build such separated chambers for BEC production and BEC science. While some of the design considerations and details might only be useful to few researchers outside, it is a partial record of the structure and functionality of the BEC-III apparatus. Clearly this is not the only way to build 'science chambers,' but it is ours and it is especially dear to me.

The first success of the science chamber was loading a BEC into a macroscopic magnetic trap from the optical tweezers, which is described in the next chapter. After this initial success, we broke vacuum in the science chamber (and maintained UHV in the main chamber), and replaced the macroscopic wire with miniaturized wires on an atom-chip. In addition, we installed a mechanical shutter for blocking the MOT light. This shutter was one of the key elements for our success in making the continuous BEC; see chap. 5. The successful bakeout of the science chamber with a turn-around time of less than three weeks was very satisfying. All of the set goals were accomplished.

It is said that the best form of flattery is copying or reproduction; thus, the best indication of our success was that an (almost) identical vacuum chamber has now been successfully implemented for the rubidium BEC-IV apparatus. They plan to use the same moving optical tweezers technique for their science chamber.

Chapter 4

Macroscopic and miniaturized wiretraps

In this chapter I will describe the first experiments in the science chamber, where we loaded transported atoms into both macroscopic and miniaturized single-wire magnetic traps. This work is presented in these papers:

- *T. L. Gustavson, A. P. Chikkatur, A. E. Leanhardt, A. Görlitz, S. Gupta, D. E. Pritchard and W. Ketterle, "Transport of Bose-Einstein Condensates with Optical Tweezers" , Phys. Rev. Lett.* **88***, 020401-4 (2002). Included in Appendix E.*
- *A. E. Leanhardt, A. P. Chikkatur, D. Kielpinski, Y. Shin, T. L. Gustavson, W. Ketterle and D. E. Pritchard, "Propagation of Bose-Einstein condensates in a magnetic waveguide" , Phys. Rev. Lett.* **89***, 040401-4 (2002).*

The route to BEC required a marriage between optical trapping techniques and magnetic trapping. Although, the first trapping of neutral atoms with magnetic fields was facilitated by using laser cooled atoms [134], it was only in 1994-95 that the techniques were combined with rf-evaporation to finally reach BEC [22]. Magnetically trapped atoms continue to be workhorse of the BEC industry[1], and the trend has been to produce magnetic traps that are smaller and use less power[136]. Both mesoscopic [137, 138] and micro-fabricated [139–146] magnetic traps and guides using simple wire configurations have already been implemented for cold neutral atoms. As our first demonstration of the utility of transported BECs, we loaded a BEC from the optical tweezers into a single wire Ioffe-Pritchard trap. After this initial work, we then loaded a transported BEC into a micro-fabricated magnetic trap and waveguide formed by running currents in lithographic wires on substrates, similar to integrated circuit chips. A key goal of using BECs in these magnetic waveguides is to enable small scale atom interferometers. This work is still in progress and will be the focus of Aaron

[1] Except for the Chapman group who produced the first all optical BEC [135].

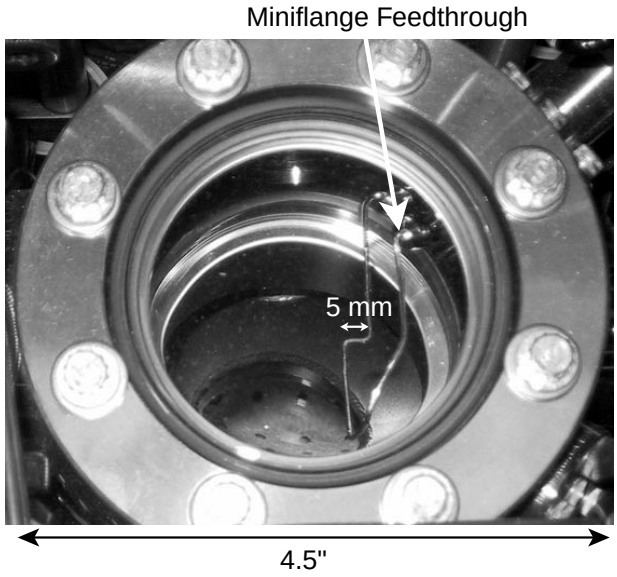

Figure 4-1: A photo of the Z-shaped wiretrap in the science chamber. The central segment is labelled and is 5 mm in length. The end segments are connected to a miniflange feedthrough (rated to maximum current of 5 A).

Leanhardt's future Ph.D. thesis. Thus, I will only highlight some of the key features of this work and the advantages of using transported condensates.

4.1 Mesoscopic Z-wiretrap

The mesoscopic wire trap we chose to load was a Z-shaped wiretrap (wire diameter = 1.27 mm) [140, 147] (see fig. 4-1). The wire was connected using one of the miniflange feedthroughs of the science chamber (see sec. 3.2.3). The length of central segment of the 'Z' was $L = 5$ mm long. The current flowing through this wire combined with an external magnetic field produced a 2D quadrupolar field configuration near a field zero. It is this field configuration that was used to produce the magnetic waveguides [138]. The current in the end segments of the Z provide axial confinement and allows for a non-zero offset field for the trap. The magnetic field configuration is of a Ioffe-Pritchard type [147]. The trap center is located at $z_0 = (\mu_0/2\pi)I_w/B_0$ below the central wire, where the external bias field B_0 is equal and opposite in direction to the magnetic field produced by the current I_w in the wire. The axial curvature provided by the two end segments is $B'' \propto B_0/L^2$ and the bias field at the trap bottom $B_{bot} \propto (I_w z_0)/(4z_0^2 + L^2)$ [147]. The radial gradient B' is $(2\pi/\mu_0)B_0^2/I_w$, and the radial trap frequency is proportional to $B'/\sqrt{B_{bot}}$.

The optical tweezers transported the BEC such that it was about 750 μm below the central segment of the Z-wiretrap. To transfer the BEC into the wiretrap, the current in the wire I_w and the currents producing the bias field B_0 were linearly ramped up in 1 s. The

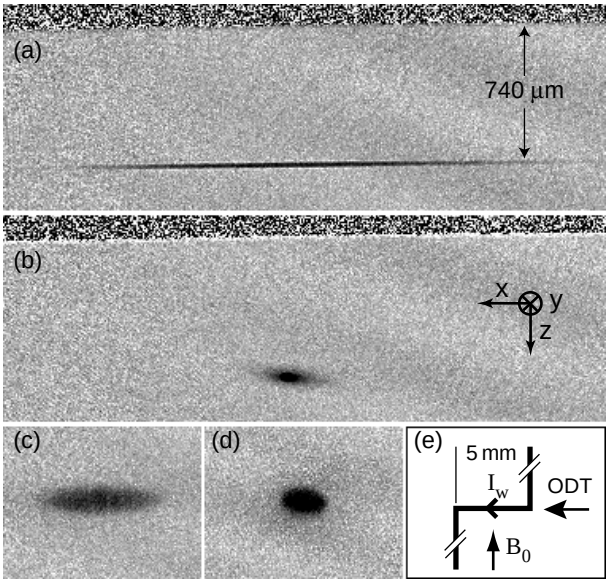

Figure 4-2: Absorption images of condensates in the science chamber, side view. All images have the same scale. Condensates of $\simeq 6 \times 10^5$ atoms in: a) optical trap and b) wiretrap. The center segment of the Z-shaped wire is visible as a dark speckled horizontal strip and is 740 μm above the trapped atoms. Condensate released from: c) an optical trap after 10 msec time-of-flight and d) wiretrap after 23 ms time-of-flight. e) Schematic of the wiretrap, top view. $I_w = 2$ A is the current through the wire, $B_0 = 2.9$ G is the bias field. Atoms are trapped *below* the 5 mm long central segment of the wire, which is aligned with the optical trap axis. The supporting end segments, which provide field curvature, are truncated in the figure. The wiretrap was located 36 cm from where the condensates were produced. The directions relative to the wiretrap is defined in b), where the $+y$-direction is into the page.

optical trap and the wiretrap were aligned to be at the same location using magnetic fields. The vertical height was controlled by the magnetic field B_y and the other radial direction was controlled by B_z, such that $B_0 = \sqrt{B_y^2 + B_z^2}$. See fig. 4-2e. The optical trap was then slowly ramped down to zero, transferring the condensate into the magnetic wiretrap. Nearly 100% efficient transfer was achieved for $B_0 = 2.9$ G ($B_y = 2.7$ G and $B_z = 0.92$ G) and $I_w = 2.0$ A. The residual magnetic fields in the science chamber, estimated to be about 300 mG, were not compensated. The trap frequencies were measured to be 36.0 ± 0.8 Hz radially and 10.8 ± 0.1 Hz axially. The lifetime of the condensate in the wiretrap was measured to be 5 ± 1 s 750 μm^2 from the edge of the wire. The lifetime was much shorter (100 ± 25 ms) when the condensate was moved closer to the wire (80 μm); see fig. 4-3. This lifetime was improved by adding a radio frequency shield to limit the trap depth [100]. By reducing the current in the wire, condensates were also moved to within a few microns from the wire surface (see fig. 4-4).

These initial experiments (presented in [2]) were geared towards testing the tweezers

[2]The centroid of the current density was 0.64 mm away from the wire edge.

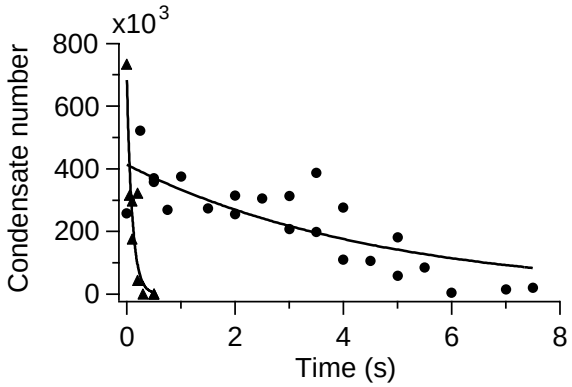

Figure 4-3: Lifetime of the wiretrap with the trap position at 750 μm (circles) and 80 μm (triangles). Exponentials fit to the data are shown, where the $1/e$ lifetimes were measured to be 5 ± 1 s for 750 μm and 100 ± 25 ms for 80 μm.

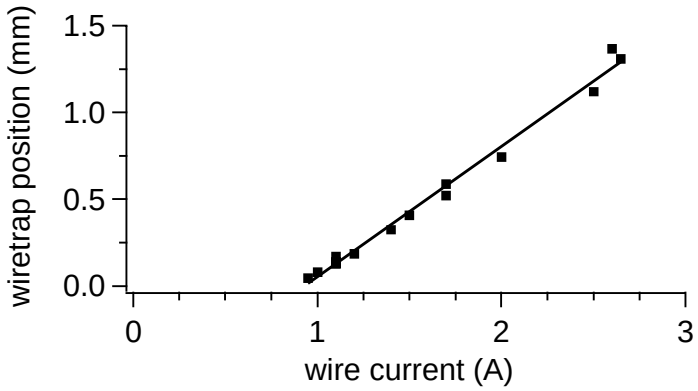

Figure 4-4: The position of the wiretrap as a function of the current in the wire. The external field was maintained at 2.9 G throughout, and so the trap frequency varied as the trap position was translated.

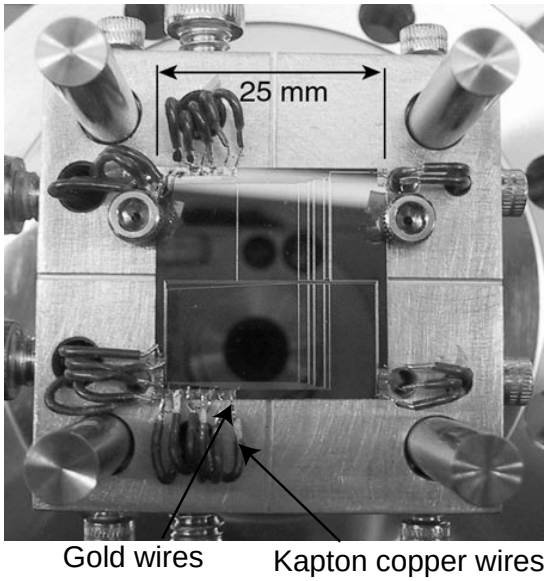

Figure 4-5: A photo of the atom chip. The silicon wafer, at the center, is pressed against the aluminum block with two small screws. Below the aluminum block is the feedthrough. The connections to the feedthrough are made using kapton-insulated copper wires. Near the chip, the copper wires are bonded to a thin gold ribbon, which are then wire-bonded to 1 mm copper pads on the chip.

technology and understanding the basics of condensates in wiretraps. Immediately afterwards we decided to push the size of the wire from about a mm to tens of microns, using lithographic wires.

4.2 Atom chip and magnetic waveguides

As mentioned earlier, a key application for BEC tweezers was to load condensates into micro-fabricated magnetic waveguides [139–146]. These waveguides are made using lithographically imprinted wires on either sapphire or silicon chips; hence the term 'atom chip'. The waveguides, analogous to fiber optics for light, may lead to improved manipulation of condensates, enabling sensitive atom interferometers. An alternative method of loading BEC into waveguides is to make a BEC on an atom chip [122, 148] directly. This requires designing structures on (or behind) the chip that allow for large currents needed for a large trap depth necessary for confining laser cooled atoms. The advantage of tweezers is that we separate the BEC production from chip technology. Therefore, we can build magnetic traps on our chips which dissipate only a few watts of power and can be more flexible. In addition, we can have quick turn-around time for testing new chips and designs.

A photo of the first chip is shown in fig. 4-5. We mounted this chip using the top 4.5" flange of the science chamber (see sec. 3.2.3) such that the chip was about 1 mm above the

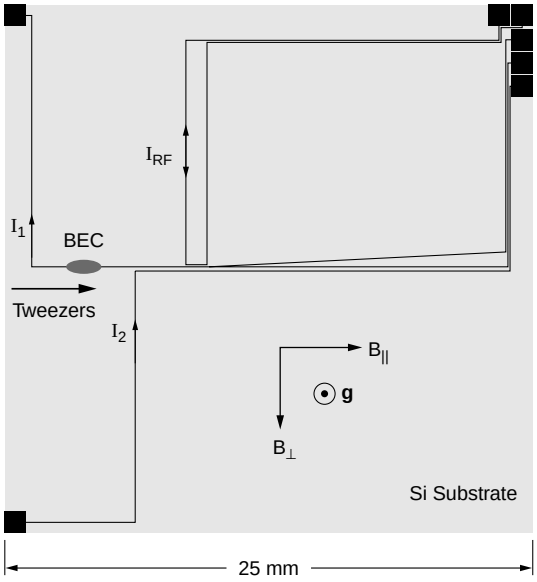

Figure 4-6: Microfabricated magnetic trap and waveguide. Optical tweezers loaded a Bose-Einstein condensate into the Z-wire trap formed by currents I_1 and I_2 in conjunction with the magnetic bias field $B_\perp$. Lowering I_2 to zero released the condensate into a single-wire magnetic waveguide. Atom flow was from left to right. The condensate was trapped above the plane of the paper and the gravitational force, $\mathbf{g}$, points out of the page. Note that the 'lab' directions as defined in fig. 4-2b are such that $+\hat{y}$ is in the direction of $\mathbf{g}$, $+\hat{x}$ is along $B_{||}$, and $-\hat{y}$ is along $B_\perp$. All microfabricated features are drawn to scale.

center of the chamber, where the transported BEC arrives from the main chamber. The optical tweezers BEC transfer was made using the air-bearing Aerotech translation stage. Similar to the macroscopic Z-wiretrap, we planned to load a BEC from the tweezers into a microscopic Z-wiretrap that was formed by wires on the chip.

The chip was a 600 μm thick, 25 mm-square silicon wafer that was mounted on an aluminum block. The connections from the chip to the outside were made using a $2\frac{3}{4}$" feedthrough with 24 connections. The kapton wires from the feedthrough were bonded to a 5×2 mil gold ribbon which were individually wire-bonded to 1 mm-square copper pads on the chip. The wires on the chip were initially etched using $e-$beam lithography and then electroplated with copper upto 10 μm height[3]. The wires were all 50 μm wide and the minimum separation distance between wires was 50 μm (100 μm center-to-center). The schematic of the wires is shown in fig. 4-6. Although the initial chip was intended to test primitive atom interferometers, we were unable to do so since only about 30% of 24 wire connections survived the bakeout. Luckily, we were able to still load atoms into a microscopic Z-wiretrap using the surviving connections (see fig. 4-6).

Transported BECs of about 2-3 million atoms were initially loaded into a Z-wiretrap

[3]The MIT Microsystems Technology Laboratories (MTL) made the chip for us.

formed by currents I_1 and I_2 along with an orthogonal magnetic bias field $B_\perp$ (see fig. 4-6). Typical loading conditions were $I_1 = I_2 = 1.2$ A and $B_\perp = 5.4$ G, corresponding to a separation of 450 μm between the BEC and the microchip. The currents were ramped up linearly in 250 ms. A longitudinal bias field, $B_{||}$, tailored the transverse trap frequency while nominally keeping the trap center in the same location relative to the surface of the microchip. Transfer efficiency from the optical tweezers to the Z-wire trap was near unity and BEC lifetimes over 10 s were observed with the application of a RF shield [100] produced by the current I_{RF} on an auxiliary wire as shown in fig. 4-6.

The BEC was transferred into the waveguide by linearly ramping the current I_2 to zero in 250 ms. The atoms were smoothly accelerated into the waveguide by the remaining endcap of the Z-wire trap. Downstream, the effect of this endcap was negligible and we observed BEC propagation at a constant velocity of 3.0 cm/s after a propagation distance of 4 mm for $I_1 = 1200$ mA. Upon releasing the BEC from the Z-wire trap, its longitudinal velocity was controlled by applying an external magnetic field gradient of variable amplitude for a fixed time. The field gradient was linearly ramped up and down over 6.5 ms to prevent creating excitations and was held constant for 52 ms. With modest gradients of $0 - 0.6$ G/cm, we were able to vary the atomic velocity over the range $3.0 - 6.6$ cm/s corresponding to longitudinal kinetic energies in the range $25 - 120$ kHz.

Releasing the BEC into the waveguide produced little variation in its transverse confinement and position relative to the microchip. The longitudinal potential experienced by the propagating atoms was determined by the local magnetic field (due to the Zeeman interaction) and vertical position of the guide center (due to the gravitational interaction).

BEC propagation in the single wire magnetic waveguide was very smooth unless it was perturbed (see also [149]). Perturbations to the guiding potential arise from geometric deformations of the current carrying wires on the substrate. The extent to which such deformations alter the potential experienced by the atoms depends on the atom-wire separation distance, r, longitudinal extent of the perturbation, ℓ, wire width, w, and wire height, h. Under our guiding conditions ($r \gg w, h$) the waveguide potential only responds to changes in the centroid of the current density. Preliminary experiments have shown that these changes in the direction of the current density centroid can result in large excitations of the BEC as it propagates in the waveguide [3]. Similar perturbations also fragment the condensate axially when it is brought closer than 150 μm from the wire [3]. These preliminary experiments and further experiments will be described in a future Ph.D. thesis by Aaron Leanhardt.

In addition, initial efforts to push the condensate into the quasi-1D limit [18, 150] were not successful. We tried to enter the regime both by 'stretching' out the condensate in the waveguide [18] and by reducing the number of atoms in the condensate. However, we were not able to obtain a definite signal that the condensates were in the 1D regime. Due to the fragmentation mentioned above, we had to work with condensates far from the wire, which

resulted in a weaker radial trap frequency. Stronger radial confinement will require us to bring BECs closer to the wire without fragmentation.

4.3 Discussion

Future work will explore the utility of BEC for miniature atom interferometers, gyroscopes, etc. The work of this thesis has provided key technologies for that and also revealed potential problems to be overcome.

We have demonstrated that optical tweezers can be combined with atom chip technology. Our first experiments indicated that the manufacturing process of these chips are crucial for a successful implementation of atom interferometers on a chip. The fragmentation and short lifetimes were also observed in other laboratories [122, 148, 151]. It is important to understand and eliminate the fragmentation of the condensate at short distances from the microscopic wires and to increase the lifetime of condensates at these close distances. Shorter distances allow us to get to higher radial trap frequencies and into the quasi-1D regime where we need to operate the atom interferometers. This regime is important because population in the higher radial modes can lead to loss of coherence in the beam splitter. These first experiments with miniaturized atom chips will explore the new possibilities for BEC beams [152]. Experiments could include a condensate beam-splitter on a chip, an atom interferometer, and studies of quantum point contact [153]. Along with other approaches [122, 148, 154], our BEC tweezers technique will have invaluable contributions to this new field.

Chapter 5

Generation of a Continuous Source of Bose-Einstein Condensed atoms

In this chapter I will describe the first experiments on continuous Bose-Einstein condensation, a crucial step towards continuous atom lasers. This work was presented in the following publication:

- *A. P. Chikkatur, Y. Shin, A. E. Leanhardt, D. Kielpinski, E. Tsikata, T. L. Gustavson, D. E. Pritchard and W. Ketterle, "A Continuous Source of Bose-Einstein Condensed Atoms", Science* **296***, 2193 (2002). Included in Appendix F.*

Optical lasers are ubiquitous in today's world. They are used in bar-code scanners, optometrist offices for laser surgery, security systems, CD players, rock concerts, telecommunications, precision cutting tools, laser pointers, etc. The laser, when invented in 1960 [155, 156], was not envisioned for such widespread public use, but as a research tool for improving atomic and molecular spectroscopy and for telecommunication [157]. Similarly, the atom lasers [107–110] of today are thought to be useful for fundamental atom optics research. However, as of now, the atom laser is a solution waiting for a problem[1]. Some reasons for this are highlighted by differences between optical and atom lasers. Unlike optical lasers, atom lasers are much more difficult to produce and are extremely fragile. In addition, continuous atom lasers have not yet been demonstrated. The atom lasers have all been operated in *pulsed* mode since condensed atoms were outcoupled until the condensate was depleted. After the depletion, it took tens of seconds to form another BEC to outcouple from. This is unlike the optical regime where it took only six months from the pulsed ruby laser [155] to the continuous-wave (cw) HeNe laser [156]. In this chapter, I will describe the first demonstration of a continuous BEC source, which is a key element of a cw atom laser. This was only possible in the BEC-III apparatus where condensates could be continuously stored in a reservoir trap in the science chamber while new condensates were being produced

[1] After its invention, the cw HeNe laser was immediately used to transmit telephone signals [157].

in the main chamber to be merged with the continuous BEC in the reservoir. This physical separation of the BEC production from the BEC storage was crucial.

5.1 What is an atom laser?

Many people initially objected to the term 'atom laser' since 'LASER' was an acronym denoting *light amplification by stimulated emission of radiation.* However, as Dan Kleppner has eloquently pointed out [23], the term 'laser' is no longer an acronym but is used to mean a source of radiation in the coherent state. Whether the radiation is photons or atoms is immaterial. In this sense, outcoupling of coherent atoms via stimulated processes is an atom laser [24]. Analogous to its optical cousin, the cavity for an atom laser is the atom trap and the gain medium is the thermal cloud from which evaporative cooling and Bose stimulation enhances the scattering rate into the coherent state [158]. The threshold for 'atom lasing' is the critical temperature T_c. There are of course some differences. The key one being that atoms cannot be destroyed (chemical potential $\mu \neq 0$ and number conservation is strictly held) whereas photons can be absorbed into matter ($\mu \equiv 0$ and there is no number conservation). Secondly, optical lasing typically uses a non-equilibrium inversion process, whereas the formation of a condensate occurs near a thermal equilibrium.

The first atom laser was demonstrated when the first order coherence of BECs was shown using the now classic two condensate interference experiment [89], and when the atoms were outcoupled using pulsed RF[2] [107]. Currently, we have many outcoupling schemes: the mode-locked outcoupler from 1D optical lattices [108], the quasi-continuous Raman outcoupler [110] and the continuous RF outcoupling [109]. However, as mentioned earlier, all of these produce a pulsed atom laser simply because the outcoupling is from a pulsed source.

Initial theoretical work on cw-atom lasers studied optical pumping of incoming atoms into the laser mode [159–161]. While not fundamentally impossible, this method suffers from heating due to reabsorption of scattered light [162]. More recently, evaporative cooling of a slow atomic beam from the typical phase-space density of laser cooling (10^{-6}) into quantum degeneracy has been studied [163]. Prior to our work, experimental efforts have been focused on the production and guiding of a beam of laser-cooled atoms [164–166]. These groups plan to continuously cool the atoms into degeneracy while they are guided. It is important to note that the optical pumping scheme is an open system and hence not in thermal equilibrium [3], whereas both our scheme and the magnetic guiding schemes maintain the system in thermal equilibrium.

[2] One might wonder if ballistic expansion of BEC, by turning off the trap suddenly, can also be considered as a singly pulsed atom laser.

[3] There is no need for collisions anywhere.

5.2 Why was continuous BEC hard to make?

A continuous BEC has been difficult to make simply because of the enormous parameter space that needs to be traversed to make and store BECs. A typical cooling cycle for BECs involves laser cooling followed by evaporative cooling. During laser cooling, atoms scatter around 10^7 photons/s, whereas during evaporative cooling, light scattering must be less than 10^{-1} photons/s, since any scattering would cause heating and trap loss. Also, atoms are cooled by a factor of a thousand from about 100 μK to 100 nK temperatures during evaporative cooling. This requires a near perfect isolation of the hot atoms from the cold, as a single 100 μK atom has enough energy to knock thousands of atoms out of the condensate.

A continuous atom laser requires the continuous presence of condensed atoms in a trap. This can implemented either by pulsed generation or by continuous generation [164–166]. The pulsed generation with continuous storage scheme, which we have implemented, is similar to a scheme in which a pulsed optical laser delivers photons to an external storage cavity from which a cw laser beam can then be extracted. In both cases, the problem is more of a technical nature. The key technical problems that need to be solved for making a continuous BEC source are:

- The continuous condensate stored in a reservoir trap needs to be separated from the pulsed source.
- During laser cooling, the scattered light must be shielded from the continuous condensate.
- The effect of stray magnetic fields during the turn-on and operation of the magnetic trap must have minimal (or no) impact on the reservoir trap holding the continuous BEC.
- Finally, a successful method of merging condensates has to be found.

5.3 Solutions to technical problems

The technical problems described above, of course, have technical solutions. Sometimes, simple technical solutions can solve seemingly complicated problems[4].

5.3.1 Physical separation of the reservoir trap

The apparatus described in chapter 3 was ideally suited for producing a continuous BEC, since we could use the tweezers to transport condensates from where they were produced into a physically separated reservoir trap. The reservoir trap was in the science chamber,

[4]The RF outcoupler [107] was one such technical solution to the 'difficult' problem of output coupling [158].

about 32 cm away from the production of the condensates in the main chamber (see fig. 5-1). This solved the first problem of physically separating cold BEC atoms from the 'hot' laser-cooled atoms.

5.3.2 Beam shutter to block the MOT light

To prevent laser light from affecting the condensate in the reservoir trap, we used a simple mechanical shutter to block the view from the science chamber to the main chamber (see fig. 5-1). The science chamber was connected to the main chamber through a gate valve and bellows (sec. 3.2.3). Thus, we had an aperture of 1.37" diameter between the science chamber and the main chamber. To minimize the amount of MOT light scattered into the science chamber, the 1.37" aperture was reduced to 1 cm[5] by an aluminum plate that was attached internally in the science chamber using the 'Groove Grabber' technology implemented Kimball Physics vacuum chambers. While the MOT was operated, we had two sources of light entering the science chamber through the aperture: scattered light from MOT and repumping beams and the fluorescence from the confined atoms in the MOT itself. The condensate lifetime in the science chamber was not reduced when only the MOT light was on, hence the effect of scattered light was negligible[6]. However, during its operation, about 10^{15} photons/s are scattered from the 10^{10} trapped atoms in the dark MOT. This leads to about a mW of isotropically scattered fluorescence, which leads to several Hz of photon scattering 32 cm away. Thus, without shielding this fluorescence from the MOT, a BEC in the science chamber was destroyed rather quickly. In addition, the inside of the science chamber was well polished such that any light that scatters into the science chamber could bounce around a few times before exiting the chamber through the windows.

Thus, to shield the condensate from the light scattered by trapped MOT atoms, we implemented a simply shutter that blocked the 1 cm aperture. A pneumatic linear feedthrough was attached to the bottom flange of the 4" pumping tube. The feedthrough was connected to an aluminum plate that acted as shutter (see fig. 5-1). The shutter was translated up and down using UHV bellows connected to the pneumatic linear actuator. Unfortunately, during the motion of the shutter, some residual gas was released[7], which increased the background pressure, limiting the lifetime of the atoms in the science chamber to 22 s. The shutter blocked the 1 cm aperture only during the 2 s that the MOT was on in the main chamber (see fig. 5-3). In order to reduce vibrations from the shutter, it was slowly raised up and down such that it took about a second to fully close the aperture.

[5] 1 cm aperture was large enough for the tweezers beam to enter the science chamber without any clipping of the beam.

[6] Note that the MOT light was 1.7 GHz detuned from resonance with the condensate atoms and it was only the scattered repumping light that was would have been most detrimental.

[7] The speed of the shutter motion was minimized to reduce outgassing.

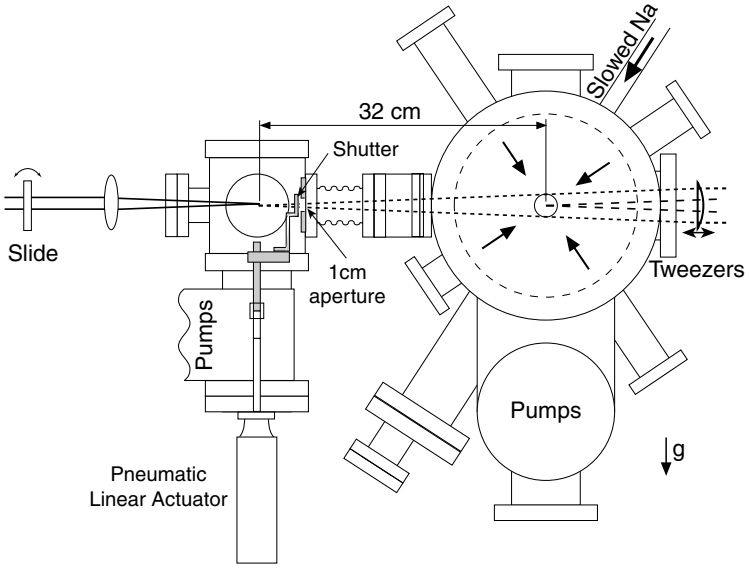

Figure 5-1: A schematic of the setup for continuous BEC. On the right is the main chamber where the BEC is produced. A tweezers beam transports the BEC from the main to the science chamber, where a reservoir trap maintains condensed atoms. The beam shutter used for blocking the MOT light is shown in gray. We merged the transported condensates with the condensate in the reservoir by tilting a glass slide in the reservoir trap infrared beam.

5.3.3 Optical reservoir trap

It was important to use an optical trap as the reservoir trap to minimize effects of stray magnetic fields from the cloverleaf magnetic traps since optically confined atoms are not sensitive to magnetic bias field; only field gradients can affect them. The field gradients were less than 100 mG/cm in the science chamber.

We initially tried to hold atoms in the science chamber in a magnetic Z-wiretrap (see sec. 4.2, [3]), but the atoms were lost when the magnetic fields for the Zeeman slower and the MOT were switched on, displacing the center of the magnetic trap. Another problem with a magnetic trap is its long range. Magnetic forces can accelerate the condensate in the tweezers as it approaches the magnetic trap, and the new condensate will violently collide with the condensate in the reservoir. Optical traps, on the other hand, have a more limited trap volume and depth. Hence, we can bring the condensates as close as the traps' beam waist before they are affected by each other's presence.

As mentioned earlier (sec. 3.10.1), the laser light for the reservoir trap was produced by a 1064 nm laser that was coupled through an optical fiber. The intensity of the light was controlled by an AOM before the fiber. The optical axis of the laser beam for the continuous reservoir was parallel to the tweezers beam with a vertical displacement of 70 μm, which was sufficient to ensure that the two traps did not affect each other before the merger (see

fig. 5-2). The trap characteristics were similar to the tweezers trap, which used 50 mW of laser power focused to $1/e^2$ beam waist radius of w_0 =26 μm with a radial trapping frequency of 440 Hz and a depth of about 2.7 μK. In order to prevent the two beams from interfering during the merger, the polarization of the reservoir trap beam had to be orthogonal to the polarization of the tweezers beam. The AOMs for the two beams had a frequency difference of 10 MHz, so one might nominally expect that polarization of the beams would not matter, since any intensity grating would be rapidly washed away due to the 10 MHz frequency difference. However, the merger was only successful when the polarization of beams was mostly orthogonal.

5.3.4 Condensate merger

Condensates held in the tweezers beam were transferred into the reservoir by slowly lowering the reservoir trap to the position of the tweezers focus over 500 ms (see fig. 5-2B-H). It was critical to merge the condensates along the tightly confining radial direction. The large radial trap frequencies ($>$ 400 Hz) ensured that the merger could be done quickly and yet be almost adiabatic, and that the radial excitations during the merger could be damped out quickly. Tilting of a glass slide in the reservoir beam optical path allowed us to translate the reservoir trap vertically as shown in fig. 5-2A[8]. Initially, we tried to merge the condensates 'directly,' without any vertical translation. This resulted in severe heating and atom loss. Thus, the vertical translation was essential.

The collinear arrangement and the similar trapping frequencies ensured good overlap and "mode matching" during the merger of the two traps. The finite trap depth of the optical trap ensured dissipation by evaporative cooling. The merging of two separate condensates with a random relative phase into one condensate requires dissipation to damp out excitations caused by the merger. Assuming that the merger creates a soliton-like excitation at the interface of the two condensates, the excitation energy per atom is approximately equal to the chemical potential times the ratio of the healing length to the condensate size ($E \sim \mu \frac{\xi}{R_{TF}}$). In our experiment, this energy was typically of the order of a nanokelvin and could be dissipated by evaporative cooling with only a small loss in the number of condensed atoms.

It is important that the merger process be adiabatic simply to reduce excitations during the merger. Fast mergers would be like a collision between the two condensates(sec. 2.6.4,[1]).

5.4 Making the continuous BEC

Finally, after solving the technical problems, we demonstrated the continuous BEC. Due to the relatively short lifetime (20 s), the production cycle for condensates had to be shortened

[8]Note that the slide was placed between a pair of beam expanding lenses.

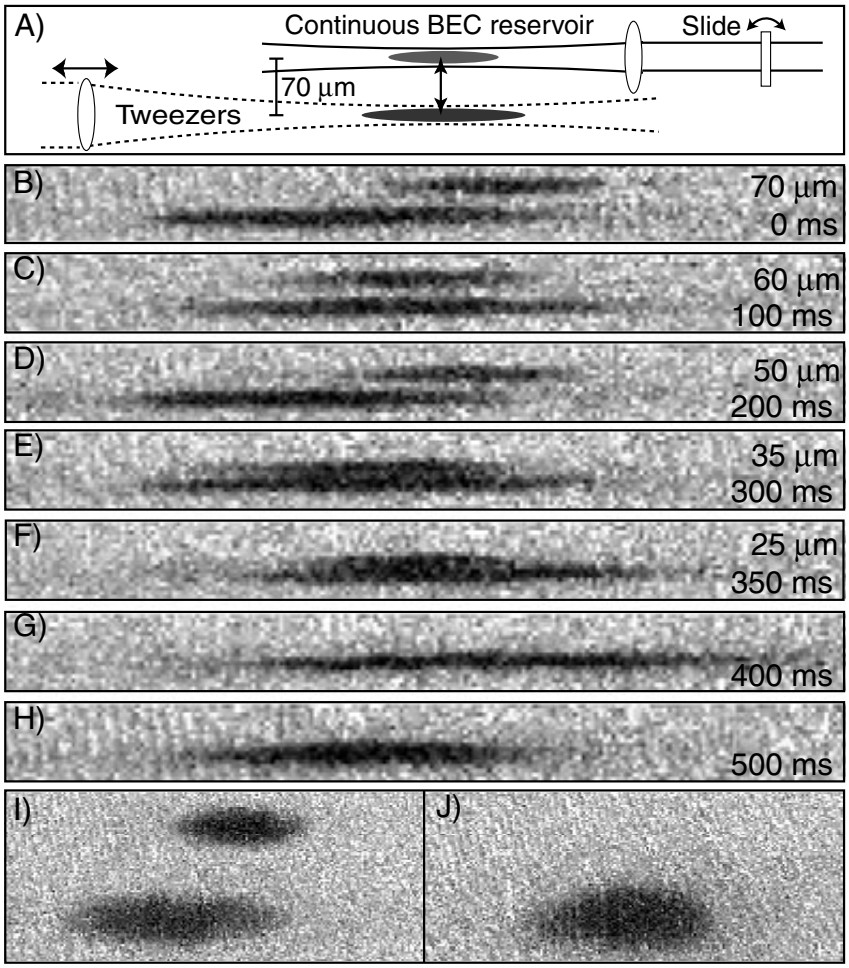

Figure 5-2: Merging of two condensates. A) Arrangement of the two optical traps. Both optical traps were horizontal. The focus of the tweezers beam was translated about 0.3 m from the production chamber to the science chamber. The tweezers beam placed a new condensate 70 μm below the condensate held in the reservoir. The merging of the two condensates was accomplished by tilting a glass slide, which translated the reservoir laser beam vertically. The schematic is not drawn to scale. The absorption images B-H), taken after 2 ms of ballistic expansion, show the approach and merging of the two condensates. The relative distance between the two traps and the elapsed time are given in the figure. The total time for the merger was 500 ms. In images G) and H), the traps overlapped. Image I) is an absorption image before the merger with 12 ms of ballistic expansion for the condensate trapped by the tweezers and 9 ms for the condensate in the continuous reservoir. Image J) is an absorption image after complete merger with 12 ms of ballistic expansion. The field of view is 0.2×4.2 mm^2 (B-H) and 0.7×1.7 mm^2 (I,J).

from the usual 25 s to 12 s. This was achieved primarily by shortening the evaporation cycle from 20 s to 8 s. The shortened cycle reduced the typical condensate number before the transfer into the tweezers beam to 6×10^6 atoms, which is a factor of three lower than our usual operating conditions. Nonetheless, the number of condensed atoms transported to the science chamber did not change noticeably. Larger condensates suffered from stronger three-body loss during the transfer from the magnetic to the tweezers trap. After making the BEC, it was transferred into the tweezers laser beam as discussed in chap. 3. The tweezers beam transported the condensates into the science chamber in 1.25 s using the air bearing translational stage (see sec. 3.10.5). After the initial excitations of the tweezers BEC had damped out in 1 s, the glass slide was tilted in 500 ms and the reservoir trap was lowered 70 μm to the position of the tweezers focus and the condensates were merged (fig. 5-2). The intensity of the tweezers beam was then linearly ramped to zero in another 500 ms, and the reservoir was raised back to its original position. After careful optimization of all parameters, condensates could be merged with 25% loss in the total atom number (see fig. 5-4). This loss was partially due to three-body recombination in the combined trap and partially due to the dissipation of excitations caused during the merger.

Within the next 18 s, a new condensate was produced, transported into the science chamber, and merged with the condensate reservoir. This cycle was repeated many times to create a continuous source of condensed atoms. See fig. 5-3 for the timing sequence in the cycle.

In 5-3a, the dashed black line is the power for the tweezers beam. Note the sixfold increase in power during the 1.25 s transfer. The solid black line is the power for the reservoir beam, which was kept at 50 mW most of the time except during the merger, when it was slightly lowered to 40 mW. It was raised back up to 50 mW when the mechanical shutter was being closed. The gray dotted line depicts the vertical position of the reservoir trap relative to the tweezers beam position. Nominally, the reservoir was 70 μm above the tweezers beam except during the merger. The shaded region indicates the time during which the MOT light was on (2.25 s). At this time, the shutter (gray solid line in fig. 5-3a) was up and it blocked the MOT light from entering the science chamber. The sequence of magnetic trap currents is shown in fig. 5-3b. For magnetic bias fields, gradients and curvatures made by these currents, see sec. 3.6. The black solid line is the current in the cloverleaf gradient coils. During evaporation, it was ramped up to 496 A to increase the collision rate during evaporative cooling and then ramped down to 227 A near the end of the evaporation cycle. As noted earlier, the rf evaporation cycle from 30 MHz to about 1 MHz was reduced to 8 s from the typical 20 s. The current in the curvature coils (black dashed line) was kept at 97 A throughout except during decompression when it was lowered to 6 A. During the decompression, the current in the gradient coils were reduced from 227 A to 34 A. The solid gray line is the extra 30 A of negative current in the curvature coils used for mode-matching the magnetic trap to the MOT (see [26]), and the gray dotted line

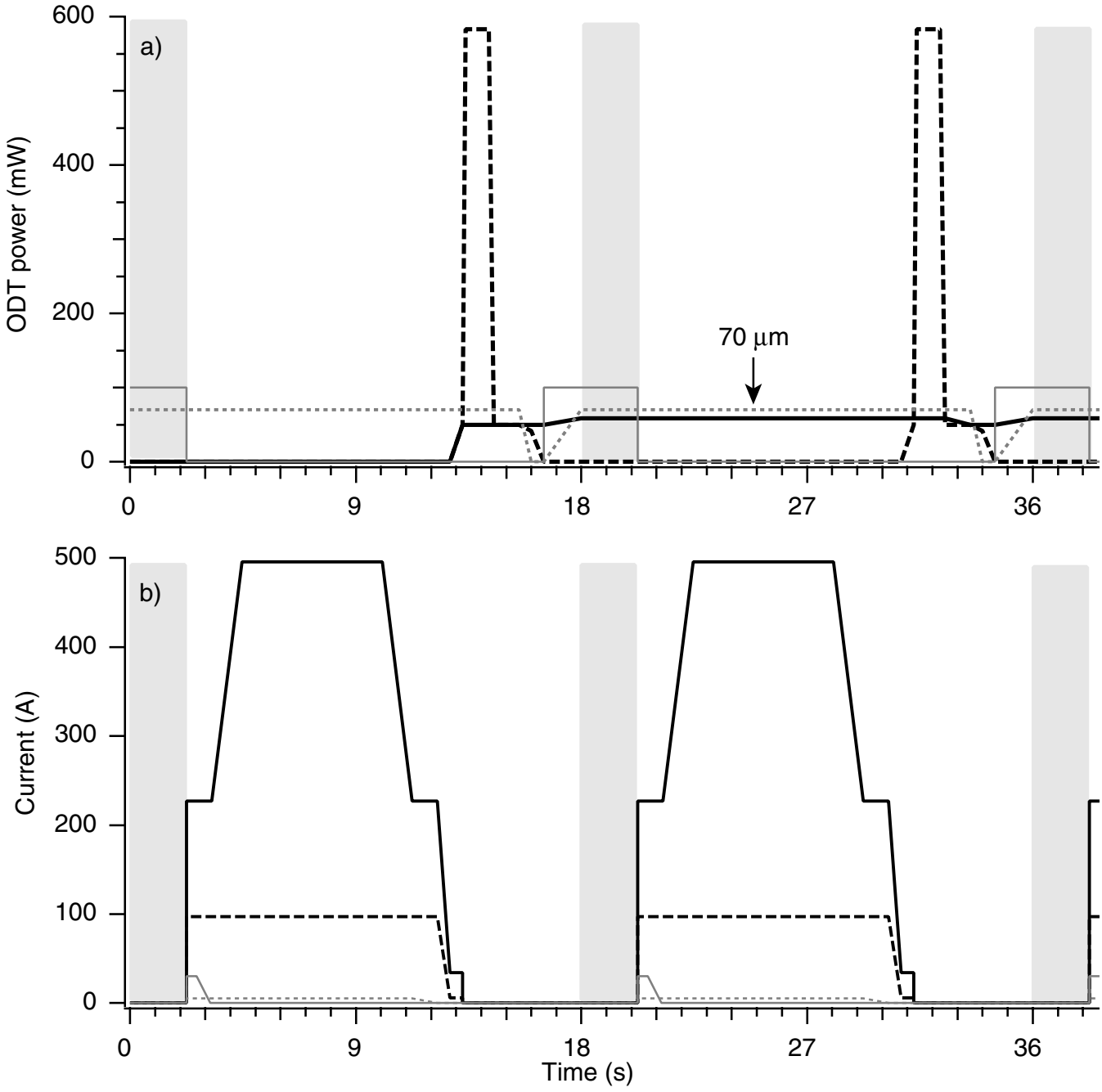

Figure 5-3: Making a continuous BEC. The timing schemes for a) the optical traps and b) the currents for the magnetic trap are shown for the initial loading of the condensate into the reservoir (0-18 s) and the next cycle (> 18 s). Further cycles just repeated the cycle shown from 18-36 s. Data from four such cycles are shown in fig. 5-4. The black solid and dashed lines in a) depict the optical power of the reservoir and the tweezers beams, respectively. The gray dashed line indicates the vertical position of the reservoir trap relative to the tweezers trap in the science chamber and the gray solid line is the position of mechanical shutter which was closed during MOT operation. The gray shaded region indicates the time when the MOT is on. In b), the current in the cloverleaf gradient coils, the curvature/anti-bias coils, the extra 'bias' coil and the external $y-$compensation coils are shown as solid black, dashed black, solid gray and dotted gray lines, respectively.

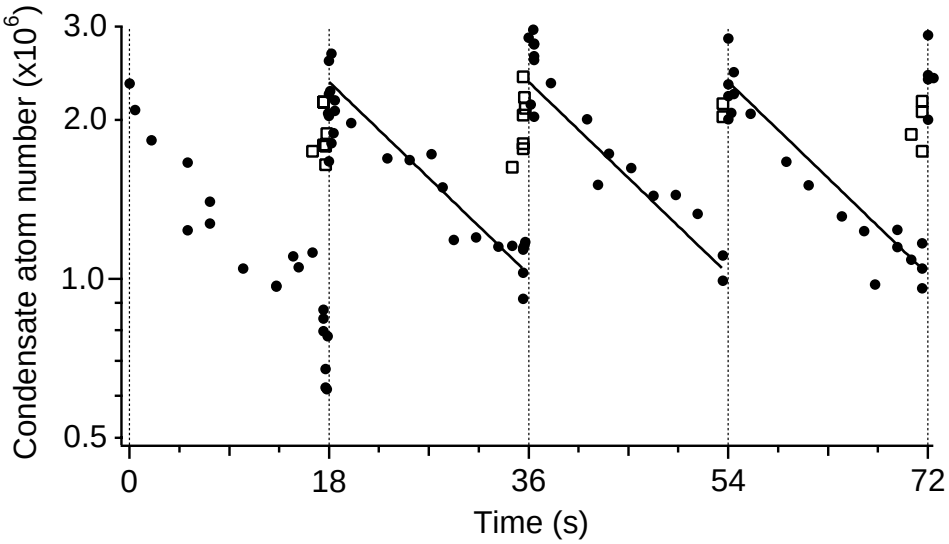

Figure 5-4: A continuous source of Bose-Einstein condensed atoms. The solid circles in the semi-log plot represent the atom number in the continuous reservoir and the open squares show the number of condensate atoms transferred from the production chamber. The dashed lines indicate the beginning of a new cycle and the solid lines are exponentially decaying curves determined by a simultaneous fit to the three cycles after the first cycle. The number of atoms for each data point was obtained from a separate absorption image, similar to Figs. 1I,J.

is the current in the extra $y-$compensation coils used for lowering the offset field of the magnetic trap. It is ramped down during the 'bias' decompression (see sec. 3.10.4).

The number of atoms in both optical traps was determined from absorption images taken after ballistic expansion (fig. 5-2I-J). Pure condensates with negligible thermal fraction were observed in both traps. Fig. 5-4 demonstrates the continuous presence of more than a million condensate atoms in the reservoir. The optical tweezers delivered a fresh condensate with 2.0×10^6 atoms in each cycle. Before the merger, the number of condensed atoms in the reservoir had decayed to 1.0×10^6 atoms, and grew to 2.3×10^6 atoms after the merger. These numbers were obtained from a simultaneous exponential fit for the three cycles following the first cycle (Fig. 2) with a statistical error of 0.05×10^6 atoms. Therefore, the merged condensate is significantly larger than each of the two condensates before the merger. During the 18 s production and transfer cycle, the condensate in the reservoir decayed with a $1/e$ lifetime of 22 ± 1 s, mainly limited by background pressure.

5.4.1 Crossed-dipole continuous BEC

In a preliminary experiment, we were also able to produce a continuous BEC using the reservoir and tweezers traps in a crossed-dipole configuration, where the axis of the tweezers beam was perpendicular to the reservoir trap. The timing of the transfer was similar to the

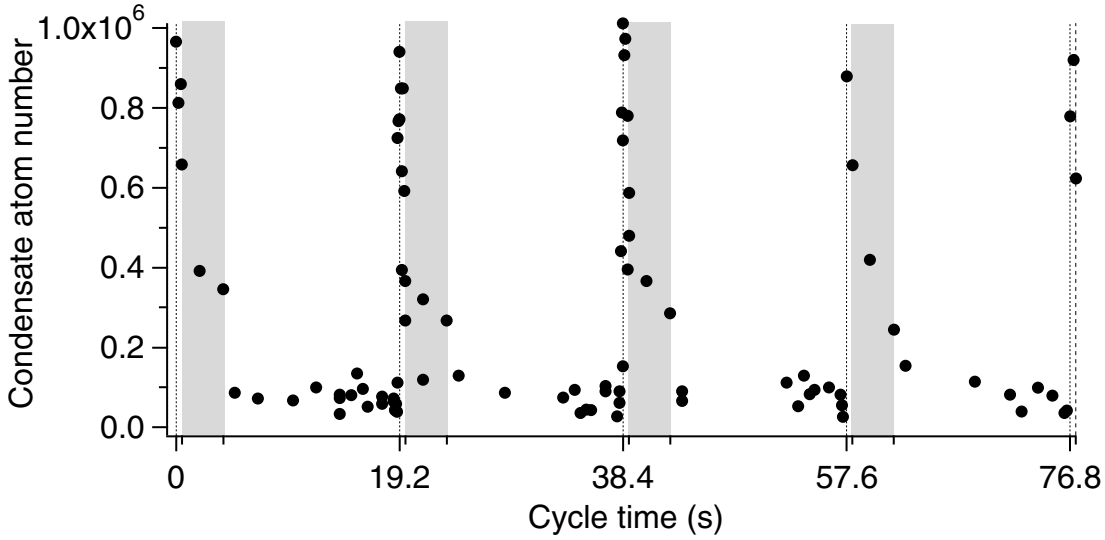

Figure 5-5: A continuous source of Bose-Einstein condensed atoms in the crossed-dipole configuration. The solid circles represent the atom number in the continuous reservoir. The dashed lines indicate the beginning of a new cycle. Each cycle was 19.2 s long. The dashed region indicates the time during which the MOT was on. The number of atoms for each data point was obtained from a separate absorption image, similar to Figs. 1I,J.

parallel configuration, except that we used a 9 s evaporation cycle and the MOT was on for 2.05 s (instead of 2.25). Thus, the production cycle was 19.2 s long. The key difference between the crossed dipole and the parallel configurations was that we used condensate atoms in the $m_F = 0$ hyperfine state rather than the $m_F = -1$ state to make the BEC. In fact, only the magnetically insensitive $m_F = 0$ atoms survived in the reservoir trap and $m_F = -1$ atoms were forced out of the trap by a field gradient. In the crossed configuration, the weak axis of the reservoir trap was along the direction of the strongest field gradient in the science chamber, which was from the ion pump (see fig. 3-2). Once the BEC was loaded from the magnetic trap into the tweezers beam, we transferred the BEC atoms from the $m_F = -1$ into the $m_F = 0$ state using a Landau-Zener transfer in the main chamber[9] [100], and then translated the atoms into the science chamber. We typically transferred about one million $m_F = 0$ condensed atoms in the science chamber. By tilting a slide we lowered the reservoir trap to the location of the tweezers beam with the new condensate and merged the two. See fig. 5-5.

However, compared to the parallel configuration, the atom number in the reservoir was lower by an order of magnitude. Although we never lost all of the condensate, we only had about 100,000 atoms in the reservoir atoms during the production cycle. This was due to a rapid loss of atoms when the two traps overlapped, possibly due to three-body recombination resulting from increased density. In the crossed configuration, during the

[9]In 400 ms, we ramped a bias field to about 4 G in the main chamber for the 5 ms transfer.

merger, we have tight confinement in all directions, whereas in the parallel configuration (fig. 5-2A) the axial direction is weaker than the radial direction even during the merger. In addition, we noticed a sudden drop in the atom number, when the mechanical shutter blocking the MOT light was opened. We suspected that it might be due to residual gases released during the opening/closing of the shutter. As noted earlier, the optical trap oriented perpendicular to the tweezers beam was not as robust as in the collinear configuration due to the field gradients from the ion pump.

The collinear configuration is significantly better than the crossed-dipole configuration. Apart from the obvious fact that we had more atoms in the parallel case, the number of condensed atoms in the reservoir also *increased* after each merger, whereas it *decreased* in the crossed case due to excessive three-body recombination.

5.5 Phase of the continuous BEC

An interesting aspect of the continuous BEC is its phase. In the experiments, we have demonstrated a continuous presence of condensed atoms, but the condensate phase was not measured. Measuring the phase of a condensate is not a trivial task. Apart from an overall global phase, all condensates evolve with a phase factor $e^{-i\frac{\mu t}{\hbar}}$, and this phase will change as the chemical potential μ of the condensate changes due to the finite lifetime of the condensate. This phase diffusion due to change in atom number of a *single* condensate has never been measured. So far, the phase evolution of condensates has been traced only over sub-second time intervals [108, 167]. Also, the phase diffusion of a condensate trapped in a 2D optical lattice has been observed [104], although the dephasing was attributed to residual lattice vibration. A measurement of the phase of the continuous BEC source would require separating a small part of the source as a local oscillator, and maintaining its phase over the duration of the entire experiment. This seems to be out of the reach of current experiments.

The most interesting phase question arises during the condensate merger process. The freshly prepared condensates have a random phase relative to the condensate in the reservoir trap, and therefore, in the current experiment, the phase of the source after replenishment will be random relative to the phase before the merger. One might speculate that in the limit of a large continuously held condensate merging with a smaller condensate, the phase of the large condensate should dominate. Each replenishment would create some excitation, and relaxation would result in a condensate with a slightly modified phase, a process reminiscent of phase diffusion in an optical laser. However, quantum tunnelling of condensates between the two traps might strongly affect the overall phase if the merger process is adiabatic. Since a non-adiabatic merger might increase the induced phase excitations, it is completely unclear whether the phase of the merged condensate could be controlled and maintained to be the same as before the merger. These and other aspects of phase dispersion and diffusion

during the merger warrant further theoretical studies [168].

In principle we might be able to use the phase-coherent matter wave amplification technique [14, 169] to phase coherently replenish a stationary continuous BEC source. For example, if we had a stationary source that overlapped with the moving condensate dressed by a laser beam, light scattering could phase-coherently amplify the condensate in the reservoir using atoms from the moving condensate. In this scheme, the necessary dissipation is provided by the optical pumping process.

5.6 Discussion

The continuous BEC can easily be combined with any of the outcoupling schemes [108–110] to produce a cw atom laser. The best outcoupling scheme might be to use a pair of Bragg beams[10]. The variation of the atom number in the continuous source need not necessarily lead to intensity fluctuations of the atom laser output. By varying the intensity of the outcoupling Bragg beams with some feedback, we could compensate for the cyclic variation in the density of the continuous BEC source, thereby outcoupling a continuous atomic matter wave with constant amplitude.

In principle, multiple replenishments of a condensate could lead to a vast improvement in the size of the condensates. With an improved lifetime in the science chamber, the condensate number might increase after each merge, whereas in the current experiments it reached equilibrium after just two fillings due to the limited lifetime of 22 s. However, the accumulation of more atoms in an optical trap will increase the density, and therefore, the loss of atoms by inelastic processes. This loss could be mitigated by an increase in trap volume as was realized using cylindrical optics [18, 19]. Thus, condensates with atom number $> 10^8$ could in principle be produced. This would be larger than any condensate produced thus far using the standard combination of laser cooling and evaporative cooling.

Finally, this is the first time that a BEC has been transferred from one optical trap to another. All previous BEC manipulation experiments dealt with transferring BECs from magnetic to optical traps [6].

[10] In this experiment, we did not add any outcoupling beams, since the intensity of the atom laser output would be too small to detect using our current imaging system. We need to improve the atom number by about a factor of 10.

Chapter 6

Outlook

During my five year graduate career at MIT, the field of Bose-Einstein Condensation has grown enormously and matured as new groups and new ideas sprouted across the world. When I joined the MIT group in 1997, it was only a handful of groups in the U.S. studying BEC, but since then many more groups have begun BEC experiments both in the U.S. and in Europe and Asia. In addition, it is no longer just rubidium, sodium and lithium atoms that have condensed, but the family has increased to include hydrogen [132], potassium [170], meta-stable He^* [171, 172], and, most recently, cesium [173]. The variety of magnetic and optical trapping techniques for BEC manipulation has increased, including the realization of the all-optical BEC [135].

The field of BEC is being driven on two ends of a spectrum. One end exploring physics with minimal interactions and small atom number, which is useful for precision measurements, atom laser and atom interferometer experiments. The BEC in this case is the perfect input state for manipulation of atoms. On the other end, condensates with maximal interactions and large atom numbers are used to explore the boundary between condensed matter and atomic physics. Collective effects become important and studies of superfluidity, vortex physics, superradiance, etc. have been explored. Recently, with BEC in 3D optical lattices [174], the field is also expanding into exploring strongly correlated systems.

The addition of moving optical tweezers combined with a science chamber expands the phase space of both types of BEC experiments that can be easily accomplished. The advantage with this technique is that we need not compromise on BEC production and maintain the usual infrastructure for production, yet at the same time, we are free to put in as many experimental devices into the vacuum chamber as we wish. The turn-around time, including bakeout, for new devices is only 2-3 weeks. A high resolution imaging system can easily be implemented in the science chamber such that low atom numbers can easily be observed, for example, in magnetic waveguides that might be used for atom interferometers. The initial experiments with miniaturized magnetic waveguides [3] have shown the potential to realize full-scale atom interferometers, although they were limited by the nano-fabrication process itself [3]. Once better fabrication processes are developed, micro-manipulation of

BECs using miniaturized wires could lead to new BEC waveguide physics [153] with a scope for precision measurements [175]. In fact, it might even be possible for these waveguides to be combined with a cw-atom laser using the continuous BEC.

Another interesting area of study with the science chamber is surface effects on BECs. Quantum reflection [176, 177] of cold atoms from surfaces is a very interesting field of study, especially with condensates. Typically, the van der Waals ($-\frac{C_3}{r^3}$) and the Casimir ($\sim \frac{1}{r^4}$) surface-atom interactions are attractive such that atoms stick to the surface. However, if the atoms near the surface have very low velocities, their deBroglie wavelength is very large such that the probability of an atom to be present near the surface is very small. Hence, the atoms are reflected despite the attractive force. The typical range of the van der Waals force is around 1 μm. The characteristic scale for a BEC is its healing length, $\xi = (8\pi na)^{-1/2}$. Thus, for sodium BEC to be reflected from a surface, its healing length must be longer than a micron, which implies a condensate density less than $1.5 \times 10^{13}\text{cm}^{-3}$ and a speed of sound less than 2 mm/s. Typically, trapped condensate densities are in the range of 10^{14}cm^{-3}, and decompressing density by an order of magnitude is no easy task due to the weak dependence of the condensate density on atom number ($n \propto N^{2/5}$). The best way to reduce density is to lower the trap frequencies ($n \propto \overline{\omega}^{6/5}$), which is difficult due to the gravity. Nonetheless, under microgravity (or compensated gravity) conditions, it should be possible to observe quantum reflection of Bose condensates from surfaces. In fact, an initial experiment attempting to observe such reflection from a glass slide failed due to high condensate density and residual axial sloshing of the optically trapped condensate. If quantum reflection is indeed observed, one can hope to 'trap' condensates in a watch glass or guide them through hollow glass fibers without the condensate being destroyed.

Using condensates in the miniaturized Z-wiretrap, we produced vortices using a topological phase [5] by reversing the magnetic bias field of an Ioffe-Pritchard magnetic trap. Using this technique, we can hope to study complicated topological structures using spinor BECs such as Skyrmions, Mermin-Ho and Anderson-Toulouse vortices [178]. Quantum wavefunction engineering with BECs will produce new and interesting BEC physics, especially when combined with both optical and magnetic trapping techniques.

Finally, the collisions physics which we initially explored [1] will continue to lead to new and interesting physics. Not only can we explore the rich boundary between microscopic and macroscopic manifestation of superfluidity, we can also create entangled beams using BEC collisions [57]. These entangled beams can perhaps be combined with atom interferometers to explore issues of decoherence and quantum computing.

The field of BEC has grown enormously during my tenure at MIT. The expanding number of groups and places with BEC is just one signature of this growth. Many a times in the past, atomic physics had been pronounced dead by many important people, however, each time a new phenomenon, with new physics, has 'rescued' the field. I believe that the field of BEC is still on the verge of reaching its zenith. The best is yet to come...

Appendix A

Designs for the BEC-III vacuum chamber

This appendix includes the designs for the science chamber that were developed mainly by my colleague Todd Gustavson. The following pages contain the designs sent to Sharon Vacuum and UKAEA for making the chamber.

The chamber was constructed out of non-magnetic 304 stainless steel. The figures in this appendix are drawn to scale and all units are in inches. All flanges had clearance holes. Note that some flanges in the figures are rendered transparent to avoid obscuring hidden flanges.

Fig 1a. Trapping Chamber: Front view

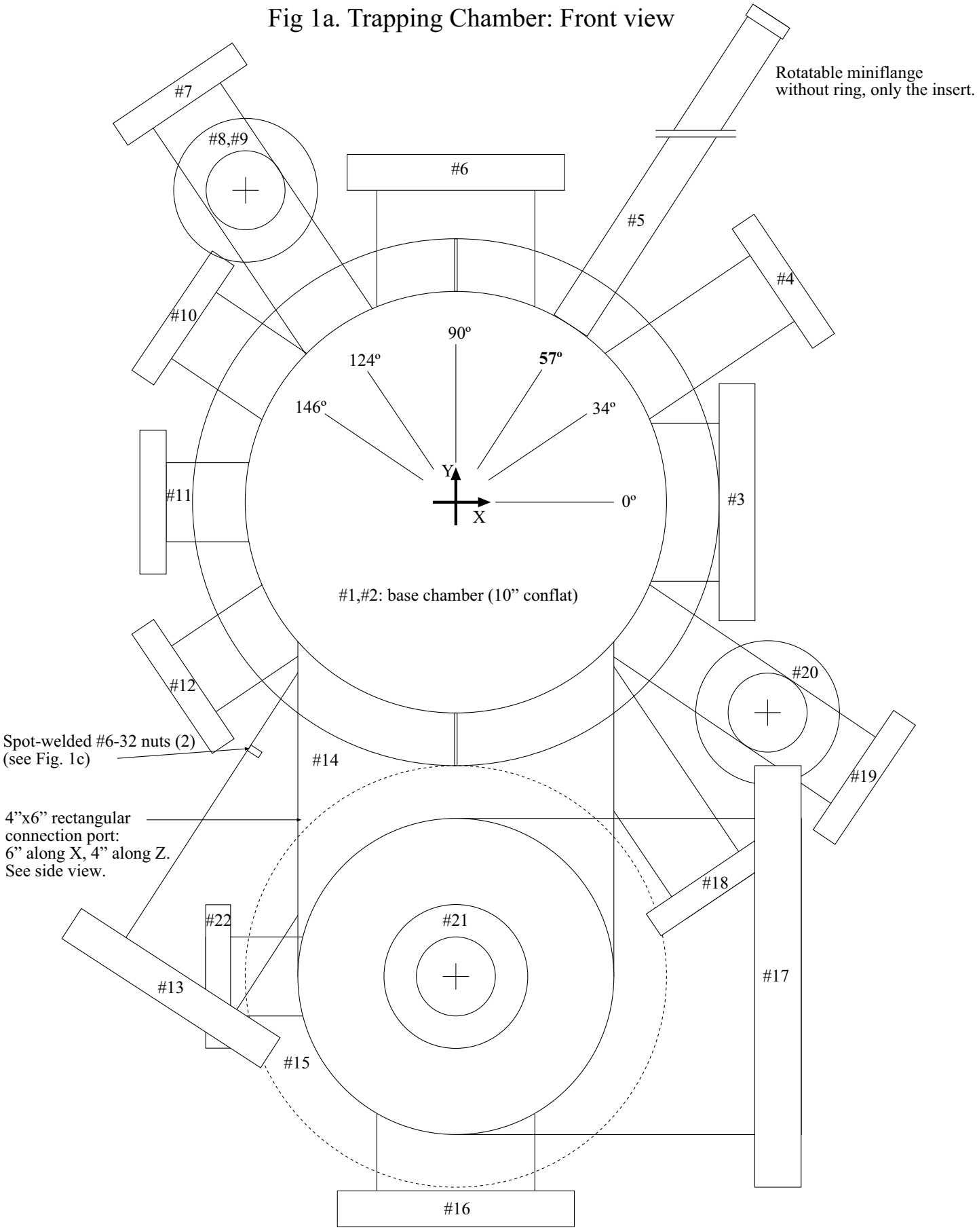

Fig 1b. Trapping Chamber: Side view

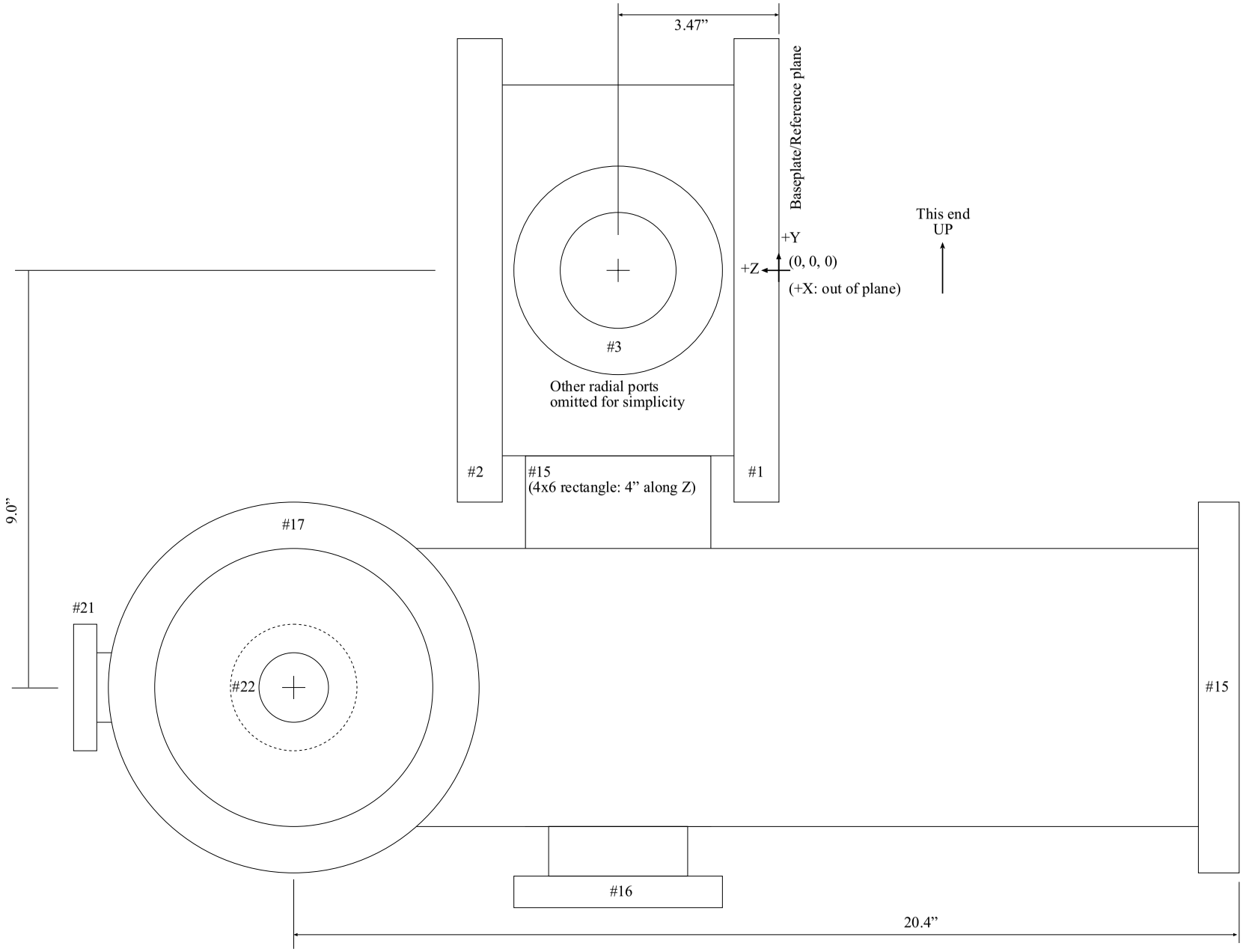

Fig.#1c Port 13 Nut spot-weld

View through Port#13 flange

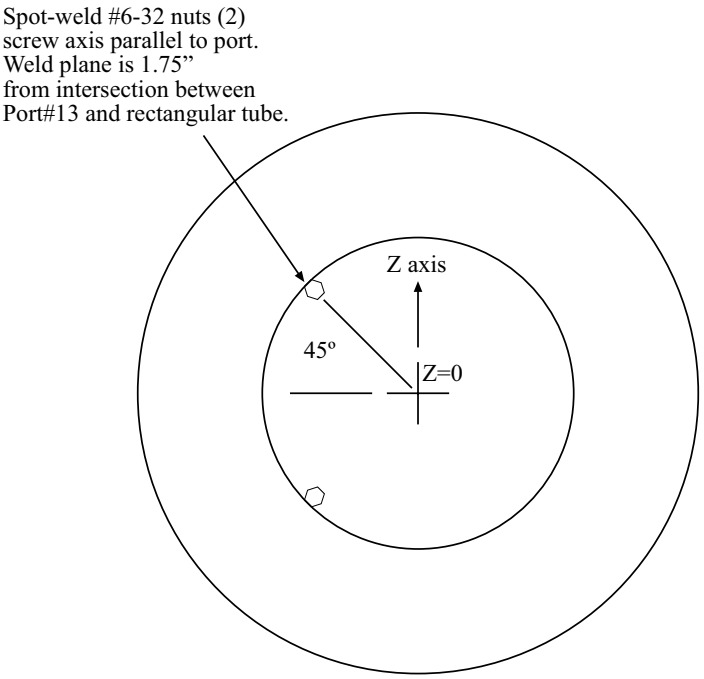

These nuts were used to attach a 2.4”diameter aluminum piece with an off-centered 1” hole. The piece prevented some of the reflected dosium atoms were entering the main chamber. See section 3.2.2.

Fig 1d. Trapping Chamber: Bottom view
Mounting lug positions

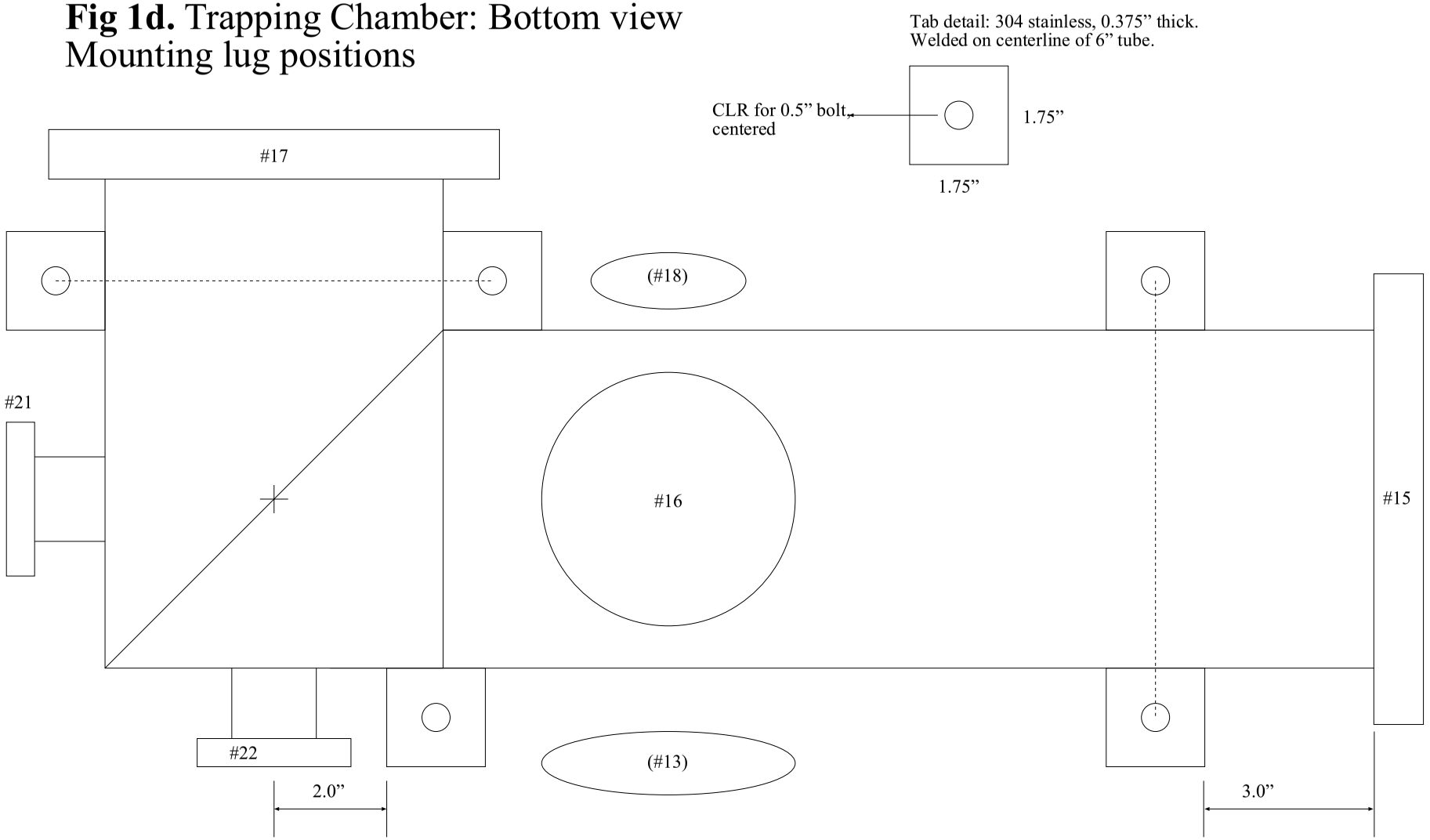

Fig. 2a Large Bucket Window
Front view (non-vacuum side)

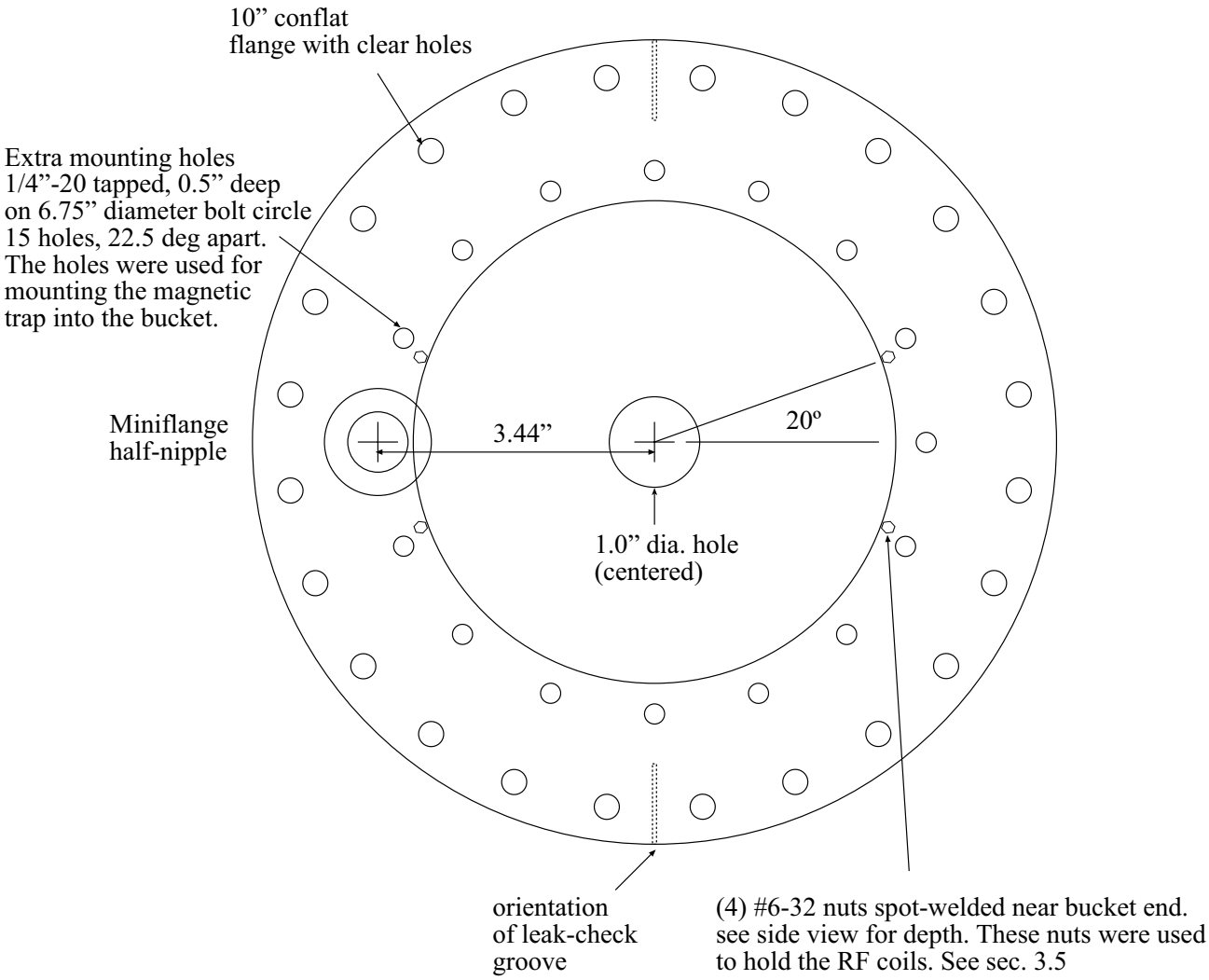

Fig.#2b Large Bucket Window: Side

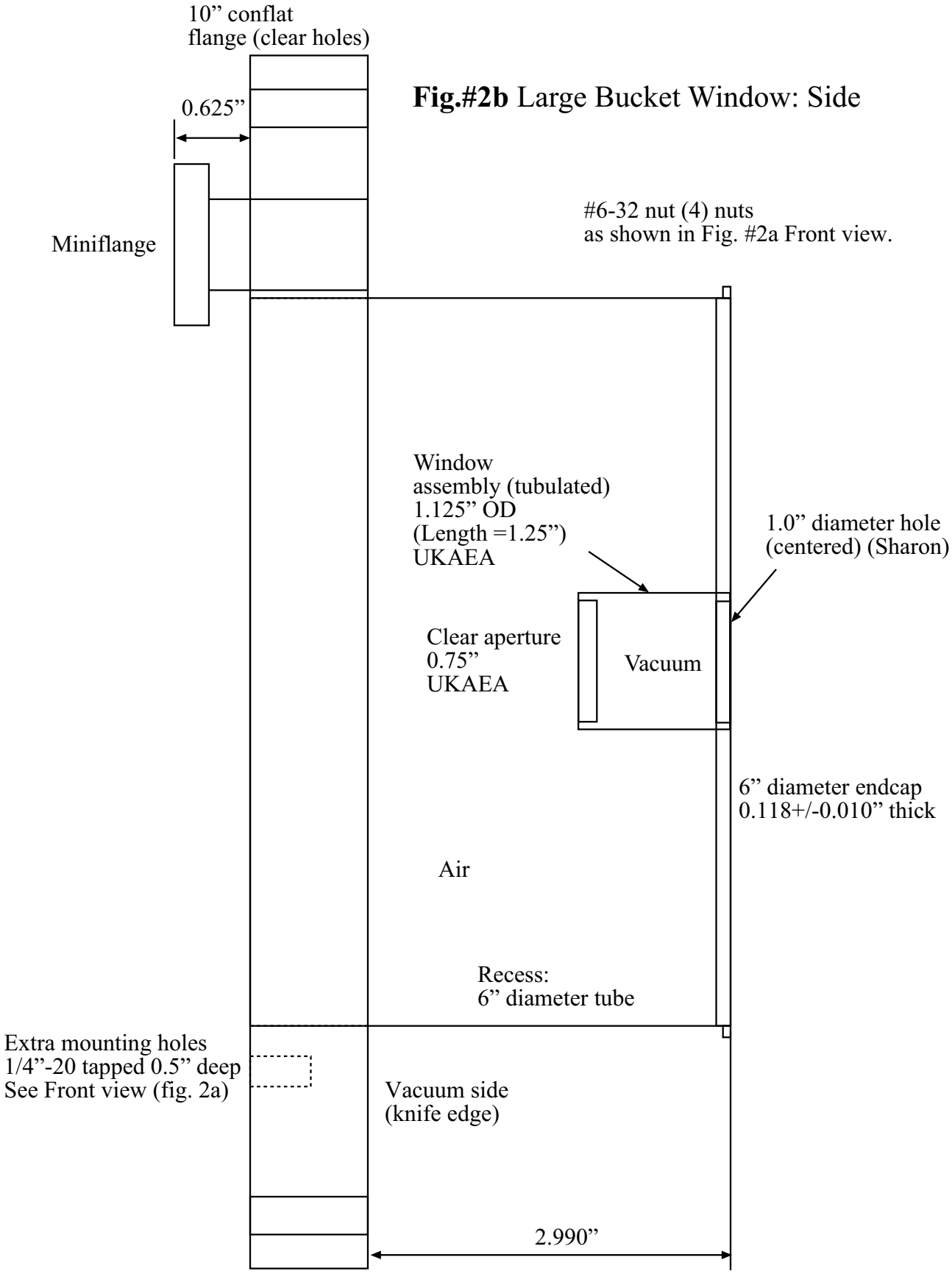

Fig 3: Recessed window (UKAEA)

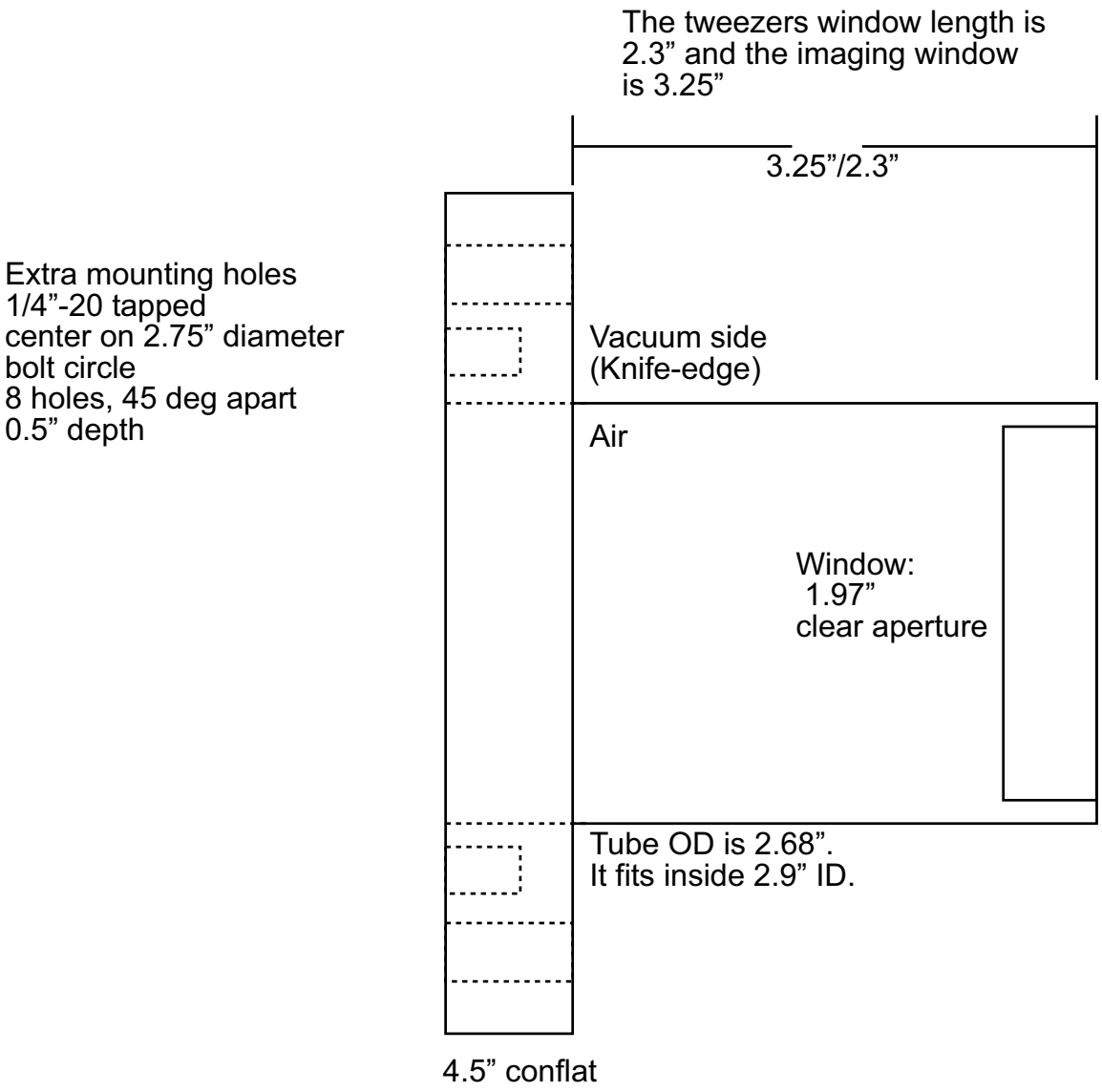

Appendix B

Designs for the Oven

This appendix includes the designs for the science chamber that were developed mainly by my colleague Deep Gupta. The following pages contain the designs sent to MIT Central Machine Shop for custom oven parts.

Fig 1a: Copper Nozzle

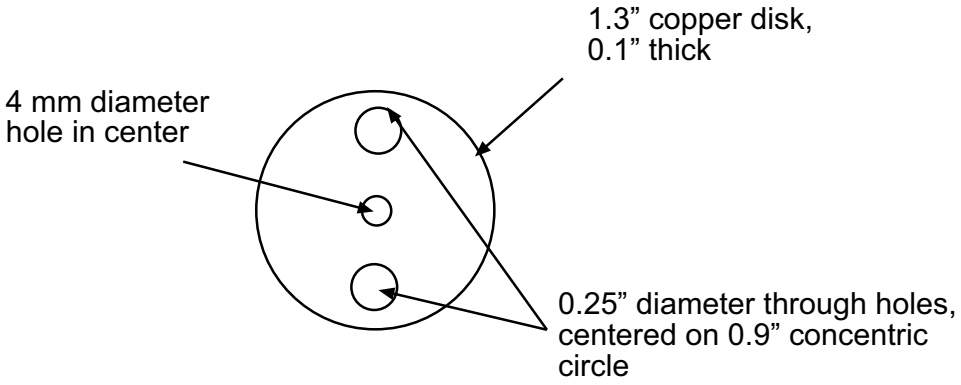

Fig 1b: 2-3/4” double sided flange for Nozzle

TOP VIEW

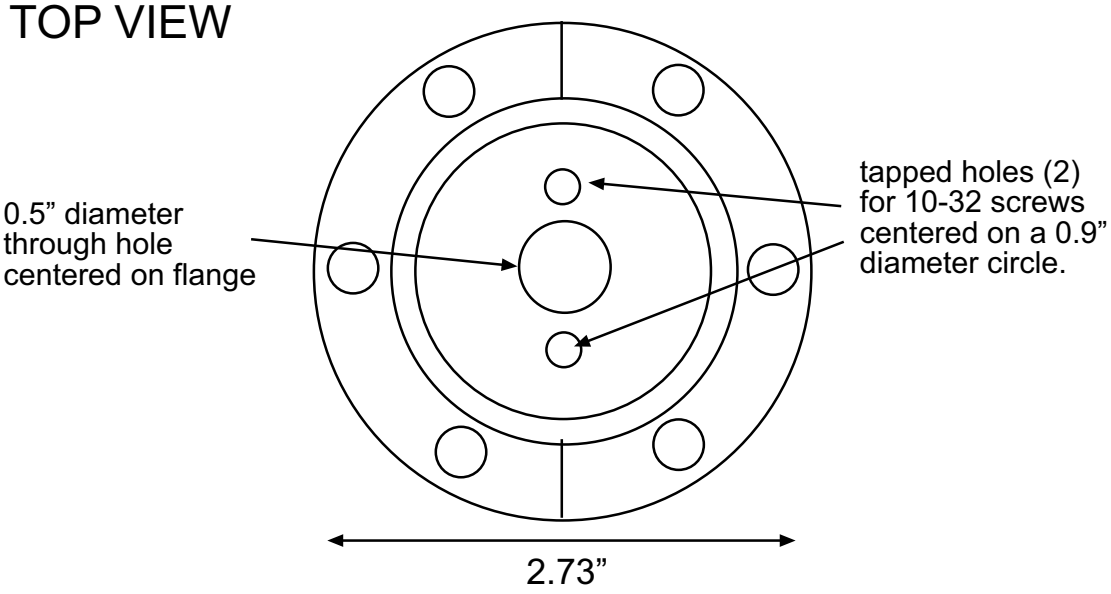

SIDE VIEW

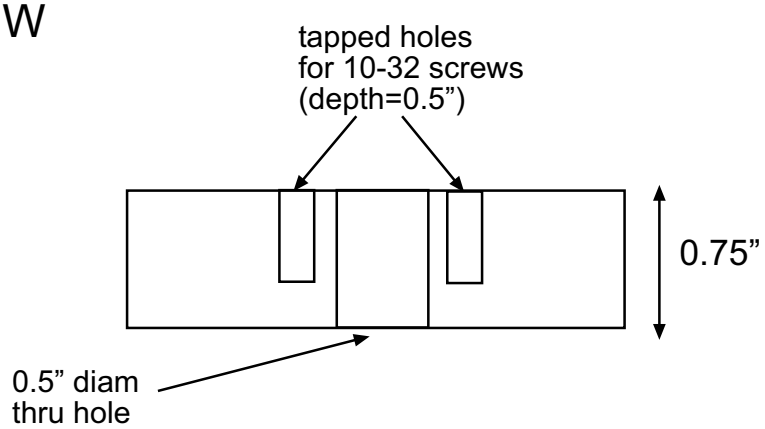

Fig 2: L-shaped copper coldplate

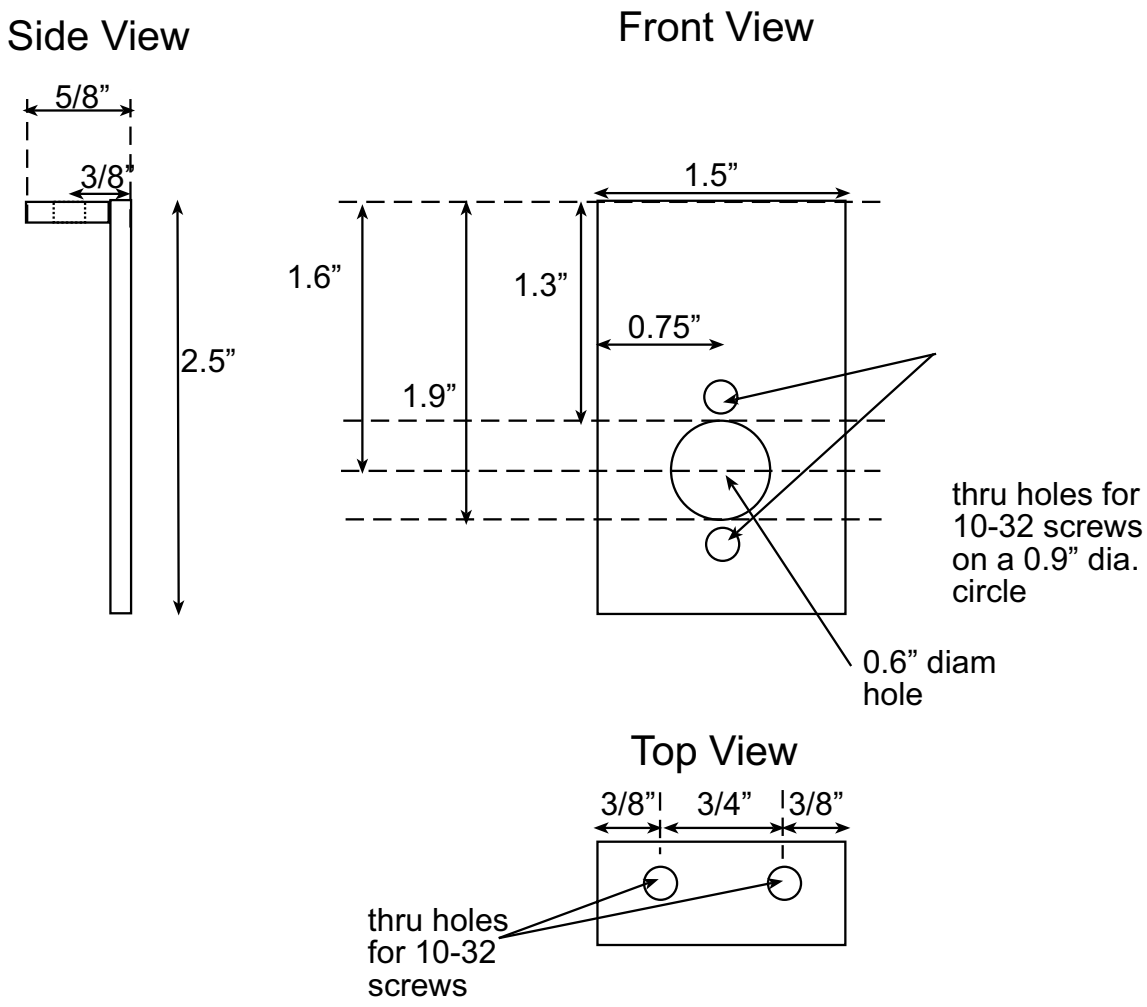

Fig 3: Copper skimmer

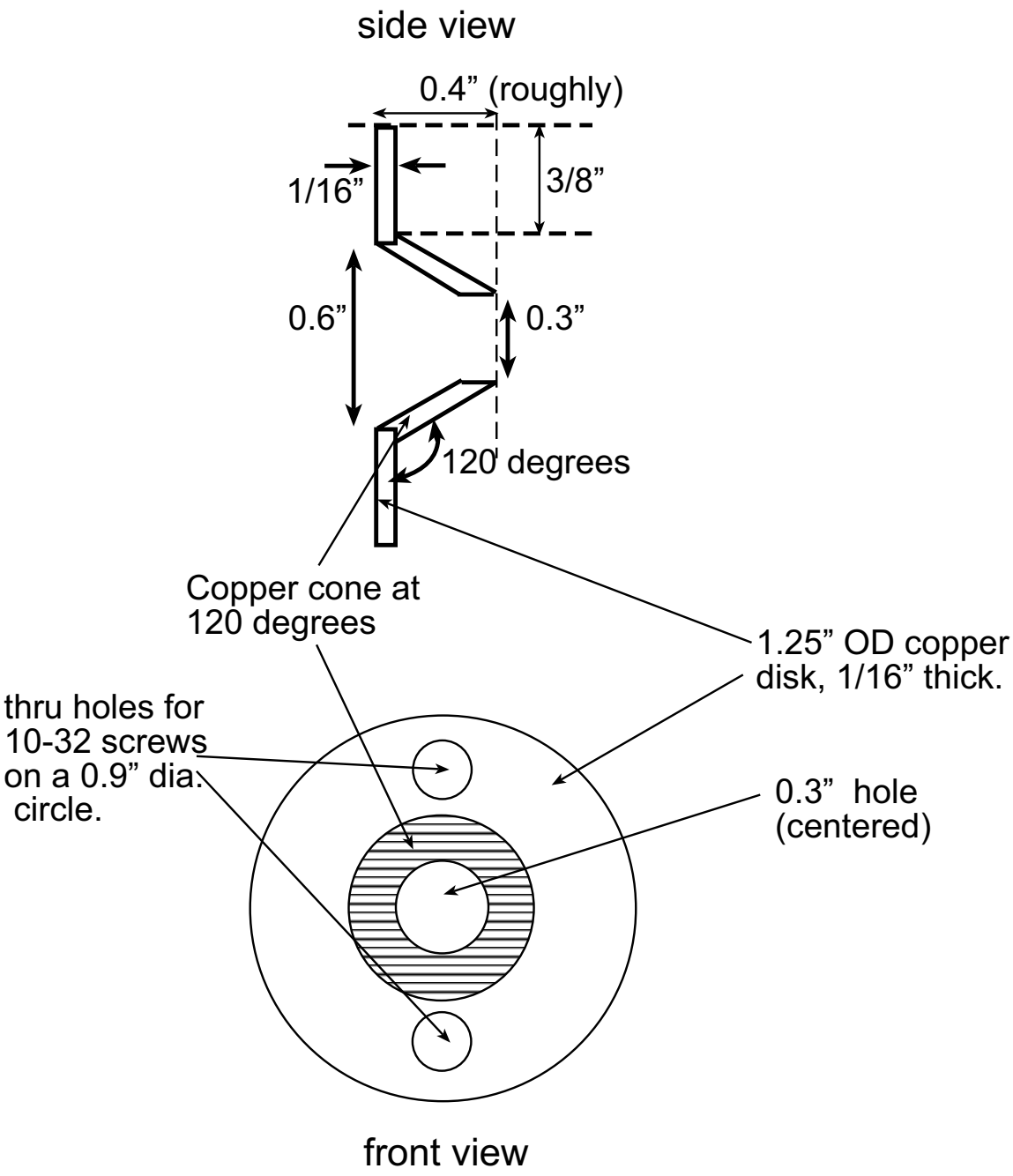

Fig 4: Cold plate feedthrough

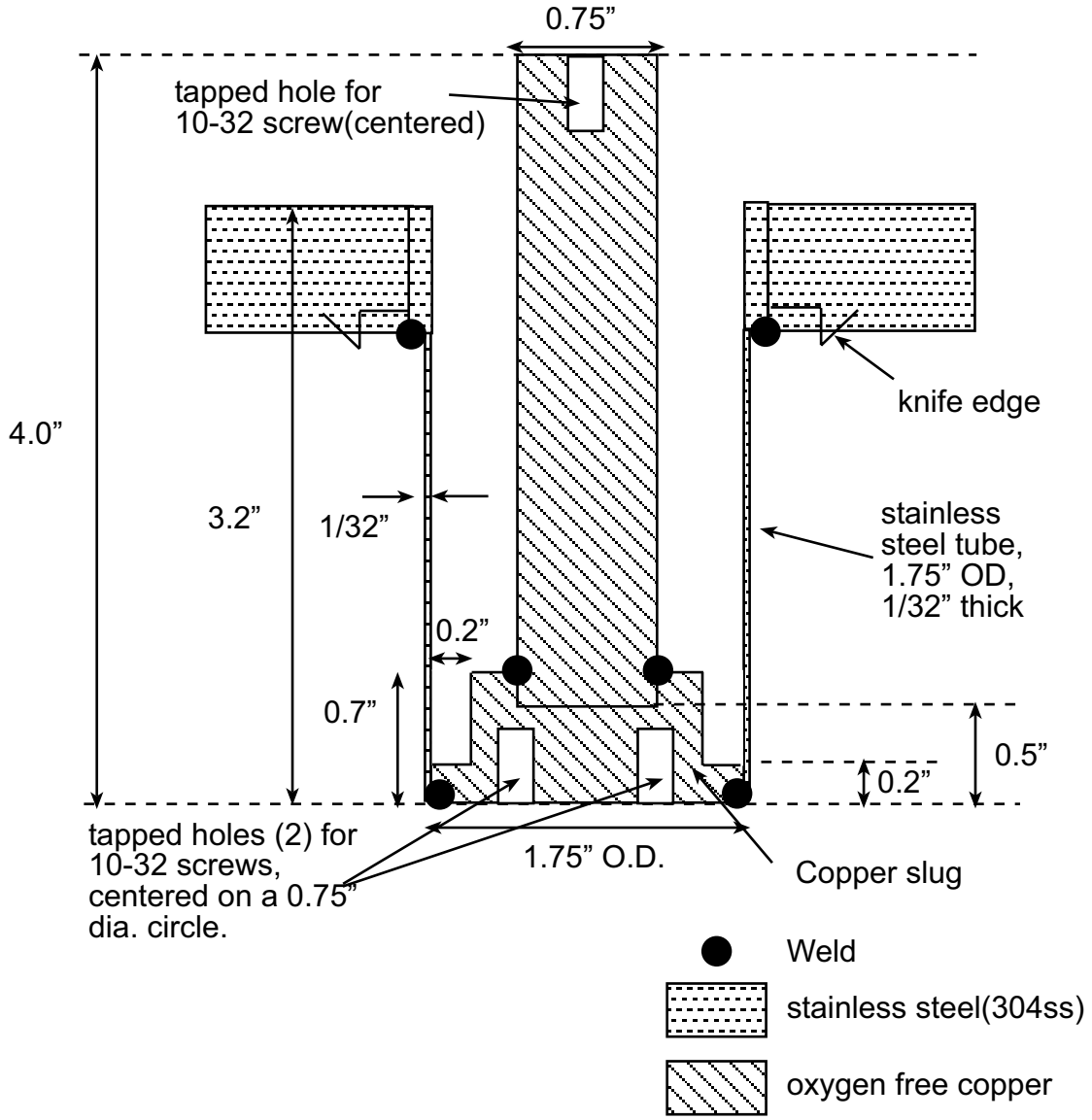

Fig 5: Differential pumping tube

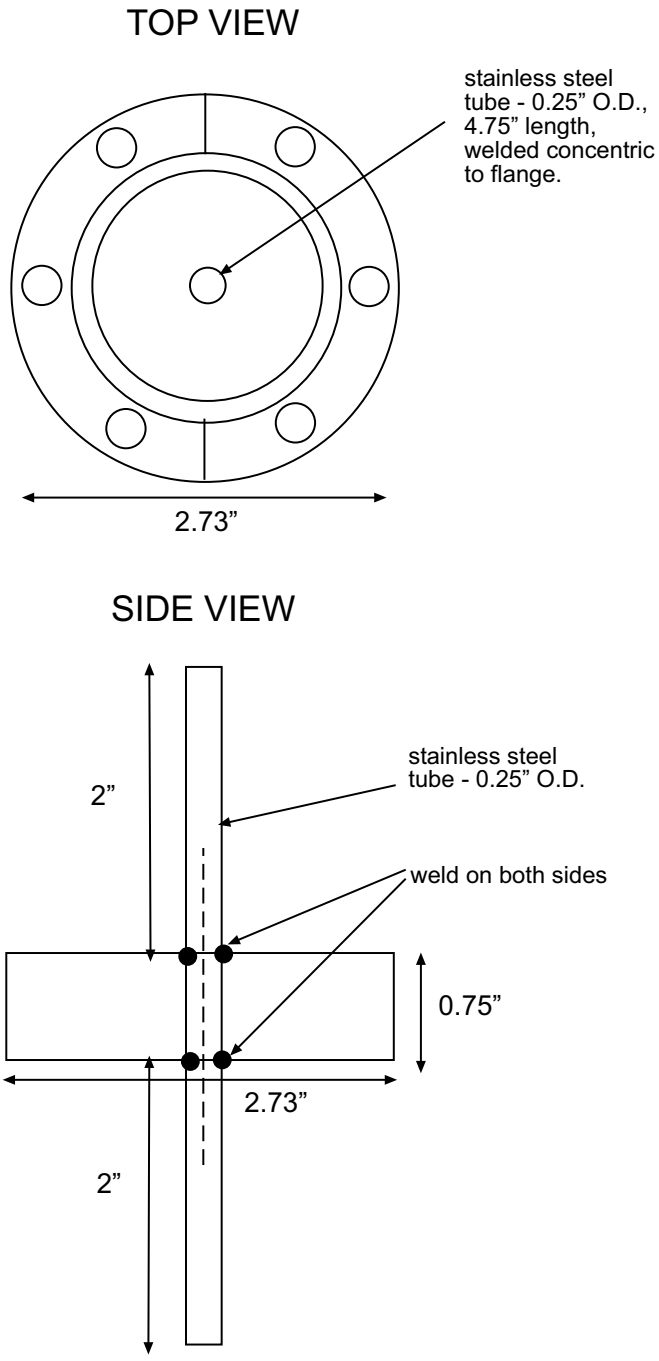

Appendix C

Companies

A few of the major companies from where we bought equipment is listed below. Wherever appropriate, contact information is given.

C.1 Vacuum hardware

1 Sharon Vacuum

The custom designed vacuum chamber (see appendix A) was built by Sharon vacuum in Massachusetts. Sharon also built the large buckets shown in fig. 2a,b of appendix A. These buckets were then sent off to UKAEA (see below) to put on the 1" windows. Sharon also built the same chamber again for BEC-IV.

Contact information:
Sharon Vacuum
69 Falmount Ave.
Brockton, MA 02301
Tel: 508-588-2323

2 UKAEA

UKAEA is based in U.K. and they made the windows with the large clear aperture. We used to them to make the bucket windows. These windows were then welded onto the buckets made by Sharon Vacuum. In addition, they made the smaller bucket windows shown in fig. 3 of appendix A. The windows were attached to steel using non-magnetic diffusion bonding.

Contact information:
Simon Hanks, External Sales Manager
UKAEA
D4/05, Culham Science Centre
Abingdon, Oxon, OX14 3DB

Tel: 011-1235-463708

3 Varian Vacuum Technologies

- Two VacIon Plus 75 L/s Noble diode ion pump, one 75 L/s Starcell ion pump (which is good when combined with a TSP) and one 55 L/s Ion pump for the slower.
- Three UHV-24p nude tungsten ionization gauges and one Bayard-Alpert (BA) ion gauge for the oven. The BA gauge is more rugged to frequent exposure to air compared to the UHV gauges.
- Controllers, cards and cables for the ion gauges and pumps.
- Three TSP filaments and one cryoshield.

4 MDC Vacuum Products Corp.

- Two pneumatically operated gate valves. Model# GV1500M-P-11 with a Kalrez seal for high temperature bake-ability (250°C in the open position).
- Four all-metal manually operated valves Model# MAV-150-VG.

5 Spectrum Thin Films

The company provided anti-reflection coatings for our vacuum windows for broadband visible and 1064 nm.

Contact information:
Spectrum Thin Films
100-E Knickerbocker Ave.
Bohemia, NY 11716
Tel: 631-589-3514

6 Insulator Seal

- Mini-flange floating shield single ended feedthrough for the RF coils. See sec. 3.5.
- KAP2 - Kapton insulated wire (single conductor) for RF coils. 0.89 mm OD and 0.61 mm wire OD. Maximum current of 5.5 A.
- 4 copper conductor (15 A max) mini-flange feedthrough for the macroscopic Z-wire trap.
- winged gaskets.

7 Cooke Vacuum

- The Chevron baffle for protecting the oven ion pump. See sec. 3.3.1.

C.2 Optics

1 Newport corporation

Newport RS4000-58-18 optical table 5' × 8' × 18".
The top skin is made of 304 stainless steel. The table is mounted on four R1-2000-410tc non-isolating 10" legs. The legs are tied together on tie-bars with have retractable casters (TBC-58).

2 Thorlabs: Various opto-mechanical elements.

C.3 Wire for solenoids

1 Small Tube Products

We used 1/8" square OD, 0.032" wall copper wire, made of copper alloy 101. It costs almost a dollar a foot and the lead time is on the order of a month.

Contact information:
Small Tube Products
PO Box 1674
Altoona, PA 16603-1674
Contact Debbie Valentino
Tel 814-695-4491(x221)

2 Essex Group Inc

The wire from Small Tube products was insulated by Essex Group using Double Dacron Glass Fuse (DDG). This increased the OD of the tube from 0.32 cm to about 0.35 cm. This cost about 30c a foot and the lead time is only a few days.

Contact Information:
Essex Group Inc.
Magnet Wire and Insulation
3201 Woodpark Blvd
Charlotte, NC 28206
Contact - Wayne
Tel: 704-598-0222

3 Dexter Corp. The white epoxy for the holding the slower solenoid and cloverleaf coils were obtained from Dexter Corp. We used Epoxi-Patch Kit 1C White, which a maximum temperature rating of 150°C. It can be obtained from a local supplier. We bought it from Industrial Sales in Tweksbury, MA.

C.4 Bakeout

1 Dycor LC100M Mass spectrometer

2 Plastics Process Inc.: Band heaters

3 Omega: Heater tapes

C.5 Powersupplies

1 Lambda EMI

2 Sorenson

3 Agilent Technologies

4 Xantrex

C.6 Translation stage

1 Aerotech Inc.

ABL20040: linear air-bearing stage with 400 mm travel required 80 psi of clean dry air. The position of the stage could be read-out using a non-contact linear encoder that is repeatable to 0.3 μm.

Contact Information:
Aerotech Inc.
101 Zeta Drive
Pittsburgh, PA 15238
Tel: 412-967-6440

2 Galil Motion Control

We bought the motion controller for the translational stage from this company.

Contact Information:
Galil Motion Control Inc.
575 Maude Court
Sunnyvale, CA 94086
Tel: 408-746-2315

3 Rock of Ages

Impala black granite surface plate: $44'' \times 10'' \times 6''$ thick. Top finish flat to $0.00012''$ with M8 threaded inserts. $\frac{1}{4} - 20$ threaded inserts on the bottom.

Contact Information:
Rock of Ages
Precision Granite Products
RR 1, Box 1140
560 Graniteville Road Graniteville, VT 05654
Tel: 802-476-2294

Appendix D

Suppression and enhancement of impurity scattering in a Bose-Einstein condensate

This appendix includes the following paper [2]: A. P. Chikkatur, A. Görlitz, D. M. Stamper-Kurn, S. Inouye, S. Gupta, and W. Ketterle, "Suppression and enhancement of impurity scattering in a Bose-Einstein condensate," *Phys. Rev. Lett.* **85**, 483-486 (2000).

Suppression and Enhancement of Impurity Scattering in a Bose-Einstein Condensate

A. P. Chikkatur, A. Görlitz, D. M. Stamper-Kurn,* S. Inouye, S. Gupta, and W. Ketterle
Department of Physics and Research Laboratory of Electronics, Massachusetts Institute of Technology, Cambridge, Massachusetts 02139
(Received 23 March 2000)

Impurity atoms propagating at variable velocities through a trapped Bose-Einstein condensate were produced using a stimulated Raman transition. The redistribution of momentum by collisions between the impurity atoms and the stationary condensate was observed in a time-of-flight analysis. The collisional cross section was dramatically reduced when the impurity velocity was reduced below the condensate speed of sound, in agreement with the Landau criterion for superfluidity. For large numbers of impurity atoms, we observed an enhancement of atomic collisions due to bosonic stimulation. This enhancement is analogous to optical super-radiance.

PACS numbers: 03.75.Fi, 34.50.–s, 67.90.+z

One manifestation of superfluidity is that objects traveling below a critical velocity v_L through a superfluid propagate without dissipation. Landau [1] used simple kinematic arguments to derive an expression for the critical velocity $v_L = \min[E(p)/p]$, where $E(p)$ is the energy of an elementary excitation with momentum p.

When superfluid ^{4}He was forced through capillaries, adsorbed films, and tightly packed powders [2], the onset of dissipation was found at velocities much lower than the Landau critical velocity due to turbulence and vortex formation in the superfluid. The Landau critical velocity can usually be observed only by moving *microscopic* particles through the superfluid which do not create a macroscopic flow pattern. Studies of superfluidity with microscopic objects were pursued in liquid ^{4}He by dragging negative ions through pressurized ^{4}He [3], and by scattering ^{3}He atoms off superfluid ^{4}He droplets [4].

Atomic Bose-Einstein condensates are superfluid gases and show phenomena analogous to superfluid liquids, albeit at 8 orders of magnitude lower density. For a homogeneous gaseous Bose-Einstein condensate, the Bogoliubov spectrum indicates a Landau critical velocity equal to the speed of sound $v_L = c \equiv \sqrt{\mu/M}$, where μ is the chemical potential and M is the mass of condensate atoms. The first evidence for a critical velocity in a Bose condensate was obtained by stirring the condensate with a *macroscopic* object (a laser beam) [5]. The observed critical velocity was much lower than the speed of sound. Recent studies of superfluidity have revealed quantized vortices [6,7] and a nonclassical moment of inertia [8].

In this Letter, we report on a study of the motion of *microscopic* impurities through a gaseous Bose-Einstein condensate. The impurity atoms were created using a stimulated Raman process which transferred a small fraction of the condensate atoms into an untrapped hyperfine state with well-defined initial velocity. As these impurities traversed the condensate, they dissipated energy by colliding with the stationary condensate, which resulted in a redistribution of momenta of the impurities. As the impurity velocity was reduced below the speed of sound, we observed a dramatic reduction in the probability of collisions, which is evidence for superfluidity in Bose-Einstein condensates.

Our experiments were performed on Bose-Einstein condensates of sodium atoms in the $|F = 1, m_F = -1\rangle$ hyperfine ground state. Condensates of $\sim 10^7$ atoms were created using laser and evaporative cooling and stored in a cylindrically symmetric magnetic trap [9] with an axial trapping frequency of 16 Hz. The density of the condensate was varied by adiabatically changing the radial trapping frequency between 165 and 33 Hz. Hence, the peak speed of sound ranged between 1.1 and 0.55 cm/s.

Impurity atoms were created using a Raman transition, in which the condensate was exposed to a pair of laser beams. The laser beams had orthogonal linear polarizations, thus driving a Raman transition from the trapped $|F = 1, m_F = -1\rangle$ state to the untrapped $|F = 1, m_F = 0\rangle$ hyperfine ground state [10]. The beams passed through two acousto-optic modulators operating with a frequency difference $\omega = \omega_{\mathrm{Zm}} + \hbar q^2/(2M)$, where $\hbar\omega_{\mathrm{Zm}}$ is the Zeeman splitting between the $|m_F = -1\rangle$ and $|m_F = 0\rangle$ states in the offset field of the magnetic trap. The momentum transfer from the light field to the $m_F = 0$ atoms is $\hbar q = 2\hbar k \sin\theta/2$, where k is the light wave vector and θ is the angle between the two laser beams. The Raman light fields were typically pulsed on for about 10 μs at an intensity of several mW/cm^2. The fraction of transferred atoms was varied by changing the light intensity.

Collisions between the impurities and the condensate were analyzed by time-of-flight absorption imaging. For this, the magnetic trap was suddenly switched off 4 ms after the Raman pulse, by which time the impurity atoms had fully traversed the condensate. After an additional 5 ms, a magnetic field gradient was pulsed on for 30 ms, spatially separating the $m_F = 0$ atoms from the condensate. After a total time of flight of typically 60 ms, all atoms were optically pumped into the $|F = 2, m_F = 2\rangle$ state and resonantly imaged on the cycling transition.

Collisions at ultracold temperatures are in the s-wave regime. The products of such collisions between free

particles are evenly distributed [11] in momentum space over a spherical shell around the center-of-mass momentum of the collision partners. A time-of-flight picture records the momentum distribution of the released cloud. Thus, collisions between the condensate and the impurities are visible as a circular halo which represents the line-of-sight integrated spherical shell. Figure 1 shows a typical absorption image of collisions in the free particle regime for impurity atoms with a velocity of $2\hbar k/M = 6$ cm/s, produced by counterpropagating Raman beams.

To probe for superfluidity, we produced impurity atoms at low velocities (7 mm/s) by using Raman beams which intersected at an angle of $\approx 14°$ and aligned symmetrically about the radial direction, so that the difference vector $\mathbf{q} = \mathbf{k_1} - \mathbf{k_2}$ was directed axially [12]. The trajectory of the impurity atoms was initially in the axial direction, but was soon modified by two forces: a downward gravitational acceleration along a radial direction (into the page in images and hereafter denoted as the z axis), and the radial mean-field repulsion of the $m_F = 0$ impurities from the $m_F = -1$ condensate.

The small axial velocity imparted by the Raman beams is crucial for distinguishing the products of elastic collisions from the unscattered impurities in time-of-flight imaging. Figure 2a shows a time-of-flight image of impurity scattering for the case of a low density condensate (small c). The axial velocity imparted by Raman scattering displaces the unscattered $m_F = 0$ atoms upward in the image, whereas collisions with the stationary condensate produce impurity atoms with smaller axial velocities which then appear below the unscattered atoms in the image. The acceleration of the impurities due to gravity and mean field precluded the observation of well-defined collision halos as shown in Fig. 1. In contrast, Fig. 2b shows a time-of-flight image for the case of a high density condensate (large c), for which the number of collided atoms is greatly diminished, indicating the suppression of impurity collisions due to superfluidity.

The number of collided atoms was determined by counting impurity atoms in a region of the time-of-flight image below the unscattered impurity atoms, which also contained Raman outcoupled thermal $m_F = 0$ atoms. Hence, the number of collided atoms in the counting region was obtained by subtracting the thermal background which was determined by counting a similar sized region above the unscattered impurity atoms where we expect few collision products. This number was doubled to obtain the total number of collided atoms since we expect only about half of the collision products to be in the counting region; the remainder was overlapped with the unscattered impurities because the distribution of unscattered atoms has an axial width roughly equal to the axial displacement of Raman scattered atoms in the time-of-flight images.

In studying these collisions, we discovered that the fraction of collided atoms increased with the number of outcoupled impurities (see Fig. 3). According to a perturbative treatment described below, the collision probability should be independent of the number of impurities. If the number of outcoupled atoms is increased, one would expect the collision probability to *decrease* slightly due to the reduction in the condensate density, or to *increase* slightly because the smaller condensate density implies a smaller critical velocity for dissipation. However, these effects are smaller (10%–20%) than the observed twofold increase in the collided fraction.

Rather, this large increase can be explained as a collective self-amplification of atomic scattering, akin to the recently observed super-radiant amplification of light scattering from a Bose-Einstein condensate [13]. Collisions between impurity atoms and the condensate transfer

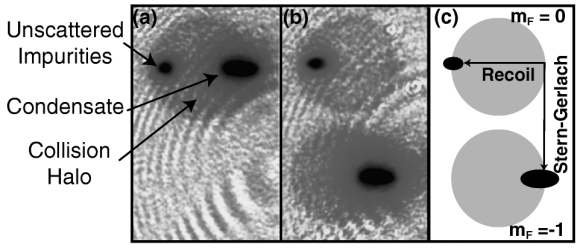

FIG. 1. Observation of s-wave halos created by elastic collisions between the condensate and impurity atoms traveling at 6 cm/s radially (right to left in images). (a) Absorption image after 50 ms of time of flight shows the velocity distribution after collisions between the condensate and the outcoupled $m_F = 0$ atoms. The collisional products are distributed over a sphere in momentum space. (b) Same as (a), but using a Stern–Gerlach-type magnetic field gradient along the condensate axis to separate the $m_F = 0$ atoms (top) from the $m_F = -1$ condensate [bottom, see (c)]. The fringes are an imaging artifact. Images are 4.5 mm × 7.2 mm. Note: the imaging axis is tilted by 45° with respect to the plane shown in (c).

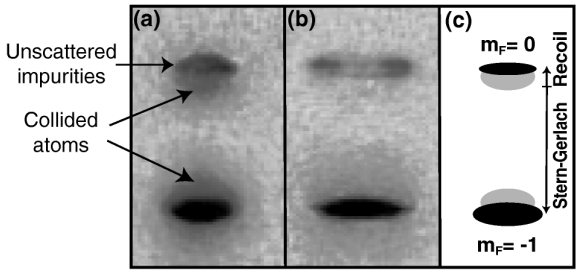

FIG. 2. Superfluid suppression of collisions. The impurity $m_F = 0$ atoms (top) traveled at 7 mm/s along the condensate axis (upward in image) and were separated from the condensate (bottom) by a magnetic field gradient applied during ballistic expansion [see (c)]. (a) Absorption image after 50 ms of time of flight shows the collisional products as indicated by the arrow. For this image, $v_g/c = 2.7$ (see text), and the collided fraction is about 20%. (b) Similar image as (a) with $v_g/c = 1.6$, where the collisions are suppressed. The outcoupled atoms (impurities) were distorted by mean-field repulsion. The images are 2.0 mm × 4.0 mm.

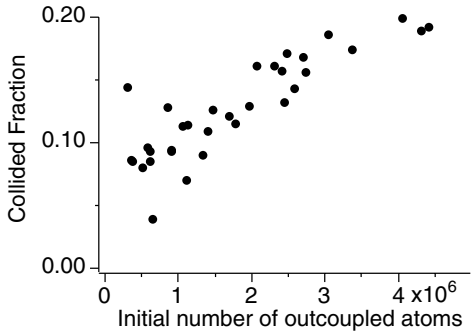

FIG. 3. Collective amplified elastic scattering in a Bose-Einstein condensate. Shown is the fraction of collided atoms vs the number of initially outcoupled atoms. For this data, $v_g/c = 4.9$ and the chemical potential was 1.8 kHz.

atoms from a macroscopically occupied initial state to final momentum states which were previously empty. The population in these final states can stimulate further scattering by bosonic enhancement and this effect increases for larger outcoupling. This collisional amplification is not directional, and is similar to the recently observed optical omnidirectional superfluorescence [14]. In contrast, the observation of four-wave mixing of atoms [15] represents the case where collisions were stimulated by a single macroscopically occupied final mode.

Figure 4 shows the decrease of collision probability as the velocity of the impurity atoms approached the speed of sound in the condensate. The collision probability was determined by averaging over many iterations of the experiment with the number of outcoupled atoms kept below 10^6 to minimize the collective enhancement. For our experimental conditions, the impurity velocity was

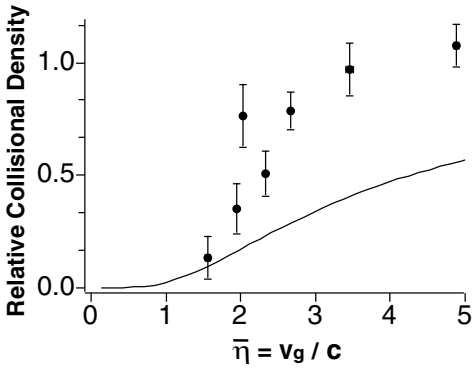

FIG. 4. Onset of superfluid suppression of collisions. Shown is the observed collisional density normalized to the predicted collisional density in the limit of high velocities C_∞ as the density of the condensate was increased (plotted from right to left). The collisional density is proportional to the collision probability of the impurities (see text). The x axis is $\overline{\eta} = v_g/c$ which is a measure of the impurity velocity over the speed of sound. The solid line is the theoretically expected collisional density calculated by a numerical integration of Eq. (1). The error bars represent the statistical uncertainty.

predominantly determined by the gravitational acceleration $g = 9.8\ \mathrm{m/s^2}$, which imparted an average velocity of $v_g = \sqrt{2gz_c}$, where z_c is the Thomas-Fermi radius of the condensate in the z direction. This downward velocity ranged from 17 mm/s for tightly confined condensates to 26 mm/s for loosely confined condensates, and was larger than the initial 7 mm/s velocity imparted by Raman scattering. Thus, the effect of superfluidity on impurity scattering depends primarily on the parameter $\overline{\eta} = v_g/c$ which is the ratio of the typical impurity velocity v_g to the speed of sound at the center of the condensate $c = \sqrt{\mu/M}$. Experimentally, $\overline{\eta}$ is determined using the radial trapping frequency and the chemical potential μ which is determined from the expansion of the condensate in the time-of-flight images [9].

Scattering of impurities from a Bose-Einstein condensate has been studied theoretically in Refs. [16,17]. The predicted cross section for collisions between an $m_F = 0$ impurity atom at momentum $\hbar\mathbf{k}$ and a $m_F = -1$ condensate of density n_0 is obtained by calculating the collision rate Γ using Fermi's golden rule:

$$\Gamma = n_0\left(\frac{\hbar a}{M}\right)^2 \int dq\, d\Omega\, q^2 S(q) \times \delta\left(\frac{\hbar\mathbf{k}\cdot\mathbf{q}}{M} - \frac{\hbar q^2}{2M} - \omega_q^B\right) = n_0\sigma(\eta)v\,,$$

Here, $S(q) = \omega_q^0/\omega_q^B$ is the static structure factor of the condensate with $\hbar\omega_q^0 = \hbar^2q^2/2M$ and $\hbar\omega_q^B = \sqrt{\hbar\omega_q^0(\hbar\omega_q^0 + 2\mu)}$ being the energies of a free particle and a Bogoliubov quasiparticle of momentum q, respectively. The collision cross section is $\sigma(\eta) = \sigma_0 F(\eta)$, where $\eta = v/c$, $v = \hbar k/M$ is the impurity velocity, and $\sigma_0 = 4\pi a_{0,-1}^2$, where $a_{0,-1} = 2.75$ nm [18] is the scattering length for s-wave collisions between the $|m_F = 0\rangle$ and $|m_F = -1\rangle$ states of sodium. For $\eta < 1$, $F(\eta) = 0$ and, for $\eta > 1$, $F(\eta) = 1 - 1/\eta^4 = \log(\eta^4)/\eta^2$.

We can approximate our experiment by considering the motion of the $m_F = 0$ atoms under the gravitational acceleration alone and ignoring the effects of the initial axial velocity and mean-field expulsion [19]. The $m_F = 0$ atoms falling through the condensate experience a collisional density $C(\eta) = \int dz\, n(x,y,z)\sigma(\eta)$, where $n(x,y,z)$ is the condensate density, and η is determined by the local condensate density and the downward impurity velocity. The collisional density relative to its value at large velocities C_∞ is given by

$$\frac{C(\overline{\eta})}{C_\infty} \approx \frac{\int d\mathbf{r}\, n_I(\mathbf{r}) \times \int dz'\, n(\mathbf{r}')\sigma_0 F(\eta)}{\int d\mathbf{r}\, n_I(\mathbf{r}) \times \int dz'\, n(\mathbf{r}')\sigma_0}\,, \qquad (1)$$

where we assume that the condensate density $n(\mathbf{r})$ is in the Thomas-Fermi limit [9] and that the initial impurity density $n_I(\mathbf{r}) \propto n(\mathbf{r})$ [20]. The solid line in Fig. 4 was determined by numerically integrating Eq. (1). To compare the collision probability for the different data points, we divided

the observed collided fraction by $C_\infty = (5/12) \times n_0 \sigma_0 z_c$. The observed decrease in the collisional density for small $\overline{\eta}$ (Fig. 4) shows the superfluid suppression of collisions. Numerical simulations ruled out the possibility that the observed decrease in collisional density could be caused solely by variations of the path length of particle trajectories due to mean-field repulsion and initial velocity.

The measured values in Fig. 4 are systematically larger by a factor of about 2 than expected theoretically. This discrepancy is also seen for impurity collisions at velocities of 6 cm/s for which superfluidity should play no role. While we cannot presently account for this systematic error in measuring absolute densities, the observation of suppression of collisions due to superfluidity is robust, since it requires only a relative comparison of collision probabilities at different $\overline{\eta}$.

The method presented here can generally be used to study ultracold collisions. In this study, we focused on collisions between atoms in different hyperfine states. By driving a Bragg transition [21] instead of a Raman transition, we have also observed collisions between atoms in the same internal state. At a velocity of 6 cm/s, we found the collision cross section to be 2.1 ± 0.3 times larger than in the Raman case, reflecting the exchange term in elastic collisions for identical particles that increases the cross section from $4\pi a^2$ to $8\pi a^2$.

Raman transitions are one way to realize output couplers for atom lasers [10,22,23]. Theoretical treatments of atom lasers have typically considered only the condensate and the outcoupled atoms in a two-mode approximation and ignored the modes accessible by collisions [24]. However, our experiment shows that, as the outcoupled atoms pass through the condensate, they collide and populate modes coupled by atomic scattering [25]; the collisions may even be enhanced by bosonic stimulation. In principle, such collisional losses can be avoided by *lowering* the density. However, an alternative route to suppressing collisions is to *increase* the density until the speed of sound is larger than the velocity of the outcoupled atoms, thus realizing a "superfluid" output coupler. Therefore, Raman transitions with small recoil or rf output couplers [22] might be most suitable for realizing atom lasers with large condensates.

In conclusion, we have studied collisions between impurity atoms and a Bose-Einstein condensate. Both the observed superfluid suppression of collisions and the collective enhancement are crucial considerations for the future development of intense atom lasers.

We are grateful to D. E. Pritchard and Y. Band for valuable discussions. This work was supported by ONR, NSF, JSEP, ARO, NASA, and David and Lucile Packard Foundation. A. P. C. acknowledges additional support from the NSF, A. G. from DAAD, and D. M. S. K. from JSEP.

*Present address: Norman Bridge Laboratory of Physics, California Institute of Technology 12-33, Pasadena, CA 91125.

[1] L. D. Landau, J. Phys. (Moscow) **5**, 71 (1941).
[2] D. R. Tilley and J. Tilley, *Superfluidity and Superconductivity* (IOP, New York, 1990), pp. 41–53.
[3] L. Meyer and F. Reif, Phys. Rev. **123**, 727 (1961); D. R. Allum, P. V. E. McClintock, A. Phillips, and R. M. Bowley, Philos. Trans. R. Soc. London A **284**, 179 (1977).
[4] J. Harms and J. P. Toennies, Phys. Rev. Lett. **83**, 344 (1999).
[5] C. Raman *et al.,* Phys. Rev. Lett. **83**, 2502 (1999).
[6] M. R. Matthews *et al.,* Phys. Rev. Lett. **83**, 2498 (1999).
[7] K. W. Madison, F. Chevy, W. Wohlleben, and J. Dalibard, Phys. Rev. Lett. **84**, 806 (2000).
[8] O. M. Marago *et al.,* Phys. Rev. Lett. **84**, 2056 (2000).
[9] W. Ketterle, D. S. Durfee, and D. M. Stamper-Kurn, in *Bose-Einstein Condensation in Atomic Gases,* Proceedings of the International School of Physics "Enrico Fermi," Course CXL, edited by M. Inguscio, S. Stringari, and C. E. Wieman (IOS Press, Amsterdam, 1999).
[10] E. W. Hagley *et al.,* Science **283**, 1706 (1999).
[11] K. Gibble, S. Chang, and R. Legere, Phys. Rev. Lett. **75**, 2666 (1995).
[12] D. M. Stamper-Kurn *et al.,* Phys. Rev. Lett. **83**, 2876 (1999).
[13] S. Inouye *et al.,* Science **285**, 571 (1999).
[14] A. I. Lvovsky, S. R. Hartmann, and F. Moshary, Phys. Rev. Lett. **82**, 4420 (1999).
[15] L. Deng *et al.,* Nature (London) **398**, 218 (1999).
[16] E. Timmermans and R. Côté, Phys. Rev. Lett. **80**, 3419 (1998).
[17] Z. Idziaszek, K. Rzazewski, and M. Wilkens, J. Phys. B **32**, L205 (1999).
[18] E. Tiesinga *et al.,* J. Res. Natl. Inst. Stand. Technol. **101**, 505 (1996); T.-L. Ho, Phys. Rev. Lett. **81**, 742 (1998).
[19] A numerical simulation showed that including these effects changes the collisional density by less than 20%.
[20] The Raman transition strength is uniform over the entire condensate since the frequency broadening due to finite pulse length (16 kHz) was larger than the broadening due to mean field ($\sim$2 kHz).
[21] J. Stenger *et al.,* Phys. Rev. Lett. **82**, 4569 (1999).
[22] M.-O. Mewes *et al.,* Phys. Rev. Lett. **78**, 582 (1997); I. Bloch, T. W. Hänsch, and T. Esslinger, Phys. Rev. Lett. **82**, 3008 (1998).
[23] B. P. Anderson and M. A. Kasevich, Science **282**, 1686 (1998).
[24] For example, R. J. Ballagh, K. Burnett, and T. F. Scott, Phys. Rev. Lett. **78**, 1607 (1997); Y. B. Band, P. S. Julienne, and M. Trippenbach, Phys. Rev. A **59**, 3823 (1999).
[25] Motivated by our results, collisions were recently included in a theoretical treatment of interaction between condensates: Y. B. Band, M. Trippenbach, J. P. Burke, Jr., and P. S. Julienne, Phys. Rev. Lett. **84**, 5462 (2000).

Appendix E

Transport of Bose-Einstein Condensates with Optical Tweezers

This appendix includes the following paper [2]: T. L. Gustavson, A. P. Chikkatur, A. E. Leanhardt, A. Görlitz, S. Gupta, D. E. Pritchard and W. Ketterle, "Transport of Bose-Einstein Condensates with Optical Tweezers" , *Phys. Rev. Lett.* **88**, 020401 (2002).

Transport of Bose-Einstein Condensates with Optical Tweezers

T. L. Gustavson, A. P. Chikkatur, A. E. Leanhardt, A. Görlitz,* S. Gupta, D. E. Pritchard, and W. Ketterle†

Department of Physics, MIT-Harvard Center for Ultracold Atoms, and Research Laboratory of Electronics, Massachusetts Institute of Technology, Cambridge, Massachusetts 02139

(Received 28 August 2001; published 21 December 2001)

We have transported gaseous Bose-Einstein condensates over distances up to 44 cm. This was accomplished by trapping the condensate in the focus of an infrared laser and translating the location of the laser focus with controlled acceleration. Condensates of order 10^6 atoms were moved into an auxiliary chamber and loaded into a magnetic trap formed by a Z-shaped wire. This transport technique avoids the optical and mechanical access constraints of conventional condensate experiments and creates many new scientific opportunities.

DOI: 10.1103/PhysRevLett.88.020401 PACS numbers: 03.75.Fi, 32.80.Pj, 39.25.+k

Since the achievement of Bose-Einstein condensation (BEC) in dilute gases of alkali atoms in 1995, intensive experimental and theoretical efforts have yielded a great deal of progress in understanding many aspects of BEC [1,2]. Bose-Einstein condensates are well-controlled ensembles of atoms useful for studying novel aspects of quantum optics, many-body physics, and superfluidity. Condensates are now used in scientific studies of increasing complexity requiring multiple optical and magnetic fields as well as proximity to surfaces.

Conventional condensate production techniques severely limit optical and mechanical access to experiments due to the many laser beams and magnetic coils needed to create BECs. This conflict between cooling infrastructure and accessibility to manipulate and study condensates has been a major restriction to previous experiments. So far, most experiments are carried out within a few millimeters of where the condensate was created. What is highly desirable is a condensate "beam line" that delivers condensates to a variety of experimental platforms. Transport of charged particles and energetic neutral particles between vacuum chambers is standard, whereas it is a challenge to avoid excessive heating for ultracold atoms. Thus far, transport of large clouds of atoms has only been accomplished with laser-cooled atoms at microkelvin temperatures [3,4]. Condensates are typically a few orders of magnitude colder and hence much more sensitive to heating during the transfer.

In this Letter, we demonstrate an application of optical tweezers that can transfer Bose condensates over distances of at least 44 cm (limited by the vacuum chamber) with a precision of a few micrometers. This separates the region of condensate production from that used for scientific studies. The "science chamber" has excellent optical and mechanical access, and the vacuum requirements in this region may well be less stringent than those necessary for production of BEC. This technique is ideally suited to deliver condensates close to surfaces, e.g., to microscopic waveguides and into electromagnetic cavities. We have used this technique to transfer condensates into a macroscopic wiretrap [5–10] located 36 cm away from the point where the condensates were produced.

An alternative but less flexible method to create condensates close to surfaces is to evaporatively cool directly in a wiretrap, as was accomplished very recently [11,12]. Recently, small condensates were also produced directly in an optical trap [13], eliminating the complexities of magnetic trapping. Although evaporation in these small traps can be very fast due to the tight confinement, the small trap volume fundamentally limits the number of condensed atoms. In contrast, the optical tweezers method combines delivery of condensates into microtraps with the well-established techniques of creating large condensates.

The experiment was carried out in a new sodium condensation apparatus that is an evolution of the original MIT design, which has been described previously [14]. The main challenge was to integrate two additional viewports for the optical tweezers into the stainless steel ultrahigh vacuum (UHV) chamber. The optical tweezers beam had to be perpendicular to gravity, due to the relatively weak axial confinement. As a result, the atomic beam and the Zeeman slower could not be arranged horizontally as in our previous BEC apparatus. The slower was placed at an angle of 33° from vertical. The magnetic trap coils were mounted outside the vacuum in recessed ports. A schematic is shown in Fig. 1. The science chamber was isolated from the trapping chamber by a gate valve that allows the science chamber to be modified or even replaced without compromising the UHV trapping chamber.

The trapping and science chambers were each pumped by separate ion and titanium sublimation pumps, reaching pressures $\simeq 10^{-11}$ torr. The oven chamber was differentially pumped relative to the trapping chamber and can support a factor of 10^5 pressure difference. The Zeeman slower combined decreasing and increasing magnetic field slowing (a so-called "spin-flip slower") and delivered $>10^{11}$ slowed atoms/s, and $\simeq 10^{10}$ atoms were loaded into a dark spontaneous force optical trap (dark-SPOT) type magneto-optical trap (MOT) after 3 s [1].

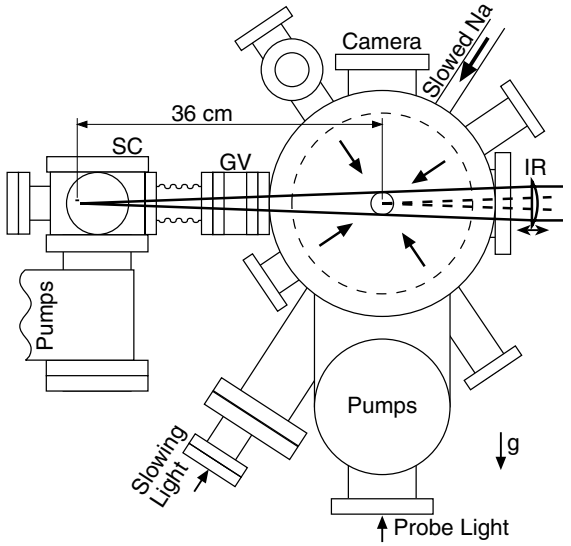

FIG. 1. Schematic of the apparatus, side view. The science chamber (labeled SC) is isolated by a gate valve (GV) from the trapping chamber. The large circle represents a 10 in. Conflat nipple and the dashed circle is the chamber wall. The magnetic trap coils are mounted in 6 in. recessed ports (not shown), bolted onto the 10 in. nipple. The central arrows represent four of the six orthogonal MOT beams. The other two MOT beams pass through the small windows indicated by the small central circle. The end of the Zeeman slower, shown at the top right, is 33° from vertical. The optical tweezers transfer beam is horizontal, with its focus shifting from the MOT position a distance of 36 cm to the Z-shaped wiretrap in the science chamber. Drawn to scale.

Atoms were transferred into an Ioffe-Pritchard–type magnetic trap wound in a cloverleaf configuration with a radial gradient of 140 G/cm, axial curvature of 100 G/cm^2, and axial bias field of 100 G. The atoms were then compressed radially in 3.5 s by reducing the axial bias field. Forced rf evaporative cooling took a total of 30 s during which the gradient field was ramped from 140 to 280 G/cm in 4.5 s for additional compression, held constant at 280 G/cm for 21 s, then finally ramped down in 4.5 s to 140 G/cm to minimize three-body loss. Typical condensates contain $(10-20) \times 10^6$ atoms, and we expect to increase these numbers with further optimization.

The condensate in the magnetic trap had to be decompressed considerably in order to reduce density dependent losses during the transfer and to improve spatial overlap with the optical tweezers (optical dipole trap), because its long axis was along the radial direction of the magnetic trap. The magnetic trap was first decompressed by increasing the axial bias field, which decreased the radial trapping frequency from 200 to 85 Hz. The condensate was further decompressed by lowering the current by a factor of 10 in both the gradient and curvature coils simultaneously.

The optical dipole trap was produced by focusing an infrared laser (1064 nm) onto the center of the magnetic trap [15]. The output of the laser was spatially filtered by a single-mode fiber and its intensity was adjusted with an acousto-optic modulator placed before the fiber. After the fiber, the beam was expanded and collimated, and then focused by a 500 mm achromatic lens placed on a translational stage. This focus was imaged onto the condensate by a relay telescope, yielding a $1/e^2$ beam waist radius at the condensate of $w_0 = 24\ \mu$m.

The condensate was transferred by ramping the infrared laser light linearly up to 180 mW in 600 ms and then suddenly switching off the decompressed magnetic trap. The infrared beam was aligned transversely to within $\sim 20\ \mu$m of the condensate. The optical trap depth is proportional to P/w_0^2, where P is the power, and was 11 μK for 180 mW [16]. The transfer efficiency into the optical trap was close to 100%. The laser light was then ramped down to 90 mW during the first second of the transfer into the science chamber, in order to minimize three-body loss. The measured optical trap frequencies at 90 mW were 4 Hz axially and 440 Hz radially.

The transport of the condensate to the science chamber was accomplished by translating the 500 mm lens. This was achieved using a linear translation stage (MICOS/Phytron No. MT-150-400-DC220) with 400 mm maximum travel, 0.5 μm encoder resolution, and 120 mm/s maximum velocity. The stage was driven by a dc brushless servo motor, chosen to minimize vibration. A feedback loop in the motor controller servoed the stage position to a trajectory specified in terms of jerk (derivative of acceleration), acceleration, velocity, and distance. Efficient transfer requires smooth, adiabatic motion. We used a trapezoidal acceleration profile that increased with constant jerk, had a flat top upon reaching maximum acceleration, and decreased at constant jerk, followed by a period of zero acceleration upon reaching maximum velocity. For deceleration, the opposite procedure was followed. Initially, we found that mechanical vibrations in the translation stage motion caused loss of atoms due to severe heating. This problem was eliminated by adding two stages of vibration isolation using rubber dampers and lead weights, which reduced the vibrations by a factor of 100.

Once accomplished, the transfer was quite robust and worked for a range of motion parameters, up to 200 mm/s^2 acceleration, 80 mm/s velocity, $\sim$1000 mm/s^3 jerk, and with transfer times as short as 4 s. The best transfer was achieved with the following maximum values: jerk = 20 mm/s^3, acceleration = 37 mm/s^2, and velocity = 70 mm/s, yielding a total transfer time of 7.5 s. Routinely we were able to transfer condensates with more than 6×10^5 atoms into the science chamber. A complete systematic study of motion parameters was not practical due to large shot-to-shot fluctuations in the number of atoms transferred. We attribute this to alignment uncertainty of the optical tweezers due to variations in the compression of the rubber vibration dampers when the stage was moved back and forth. We plan to eliminate this problem by installing a smoother translation stage.

The lifetimes of the atoms in the optical dipole trap in both the trapping and science chambers are shown in Fig. 2. In the trapping chamber, the initial loss was due to three-body decay and then the lifetime of 20 ± 2 s was limited mainly by background gas collisions. In the science chamber, the measured lifetime of 16 ± 4 s was limited by background gas collisions. The noise in the lifetime data in the science chamber was due to shot-to-shot fluctuations in the transfer. In general, the pressure and thus the background-limited lifetimes in the science and trapping chambers need not be equal, since the time required to perform experiments may be shorter than the time needed for evaporative cooling. The number of transferred atoms was about 4 times lower than the number remaining in the optical trap after simply holding atoms in the trapping chamber for 7.5 s, which implies that the loss during the translation of the condensate was comparable to the loss from the initial three-body decay. By using a large volume dipole trap with an elliptical focus in which three-body recombination is greatly diminished [17], it should be possible to deliver multimillion atom condensates. First attempts to translate such an elliptical focus failed, probably due to aberrations in the focusing optics.

To demonstrate the utility of the optical tweezers transport, we delivered condensates into a magnetic trap formed by a current I_w in a Z-shaped macroscopic wire [18,19] (diameter = 1.27 mm) and a bias field B_0 coplanar with the Z-shaped wire and orthogonal to its central segment, as shown in Fig. 3. The length of the central wire was $L = 5$ mm, and the supporting end segments were longer than 25 mm. The trap position is located at $z_0 = (\mu_0/2\pi)I_w/B_0$ below the central wire, where the external bias field is equal and opposite in direction to the magnetic field produced by the wire. The two end segments provide the axial curvature $B'' \propto B_0/L^2$ and produce a bias field at the trap bottom $B_{\rm bot} \propto (I_w z_0)/(4z_0^2 + L^2)$ [19]. The radial gradient B' is $(2\pi/\mu_0)B_0^2/I_w$, and the radial trap frequency is proportional to $B'^2/B_{\rm bot}$.

The optical trap was aligned to overlap the original condensate in the trapping chamber magnetic trap and to be about 1 mm below the wire in the science chamber. The current in the wiretrap and the current producing the bias field B_0 were linearly ramped up in 1 s. The optical trap was then slowly ramped down to zero, transferring the condensate into the magnetic wiretrap. Nearly 100% efficient transfer was achieved for $B_0 = 2.9$ G and $I_w = 2.0$ A [20]. The trap frequencies were measured to be 36.0 ± 0.8 Hz radially and 10.8 ± 0.1 Hz axially. The lifetime of the condensate in the wiretrap was measured to be 5 ± 1 s. This lifetime could probably be improved by adding a radio frequency shield to limit the trap depth [14]. By reducing the current in the wire, condensates were also moved to within a few microns from the wire surface.

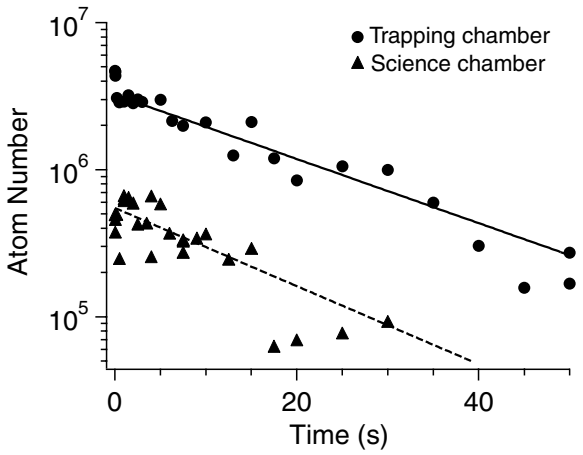

FIG. 2. Lifetime of optically confined Bose-Einstein condensates in the trapping and science chambers. The number of condensed atoms is plotted vs trapping time. Circles and triangles represent data in the trapping and science chambers, respectively. Both traps had the same characteristics with 90 mW power and trap frequencies of 4 Hz axially and 440 Hz radially. The fluctuations in the science chamber data are mainly due to alignment irreproducibilities in the translation stage (see text). The lines are exponential fits to the data. The lifetimes in the main and the science chambers were 20 ± 2 and 16 ± 4 s, respectively.

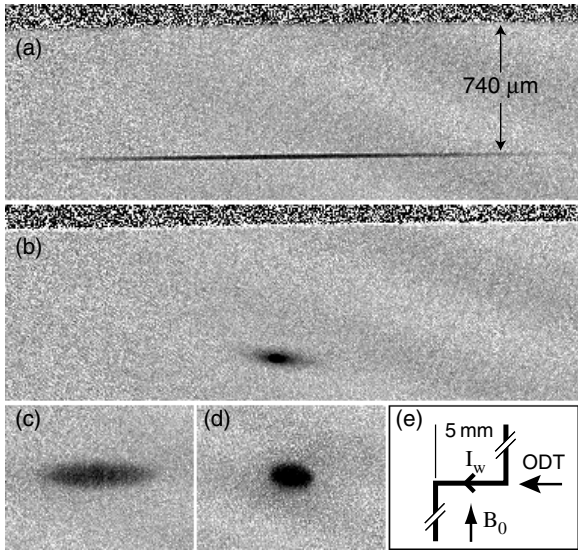

FIG. 3. Absorption images of condensates in the science chamber, side view. All images have the same scale. Condensates of $\simeq 6 \times 10^5$ atoms are shown in (a) optical trap and (b) wiretrap. The center segment of the Z-shaped wire is visible as a dark speckled horizontal strip and is 740 μm above the trapped atoms. The condensate was released from (c) an optical trap after 10 msec time of flight and (d) wiretrap after 23 ms time of flight. (e) Schematic of the wiretrap, top view. $I_w = 2$ A is the current through the wire, and $B_0 = 2.9$ G is the bias field. Atoms are trapped below the 5-mm-long central segment of the wire, which is aligned with the optical trap axis. The supporting end segments, which provide field curvature, are truncated in the figure. The wiretrap was located 36 cm from where the condensates were produced.

In conclusion, we have used an optical dipole trap as a tool for moving and manipulating condensates over a range of 44 cm, and used this tool to load atoms into a magnetic trap 36 cm away from the center of the trapping chamber. The ability to move and position condensates allows them to be produced under optimal conditions, then moved to another region to perform experiments requiring maximal optical and mechanical access. This flexibility will be important for the next generation of BEC experiments, many of which may require close proximity between condensates and other materials.

One key application that is hotly pursued by several groups is to load condensates into microfabricated magnetic waveguides built using lithographic wires on substrates, similar to integrated circuit chips [11,12,18, 21–25]. Such waveguides, analogous to fiber optics for light, may lead to improved manipulation of condensates, enabling sensitive atom interferometers. Other applications include studies of condensate-surface interactions [26,27] and experiments which require extreme magnetic shielding such as some proposed studies of spinor condensates [28,29]. Another possible application is producing a continuous atom laser. Previously demonstrated atom lasers work by depleting a single condensate [30–33]. A continuous atom laser could be produced by repeatedly transferring condensates into a reservoir from which atoms are continually outcoupled. The dipole trap could be used to transfer atoms into an optical or magnetic trap reservoir that is spatially separated from the condensate production region to avoid losses due to scattered light. Finally, one could move condensates into high finesse optical or microwave cavities.

This work was funded by ONR, NSF, ARO, NASA, and the David and Lucile Packard Foundation. A. E. L., A. P. C., and A. G. acknowledge additional support from NSF, JSEP, and DAAD, respectively. We are indebted to T. Rosenband and S. Inouye for their important contributions to the apparatus. We thank D. Schneble for a critical reading of the manuscript.

*Current address: Universität Stuttgart, 5. Physikalisches Institut, Stuttgart, Germany.

†Electronic address: http://cua.mit.edu/ketterle_group/

[1] W. Ketterle, D. Durfee, and D. Stamper-Kurn, in *Proceedings of the International School of Physics—Enrico Fermi,* edited by M. Inguscio, S. Stringari, and C. Wieman (IOS Press, Tokyo, 1999), p. 67.

[2] F. Dalfovo, S. Giorgini, L. P. Pitaevskii, and S. Stringari, Rev. Mod. Phys. **71**, 463 (1999).

[3] M. Greiner, I. Bloch, T. W. Hänsch, and T. Esslinger, Phys. Rev. A **63**, 031401 (2001).

[4] T. Kishimoto, P. Schwindt, Y.-J. Wang, W. Jhe, D. Anderson, and E. Cornell, DAMOP/DAMP Poster (London, Ontario, Canada, 2001).

[5] J. Schmiedmayer, Eur. Phys. J. D **4**, 57 (1998).

[6] J. Fortagh, A. Grossman, C. Zimmermann, and T. W. Hänsch, Phys. Rev. Lett. **81**, 5310 (1998).

[7] J. Denschlag, D. Cassettari, and J. Schmiedmayer, Phys. Rev. Lett. **82**, 2014 (1999).

[8] J. Denschlag, D. Cassettari, A. Chenet, S. Schneider, and J. Schmiedmayer, Appl. Phys. B **69**, 291 (1999).

[9] J. Fortagh, H. Ott, A. Grossman, and C. Zimmermann, Appl. Phys. B **70**, 701 (2000).

[10] M. Key, I. G. Hughes, W. Rooijakkers, B. E. Sauer, E. A. Hinds, D. J. Richardson, and P. G. Kazansky, Phys. Rev. Lett. **84**, 1371 (2000).

[11] H. Ott, J. Fortagh, G. Schlotterbeck, A. Grossmann, and C. Zimmermann, Phys. Rev. Lett. **87**, 230401 (2001).

[12] W. Hänsel, P. Hommelhoff, T. W. Hänsch, and J. Reichel, Nature (London) **413**, 498 (2001).

[13] M. D. Barrett, J. A. Sauer, and M. S. Chapman, Phys. Rev. Lett. **87**, 010404 (2001).

[14] M.-O. Mewes, M. Andrews, N. van Druten, D. Kurn, D. Durfee, and W. Ketterle, Phys. Rev. Lett. **77**, 416 (1996).

[15] D. M. Stamper-Kurn, M. R. Andrews, A. P. Chikkatur, S. Inouye, H.-J. Miesner, J. Stenger, and W. Ketterle, Phys. Rev. Lett. **80**, 2027 (1998).

[16] The counter-rotating term adds 29% more to the trap depth calculated using the rotating wave approximation.

[17] A. Görlitz *et al.,* Phys. Rev. Lett. **87**, 130402 (2001).

[18] J. Reichel, W. Hänsel, and T. W. Hänsch, Phys. Rev. Lett. **83**, 3398 (1999).

[19] A. Haase, D. Cassettari, B. Hessmo, and J. Schmiedmayer, Phys. Rev. A **64**, 043405 (2001).

[20] The residual magnetic fields in the science chamber, estimated to be about 300 mG, were not compensated.

[21] J. D. Weinstein and K. G. Libbrecht, Phys. Rev. A **52**, 4004 (1995).

[22] D. Müller, D. Z. Anderson, R. J. Grow, P. D. D. Schwindt, and E. A. Cornell, Phys. Rev. Lett. **83**, 5194 (1999).

[23] N. H. Dekker, C. S. Lee, V. Lorent, J. H. Thywissen, S. P. Smith, M. Drndić, R. M. Westervelt, and M. Prentiss, Phys. Rev. Lett. **84**, 1124 (2000).

[24] D. Cassettari, A. Chenet, R. Folman, A. Hasse, B. Hessmo, P. Krüger, T. Maier, S. Schneider, T. Calarco, and J. Schmiedmayer, Appl. Phys. B **70**, 721 (2000).

[25] R. Folman, P. Krüger, D. Cassettari, B. Hessmo, T. Maier, and J. Schmiedmayer, Phys. Rev. Lett. **84**, 4749 (2000).

[26] F. Shimizu, Phys. Rev. Lett. **86**, 987 (2001).

[27] C. Henkel and M. Wilkens, Europhys. Lett. **47**, 414 (1999).

[28] C. K. Law, H. Pu, and N. P. Bigelow, Phys. Rev. Lett. **81**, 5257 (1998).

[29] T.-L. Ho and S. K. Yip, Phys. Rev. Lett. **84**, 4031 (2000).

[30] M.-O. Mewes, M. Andrews, D. Kurn, D. Durfee, C. Townsend, and W. Ketterle, Phys. Rev. Lett. **78**, 582 (1997).

[31] B. Anderson and M. Kasevich, Science **282**, 1686 (1998).

[32] I. Bloch, T. W. Hänsch, and T. Esslinger, Phys. Rev. Lett. **82**, 3008 (1999).

[33] E. Hagley, L. Deng, M. Kozuma, J. Wen, K. Helmerson, S. Rolston, and W. Phillips, Science **283**, 1706 (1999).

Appendix F

A Continuous Source of Bose-Einstein Condensed Atoms

This appendix includes the following paper [4]: A.P. Chikkatur, Y. Shin, A. E. Leanhardt, D. Kielpinski, E. Tsikata, T. L. Gustavson, D. E. Pritchard and W. Ketterle, "A Continuous Source of Bose-Einstein Condensed Atoms", *Science* **296**, 2193 (2002).

A Continuous Source of Bose-Einstein Condensed Atoms

A. P. Chikkatur,* Y. Shin, A. E. Leanhardt, D. Kielpinski, E. Tsikata, T. L. Gustavson, D. E. Pritchard, W. Ketterle

A continuous source of Bose-Einstein condensed sodium atoms was created by periodically replenishing a condensate held in an optical dipole trap with new condensates delivered using optical tweezers. The source contained more than 1×10^6 atoms at all times, raising the possibility of realizing a continuous atom laser.

The gaseous Bose-Einstein condensate (BEC) is a macroscopic quantum system with analogies to superconductors, superfluids, and optical lasers (*1*, *2*). However, unlike these other systems, BECs have so far been only produced in pulsed mode. As with optical lasers, pulsed operation has less stringent technical requirements. In the optical domain, the leap from a pulsed ruby laser (*3*) to a more complex continuous wave (CW) helium-neon laser (*4*) took only about 6 months, whereas for atomic condensates, it has taken considerably longer to produce a continuous source of coherent atoms. Such a source is the most crucial prerequisite for realizing continuous atom lasers.

The challenge in realizing a continuous BEC source originates in the extreme parameter space covered during a typical cooling cycle required for BEC production, which consists of laser cooling followed by evaporative cooling. During optical cooling, atoms scatter around 10^7 photons/s, whereas during evaporative cooling any photon scattering would cause heating and trap loss and, therefore, has to be less than 10^{-1} photons/s. During evaporative cooling, atoms are cooled by a factor of a thousand from about 100 μK to sub-microkelvin temperatures. This requires a near-perfect isolation of the hot atoms from the cold, because a single laser-cooled atom has enough energy to knock thousands of atoms out of the condensate.

Until now, little progress has been made toward continuous Bose-Einstein condensation. Early theoretical work considered the realization of a continuous-atom laser using optical pumping of incoming atoms into the laser mode (*5*, *6*). More recently, evaporative cooling of a slow atomic beam from the typical phase-space density of laser cooling (10^{-6}) into quantum degeneracy has been suggested (*7*). Experimental work has so far only addressed the production and guiding of a beam of laser-cooled atoms (*8*–*10*).

Our approach in this work is based on our recent realization of moving optical tweezers for BECs (*11*, *12*). Here, we use the tweezers to transport sodium condensates from where they are produced into a reservoir trap. The freshly produced condensates periodically replenish the condensate in the reservoir trap, thereby continuously maintaining a condensate of more than 10^6 atoms.

Merging of two separate condensates with a random relative phase into one condensate requires dissipation to damp out the excitations caused by the merger. Assuming that the merger creates a solitonlike excitation at the interface of the two condensates, the excitation energy per atom is approximately equal to the chemical potential times the ratio of the healing length to the condensate size. In our experiment, this energy was typically on the order of a nanokelvin and could be dissipated by evaporative cooling with a only a small loss in the number of condensed atoms.

Periodic Replenishment of an Optical Trap

The continuous reservoir was an optical trap located in the "science chamber" of the experimental apparatus that has been described in detail in (*11*). Condensates were produced in the "production chamber" by a combination of laser cooling and evaporative cooling (*1*). The magnetically trapped condensate was then adiabatically decompressed and transferred into the focus of the tweezers beam (*13*). The optical traps for both the tweezers and the continuous reservoir were produced with focused infrared (1064 nm) laser beams with similar trap parameters. The intensities of the beams were controlled independently with two acousto-optic modulators, and the beams were spatially filtered by separate single-mode fibers. The laser beam for the tweezers was expanded and focused by a 500-mm achromatic lens placed on an air-bearing translation stage. Fifty mW of laser power focused to $1/e^2$ beam waist radius of $w_0 = 26$ μm created a cigar-shaped trap with a radial trapping frequency of 440 Hz and a depth of about 2.7 μ*K*. Translation of the 500-mm lens moved condensates in the focus of the tweezers beam by ~0.3 m from the production chamber into the science chamber (*11*). The condensates were transported in 1.25 s and held for 1 s to allow condensate excitations to damp out; only small residual dipole oscillations remained.

The optical axis of the laser beam for the continuous reservoir was parallel to the tweezers beam with a vertical displacement of about 70 μm, which was sufficient to ensure that the two traps did not affect each other before the merger. The vertical distance between the two traps was controlled by tilting a glass slide in the optical path of the laser beam for the reservoir (Fig. 1A). Condensates held in the tweezers beam were transferred into the reservoir by slowly lowering the reservoir trap to the position of the tweezers focus over 0.5 s (see Fig. 1, B to H). The intensity of the tweezers beam was then linearly ramped to zero in another 0.5 s, and the reservoir was raised back to its original position. Within the next 18 s, a new condensate was produced, transported into the science chamber, and merged with the condensate reservoir. This cycle was repeated many times, and thus, a continuous source of condensed atoms was realized.

The number of atoms in both optical traps was determined from absorption images taken after ballistic expansion (Fig. 1, I and J). Pure condensates with negligible thermal fraction were observed in both traps. Figure 2 demonstrates the continuous presence of more than a million condensate atoms in the reservoir. The optical tweezers delivered a fresh condensate with 2.0×10^6 atoms in each replenishment cycle. Before the merger, the number of condensed atoms in the reservoir had decayed to 1.0×10^6 atoms and grew to 2.3×10^6 atoms after the merger. These numbers were obtained from a simultaneous exponential fit for the three cycles after the first cycle (Fig. 2), with a statistical error of 0.05×10^6 atoms. Therefore, the merged condensate is significantly larger than each of the two condensates before the merger. During the 18 s production and transfer cycle, the condensate in the reservoir decayed with a $1/e$ lifetime of 22 ± 1 s, limited by background pressure.

Overcoming Technical Problems

To maintain a continuous BEC reservoir while making a new condensate, several problems had to be addressed: stray resonant light during laser cooling, stray magnetic fields during laser and evaporative cooling, fast production of condensates in the production chamber, and merging of two condensates without excessive heating and atom loss.

Stray resonant light scattered by the atoms trapped in the magneto-optical trap

Department of Physics, MIT-Harvard Center for Ultracold Atoms, and Research Laboratory of Electronics, Massachusetts Institute of Technology, Cambridge, MA 02139, USA.

*To whom correspondence should be addressed. E-mail: ananth@mit.edu

(MOT) was detrimental to the condensed atoms stored in the reservoir. This light had a direct line-of-sight to the reservoir through the 1-cm aperture separating the production and science chambers. At a distance of about 0.3 m from the MOT, an estimated 1 mW of isotropically scattered resonant light leads to photon scattering rates of several Hz, and indeed, we observed an immediate loss of the condensate in the reservoir when this light was not blocked by a mechanical shutter. The shutter consisted of a simple aluminum plate that covered the aperture between the two chambers during the 2 s that the MOT was on. It was operated with a pneumatic linear actuator using ultrahigh vacuum bellows. Unfortunately, during the motion of the shutter, some residual gases were released, which increased the background pressure, limiting the lifetime of the atoms in the science chamber to 22 s.

Due to this relatively short lifetime, the production cycle for condensates had to be shortened from the usual 35 to 12 s. This was achieved primarily by shortening the evaporation cycle from 30 to 9 s. The shortened cycle reduced the typical condensate number before the transfer into the tweezers beam to 6×10^6 atoms, which is a factor of three lower than our usual operating conditions. Nonetheless, the number of condensed atoms transported to the science chamber did not change noticeably. The smaller condensates suffered from less three-body loss during the transfer from the magnetic to the tweezers trap.

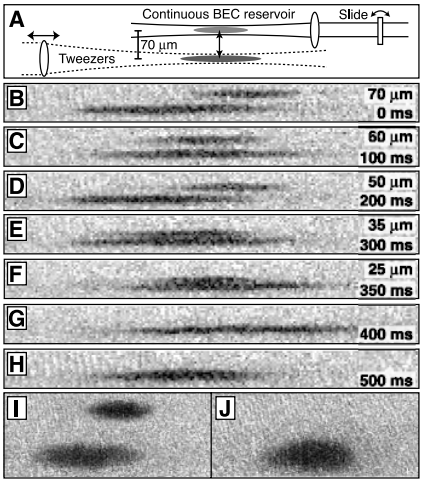

Fig. 1. Merging of two condensates. (**A**) Arrangement of the two optical traps. Both optical traps were horizontal. The focus of the tweezers beam was translated about 0.3 m from the production chamber to the science chamber. The tweezers beam placed a new condensate 70 μm below the condensate held in the reservoir. The merging of the two condensates was accomplished by tilting a glass slide, which translated the reservoir laser beam vertically. The schematic is not drawn to scale. The absorption images (**B** to **H**), taken after 2 ms of ballistic expansion, show the approach and merging of the two condensates. The distance between the two traps and the elapsed time are given. In (G) and (H), the traps overlapped. (**I**) is an absorption image before the merger with 12 ms of ballistic expansion for the condensate trapped by the tweezers and 9 ms for the condensate in the continuous reservoir. (**J**) is an absorption image after complete merger, with 12 ms of ballistic expansion. The field of view is 0.2 × 4.2 mm (B) to (H) and 0.7 × 1.7 mm (I) and (J).

It was essential to use an optical-dipole trap for the continuous condensate source, because atoms in optical traps are insensitive to stray magnetic bias fields produced during the condensate production cycle. We initially tried to hold atoms in the science chamber in a magnetic trap (*12*), but the atoms were lost when the magnetic fields for the "Zeeman slower" and the MOT were switched on and displaced the center of the magnetic trap. Another problem with a magnetic trap is its long range. Magnetic forces would accelerate the condensate in the tweezers as it approached the magnetic trap, and the new condensate would collide violently with the condensate in the reservoir. Optical traps, on the other hand, have a more limited trap volume and depth. Hence, we could bring the condensates as close as the traps' beam waist before they were affected by each other's presence.

Condensate atoms in the reservoir were immune to magnetic bias fields, but not to stray field gradients, because the atoms were in the magnetically sensitive $|F = 1, m_F = -1\rangle$ hyperfine state. However, no detrimental effects were observed during BEC production, consistent with gradient fields measured to be below 100 mG/cm. We also produced a continuous BEC source containing atoms in the magnetically insensitive $|F = 1, m_F = 0\rangle$ hyperfine state. For that, a Landau-Zener sweep (*1*) transferred condensate atoms from the $m_F = -1$ to the $m_F = 0$ state after the condensate was loaded into the tweezers beam in the production chamber. The number of condensed atoms in the reservoir trap was similar to the number measured for $m_F = -1$ atoms.

Finally, the key step in realizing a continuous condensate source was adding the freshly prepared condensates to the reservoir trap with minimal excitations of the condensate. It was critical to merge the condensates along the tightly confining radial direction. The large radial trap frequencies (>400 Hz) ensured that the merger could be done quickly and yet be almost adiabatic and that the radial excitations during the merger could be damped out quickly. The collinear arrangement and the similar trapping frequencies ensured good overlap and "mode matching" during the merger of the two traps. After careful optimization of all parameters, condensates could be merged with a 25% loss in the total atom number (Fig. 2). These losses are due partially to three-body recombination in the combined trap and partially to the dissipation of excitations caused during the merger. The finite trap depth of the optical trap ensured dissipation by evaporative cooling.

In a preliminary experiment, we showed that it was also possible to merge two condensates in a crossed dipole configuration, where the axis of the tweezers beam was perpendicular to the reservoir trap. We produced a continuous BEC source in this configuration as well, albeit with atom numbers lower by an order of magnitude. We observed rapid loss of atoms when the two traps overlapped, possibly due to three-body recombination resulting from increased density.

In principle, multiple replenishments of a condensate could lead to a vast improvement in the size of the condensates. With an improved lifetime in the science chamber, the condensate number would increase after each merge, whereas we reached equilibrium after just two fillings due to the limited lifetime of 22 s. However, the accumulation of more atoms in an optical trap will increase the density, and therefore, the loss of atoms by inelastic processes. This loss could be mitigated by an increase in trap volume, as was realized using cylindrical optics (*14*, *15*). With such improvements, it

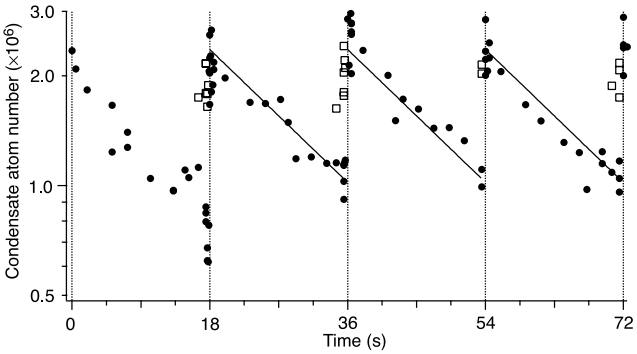

Fig. 2. A continuous source of Bose-Einstein condensed atoms. The solid circles in the semi-log plot represent the atom number in the continuous reservoir, and the open squares show the number of condensate atoms transferred from the production chamber. The dashed lines indicate the beginning of a new cycle, and the solid lines are exponentially decaying curves determined by a simultaneous fit to the three cycles after the first cycle. The number of atoms for each data point was obtained from a separate absorption image, similar to the ones in Fig. 1, I and J.

should be possible to transfer condensates containing more than 10^7 atoms and accumulate more than 10^8 atoms in the continuous source. This would be larger than any condensate produced thus far using the standard combination of laser cooling and evaporative cooling.

Outlook: Condensate Phase and CW Atom Lasers

An interesting aspect of the continuous BEC is its phase. So far, the phase evolution of condensates have been traced only over sub-second time intervals (*16*, *17*). A measurement of the phase of the continuous BEC source would require separating a small part of the source as a local oscillator and maintaining its phase over the duration of the entire experiment. Although this seems to be out of the reach of current experiments, one may speculate on how the phase would evolve during replenishment of a condensate. The freshly prepared condensates have a random phase relative to the condensate in the reservoir trap, and therefore, in the current experiment, the phase of the source after replenishment will be random relative to the phase before the merger. However, in the limit of a large continuously held condensate merging with a smaller condensate, one would expect the phase of the large condensate to dominate. Each replenishment would create some excitation, and relaxation would result in a condensate with a slightly modified phase, a process reminiscent of phase diffusion in an optical laser. This and other aspects of the merger warrant future theoretical studies, such as of phase coherence, dissipation, and the role of quantum tunnelling during the merger.

In principle, it would be possible to replenish a stationary continuous BEC source with an incoming moving condensate using phase coherent amplification (*18*, *19*). While a stationary source overlaps with a moving condensate dressed by a laser beam, light scattering could phase-coherently amplify the condensate in the reservoir using atoms from the moving condensate. In this scheme, the necessary dissipation is provided by the optical pumping process.

All atom lasers to date (*16*, *20*–*22*) have operated in a pulsed mode. Coherent streams of atoms were generated until a single condensate was completely depleted. Using our continuous BEC source, one could implement CW-outcoupling and create a truly continuous atom laser. By varying the intensity of the outcoupling field with some feedback, one could compensate for the cyclic variation in the density of the continuous BEC source, thereby outcoupling a continuous atomic-matter wave with constant amplitude. The optical analog of this configuration would be a pulsed laser that delivers photons to an external storage cavity from which a CW laser beam is then extracted. Although a long storage time for photons is not feasible, it is straightforward for atoms. Furthermore, the merger of several pulses requires dissipation and cooling, and therefore interactions, which are present between atoms, but not between photons.

Conclusion

In this work, techniques were developed to produce a new condensate in proximity to another condensate and to merge condensates. We have used these techniques to create a continuous source of Bose-Einstein condensed atoms.

References and Notes

1. W. Ketterle, D. Durfee, D. Stamper-Kurn, *Proceedings of the International School of Physics-Enrico Fermi*, M. Inguscio, S. Stringari, C. Wieman, Eds. (IOS Press, Amsterdam, 1999), pp. 67–176.
2. F. Dalfovo, S. Giorgini, L. P. Pitaevskii, S. Stringari, *Rev. Mod. Phys.* **71**, 463 (1999).
3. T. H. Maiman, *Nature* **187**, 493 (1960).
4. A. Javan, W. R. Bennett, D. Herriott, *Phys. Rev. Lett.* **6**, 106 (1961).
5. R. J. C. Spreeuw, T. Pfau, U. Janicke, M. Wilkens, *Europhys. Lett.* **32**, 469 (1995).
6. M. Olshanii, Y. Castin, J. Dalibard, *Proceedings of the 12th International Conference on Laser Spectroscopy*, M. Inguscio, M. Allegrini, A. Sasso, Eds. (World Scientific, New York, 1996), pp. 7–12.
7. E. Mandonnet *et al.*, *Eur. Phys. J. D* **10**, 9 (2000).
8. B. K. Teo, G. Raithel, *Phys. Rev. A* **63**, 031492(R) (2001).
9. P. Cren, C. F. Roos, A. Aclan, J. Dalibard, D. Guéry-Odelin (2002). Preprint, http://xxx.lanl.gov/abs/cond-mat/0203618.
10. W. Rooijakkers, M. Vengalattore, R. Conroy, M. Prentiss, personal communication.
11. T. L. Gustavson *et al.*, *Phys. Rev. Lett.* **88**, 020401 (2002).
12. A. E. Leanhardt *et al.*, (2002). Preprint, http://xxx.lanl.gov/abs/cond-mat/0203214.
13. D. M. Stamper-Kurn *et al.*, *Phys. Rev. Lett.* **80**, 2027 (1998).
14. A. Görlitz, *et al.*, *Phys. Rev. Lett.* **87**, 130402 (2001).
15. A. Görlitz *et al.*, in preparation.
16. B. Anderson, M. Kasevich, *Science* **282**, 1686 (1998).
17. D. S. Hall, M. R. Matthews, C. E. Wieman, E. A. Cornell, *Phys. Rev. Lett.* **81**, 1543 (1998).
18. S. Inouye *et al.*, *Nature* **402**, 641 (1999).
19. M. Kozuma *et al.*, *Science* **286**, 2309 (1999).
20. M.-O. Mewes *et al.*, *Phys. Rev. Lett.* **78**, 582 (1997).
21. I. Bloch, T. W. Hänsch, T. Esslinger, *Phys. Rev. Lett.* **82**, 3008 (1999).
22. E. Hagley *et al.*, *Science* **283**, 1706 (1999).

23. Funded by the Office of Naval Research, NSF, Army Research Office, NASA, and the David and Lucile Packard Foundation. A.E.L. acknowledges additional support from NSF. We thank Z. Hadzibabic for a critical reading of the manuscript.

12 April 2002; accepted 8 May 2002

Coherent Spin Oscillations in a Disordered Magnet

S. Ghosh,[1] R. Parthasarathy,[1] T. F. Rosenbaum,[1]* G. Aeppli[2]

Most materials freeze when cooled to sufficiently low temperature. We find that magnetic dipoles randomly distributed in a solid matrix condense into a spin liquid with spectral properties on cooling that are the diametric opposite of those for conventional glasses. Measurements of the nonlinear magnetic dynamics in the low-temperature liquid reveal the presence of coherent spin oscillations composed of hundreds of spins with lifetimes of up to 10 seconds. These excitations can be labeled by frequency and manipulated by the magnetic fields from a loop of wire and can permit the encoding of information at multiple frequencies simultaneously.

Magnetic solids offer arrays of quantum degrees of freedom, or spins, that interact with each other in a manner and strength ranging from the long-range ferromagnetism of iron and nickel to the nano-antiferromagnetism of vortices in high-temperature superconductors. Unfortunately, there is a large barrier to exploiting quantum effects in magnetic solids; namely, the rarity of coherence effects that can be simply manipulated and observed (*1*). In particular, it is difficult to create the magnetization oscillations corresponding to prepared superpositions of states, which are so straightforwardly created in liquid-phase nuclear magnetic resonance experiments. The "decoherence" for the solid magnets is generally attributed to disorder and to the coupling of the electronic spins to other degrees of freedom, such as nuclear spins, atomic motion, and conduction electrons. Here we describe coherence effects in a magnet, $LiHo_{0.045}Y_{0.955}F_4$, which is highly disordered but does not suffer from coupling to either conduction electrons or to atomic motions, because it is a strongly ionic insulator with the spins derived from small, nonoverlapping electronic orbitals.

[1]The James Franck Institute and Department of Physics, The University of Chicago, Chicago, IL 60637, USA. [2]NEC Research Institute, 4 Independence Way, Princeton, NJ 08540, USA.

*To whom correspondence should be addressed. E-mail: t-rosenbaum@uchicago.edu

Bibliography

[1] A. P. Chikkatur, A. Görlitz, D. M. Stamper-Kurn, S. Inouye, S. Gupta, and W. Ketterle, "Suppression and enhancement of impurity scattering in a Bose-Einstein condensate," Phys. Rev. Lett. **85**, 483 (2000).

[2] T. L. Gustavson, A. P. Chikkatur, A. E. Leanhardt, A. Görlitz, S. Gupta, D. E. Pritchard, and W. Ketterle, "Transport of Bose-Einstein Condensates with Optical Tweezers," Phys. Rev. Lett. **88**, 020401 (2002).

[3] A. E. Leanhardt, A. P. Chikkatur, D. Kielpinski, Y. Shin, T. L. Gustavson, W. Ketterle, and D. E. Pritchard, "Propagation of Bose-Einstein condensates in a magnetic waveguide," Phys. Rev. Lett. **89**, 040401 (2002).

[4] A. P. Chikkatur, Y. Shin, A. E. Leanhardt, D. Kielpinski, E. Tsikata, T. L. Gustavson, D. E. Pritchard, and W. Ketterle, "A Continuous Source of Bose-Einstein Condensed Atoms," Science **296**, 2193 (2002), published online in Science Express on May 16, 2002. http://www.sciencemag.org/cgi/content/abstract/1072825.

[5] A. E. Leanhardt, A. Görlitz, A. P. Chikkatur, D. Kielpinski, Y. Shin, D. Pritchard, and W. Ketterle, "Imprinting Vortices in a Bose-Einstein Condensate using Topological Phases," Phys. Rev. Lett. **89**, 190403 (2002).

[6] D. M. Stamper-Kurn, M. R. Andrews, A. P. Chikkatur, S. Inouye, H.-J. Miesner, J. Stenger, and W. Ketterle, "Optical confinement of a Bose-Einstein condensate," Phys. Rev. Lett. **80**, 2027 (1998).

[7] D. M. Stamper-Kurn, H.-J. Miesner, A. P. Chikkatur, S. Inouye, J. Stenger, and W. Ketterle, "Reversible formation of a Bose-Einstein condensate," Phys. Rev. Lett. **81**, 2194 (1998).

[8] J. Stenger, S. Inouye, D. M. Stamper-Kurn, H.-J. Miesner, A. P. Chikkatur, and W. Ketterle, "Spin domains in ground-state Bose-Einstein condensates," Nature **396**, 345 (1998).

[9] H.-J. Miesner, D. M. Stamper-Kurn, J. Stenger, S. Inouye, A. P. Chikkatur, and W. Ketterle, "Observation of metastable states in spinor Bose-Einstein condensates," Phys. Rev. Lett. **82**, 2228 (1999).

[10] J. Stenger, S. Inouye, A. P. Chikkatur, D. M. Stamper-Kurn, D. E. Pritchard, and W. Ketterle, "Bragg spectroscopy of a Bose-Einstein condensate," Phys. Rev. Lett. **82**, 4569 (1999).

[11] D. M. Stamper-Kurn, H.-J. Miesner, A. P. Chikkatur, S. Inouye, J. Stenger, and W. Ketterle, "Quantum tunneling across spin domains in a Bose-Einstein condensate," Phys. Rev. Lett. **83**, 661 (1999).

[12] S. Inouye, A. P. Chikkatur, D. M. Stamper-Kurn, J. Stenger, D. E. Pritchard, and W. Ketterle, "Superradiant Rayleigh scattering from a Bose-Einstein condensate," Science **285**, 571 (1999).

[13] D. M. Stamper-Kurn, A. P. Chikkatur, A. Görlitz, S. Inouye, S. Gupta, D. E. Pritchard, and W. Ketterle, "Excitation of phonons in a Bose-Einstein condensate by light scattering," Phys. Rev. Lett. **83**, 2876 (1999).

[14] S. Inouye, T. Pfau, S. Gupta, A. P. Chikkatur, A. Görlitz, D. E. Pritchard, and W. Ketterle, "Observation of phase-coherent amplification of atomic matter waves," Nature **402**, 641 (1999).

[15] R. Onofrio, C. Raman, J. M. Vogels, J. R. Abo-Shaeer, A. P. Chikkatur, and W. Ketterle, "Observation of Superfluid Flow in a Bose-Einstein Condensed Gas," Phys. Rev. Lett. **85**, 2228 (2000).

[16] A. Görlitz, A. P. Chikkatur, and W. Ketterle, "Enhancement and suppression of spontaneous emission and light scattering by quantum degeneracy," Phys. Rev. A **36**, 041601(R) (2001).

[17] S. Inouye, S. Gupta, T. Rosenband, A. P. Chikkatur, A. Görlitz, T. L. Gustavson, A. E. Leanhardt, D. E. Pritchard, and W. Ketterle, "Observation of vortex phase singularities in Bose-Einstein condensates," Phys. Rev. Lett. **87**, 080402 (2001).

[18] A. Gölitz, J. M. Vogels, A. E. Leanhardt, C. Raman, T. L. Gustavson, J. R. Abo-Shaeer, A. P. Chikkatur, S. Gupta, S. Inouye, T. Rosenband, and W. Ketterle, "Realization of Bose-Einstein condensates in lower dimensions," Phys. Rev. Lett. **87**, 130402 (2001).

[19] A. Görlitz, T. L. Gustavson, A. E. Leanhardt, R. Löw, A. P. Chikkatur, S. Gupta, S. Inouye, D. E. Pritchard, and W. Ketterle, Sodium Bose-Einstein Condensates in the F=2 State in a Large-volume Optical Trap, 2002, pre-print cond-mat/0208385.

[20] The Nobel Prize in Physics 2001;
available at http://www.nobel.se/physics/laureates/2001/.

[21] E. A. Cornell and C. E. Wieman, "Bose-Einstein Condensation in Dilute Gas: The first 70 years and some recent experiments (Nobel lecture)," Chem. Phys. Chem. **3**, 476 (2002).

[22] W. Ketterle, "When Atoms Behave as Waves: Bose-Einstein Condensation and the Atom Laser (Nobel Lecture)," Chem. Phys. Chem. **3**, 736 (2002), available at http://cua.mit.edu/ketterle_group/Projects_2002/Pubs_02/kett02_Nobel_lecture.pdf.

[23] D. Kleppner, 'Physics Today', Aug. 1997, p. 11; Jan. 1998, p. 90.

[24] W. Ketterle, *McGraw-Hill 1999 Yearbook of Science and Technology*, *companion volume to Encyclopedia of Science and Technology* (McGraw-Hill, New York, 1999), p. 43.

[25] A. Griffin, in *Bose-Einstein condensation in atomic gases*, *Proceedings of the International School of Physics Enrico Fermi, Course CXL*, edited by M. Inguscio, S. Stringari, and C. Wieman (IOS Press, Amsterdam, 1999), p. 591.

[26] D. M. Stamper-Kurn, Ph.D. thesis, Massachusetts Institute of Technology, 1999.

[27] S. Inouye, Ph.D. thesis, Massachusetts Institute of Technology, 2001.

[28] M. H. Anderson, J. R. Ensher, M. R. Matthews, C. E. Wieman, and E. A. Cornell, "Observation of Bose-Einstein Condensation in a Dilute Atomic Vapor," Science **269**, 198 (1995).

[29] K. B. Davis, M.-O. Mewes, M. A. Joffe, M. R. Andrews, and W. Ketterle, "Evaporative Cooling of Sodium Atoms," Phys. Rev. Lett. **74**, 5202 (1995).

[30] C. C. Bradley, C. A. Sackett, J. J. Tollet, and R. G. Hulet, "Evidence of Bose-Einstein Condensation in an Atomic Gas with Attractive Interactions," Phys. Rev. Lett. **75**, 1687 (1995).

[31] C. C. Bradley, C. A. Sackett, and R. G. Hulet, "Bose-Einstein Condensation of Lithium: Observation of Limited Condensate Number," Phys. Rev. Lett. **78**, 985 (1997).

[32] K. Huang, *Statistical Mechanics* (Wiley, New York, 1987).

[33] W. Pauli, "The Connection Between Spin and Statistics," Phys. Rev. **58**, 716722 (1940).

[34] F. Dalfovo, S. Giorgini, L. P. Pitaevskii, and S. Stringari, "Theory of Bose–Einstein condensation in trapped gases," Rev. Mod. Phys. **71**, 463 (1999).

[35] D. Pines and P. Nozires, *The Theory of Quantum Liquids, Vol. 1* (Addison-Wesley, Reading, MA, 1988).

[36] F. London, "The λ -phenomenon of liquid helium and the Bose-Einstein degeneracy," Nature **141**, 643 (1938).

[37] F. London, "On the Bose-Einstein Condensation," Phys. Rev. **54**, 947 (1938).

[38] J. F. Allen and A. D. Misener, "Flow of liquid helium II," Nature **141**, 75 (1938).

[39] P. Kapitza, "Viscosity of liquid helium below the λ-point," Nature **141**, 74 (1938).

[40] J. F. Allen and H. Jones, "New Phenomena Connected with Heat Flow in Helium II," Nature **141**, 243 (1938).

[41] L. Tisza, "Transport Phenomena in Helium II," Nature **141**, 913 (1938).

[42] V. P. Peshkov, Soviet Physics JETP **11**, 580 (1960).

[43] D. M. Stamper-Kurn, H.-J. Miesner, S. Inouye, M. R. Andrews, and W. Ketterle, "Collisionless and hydrodynamic excitations of a Bose-Einstein condensate," Phys. Rev. Lett. **81**, 500 (1998).

[44] N. N. Bogoliubov, "On the theory of superfluidity," J. Phys. (USSR) **11**, 23 (1947).

[45] L. Pitaevskii, "The problem of the form of the spectrum of elementary excitations of liquid helium II," Sov. Phys. JETP **12**, 155 (1960).

[46] A. Griffin, D. W. Snoke, and S. Stringari, *Bose-Einstein Condensation* (Cambridge University Press, Cambridge, 1995), (editors).

[47] C. E. Hecht, "The Possible Superfluid Behaviour of Hydrogen Atom Gases and Liquids," Physica **25**, 1159 (1959).

[48] W. C. Stwalley and L. H. Nosanow, "Possible "new" quantum systems," Phys. Rev. Lett. **36**, 910 (1976).

[49] D. G. Fried, T. C. Killian, L. Willmann, D. Landhuis, S. C. Moss, D. Kleppner, and T. J. Greytak, "Bose-Einstein Condensation of Atomic Hydrogen," Phys. Rev. Lett. **81**, 3811 (1998).

[50] H. F. Hess, "Evaporative cooling of magnetically trapped and compressed spin-polarized hydrogen," Phys. Rev. B **34**, 3476 (1986).

[51] M. Anderson, J. Ensher, M. Matthews, C. Wieman, and E. Cornell, "Observation of Bose-Einstein Condensation in a Dilute Atomic Vapor," Science **269**, 198 (1995).

[52] K. B. Davis, M.-O. Mewes, M. R. Andrews, N. J. van Druten, D. S. Durfee, D. M. Kurn, and W. Ketterle, "Bose-Einstein Condensation in a Gas of Sodium Atoms," Phys. Rev. Lett. **75**, 3969 (1995).

[53] S. Inouye, M. R. Andrews, J. Stenger, H.-J. Miesner, D. M. Stamper-Kurn, and W. Ketterle, "Observation of Feshbach resonances in a Bose-Einstein condensate," Nature **392**, 151 (1998).

[54] J. Stenger, S. Inouye, M. R. Andrews, H.-J. Miesner, D. M. Stamper-Kurn, and W. Ketterle, "Strongly enhanced inelastic collisions in a Bose-Einstein condensate near Feshbach resonances," Phys. Rev. Lett. **82**, 2422 (1999).

[55] S. Inouye, R.F.Löw, S. Gupta, T. Pfau, A. Görlitz, T. L. Gustavson, D. E. Pritchard, and W. Ketterle, "Amplification of light and atoms in a Bose-Einstein condensate," Phys. Rev. Lett. **85**, 4225 (2000).

[56] Z. Hadzibabic, C. A. Stan, K. Dieckmann, S. Gupta, M. W. Zwierlein, A. Görlitz, and W. Ketterle, "Two-Species Mixture of Quantum Degenerate Bose and Fermi Gases," Phys. Rev. Lett. **88**, 160401 (2002).

[57] J. M. Vogels, K. Xu, and W. Ketterle, "Generation of Macroscopic Pair-Correlated Atomic Beams by Four-Wave Mixing in Bose-Einstein Condensates," Phys. Rev. Lett. **89**, 020401 (2002).

[58] W. Ketterle and N. J. van Druten, in *Advances in Atomic, Molecular, and Optical Physics*, edited by B. Bederson and H. Walther (Academic Press, San Diego, 1996), Vol. 37, pp. 181–236.

[59] K. Gral, K. Rzazewski, and T. Pfau, "Bose-Einstein condensation with magnetic dipole-dipole forces," Phys. Rev. A **61**, 051601(R) (2000).

[60] S. Giovanazzi, A. Görlitz, and T. Pfau, "Tuning the dipolar interaction in quantum gases," (2002), pre-print cond-mat/0204352 v2.

[61] E. Tiesinga, C. J. Williams, P. S. Julienne, K. M. Jones, P. D. Lett, and W. D. Phillips, "A spectroscopic determination of scattering lengths for sodium atom collisions," J. Res. Natl. Inst. Stand. Technol. **101**, 505 (1996).

[62] C. Samuelis, E. Tiesinga, T. Laue, M. Elbs, H. Knckel, and E. Tiemann, "Cold atomic collisions studied by molecular spectroscopy," Phys. Rev. A **63**, 012710 (2001).

[63] M. O. Mewes, M. R. Andrews, N. J. van Druten, D. M. Kurn, D. S. Durfee, and W. Ketterle, "Bose-Einstein condensation in a tightly confining DC magnetic trap," Phys. Rev. Lett. **77**, 416 (1996).

[64] J. J. Sakurai, *Modern Quantum Mechanics* (Addison-Wesley, Reading, Massachusetts, 1994).

[65] W. Ketterle, A. Chikkatur, and C. Raman, in *Seventeenth International Conference on Atomic Physics, Florence, Italy, 2000* (American Institute of Physics, New York, 2001), pp. 337–355.

[66] W. Ketterle and S. Inouye, compte rendus de l'acadmie des sciences, Srie IV - Physique Astrophysique, vol. 2, pp. 339-380 (2001); e-print cond- mat/0101424 29.

[67] W. Ketterle and S. Inouye, "Does matter wave amplification work for fermions?," Phys. Rev. Lett. **86**, 4203 (2001).

[68] A. Einstein, "Quantentheorie des einatomigen idealen Gases. II," Sitzungsber. Preuss. Akad. Wiss. **Bericht 1**, 3 (1925).

[69] B. DeMarco, S. B. Papp, and D. S. Jin, "Pauli Blocking of Collisions in a Quantum Degenerate Atomic Fermi Gas," Phys. Rev. Lett. **86**, 5404 (2001).

[70] L. D. Landau, "The theory of superfluidity of helium II," J. Phys. (USSR) **5**, 71 (1941).

[71] A. J. Leggett, "Superfluidity," Rev. Mod. Phys. **71**, S318 (1999).

[72] D. R. Tilley and J. Tilley, *Superfluidity and Superconductivity* (IOP Publishing Ltd., New York, 1990), pp. 41–53.

[73] D. R. Allum, P. V. E. McClintock, A. Phillips, and R. M. Bowley, "The breakdown of superfluidity in Liquid ^{4}He: An experimental test of Landau's theory," Phil. Trans. R. Soc. A **284**, 179 (1977).

[74] L. Meyer and F. Reif, "Ion Motion in Superfluid Liquid Helium under Pressure," Phys. Rev. **123**, 727 (1961).

[75] T. Ellis, C. I. Jewell, and P. McClintock, "Measurement of Landau velocity in He II," Phys. Lett. **78A**, 358 (1980).

[76] N. Katz, J. Steinhauer, R. Ozeri, and N. Davidson, "Beliaev damping of quasi-particles in a Bose-Einstein condensate," (2002), pre-print cond-mat/0206234.

[77] E. Timmermans and R. Côtê, "Superfluidity in Sympathetic Cooling with Atomic Bose-Einstein Condensates," Phys. Rev. Lett. **80**, 3419 (1998).

[78] C. Raman, M. Khl, R. Onofrio, D. S. Durfee, C. E. Kuklewicz, Z. Hadzibabic, and W. Ketterle, "Evidence for a critical velocity in a Bose-Einstein condensed gas," Phys. Rev. Lett. **83**, 2502 (1999).

[79] T. Frisch, Y. Pomeau, and S. Rica, "Transition to Dissipation in a Model of Superflow," Phys. Rev. Lett. **69**, 1644 (1992).

[80] M. Crescimanno, C. G. Koay, R. Peterson, and R. Walsworth, "Analytical Estimate of the Critical Velocity for Vortex Pair Creation in Trapped Bose Condensates," Phys. Rev. A **62**, 063612 (2000).

[81] B. Jackson, J. F. McCann, and C. S. Adams, "Dissipation and Vortex Creation in Bose-Einstein Condensed Gases," Phys. Rev. A **61**, 051603(R) (2000).

[82] F. Chevy, K. W. Madison, V. Bretin, and J. Dalibard, "Interferometric detection of a single vortex in a dilute Bose-Einstein condensate," Phys. Rev. A **64**, 031601(R) (2001).

[83] K. W. Madison, F. Chevy, V. Bretin, and J. Dalibard, "Stationary States of a Rotating Bose-Einstein Condensate: Routes to Vortex Nucleation," Phys. Rev. Lett. **86**, 4443 (2001).

[84] S. Sinha and Y. Castin, "Dynamic instability of a rotating Bose-Einstein condensate," Phys. Rev. Lett. **87**, 190402 (2001).

[85] J. R. Anglin, "Local Vortex Generation and the Surface Mode Spectrum of Large Bose-Einstein Condensates," Phys. Rev. Lett. **87**, 240401 (2001).

[86] K. W. Madison, F. Chevy, W. Wohlleben, and J. Dalibard, "Vortex formation in a stirred Bose-Einstein condensate," Phys. Rev. Lett. **84**, 806 (2000).

[87] J. R. Abo-Shaeer, C. Raman, J. M. Vogels, and W. Ketterle, "Observation of Vortex Lattices in Bose-Einstein Condensates," Science **292**, 476 (2001).

[88] S. Gupta, A. Leanhardt, A. Cronin, and D. Pritchard, compte rendus de l'acadmie des sciences, Srie IV - Physique Astrophysique, vol. 2, pp. 479-479 (2001).

[89] M. R. Andrews, C. G. Townsend, H.-J. Miesner, D. S. Durfee, D. M. Kurn, and W. Ketterle, "Observation of interference between two Bose condensates," Science **275**, 637 (1997).

[90] L. Deng, E. W. Hagley, J. Wen, M. Trippenbach, Y. Band, P. S. Julienne, J. E. Simsarian, K. Helmerson, S. L. Rolston, and W. D. Phillips, "Four-wave mixing with matter waves," Nature **398**, 218 (1999).

[91] Z. Idziaszek, K. Rzazewski, and M. Wilkens, "Scattering of Atoms on the Bose-Einstein condensate," J. Phys. B **32**, L205 (1999).

[92] R. J. Ballagh, K. Burnett, and T. F. Scott, "Theory of an output coupler for a trapped Bose-Einstein condensate," Phys. Rev. Lett. **78**, 1607 (1997).

[93] Y. B. Band, P. S. Julienne, and M. Trippenbach, "Radio-frequency output coupling of the Bose-Einstein condensate," Phys. Rev. A **59**, 3823 (1999).

[94] Y. B. Band, M. Trippenbach, J. P. Burke, and P. S. Julienne, "Elastic Scattering Loss of Atoms from Colliding Bose-Einstein Condensate Wave Packets," Phys. Rev. Lett. **84**, 5462 (2000).

[95] M. Trippenbach, Y. Band, and P. Julienne, "Theory of four-wave mixing of matter waves from a Bose-Einstein condensate," Phys. Rev. A **62**, 023608 (2000).

[96] Y. Castin and R. Dum, "Bose-Einstein condensation in time dependent traps," Phys. Rev. Lett. **77**, 5315 (1996).

[97] A. J. Leggett, "Bose-Einstein condensation in the alkali gases: Some fundamental concepts," Rev. Mod. Phys. **73**, 307 (2001).

[98] V. Yurovsky, "Quantum effects on dynamics of instabilities in Bose-Einstein condensates," Phys. Rev. A **65**, 033605 (2002).

[99] F. Zambelli, L. Pitaevskii, D. M. Stamper-Kurn, and S. Stringari, "Dynamic structure factor and momentum distribution of a trapped Bose gas," Phys. Rev. A **61**, 063608 (2000).

[100] W. Ketterle, D. S. Durfee, and D. M. Stamper-Kurn, in *Bose-Einstein condensation in atomic gases*, *Proceedings of the International School of Physics Enrico Fermi, Course CXL*, edited by M. Inguscio, S. Stringari, and C. Wieman (IOS Press, Amsterdam, 1999), pp. 67–176.

[101] A. I. Lvovsky and S. R. Hartmann, "Omnidirectional Superfluoresence," Phys. Rev. Lett. **82**, 4420 (1999).

[102] A. Montina, "Impurity Scattering in a Bose-Einstein Condensate at finite temperature," (2002), pre-print cond-mat/0204129.

[103] M. Trippenbach, Y. Band, and P. Julienne, "Four-wave mixing in scattering of Bose-Einstein condensates," Opt. Express **3**, 530 (1998).

[104] M. Greiner, I. Bloch, O. Mandel, T. W. H"ansch, and T. Esslinger, "Exploring Phase Coherence in a 2D Lattice of Bose-Einstein Condensates," Phys. Rev. Lett. **87**, 160405 (2001).

[105] H. Pu and P. Meystre, "Creating Macroscopic Atomic Einstein-Podolsky-Rosen States from Bose-Einstein Condensates," Phys. Rev. Lett. **85**, 3987 (2000).

[106] L.-M. Duan, A. Srensen, J. I. Cirac, and P. Zoller, "Squeezing and Entanglement of Atomic Beams," Phys. Rev. Lett. **85**, 3991 (2000).

[107] M.-O. Mewes, M. Andrews, D. Kurn, D. Durfee, C. Townsend, and W. Ketterle, "Output Coupler for Bose-Einstein Condensed Atoms," Phys. Rev. Lett. **78**, 582 (1997).

[108] B. Anderson and M. Kasevich, "Macroscopic Quantum Interference from Atomic Tunnel Arrays," Science **282**, 1686 (1998).

[109] I. Bloch, T. W. Hänsch, and T. Esslinger, "Atom Laser with a cw Output Coupler," Phys. Rev. Lett. **82**, 3008 (1999).

[110] E. Hagley, L. Deng, M. Kozuma, J. Wen, K. Helmerson, S. Rolston, and W. Phillips, "A Well-Collimated Quasi-Continuous Atom Laser," Science **283**, 1706 (1999).

[111] M. R. Matthews, B. P. Anderson, P. C. Haljan, D. S. Hall, C. E. Wieman, and E. A. Cornell, "Vortices in a Bose-Einstein Condensate," Phys. Rev. Lett. **83**, 2498 (1999).

[112] P. Engels, I. Coddington, P. C. Haljan, and E. A. Cornell, "Nonequilibrium effects of anisotropic compression applied to vortex lattices in Bose-Einstein condensates," (2002), pre-print cond-mat/0204449.

[113] S. Burger, F. S. Cataliotti, C. Fort, F. Minardi, and M. Inguscio, "Superfluid and Dissipative Dynamics of a Bose-Einstein Condensate in a Periodic Optical Potential," Phys. Rev. Lett. **86**, 4447 (2001).

[114] G. Astrakharchik, J. Boronat, J. Casulleras, and S. Giorgini, "Superfluidity vs Bose-Einstein condensation in a Bose gas with disorder," (2001), pre-print cond-mat/0111165.

[115] I. Mazets, "Quantum acoustic bremsstrahlung of impurity atoms in a Bose–Einstein condensate," (2002), pre-print cond-mat/0205235.

[116] A. Montina, "Thermalization of an impurity cloud in a Bose-Einstein condensate," (2002), pre-print cond-mat/0205474.

[117] M. Greiner, I. Bloch, T. W. Hänsch, and T. Esslinger, "Magnetic transport of trapped cold atoms over a large distance," Phys. Rev. A **63**, 031401 (2001).

[118] T. Kishimoto, P. Schwindt, Y.-J. Wang, W. Jhe, D. Anderson, and E. Cornell, "Bose-Einstein Condensation and Wave-guide Interferometry", 2001, DAMOP/DAMP (London, Ontario).

[119] H. J. Lewandowski, D. M. Harber, D. L. Whitaker, and E. A. Cornell, "Observation of Anomalous Spin-State Segregation in a Trapped Ultracold Vapor," Phys. Rev. Lett. **88**, 070403 (2002).

[120] K. W. Madison, C. F. Bharucha, P. R. Morrow, S. R. Wilkinson, Q. Niu, B. Sundaram, and M. G. Raizen, "Quantum transport of ultracold atoms in an accelerating optical potential," Appl. Phys. B **65**, 693 (1997).

[121] E. Peik, M. B. Dahan, I. Bouchoule, Y. Castin, and C. Salomon, "Bloch oscillations and an accelerator for cold atoms," Appl. Phys. B **65**, 685 (1997).

[122] W. Hnsel, P. Hommelhoff, T. W. Hnsch, and J. Reichel, "Bose-Einstein condensation on a microelectronic chip," Nature **413**, 498 (2001).

[123] A. Ashkin, "Optical trapping and manipulation of neutral particles," Proc. Natl. Acad. Sci. USA **94**, 4853 (1997).

[124] R. Onofrio, D. S. Durfee, C. Raman, M. Khl, C. E. Kuklewicz, and W. Ketterle, "Surface excitations in a Bose-Einstein condensate," Phys. Rev. Lett. **84**, 810 (2000).

[125] D. M. Stamper-Kurn, 2002, Private communication.

[126] J. O'Hanlon, *A User's Guide to Vacuum Technology* (Wiley, New York, 1989).

[127] M. A. Joffe, Ph.D. thesis, Massachusetts Institute of Technology, 1993.

[128] W. D. Phillips, in *Laser Manipulation of Atoms and Ions*, *Proceedings of the International School of Physics Enrico Fermi, Course CXVIII*, edited by E. Arimondo, W. Phillips, and F. Strumia (North-Holland, Amsterdam, 1992), pp. 289–343.

[129] N. Ramsey, *Molecular Beams* (Oxford University Press, New York, 1959).

[130] C. Kuklewicz, Master's thesis, Massachusetts Institute of Technology, 2000.

[131] S. L. Cornish, N. R. Claussen, J. L. Roberts, E. A. Cornell, and C. E. Wieman, "Stable ^{85}Rb Bose-Einstein Condensates with Widely Tunable Interactions," Phys. Rev. Lett. **85**, 1795 (2000).

[132] D. G. Fried, T. C. Killian, L. Willmann, D. Landhuis, S. C. Moss, D. Kleppner, and T. J. Greytak, "Bose-Einstein Condensation of Atomic Hydrogen," Phys. Rev. Lett. **81**, 3811 (1998).

[133] W. Ketterle, K. B. Davis, M. A. Joffe, A. Martin, and D. E. Pritchard, "High-Densities of Cold Atoms in a Dark Spontaneous-Force Optical Trap," Phys. Rev. Lett. **70**, 2253 (1993).

[134] A. L. Migdall, J. V. Prodan, W. D. Phillips, T. H. Bergeman, and H. J. Metcalf, "First Observation of Magnetically Trapped Neutral Atoms," Phys. Rev. Lett. **54**, 2596 (1985).

[135] M. D. Barrett, J. A. Sauer, and M. S. Chapman, "All-Optical Formation of an Atomic Bose-Einstein Condensate," Phys. Rev. Lett. **87**, 010404 (2001).

[136] T. Esslinger, I. Bloch, and T. W. Hnsch, "Bose-Einstein condensation in a quadrupole-Ioffe-configuration trap," Phys. Rev. A **58**, R2664 (1998).

[137] J. Fortagh, A. Grossman, C. Zimmermann, and T. W. Hänsch, "Minaturized Wire Trap for Neutral Atoms," Phys. Rev. Lett. **81**, 5310 (1998).

[138] J. Denschlag, D. Cassettari, and J. Schmiedmayer, "Guiding Neutral Atoms with a Wire," Phys. Rev. Lett. **82**, 2014 (1999).

[139] J. D. Weinstein and K. G. Libbrecht, "Microscopic magnetic traps for neutral atoms," Phys. Rev. A **52**, 4004 (1995).

[140] J. Reichel, W. Hänsel, and T. W. Hänsch, "Atomic Micromanipulation with Magnetic Surface Traps," Phys. Rev. Lett. **83**, 3398 (1999).

[141] D. Müller, D. Z. Anderson, R. J. Grow, P. D. D. Schwindt, and E. A. Cornell, "Guiding Neutral Atoms Around Curves with Lithographically Patterned Current-Carrying Wires," Phys. Rev. Lett. **83**, 5194 (1999).

[142] N. H. Dekker, C. S. Lee, V. Lorent, J. H. Thywissen, S. P. Smith, M. Drndić, R. M. Westervelt, and M. Prentiss, "Guiding Neutral Atoms on a Chip," Phys. Rev. Lett. **84**, 1124 (2000).

[143] D. Cassettari, A. Chenet, R. Folman, A. Hasse, B. Hessmo, P. Krüger, S. Schneider, T. Calarco, and J. Schmiedmayer, "Micromanipulation of Neutral Atoms with Nanofabricated Structures," Applied Phys. B **70**, 721 (2000).

[144] R. Folman, P. Krüger, D. Cassettari, B. Hessmo, T. Maier, and J. Schmiedmayer, "Controlling Cold Atoms using Nanofabricated Surfaces: Atom Chips," Phys. Rev. Lett. **84**, 4749 (2000).

[145] H. Ott, J. Fortagh, G. Schlotterbeck, A. Grossmann, and C. Zimmermann, 2001, ICOLS XV poster (Snowbird, Utah).

[146] J. Reichel, W. Hänsel, P. Hommelhoff, R. Long, T. Rom, T. Steinmetz, and T. W. Hänsch, 2001, ICOLS XV poster (Snowbird, Utah).

[147] A. Haase, D. Cassettari, B. Hessmo, and J. Schmiedmayer, "Trapping neutral atoms with a wire," Phys. Rev. A **64**, 043405 (2001).

[148] H. Ott, J. Fortagh, G. Schlotterbeck, A. Grossmann, and C. Zimmermann, "Bose-Einstein Condensation in a Surface Microtrap," Phys. Rev. Lett. **87**, 230401 (2001).

[149] K. Bongs, S. Burger, S. Dettmer, D. Hellweg, J. Arlt, W. Ertmer, and K. Sengstock, "Waveguide for Bose-Einstein condensates," Phys. Rev. A **63**, 031602 (2001).

[150] S. Dettmer, D. Hellweg, P. Ryytty, J. J. Arlt, W. Ertmer, K. Sengstock, D. S. Petrov, G. V. Shlyapnikov, H. Kreutzmann, L. Santos, and M. Lewenstein, "Observation of Phase Fluctuations in Elongated Bose-Einstein Condensates," Phys. Rev. Lett. **87**, 160406 (2001).

[151] J. Fortagh, H. Ott, S. Kraft, and C. Zimmermann, "Surface Effects on a Bose-Einstein Condensate in a Magnetic Microtrap," (2002), pre-print cond-mat/0205310.

[152] P. Leboeuf and N. Pavloff, "Bose-Einstein beams: Coherent propagation through a guide," Phys. Rev. A **64**, 033602 (2001).

[153] J. H. Thywissen, R. M. Westervelt, and M. Prentiss, "Quantum Point Contacts for Neutral Atoms," Phys. Rev. Lett. **83**, 3762 (1999).

[154] E. A. Hinds, C. J. Vale, and M. G. Boshier, "Two-Wire Waveguide and Interferometer for Cold Atoms," Phys. Rev. Lett. **86**, 1462 (2001).

[155] T. H. Maiman, "Stimulated Optical Radiation in Ruby," Nature **187**, 493 (1960).

[156] A. Javan, W. R. Bennett, and D. Herriott, "Population Inversion and Continuous Optical Maser Oscillation in a Gas Discharge Containing a He-Ne Mixture," Phys. Rev. Lett. **6**, 106 (1961).

[157] B. Blair, 'Scientists Who Made A Difference, Ali Javan: The Gas Laser and Beyond', http://www.azer.com/aiweb/categories/magazine/42_folder/42_articles/42_javan.html.

[158] M. Holland, K. Burnett, C. Gardiner, J. I. Cirac, and P. Zoller, "Theory of an atom laser," Phys. Rev. A **54**, R1757 (1996).

[159] R. J. C. Spreeuw, T. Pfau, U. Janicke, and M. Wilkens, "Laser-like scheme for atomic-matter waves," Europhys. Lett. **32**, 469 (1995).

[160] M. Olshanii, Y. Castin, and J. Dalibard, in *Proceedings of the 12th International Conference on Laser Spectroscopy*, edited by M. Inguscio, M. Allegrini, and A. Sasso (World Scientific, Singapore, 1996), p. 7.

[161] L. Santos, F. Floegel, T. Pfau, and M. Lewenstein, "Continuous optical loading of a Bose-Einstein condensate," Phys. Rev. A **63**, 063408 (2001).

[162] D. Schneble, H. Gauck, M. Hartl, T. Pfau, and J. Mlynek, in *Bose-Einstein condensation in atomic gases*, *Proceedings of the International School of Physics Enrico Fermi, Course CXL*, edited by M. Inguscio, S. Stringari, and C. Wieman (IOS Press, Amsterdam, 1999), pp. 487–488.

[163] E. Mandonnet, R. Dum, A. Minguzzi, I. Carusotto, Y. Castin, and J. Dalibard, "Evaporative cooling of an atomic beam," Eur. Phys. J. D. **10**, 9 (2000).

[164] B. K. Teo and G. Raithel, "Loading Mechanism for Atomic Guides," Phys. Rev. A **63**, 031492(R) (2001).

[165] P. Cren, C. F. Roos, A. Aclan, J. Dalibard, and D. Guéry-Odelin, 2002, pre-print, cond-mat/0203618.

[166] W. Rooijakkers, M. Vengalattore, R. Conroy, and M. Prentiss, 2002, private communication.

[167] D. S. Hall, M. R. Matthews, C. E. Wieman, and E. A. Cornell, "Measurements of Relative Phase in Two-Component Bose-Einstein Condensates," Phys. Rev. Lett. **81**, 1543 (1998).

[168] D. Jaksch, S. Gardiner, K. Schulze, J. Cirac, and P. Zoller, "Uniting Bose-Einstein Condensates in Optical Resonators," Phys. Rev. Lett. **86**, 4733 (2001).

[169] M. Kozuma, Y. Suzuki, Y. Torii, T. Sugiura, T. Kuga, E. W. Hagley, and L. Deng, "Phase coherent amplification of matter waves," Science **286**, 2309 (1999).

[170] G. Modugno, G. Ferrari, G. Roati, R. J. Brecha, A. Simoni, and M. Inguscio, "Bose-Einstein Condensation of Potassium Atoms by Sympathetic Cooling," Science **294**, 1320 (2001).

[171] A. Robert, O. Sirjean, A. Browaeys, J. Poupard, S. Nowak, D. Boiron, C. I. Westbrook, and A. Aspect, "A Bose-Einstein Condensate of Metastable Atoms," Science **292**, 461 (2001).

[172] F. P. D. Santos, J. Lonard, J. Wang, C. J. Barrelet, F. Perales, E. Rasel, C. S. Unnikrishnan, M. Leduc, and C. Cohen-Tannoudji, "Bose-Einstein Condensation of Metastable Helium," Phys. Rev. Lett. **86**, 3459 (2001).

[173] R. Grimm group at Innsbruck (2002);
see http://exphys.uibk.ac.at/ultracold/CsBEC.html.

[174] M. Greiner, O. Mandel, T. Esslinger, T. W. Hnsch, and I. Bloch, "Quantum Phase Transition from a Superfluid to a Mott Insulator in a Gas of Ultracold Atoms," Nature **415**, 39 (2002).

[175] S. Gupta, K. Dieckmann, Z. Hadzibabic, and D. E. Pritchard, "Contrast Interferometry using Bose-Einstein Condensates to Measure h/m and α," Phys. Rev. Lett. **89**, 140401 (2002).

[176] I. A. Yu, J. M. Doyle, J. C. Sandberg, C. L. Cesar, D. Kleppner, and T. J. Greytak, "Evidence for universal quantum reflection of hydrogen from liquid ^{4}He," Phys. Rev. Lett. **71**, 1589 (1993).

[177] F. Shimizu, "Specular Reflection of Very Slow Metastable Neon Atoms from a Solid Surface," Phys. Rev. Lett. **86**, 987 (2001).

[178] T. Mizushima, K. Machida, and T. Kita, "Mermin-Ho Vortex in Ferromagnetic Spinor Bose-Einstein Condensates," Phys. Rev. Lett. **89**, 030401 (2002).